UNIVERSITÉ DE STRASBOURG

ÉCOLE DOCTORALE PHYSIQUE ET CHIMIE-PHYSIQUE

Institut de Physique et Chimie des
Matériaux de Strasbourg (IPCMS)

THÈSE présentée par :

CHAKER Ziyad

soutenue le : **22 Septembre 2017**

pour obtenir le grade de : **Docteur de l’université de Strasbourg**
Discipline/ Spécialité : **Physique et chimie du solide**

Étude par dynamique moléculaire *ab initio* des propriétés magnétiques, électroniques et structurales de matériaux lamellaires hybrides organiques-inorganiques

THÈSE dirigée par :

M. MASSOBRIO Carlo	Docteur, Université de Strasbourg (UdS)

RAPPORTEURS :

M^{me} MOLTENI Carla	Professeure, King's College de Londres
M. BOUCHER Florent	Docteur, Institut des Matériaux Jean Rouxel de Nantes

AUTRES MEMBRES DU JURY :

M^{me} PREVOT Vanessa	Docteur, Institut de Chimie de Clermont-Ferrand
M. ROBERT Vincent	Professeur, Laboratoire de Chimie Quantique (UdS)
M. ORI Guido	Docteur, Université de Strasbourg (UdS)

Ma mère me met au monde
et mon père me construit.
Ma soeur me forme
et mes amis m'entraînent.
La philosophie me crée
et ma femme me fait exister.
Mes seigneurs m'apprennent
car la science est ma passion
et l'art son exaltation.
L'histoire m'instruit,
la politique m'éduque
et l'économie me libère.
La haine de l'amour me repousse
et l'amour de la haine m'attire.
Tel est mon équilibre du monde,
ma méta-vie profonde.
Le grand sommeil me délivrera
car la fin me méprise déjà..
Cogito, ergo sum ?

Un parmi les Hommes, humain

Première partie

Résumé de thèse en français

Table des matières

Introduction

Les matériaux hybrides organiques-inorganiques forment une classe de systèmes dans lesquels plusieurs types de molécules organiques peuvent être insérées au sein d'une structure dite d'accueil, souvent de nature inorganique [1]. Ce processus d'insertion permet de contrôler précisément les propriétés physico-chimiques du composé obtenu en exploitant la flexibilité et les fonctionnalités portées par les chaînes organiques en conjonction avec les propriétés mécaniques des parties inorganiques. Les matériaux hybrides représentent donc un excellent moyen d'obtenir des structures "à la carte" visant à exploiter la synergie des réseaux inorganiques et organiques pour engendrer les propriétés souhaitées. Dans le cadre de ce travail de thèse, nous avons catégorisé les différents types de matériaux hybrides qui existent dans la littérature en utilisant plusieurs paramètres comme la dimension du système, la nature des liaisons chimiques ou la voie de synthèse utilisée. Cependant, dans une telle classification, de nombreuses distinctions relatives à la structure, aux propriétés électroniques et magnétiques restent très difficiles à prédire du fait de la complexité intrinsèque à ces structures hybrides. C'est dans ce contexte que s'inscrit notre étude théorique de ces matériaux, utilisant les méthodes de la théorie de la fonctionnelle de la densité (DFT) jointes aux techniques de dynamique moléculaire (MD) dans l'approche Car-Parrinello (CPMD) [2]. Nous utilisons cette méthode afin d'opérer simultanément des calculs de structure électronique et de dynamique moléculaire pour des systèmes allant jusqu'à 608 atomes dans la cellule de simulation.

Dans un premier temps, nous avons développé un protocole permettant d'étudier l'évolution des propriétés de matériaux hybrides spécifiques sous l'effet de stimuli extérieurs comme la pression ou la température. Nous avons réduit notre domaine d'étude à la famille des structures hybrides lamellaires d'hydroxyde de cuivre $Cu_2(OH)_3X$ avec X un anion échangeable (pouvant apparaître sous la forme de différentes chaînes organiques). En particulier, nous analysons, de manière systématique, un matériau très largement utilisé comme référence dans cette communauté : l'hydroxyde acétate de cuivre $Cu_2(OH)_3(CH_3COO)\bullet(H_2O)$, noté CuOHAc. En effet, sa structure est très bien caractérisée depuis la synthèse d'une forme monocristalline par Svarcova et al [3]. De plus, ses propriétés magnéto-structurales sont bien établies expérimentalement par le travail de Suzuki et al [4] dans lequel les auteurs observent une transition d'un état antiferromagnétique (AF) à un état ferromagnétique (F) sous l'effet de la pression.

Dans un second temps, nous appliquons l'ensemble des protocoles de simulation développés à l'étude de nouveaux matériaux hybrides lamellaires simples contenant des molécules de fluorènes mono- et di- phosphoniques de compositions respectives, $Cu_2(OH)_{4-x}$ $(C_{13}H_{10}O_3P)_x{\cdot}(H_2O)_y$ (x=0.31, y=0.5 à 2) et $Cu_2(OH)_{4-x}(C_{13}H_{10}O_6P_2)_x{\cdot}(H_2O)_y$ (x=0.23, y=2.5 à 3.5). Nous étudions ainsi différentes structures atomiques compatibles avec les compositions chimiques fournies expérimentalement et nous évaluons les propriétés électroniques et magnétiques de ces systèmes. Ce travail est effectué de manière combinée avec une équipe expérimentale qui synthétise et caractérise au mieux ce nouveau type d'hydroxydes lamellaires. Le but étant d'utiliser nos méthodes FPMD en guise de complément aux données expérimentales obtenues mais aussi pour aller au-delà et prédire l'éventail de propriétés associées à ces matériaux.

Chapitre 1

Les matériaux hybrides lamellaires

1.1 La chimie des hybrides organiques-inorganiques

Dans la quête de matériaux avec des structures et des propriétés spécifiques, un regain majeur d'intérêt a été récemment observé dans l'étude des matériaux hybrides organiques-inorganiques [5]. Deux exemples de ce type de structures sont les MOF ("Metal-Organic Frameworks") ainsi que les matériaux hybrides lamellaires, tous deux caractérisés par des méthodes de synthèse particulières [6, 7]. Dans le cas des MOF, des unités moléculaires sont obtenues avec des liaisons fortes entre les métaux et les molécules organiques et permettent de combiner propriétés magnétiques et chiralité ou avec la ferroélectricité [8, 9, 10]. Cependant, comme il a été montré par des expériences de diffraction aux neutrons dans des systèmes multiferroiques [11], l'interface entre les unités moléculaires devient cruciale pour le contrôle des effets coopératifs à longue distance dans ces systèmes [12]. Dans les matériaux hybrides décrits dans la littérature, les liaisons entre parties organiques et inorganiques sont souvent faibles, ce qui affecte la synergie entre les propriétés des composants [13, 14, 15, 16]. Dans ce contexte, l'hybridation des matériaux hydroxydes métalliques lamellaires aboutissant aux hydroxydes lamellaires simples (LSH) conduit à des liaisons plus fortes entre les métaux de transition et les molécules organiques formant ainsi un cristal [17]. Le contrôle des méthodes de synthèse de ce type de matériaux permet l'obtention de systèmes ferro-, antiferro- ou ferrimagnétiques [7, 18]. De nombreuses applications pour la catalyse [19], les cellules photovoltaïques [20] ou dans le cadre de l'optique non-linéaire [21] sont autant d'exemples du succès des matériaux hybrides dans le contexte technologique actuel.

L'élaboration de tels matériaux hybrides s'est développée considérablement depuis la venue de la "chimie douce" [22]. C'est en particulier les méthodes dites "sol-gel" qui sont un exemple important des possibilités de cette nouvelle chimie. Le concept de "chimie douce" tient son nom des conditions "douces" de synthèse en termes de température, de pression (ambiantes) ou de pH (relativement neutre). Le pionnier de ces méthodes est Jacques Livage [23, 24] qui a introduit ce concept au sein de la chimie moderne en s'inspirant du monde biologique et, en particulier, des processus de bio-minéralisation. En effet, le développement des processus de chimie inorganique, dans des conditions synthétiques "douces" est relié à la possibilité d'utiliser des précurseurs métal-organiques, des températures basses et à la versatilité des systèmes colloïdaux obtenus. Tous ces processus permettent un mélange entre les composants organiques et inorganiques en principe, pour tous les ratios souhaités [25]. Trois réactions chimiques sont évoquées dans la plupart des processus sol-gel : l'hydrolyse, l'oxolation et l'olation [26]. En contrôlant l'environnement (solvant, teneur en eau, pH...) et les ions métalliques utilisés, différents types de produits finaux sont obtenus. C'est en limitant l'agglomération des particules formées dans les solutions que des *sols* sont synthétisés sous la forme de colloïdes suspendus. D'un autre côté, une croissance ou agglomération importante peut se produire encapsulant des molécules de solvant et de petits monomères et un *gel* est obtenu. A partir de ces principes, une grande variété de matériaux hybrides sont produits et utilisés dans les applications évoquées plus haut [27, 28, 29, 30, 31].

Classifications des matériaux hybrides selon les critères de:

Dimensionnalité des composants inorg. (organiques)

Dimensionnalité du réseau inorganique, I^n (n = 0 to 3)

Métal-organique-métal connectivité, O^n (n = 0 to 3)

	0	*1*	*2*	*3*
0	Complexes moléculaires	chaînes inorg. hybrides	Couches inorg. hybrides	Hybrides inorg. 3D
1	Chaînes polymériques de coordination	Couches inorg.-org. mélangées	Complexes moléculaires	?
2	Polymères de coordination en couches	Réseaux 3D inorg.-org. mélangés	?	?
3	Polymères de coordination 3D	?	?	?

Types d'interactions entre parties inorg. et org.

Classe I	*Classe II*
Interactions faibles	Liaisons covalentes
Liaison-H	Liaisons de coordination
Van der Waals	Liaisons iono-covalentes
Electrostatique	Liaisons acide-base de Lewis

Méthodes chimiques de synthèse

Voie A	*Voie B*	*Voie C*	*Voie D*
Méthodes sol-gel conventionelles (hydrolyse/condensation)	Utilisation de nano-briques de base (NBB)	Procédures d'auto-assemblage combinées à l'approche NBB	Synthèse intégrative
Synthèse hydrothermale	Assemblages des NBB	Fabrication de modèles par tensioactifs organiques	Méthodes de micro-moulage
Utilisation de precurseurs pontants	Dispersion des NBB	Utilisation de precurseurs pontants	Phénomènes de séparation de phases contrôlés

FIGURE 1 – Classification des matériaux hybrides organiques-inorganiques sur la base de trois paramètres d'ordre : la **dimensionnalité de chaque composant** (I = inorganique, O = organique) dans la partie supérieure gauche, le **type de liaison chimique** entre les deux parties dans le tableau supérieur droit et la **méthode de synthèse** (partie inférieure de la figure). *Le premier tableau est adapté du tableau 1 de la référence [32] alors que les deux autres tableaux sont construits en fonction des classifications proposées dans les références [22, 33]*

Ces descriptions de méthodes de production de matériaux hybrides illustrent leur diversité et donc la difficulté de définir et classifier exactement ce type de matériaux. Nous nous fixons, dans cette section, la tâche de construire cette classification sur la base de tous les paramètres d'ordre utilisés dans la littérature. Les paramètres que nous avons identifié sont la **dimensionnalité des réseaux inorganiques et organiques**, la **nature des liaisons chimiques** ainsi que les **méthodes de synthèse** utilisées pour obtenir le produit final. Nous résumons, dans ce qui suit, l'étendue et l'utilité de ces trois paramètres et nous illustrons ces méthodes de classification dans la Figure 1.

- En considérant le critère de dimensionnalité des réseaux organiques et inorganiques (en haut à gauche de la Figure 1), on peut définir une phase dite "hôte" (ou d'accueil) et une autre dite "invité" (en anglais "guest") dans le système [20]. Un moyen formel de quantifier ces notions est celui introduit par Cheetham et al. [32]. Le réseau organique de dimensionnalité n est noté O^n et le réseau inorganique I^n (n = 0, 1, 2 ou 3), ce qui permet de caractériser de nombreux matériaux hybrides sous la forme $\mathrm{I}^n\mathrm{O}^n$.

- Une deuxième méthode de classification (tableau en haut à droite dans la Figure 1) se base sur la nature de l'interface organique-inorganique dans les hybrides. C'est en particulier la nature des liaisons chimiques entre ces deux parties constitutives qui permet une distinction. Ainsi, les matériaux hybrides avec de faibles liaisons entre ligands et métaux seraient de classe I et ceux caractérisés par des liaisons fortes (covalentes), de classe II [22].

- Enfin, une troisième classification distingue les matériaux hybrides sur la base de méthodes chimiques utilisées pour la synthèse (tableau du bas dans la figure 1). Le **protocole A** correspond aux synthèses via la chimie sol-gel conventionnelle et permet l'obtention de matériaux hybrides amorphes à travers l'hydrolyse d'alcoxides métalliques modifiés par des espèces organiques. Le **protocole B** consiste en la formation de briques de base nanométriques (NBB) qui peuvent être agglomérées ou fonctionnalisés mais aussi utilisés pour obtenir des matériaux lamellaires comme des argiles et des hydroxydes lamellaires simples ou doubles. Le **protocole C** correspond aux procédures d'auto-assemblage très utilisées dans la croissance de silices mésoporeuses fonctionnalisées. Enfin, le **protocole D** rassemble les méthodes dites de synthèse intégrative comme le micro-moulage qui permettent un bon contrôle de la forme des matériaux microscopiques obtenus.

Comme évoqué précédemment, nous étudierons exclusivement des hydroxydes lamellaires simples (LSH) car ceux-ci sont des matériaux hybrides typiques. Suivant la classification établie, les LSH sont donc de classe I ou II (dépendant des cas), caractérisés par un réseau de couches inorganiques entre lesquelles des molécules organiques sont insérées ($\mathrm{I}^2\mathrm{O}^1$) et synthétisées à travers les protocoles de type B. Les structures de base des LSH correspondent à la formule chimique : $\mathrm{M_2(OH)_3(X)}$ avec $\mathrm{X = NO_3, CH_3CO_2, Cl}$) dérivant de systèmes de type botallackite. La structure cristalline consiste en des couches quasi-planes d'octaèdres d'oxygènes autour des sites métalliques, séparés par des anions avoisinant ces sites ainsi que des molécules d'eau. Les courtes distances métal-métal ($\simeq$ 3 Å) assurent une structure lamellaire résultant en des interactions magnétiques à travers les fragments métal-oxygène-métal. C'est cette structure hybride en couche qui permet l'exploration d'états ferromagnétiques ou antiferromagnétiques à travers l'insertion de différents ligands organiques dans le système. Dans ce projet, nous nous proposons d'étudier par des méthodes théoriques les structures LSH en utilisant l'hydroxyde acétate de cuivre comme référence pour établir les protocoles de simulation les plus adaptés. Dans la prochaine section, on résume les études théoriques précédentes effectuées sur ce matériau et on introduit le type particulier de la méthode utilisée dans notre travail, la dynamique moléculaire *ab initio*.

1.2 Travaux théoriques sur les matériaux hybrides

Dépendant du type de problème étudié, les méthodes de modélisation utilisées peuvent être "classiques" (définition très générale) comme la dynamique moléculaire (MD) ou la méthode de Monte-Carlo (MC). Cependant, dans la plupart des cas, pour prendre en compte la nature des liaisons chimiques dans le système, des calculs "quantiques" sont nécessaires comme dans les méthodes de chimie quantique ou de théorie de la fonctionnelle de la densité (DFT).

Dans la Figure 2, la diversité des modèles et des systèmes d'étude sont associés afin de donner un point de vue global sur les méthodes de simulations qui sont, aujourd'hui, les plus utilisées en science des matériaux. Afin de modéliser le comportement d'un matériau, une optimisation structurale précise doit être effectuée en incluant le plus possible, les champs extérieurs de température et de pression, indispensables pour reproduire l'environnement réel du matériau. Pour ce faire, au-delà du calcul de la structure électronique, nous devons pouvoir suivre le mouvement des atomes de la structure en fonction du temps. Or, c'est exactement ce que la dynamique moléculaire permet de faire. Quand cette méthode est employée, les forces interatomiques sont calculées à partir du potentiel d'interaction choisi au départ. Lorsque ce potentiel est calculé par les méthodes "quantiques" de structure électronique, la méthode obtenue est décrite comme : dynamique moléculaire *ab initio* notée FPMD dans la suite. Nous mettons en avant cette méthode dans la figure 2 afin de définir les échelles d'espace et de temps accessibles pour ce type d'approches. En effet, nous utilisons exclusivement ces méthodes FPMD dans le cadre de ce projet, comme elles sont implémentées dans le code CPMD [2]. Nous nous intéressons principalement aux hydroxydes lamellaires simples en commençant par l'étude détaillée des propriétés structurales, électroniques et magnétiques de l'hydroxyde acétate de cuivre.

Plusieurs travaux théoriques FPMD ont permis d'étudier l'hydroxyde acétate de cuivre sous sa forme hydratée $Cu_2(OH)_3(CH_3COO)\cdot H_2O$ noté CuOHAc dans la suite. Ce type d'études permet d'estimer les propriétés électroniques et structurales des hybrides lamellaires en fonction de l'anion inséré dans le système. D'une part, l'effet de la longueur de chaîne alkyle insérée sur les propriétés du matériau hybride a fait l'objet de plusieurs études [34, 35]. D'autre part, l'existence d'un couplage magnéto-structural dans l'hydroxyde acétate de cuivre a été démontrée par Suzuki et al [4] à travers l'application d'une pression sur le matériau induisant un état ferromagnétique observable. Motivés par ces études expérimentales, Fan Yang et al. [36, 37, 7] ont publié une série de trois articles dans l'objectif de reproduire ces effets en utilisant les méthodes FPMD.

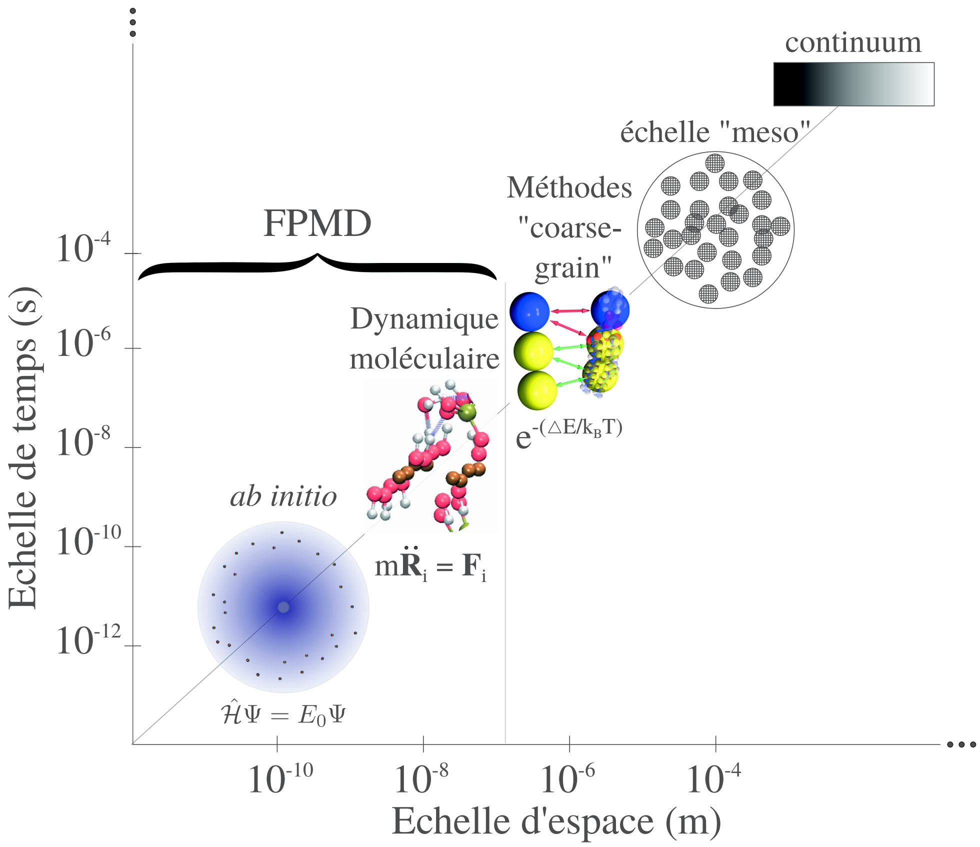

FIGURE 2 – Échelles de taille et de temps correspondantes aux différentes méthodes de modélisation existantes. Une gamme énorme de phénomènes peut être comprise par des techniques de simulation. Aux deux extrêmes se trouvent, d'un côté les modèles *ab initio* pour une description quantique afin d'obtenir la structure électronique et de l'autre, des équations de la chaleur utilisées en milieux continus, pour modéliser, par exemple, la convection thermique dans le manteau terrestre. La méthode principale utilisée dans ce projet pour décrire les propriétés structurelles et électroniques est la dynamique moléculaire à partir des premiers principes (FPMD) dans laquelle une description quantique des électrons est couplée aux mouvements classiques des ions

Le tableau de la figure 3-I illustre le premier travail de Yang et al. [36] dans lequel la densité de spin a été analysée pour le composé CuOHAc confirmant la présence d'une quantité non-négligeable de celle-ci sur les sites d'oxygènes pontant deux sites de cuivre. Une corrélation est exprimée entre le module mais aussi le signe de cette densité de spin locale avec la distance et la densité de spin des atomes de cuivres voisins. Une distinction est faite entre les oxygènes liés aux hydroxydes (en haut du tableau) et ceux liés aux acétates (en bas du tableau) pour comparer les deux cas. Les structures associées et leurs isosurfaces de densités de spin sont exposées en haut de la figure 3-I. La configuration étudiée correspond au système sans pression.

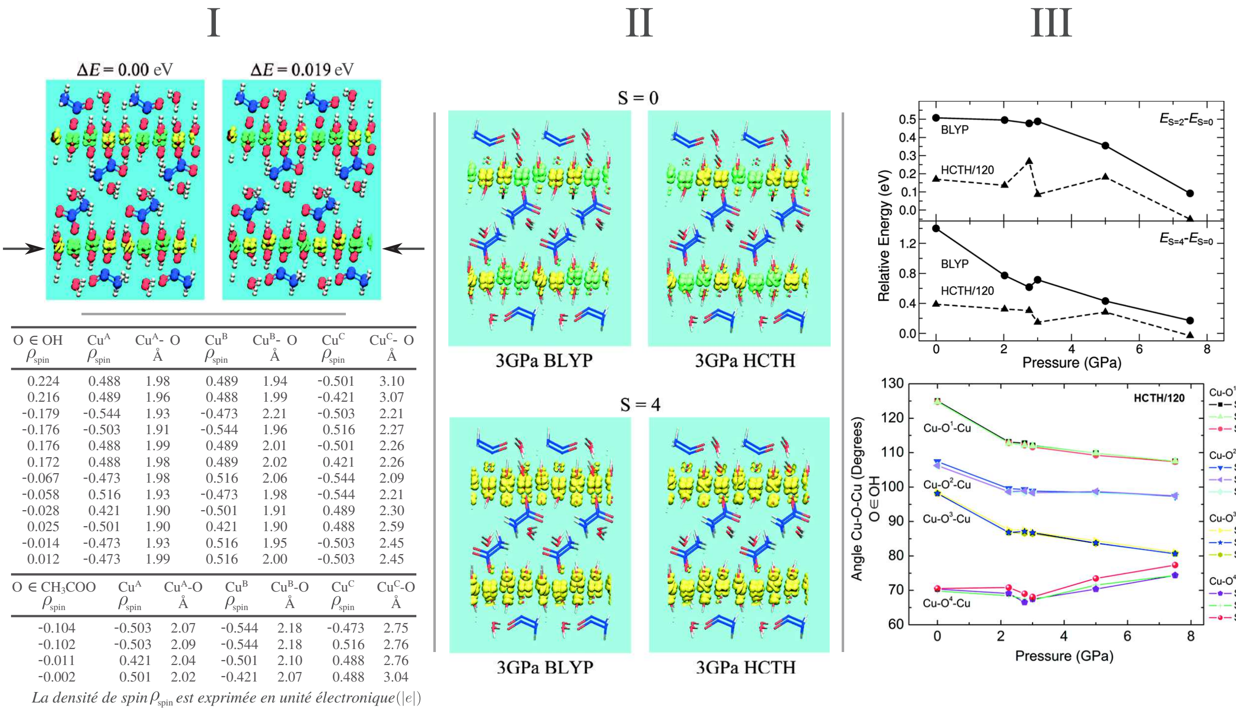

O ∈ OH ρ_{spin}	Cu^A ρ_{spin}	Cu^A- O Å	Cu^B ρ_{spin}	Cu^B- O Å	Cu^C ρ_{spin}	Cu^C- O Å
0.224	0.488	1.98	0.489	1.94	-0.501	3.10
0.216	0.489	1.96	0.488	1.99	-0.421	3.07
-0.179	-0.544	1.93	-0.473	2.21	-0.503	2.21
-0.176	-0.503	1.91	-0.544	1.96	0.516	2.27
0.176	0.488	1.99	0.489	2.01	-0.501	2.26
0.172	0.488	1.98	0.489	2.02	0.421	2.26
-0.067	-0.473	1.98	0.516	2.06	-0.544	2.09
-0.058	0.516	1.93	-0.473	1.98	-0.544	2.21
-0.028	0.421	1.90	-0.501	1.91	0.489	2.30
0.025	-0.501	1.90	0.421	1.90	0.488	2.59
-0.014	-0.473	1.93	0.516	1.95	-0.503	2.45
0.012	-0.473	1.99	0.516	2.00	-0.503	2.45

O ∈ CH_3COO ρ_{spin}	Cu^A ρ_{spin}	Cu^A-O Å	Cu^B ρ_{spin}	Cu^B-O Å	Cu^C ρ_{spin}	Cu^C-O Å
-0.104	-0.503	2.07	-0.544	2.18	-0.473	2.75
-0.102	-0.503	2.09	-0.544	2.18	0.516	2.76
-0.011	0.421	2.04	-0.501	2.10	0.488	2.76
-0.002	0.501	2.02	-0.421	2.07	0.488	3.04

La densité de spin ρ_{spin} est exprimée en unité électronique $(|e|)$

FIGURE 3 – **I)** Partie supérieure : structure optimisée de l'hydroxyde acétate de cuivre $Cu_2(OH)_3(CH_3COO) \cdot H_2O$ (CuOHAc) dans la configuration antiferromagnétique (spin total S = 0) pour les deux distributions de densité de spin les plus stables du système. Les atomes Cu sont marron, C en bleu, O en rouge, H en blanc et les surfaces solides correspondent à des isosurfaces de densité de spin (α en vert et β en jaune) à une valeur de ± 0.03 e/Å^3 (*adapté à partir de la Figure 1 de la référence [36]*). Partie inférieure : Valeurs de densité de spin (ρ_{spin}) localisées sur les deux types d'atomes d'oxygène (voir texte) en correspondance avec la densité de spin et les distances des trois atomes de cuivre voisins (*adapté du TABLEAU 4 de la référence [36]*). **II)** distribution de la densité de spin pour le système CuOHAc sous l'effet d'une pression de 3 GPa, calculée avec les fonctions d'échange-corrélation BLYP (gauche) et HCTH (droite) et pour deux états de spin total du système, S = 0 (en haut) et S = 4 (en bas). *Résultats adaptés des figures 2 et 3 de la référence [37]*. **III)** Partie supérieure : énergies totales relatives, par rapport à la configuration S = 0 (AF), des états de spin S = 2 et S = 4 du système CuOHAc en fonction de la pression appliquée et pour les deux fonctionnelles d'échanges-corrélations considérées. Partie inférieure : angles $Cu\hat{O}Cu$ en fonction de la pression, pour chaque oxygène (appartenant à $CH_3CO_2^-$) reliant les sites de cuivre dans la structure CuOHAc. Les courbes de CuO^iCu (i = 1-4) sont déplacées de manière rigide le long de l'axe des ordonnés (*la figure originale et les valeurs numériques sont repris des tableaux 2, 3 et 4 et de la figure 4 de la référence [7]*)

En 2012, Yang et al. publient un deuxième article où l'effet de la pression est pris en compte [37]. Dans ce cas, deux états magnétiques de CuOHAc, l'un anti-ferromagnétique (S=0) et l'autre ferromagnétique (S=4) sont comparés pour une pression variant de 0 à 5 GPa en utilisant deux fonctionnelles d'échange-corrélation différentes : BLYP et HCTH, toutes deux dites GGA (définies dans le chapitre 2). Le résultat à 3 GPa est illustré dans la Figure 3-II à travers une différence d'énergie E(S=4) - E(S=0) séparant les états ferromagnétique (F) et antiferromagnétique (AF) de 0.715 eV (BLYP) et 0.215 eV (HCTH) à 3 GPa. Aucune transition magnétique n'est obtenue dans ce cas. En 2014, dans un troisième article [7], les auteurs obtiennent finalement une transition entre l'état AF (S=0) et un état ferromagnétique intermédiaire (S=2) de CuOHAc en appliquant une pression supérieure à 7.5 GPa. Cette transition est obtenue uniquement pour le calcul effectué avec la fonctionnelle d'échange-corrélation HCTH/120 comme représenté dans les graphes en haut de la Figure 3-III. De plus, un changement structural abrupt autour de 2.4 GPa est mis en avant à travers l'analyse des distances Cu-O et des angles Cu-O-Cu en fonction de la pression (en bas de la Figure 3-III). Malgré ces efforts, ces deux effets (magnétiques et structuraux) ne sont pas réellement corrélés (régions de pressions très différentes) et les comparaisons aux données expérimentales ne sont que qualitatives dans ces travaux. Nous irons plus loin dans le chapitre 3, dédié à une étude précise des comportements magnétiques et de la structure de l'hydroxyde acétate de cuivre sous pression.

Le chapitre 2 est dédié à une brève introduction aux méthodes de la dynamique moléculaire *ab initio* (FPMD) accompagnée de quelques exemples des protocoles de simulation utilisés dans ce travail de thèse.

Chapitre 2

Les méthodes de dynamique moléculaire *ab initio* (FPMD)

2.1 Théorie de la fonctionelle de la densité (DFT)

Afin d'être cohérent avec l'esprit de ce résumé, nous ne présenterons que les aspects fondamentaux de la théorie et ses applications dans notre étude. La DFT permet de traiter (sous certaines approximations) un problème à N-corps tout en étant une théorie effective (approche Kohn-Sham). La DFT est donc une méthode théorique permettant de quantifier certaines propriétés cruciales (valeurs d'observables) d'un système physique (molécule, cristal ou autre) en se basant sur une quantité clé : la densité électronique n($\vec{r}$). Contrairement à la fonction d'onde Ψ, qui n'a aucune réalité physique (c'est $|\Psi|^2$ qui est une probabilité de présence), la densité n($\vec{r}$) est une caractéristique réelle observable et mesurable dans un matériau. De plus, comme nous allons le voir, les théorèmes de Hohenberg-Kohn (H-K) nous assurent la possibilité d'exprimer l'énergie en fonction de la densité électronique. Ainsi, une grande variété de propriétés peut être déduite de calculs numériques basés sur cette densité.

Tout d'abord, résumons les principaux aspects théoriques de la DFT :

- Les théorèmes de H-K établissent que toutes les propriétés d'un système défini par un potentiel externe $V_{ext}(\vec{r})$ sont déterminées par la densité électronique n($\vec{r}$) de l'état fondamental d'énergie (GS = Ground State)

  $$E_{GS} = \min_{\tilde{n}(\vec{r})} E[\tilde{n}] \qquad avec \qquad E[\tilde{n}] = F_{HK}[\tilde{n}] + \int d^3r \; \tilde{n}(\vec{r}) \, V_{ext}(\vec{r}) \tag{2.1}$$

  obtenue par la minimisation de E $[\tilde{n}]$ par rapport à toute densité test $\tilde{n}(\vec{r})$.

- Le but principal de la DFT est d'obtenir une forme explicite de la fonctionnelle de Hohenberg-Kohn $F_{HK}[n]$ constituée de la somme des contributions de l'énergie cinétique des électrons (T[n]), de l'énergie d'interaction coulombienne (J[n]) ainsi que d'une partie non classique (E_{ncl}[n]) tenant compte des effets d'échange et des corrélations.

L'apport de Kohn et Sham a été de réussir à isoler le plus possible les contributions d'échange et des corrélations en considérant tout système de particules en interaction comme un système effectif sans interactions plus une contribution additionnelle à l'Hamiltonien tenant compte de ces interactions. Ajoutons que c'est grâce aux équations mono-électroniques de K-S que la procédure auto-cohérente de minimisation de l'énergie totale du système peut se paralléliser pour optimiser l'efficacité du code utilisé.

Il nous faut maintenant aborder un aspect important de l'utilisation de la DFT : les différentes approximations disponibles pour le terme d'échange et de corrélation. C'est grâce à celles-ci que l'implémentation de la théorie a été rendue possible au fil des années. Les approximations en DFT peuvent être, grossièrement, divisées en trois grandes classes :

- les méthodes se basant sur la densité locale (Local Density Approximation : LDA),
- les méthodes prenant en compte la non-homogénéité de la densité électronique dans le système (Generalized Gradient Approximation : GGA),
- les méthodes utilisant des "fonctionnelles hybrides".

Une amélioration de la LDA qui nous intéresse tout particulièrement est la GGA (Generalized Gradient Approximation). Plus précisément, celle proposée par Becke, Lee, Yang et Parr (BLYP) [38, 39] qui apporte beaucoup dans l'approximation du terme d'échange et corrélation (XC) comparée aux approches antérieures. La GGA n'exploite plus une fonctionnelle locale (outil mathématique adapté à la LDA) mais une fonctionnelle semi-locale prenant en compte le gradient $\vec{\nabla} n(\vec{r})$ de la densité. C'est cette méthode que nous utilisons dans ce travail de thèse. Les fonctionnelles hybrides ne seront pas abordées car trop coûteuses en termes de temps de calculs au vu de la taille des systèmes que nous étudions ($>$ 280 atomes dans la boîte de simulation). Un autre aspect de la DFT est l'utilisation d'une base d'ondes planes pour décrire les fonctions d'ondes du système ce qui nécessite des approximations permettant de traiter les électrons, dits de coeur, car trop d'ondes planes sont nécessaires pour reproduire leur comportement. Nous utilisons donc des "*pseudo-potentiels*" *(PP)* construits empiriquement ce qui permet de conserver une base uniquement constituée d'ondes planes pour les calculs de structure électronique. Dans ce cadre, nous utilisons deux pseudo-potentiels différents pour traiter les atomes de cuivre (métal de transition présent dans toutes les structures que nous étudions), tous deux visants à obtenir une bonne description des propriétés magnétiques locales et des propriétés électroniques du système. La première approche est dite NLCC ("Non Linear Core Corrections") et a été introduite par Louie et al. [40] tandis que la seconde est dite *semicore* et a été développée par Reis et al. [41]. Au vu de la qualité des résultats que nous obtenons avec cette dernière, l'approche *semicore* est la méthode de choix pour nos études des nouveaux matériaux lamellaires considérés dans le chapitre 4.

Nous ne développons pas davantage sur ce sujet mais une description bien plus complète de la DFT est présente dans la version anglaise de ce travail de thèse. Nous passons donc à l'exposition de la méthode de dynamique moléculaire *ab initio* que nous illustrons par des calculs que nous avons effectué sur des systèmes modèles.

2.2 L'approche de dynamique moléculaire Car-Parrinello (CPMD)

La dynamique moléculaire (MD) est une méthode introduite par le travail de Alder et Wainwright en 1950 [42] sur l'étude des transitions de phase dans un système de sphères dures. Cette approche classique permet de modéliser un système de particules approximées comme ponctuelles (atomes, molécules ou polymères) en interaction. Considérons un système de N$_I$ atomes caractérisés par leurs positions $\vec{R}_I$=(x$_I$,y$_I$,z$_I$) avec I = 1,..,N$_I$. Ces atomes interagissent via une fonction bien définie des positions, le potentiel V($\vec{R}_I$). Les forces $\vec{f}_I$ qui s'appliquent sur ces particules s'écrivent donc comme

$$\vec{f}_I = \frac{\partial V(\vec{R}_I)}{\partial \vec{R}_I} \tag{2.2}$$

Dans cette expression, la fonction 3N$_I$ dimensionnelle est appelée un champ de force caractéristique du potentiel V choisi pour ce système. Dans ce contexte, nous pouvons basculer vers la méthode FPMD introduite par Car et Parrinello en 1985 [43] et implémentée dans le code CPMD [2]. L'idée principale de la méthode est de combiner la dynamique ionique produite par la MD avec les calculs quantiques de structure électronique de la DFT. Dans ce but, la première étape est d'identifier la quantité faisant le pont entre les deux méthodes, le potentiel d'interaction V($\vec{R}_I$). C'est en effet ce potentiel qui est calculé *ab initio* (V^{AI}($\vec{R}_I$)) et permet de faire un calcul de MD couplé à un calcul DFT pour obtenir des trajectoires FPMD. Pour notre système de N$_I$ atomes, la DFT nous informe que l'énergie totale correspondante est une fonctionnelle de la densité électronique n($\vec{r}$) (avec $\vec{r}$ les positions électroniques) et est paramétrée par les positions des ions classiques E[n($\vec{r}$),{$\vec{R}_I$}]. Dans le cadre de la formulation de Kohn-Sham de la DFT, la densité électronique s'écrit comme

$$n(\vec{r}) = \sum_{i=1}^{Occupation} |\phi_i(\vec{r})|^2 \tag{2.3}$$

avec $\phi_i(\vec{r})$, l'orbitale de Kohn-Sham correspondant à l'état "i". Le potentiel V^{AI} s'écrit alors

$$V^{AI}(\{\vec{R}_I\}) = \min_{\{\phi_i\}} E[\{\phi_i\}, \{\vec{R}_I\}] \tag{2.4}$$

Cette expression exprime le problème variationnel auquel les équations aux valeurs propres de Kohn-Sham peuvent être appliquées. Cependant, l'approche de Car et Parrinello diffère de celle-ci puisqu'elle ne transforme pas le problème de minimisation en équations aux valeurs propres mais utilise une minimisation directe au moyen du recuit simulé ("Simulated Annealing") introduit par Kirpatrick, Gelatt et Vecchi en 1983 [44]. En considérant l'ensemble de ces éléments, on peut écrire un Lagrangien de Car et Parrinello comme suit

$$\begin{aligned} L_{CP} =& 2\sum_{i=1}^{Occ} \int \mu \left|\dot{\phi}_i(\vec{r},t)\right|^2 d\vec{r} + \frac{1}{2}\sum_I M_I \dot{\vec{R}}_I^2 - E[\{\phi_i\}, \vec{R}_I] \\ & + 2\sum_{ij} \Lambda_{ij} \left(\int \phi_i^*(\vec{r},t)\phi_j(\vec{r},t) d\vec{r} - \delta_{ij} \right) \end{aligned} \tag{2.5}$$

Celui-ci modélise un système d'ions "réels" de masses M$_I$ couplés avec un système d'électrons "classiques" pour lesquelles une masse fictive μ est associée. Ainsi les deux premiers termes correspondent aux énergies cinétiques associées à ces deux types de particules. Le dernier terme assure le respect de la contrainte d'orthonormalisation des orbitales utilisées. En appliquant les équations d'Euler-Lagrange, on obtient le système d'équations de mouvements des deux sous-systèmes (électrons et ions)

$$\begin{aligned} \mu\ddot{\phi}_i(\vec{r},t) &= -\frac{1}{2}\frac{\delta E[\{\phi_i\},\{\vec{R}_I\}]}{\delta\phi_i^*(\vec{r},t)} + \sum_j \Lambda_{ij}\phi_j(\vec{r},t) \\ M_I\ddot{\vec{R}}_I &= -\frac{\partial E}{\partial \vec{R}_I(t)} \end{aligned} \tag{2.6}$$

A ces deux équations s'ajoute une troisième équation de mouvement assurant l'inclusion de champs extérieurs tels que la pression ou la température mais nous ne développons pas davantage ces points techniques dans ce résumé. Maintenant, nous présentons deux aspects importants de nos simulations qui sont les calculs des densités de spin et la prise en compte de la pression appliquée sur nos systèmes.

Dans le cas des propriétés magnétiques, on se réfère au formalisme introduit par Von Barth et Hedin [45] permettant de généraliser l'ensemble des considérations développée dans le cas sans spin au cas avec spin. Ceci est fait dans le cadre de la LSD ("Local Spin Density approximation") mais se généralise aux autres types de fonctionnelles d'échange et de corrélation sans difficulté. Ainsi, le spin est introduit de manière *ad hoc* et les orbitales de Kohn-Sham ϕ_i sont écrites dans une représentation de fonctions d'ondes à deux composantes, une par orientation de spin ($\{\alpha,\beta\}$ ou $\{\uparrow,\downarrow\}$)

$$\phi(\vec{r}) = \begin{pmatrix} \phi^\alpha(\vec{r}) \\ \phi^\beta(\vec{r}) \end{pmatrix} \tag{2.7}$$

Ces nouvelles orbitales donnent lieu aux nouvelles densités de spin n$^\alpha$ et n$^\beta$ en utilisant la relation (1.6). Dans l'approche CPMD, on ne considère que le magnétisme colinéaire. Nous ne pouvons pas fixer le moment magnétique local associé à chaque site atomique mais nous fixons la multiplicité "M" ou le spin total "S" de notre boite de simulation sachant que M = 2S+1. On peut donc fixer l'aimantation totale de notre système en fixant au départ le nombre d'états "↑" (N$^\alpha$) et "↓" (N$^\beta$) ou plus précisément leur différence

$$\begin{aligned} S &= N_\alpha - N_\beta \\ &= \int n^\alpha(\vec{r})d^3r - \int n^\beta(\vec{r})d^3r \\ &= \frac{M-1}{2} \end{aligned} \tag{2.8}$$

On illustre un résultat concret de l'application de la méthode CPMD à un système dans différents états magnétiques dans la Figure 4. Dans cette figure, on représente une boite de simulation du système d'hydroxyde acétate de cuivre que nous étudions dans le prochain chapitre. Les 32 atomes de cuivre organisés en deux couches sont mis en avant par les isosurfaces de densité de spin qui les entourent (densité de spin α en bleu et β

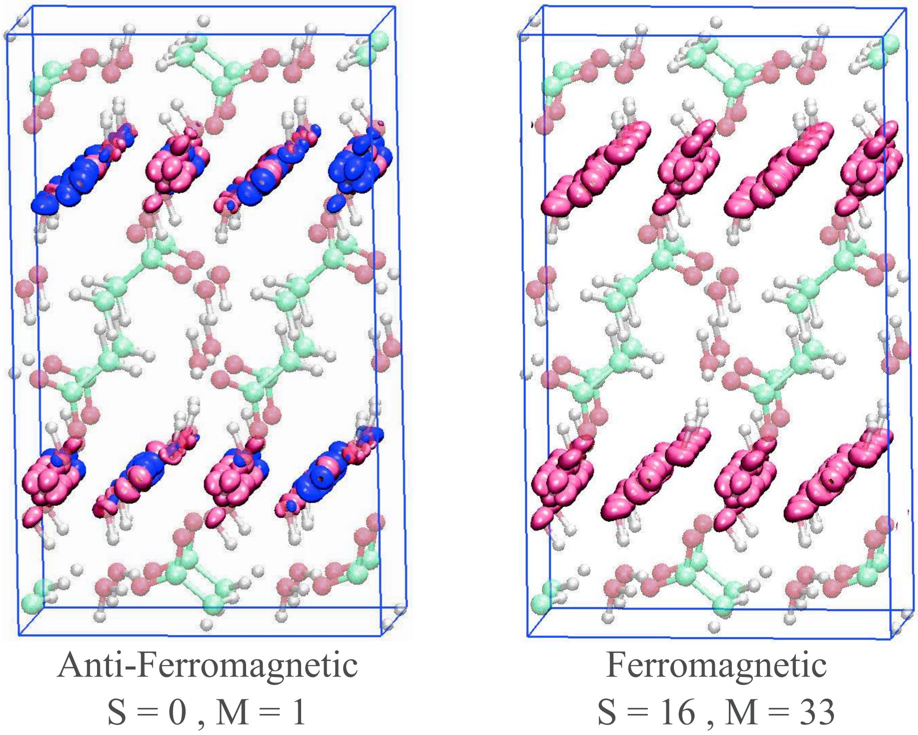

FIGURE 4 – Systèmes modèles d'hydroxyde acétate de cuivre dans l'état antiferromagnétique (partie gauche) et l'état entièrement ferromagnétique (partie droite). Ces structures ont été construites et simulées à l'aide des méthodes FPMD. Les isosurfaces de densité de spin pour les états α (bleu) et β (rose) sont mises en avant au voisinage des sites de cuivre. Les parties organiques, l'eau et les hydroxydes sont transparents pour plus de clarté dans la figure

en rose). Deux configurations magnétiques du système sont considérées : à gauche, l'état anti-ferromagnétique (S=0) où le nombre de sites bleus est égale au nombre de sites roses et, à droite, l'état ferromagnétique complet (S=16) où tous les sites de cuivre sont entouré de densité de spin β assurant l'aimantation totale imposée.

Un autre aspect important de nos simulations FPMD concerne l'application de la pression aux systèmes étudiés. On calcule la pression comme la dérivée de l'énergie totale du système E_{Ham} en fonction du volume de la boîte de simulation V_{Cell}

$$P = -\frac{\partial E_{Ham}}{\partial V_{Cell}} \tag{2.9}$$

Nous utilisons différents protocoles pour appliquer la pression et nous présentons ici celui que nous appelons "isotrope". En effet, dans ce cas, nous préservons les symétries de la structure et réduisons (ou élargissons) les paramètres de maille pour obtenir des structures compressées (ou étirées) donnant lieu à des pressions positives (ou négatives) appliquées au système. Ce processus est schématisé dans la Figure 5. Ainsi, on génère un ensemble de systèmes S_j et nous identifions la structure qui minimise l'énergie totale du système considéré pour obtenir le volume V_{GS} de la structure d'équilibre S_{GS} à pression

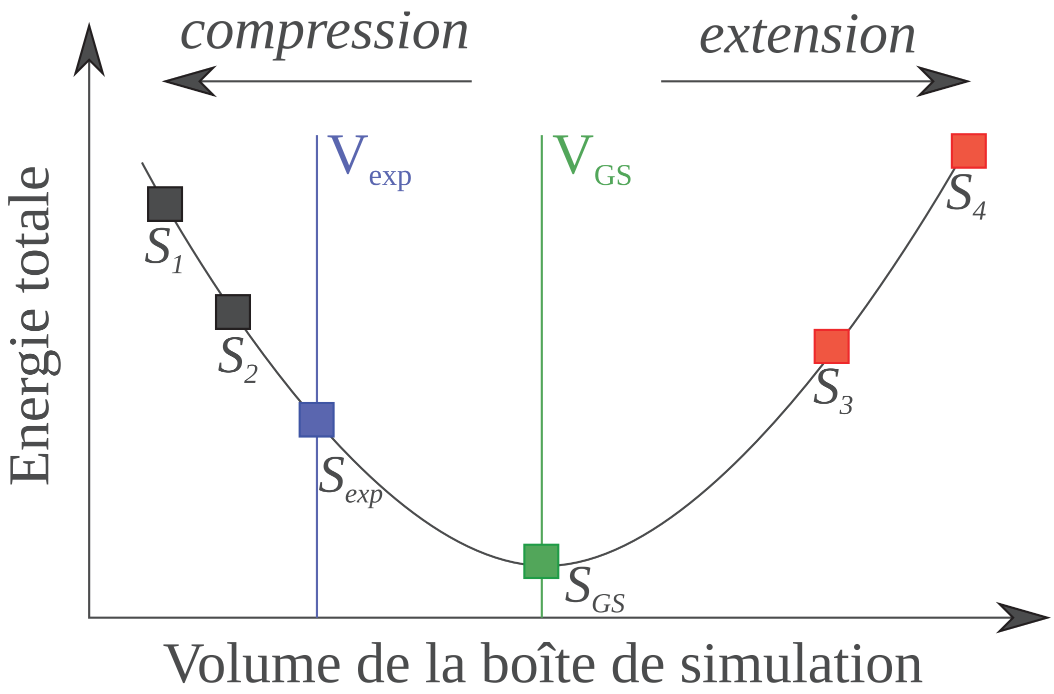

FIGURE 5 – Représentation schématique de la procédure d'évaluation de la pression appliquée sur les systèmes simulés pour la recherche de l'état fondamental structurel (P = 0 GPa). Le système expérimental est noté S_{exp} et est le système initial, puis après compression, les systèmes S_1 et S_2 sont obtenus ou après extension, les systèmes S_3 et S_4 sont obtenus. Dans la recherche de la structure d'équilibre optimisée du matériau (S_{GS} à pression nulle), on évalue la dérivée de la courbe d'énergie totale en fonction du volume de la boîte de simulation et on obtient une estimation de la pression appliquée sur le système (*voir texte*)

nulle à partir du volume V_{exp} du système expérimental S_{exp}. Grâce à cette procédure, on peut construire des systèmes à pressions positives (S_1 et S_2) et des pressions négatives (S_3 et S_4) sachant que ces dernières servent principalement à identifier V_{GS}.

Chapitre 3

L'hydroxyde acétate de cuivre (CuOHAc)

3.1 Transition magnétique induite par la pression

Les systèmes organiques-inorganiques lamellaires sont une classe de matériaux hybrides dans lesquels plusieurs types de chaînes organiques peuvent être insérés dans l'architecture hôte inorganique. Un intérêt particulier a été consacré à l'hydroxyde acétate de cuivre $Cu_2(OH)_3(CH_3COO)\cdot(H_2O)$ abrégé en CuOHAc dans la suite. Ce système appartient à la famille des composés $Cu_2(OH)_3X$ où X est un anion échangeable. L'intérêt provient de ses propriétés magnétiques modulables, fortement dépendantes de la nature des molécules organiques insérées. Grâce aux approches FPMD, nous simulons l'effet de la pression externe sur la structure microscopique du système CuOHAc. Le but de cette étude est d'identifier une transition d'un état de base anti-ferromagnétique (AF) à un état ferromagnétique (F) quand une pression isostatique externe est appliquée sur le système comme cela a été observé expérimentalement [4, 5, 12].

Les électrons de valence sont traités explicitement, tandis que l'interaction noyau-valence est prise en compte, dans le cas du cuivre, par des pseudo-potentiels générés suite au schéma de Trouiller et Martin [46]. En outre, des corrections de noyau "non-linéaires" [40] (NLCC) et une méthode dite de "*semicore*" sont utilisées dans le cas du métal et comparées afin d'extraire l'approche optimale. La boîte de simulation utilisée contient 288 atomes (32 Cu, 96 O, 32 C et 128 H), et les conditions de limites périodiques sont appliquées dans les trois directions. Les paramètres de maille sont doublés dans les directions x et y, a= 11.1552 Å, b = 12.1466 Å, c = 18.5134 Å et $\beta = 91.802°$. Les fonctions d'ondes sont développées au point Γ et une base d'ondes planes est employée avec un seuil d'énergie ("cut-off") de 90 Ry. Une contrainte sur l'état de spin total (S) est appliquée permettant d'étudier différents états magnétiques du matériau. Nous en étudions quatre différents caractérisés par des valeurs de spin S = 0 (AF) et S = 16 respectivement pour les états anti-ferromagnétiques et ferromagnétiques ainsi que deux cas intermédiaires avec S = 8 et S = 12. De plus, nous avons utilisé une procédure de "randomisation" appliquée sur les fonctions d'onde de départ (degrés de liberté électroniques) afin de produire différentes distributions de spin. Une pression est appliquée au système à travers la procédure décrite à la fin du chapitre précèdent bien que, pour ce cas, nous reproduisons les déformations observées expérimentalement dans l'article de Suzuki et al [4].

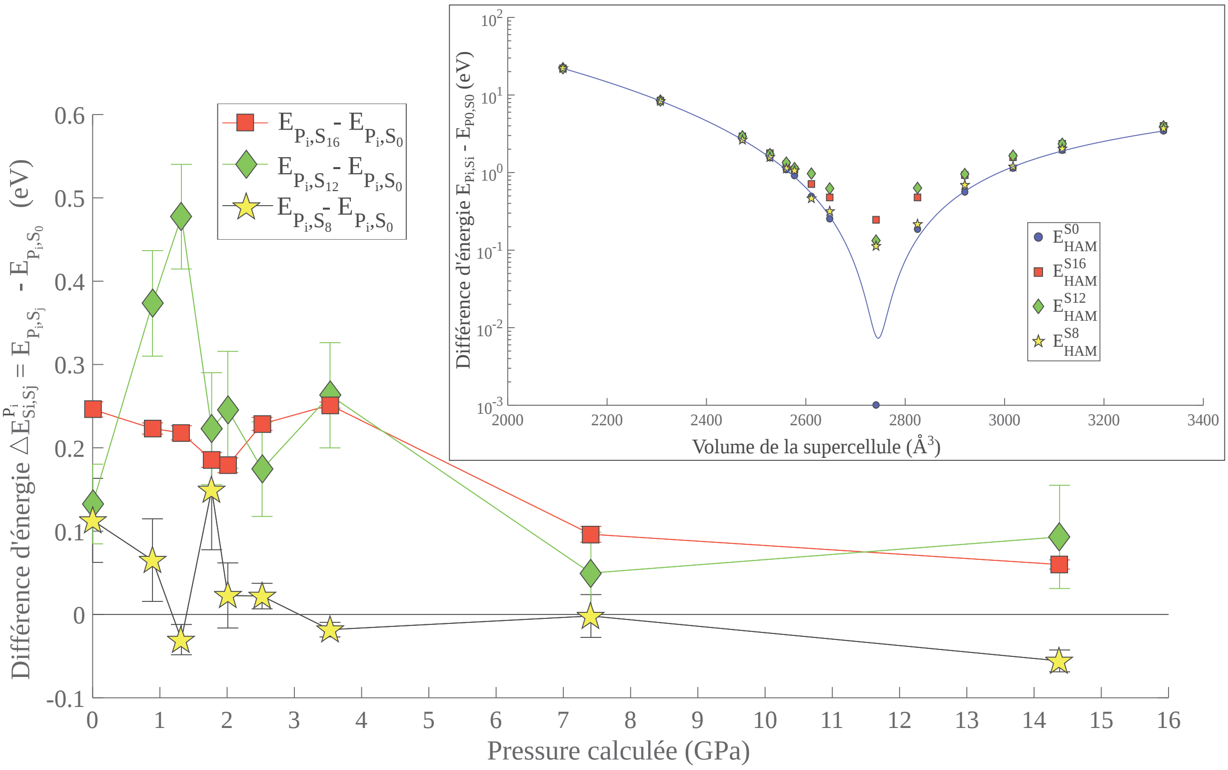

Figure 6 – **Graphe principal :** Stabilité relative (énergies totales) des deux états magnétiques intermédiaires (S = 8 et S = 12) et les systèmes entièrement ferromagnétiques (S = 16) par rapport à l'état fondamental anti-ferromagnétique (ligne en pointillées pour le cas S = 0). **Encadré** : équation d'état des structures considérées E$_{tot}$($V_{SuperCell}$)

Du fait de la minimisation de l'énergie totale du système obtenue dans le cadre de la DFT, nous calculons l'état fondamental électronique pour différents volumes (pressions) du système. Nous obtenons ainsi une courbe d'énergie en fonction du volume de la structure, comme présenté dans l'encadré de la Figure 6, dans laquelle nous identifions l'état fondamental structural du matériau correspondant au système de pression 0 GPa à un volume de 2741 Å^3. Grâce aux simulations FPMD, nous avons quantifié la différence d'énergie totale (stabilité relative) des différents états magnétiques de ce composé. Dans le graphique principal de la Figure 6, nous représentons ces différences d'énergie $\Delta E_{i,j} = E(S_i, P_j) - E(S_0, P_j)$ par rapport à la configuration AF pure (ligne horizontale en pointillés), en fonction de la pression. Nous observons que la configuration entièrement ferromagnétique (carrés rouges) et celle qui est intermédiaire, avec un spin total de S$_{12}$ (diamants verts), restent des systèmes moins stables, par rapport à la configuration AF, pour toute la gamme de pressions étudiée. Cela dit, de 1.2 à 3.5 GPa, nous voyons une concurrence claire entre la configuration AF et le cas S$_8$ (pentagrammes jaunes dans la Figure 6). De plus, à des pressions (P) plus élevées, l'état fondamental du matériau est associé de façon permanente à ce comportement plus ferromagnétique, tel qu'observé dans la Figure 6 pour $P > 3$ GPa. Les barres d'erreurs sont produites à partir de la procédure de "randomisation" appliquée sur les orbitales électroniques initiales. On remarque également que la structure ferromagnétique totale (carrés rouges) converge toujours vers le même minimum d'énergie (petites barres d'erreur). En revanche, l'abondance des distributions de spin autorisées par l'état de spin S = 8 (ou S = 12) conduit à des valeurs qui peuvent différer de 0.05 eV. Une analyse détaillée des configurations S_0 et S_8 et l'identification des topologies de spin les plus stables sont donc des étapes nécessaires pour comprendre l'origine de cette transition magnétique induite par la pression. Cette entreprise est également encouragée par le fait que le système S_8 montre une pression de transition simulée dans une plage (1.2 à 3.5 GPa) proche de la valeur expérimentale 1.2 GPa [4].

3.2 Étude des propriétés magnétiques et électroniques

Afin d'explorer plus précisément l'origine de ce couplage magnéto-structural dans le CuOHAc, nous utilisons l'analyse de densité de spin locale décrite dans le chapitre 2. La promotion du ferromagnétisme en 3D est vu à travers l'évolution des densités de spin locales obtenues sur les sites de cuivre en fonction de la pression. On obtient différentes topologies de spin pour chaque pression et pour chaque valeur de spin total imposée à la cellule primitive. Étant donné qu'une "randomisation" des conditions initiales pour les degrés de liberté électroniques est considérée, de nombreuses topologies de spin correspondent à des minimums locaux proches de l'état fondamental électronique pour une valeur de pression donnée. Un aperçu des premiers résultats relatifs à cette analyse est publié dans une revue scientifique [47] et complété dans cette section.

Dans la figure 7, nous montrons les résultats d'aimantation des deux couches de cuivre de la structure ou, plus précisément, la différence de leurs valeurs absolues ($\Delta\Sigma^S_{l_1,l_2} = \Sigma^S_{l_1} - \Sigma^S_{l_2}$), quantifiant ainsi le caractère ferrimagnétique 3D dans le système. De fait, si les deux couches présentent une amplitude d'aimantation identique avec un signe opposé alors $\Delta\Sigma^S_{l_1,l_2} = 0$ avec $\Sigma^S_{l_1} = -\Sigma^S_{l_2}$ et une configuration 3D anti-ferromagnétique (AF) est obtenue. En revanche, avec une polarisation de spin finie égale ($\Sigma^S_{l_1} = \Sigma^S_{l_2} \neq 0$) et $\Delta\Sigma^S_{l_1,l_2} \neq 0$, le ferromagnétisme 3D est obtenu. Dans la configuration intermédiaire, les deux couches portent différentes valeurs de magnétisation finies $\Sigma^S_{l_1} \neq \Sigma^S_{l_2}$ résultants en une configuration ferrimagnétique.

Trois plages de pression sont considérées, montrant des comportements magnétiques distincts identifiés par les chiffres I, II et III allant des basses pressions aux plus hautes considérées. De nombreuses topologies de spin sont obtenues pour chacun des systèmes considérés dans la partie supérieure de la Figure 7. Nous avons inclus une représentation des distributions de densité de spin des états de spin α (surfaces solides bleues autour des sites de cuivre) et β (surfaces solides vertes) obtenues pour le système CuOHAc sous pression. Nous nous concentrons uniquement sur le système d'énergie totale la plus basse à chaque valeur de pression et choisissons de montrer les configurations de spin qui sont le plus souvent obtenues à cette pression. Dans la première région (7-I), les systèmes S_0 analysés montrent principalement des aimantations finies dans les couches de cuivre, mais d'un signe opposé pour les deux couches (S0-a). Dans la région de transition de l'état AF à l'état F (7-II), nous exposons les quatre distributions dominantes obtenues pour les systèmes S_0 et S_8 exprimant l'existence d'une concurrence entre les deux configurations

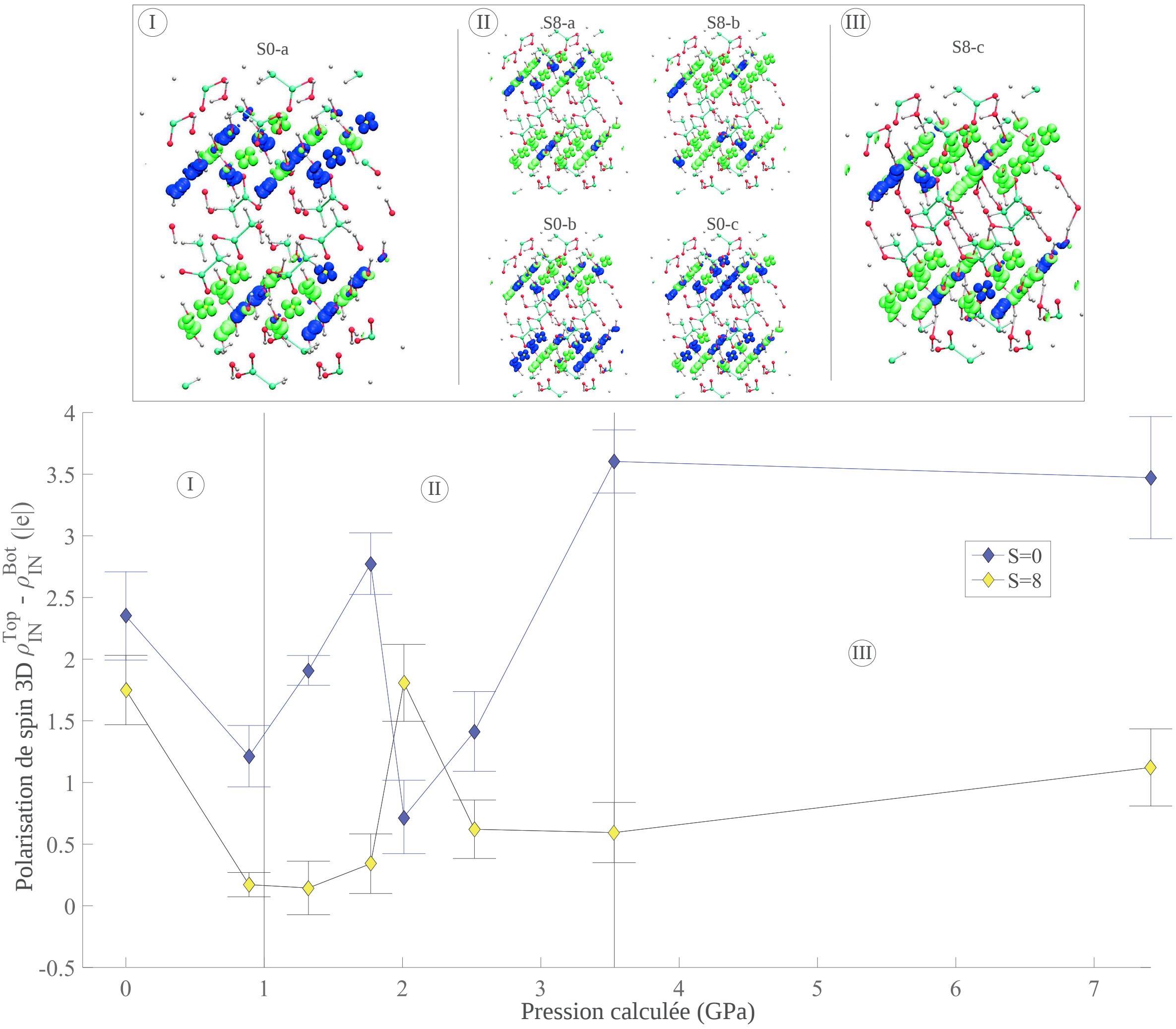

FIGURE 7 – **Partie supérieure :** isosurfaces de densité de spin ($\pm 0.03|\mathrm{e}|$) des états α (bleu) et β (vert) de l'hydroxyde acétate de cuivre dans différentes régions de pression (I : 0 à 1 GPa, II : 1 à 3.5 GPa et III : 3 à 7.5 GPa). **Partie inférieure :** différences des aimantations entre les deux couches de cuivre ($\Delta\Sigma^{S}_{l_1,l_2}$) dans la structure CuOHAc en fonction de la pression appliquée pour le système antiferromagnétique (S = 0 en bleu) et pour le système ferromagnétique (S = 8 en symboles jaunes)

magnétiques. Dans les cas S8-a et S8-b, nous obtenons respectivement les valeurs les plus élevées et les plus basses de $\Delta\Sigma^{S}_{l_1,l_2}$. À mesure que l'énergie totale du système S_8 diminue et que la transition se produit, le système S_8 se stabilise dans une configuration favorisant des valeurs similaires de magnétisations des deux couches de cuivre dans la cellule primitive débouchant sur le cas S8-c de la Figure (7-III).

Nous avons également évalué les propriétés électroniques de ce matériau en utilisant deux descriptions différentes des électrons de cœur des atomes de cuivre. A travers une comparaison détaillée des résultats obtenus en terme de structure et de propriétés magnétiques, nous avons choisi le pseudo-potentiel "*semicore*" au vu de la meilleure qualité des résultats, notamment en terme de densité de spin locale des atomes de cuivre. Nous sélectionnons un résultat à mettre en avant dans le cadre de ce résumé de thèse, c'est une comparaison de ces deux pseudo-potentiels à travers l'analyse de la bande interdite électronique de CuOHAc en fonction de la pression appliquée. En effet, nos calculs DFT nous permettent de calculer la densité d'états électroniques (DOS) à l'état fondamental du matériau et ceci, à différentes pressions. En dépit de la sous-estimation systématique bien connue de la bande interdite à partir des méthodes DFT-GGA [48], nous proposons de nous concentrer sur les variations en fonction de la pression pour les deux configurations magnétiques pertinentes pour notre étude, à savoir S_0 et S_8.

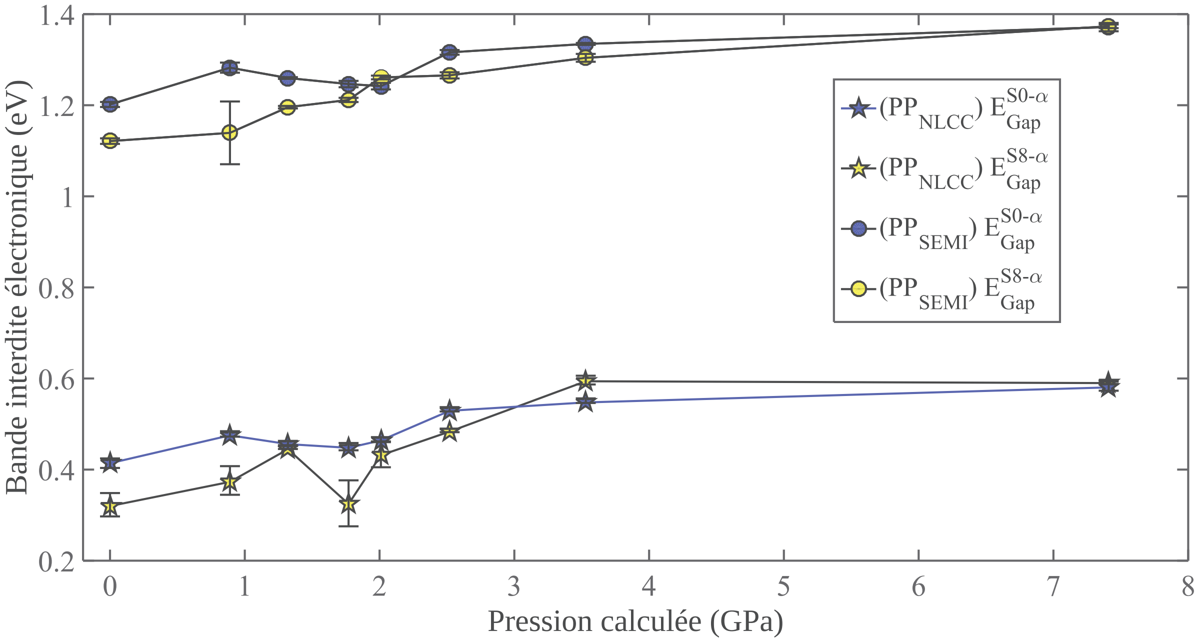

FIGURE 8 – Évolution de la bande interdite électronique du système CuOHAc en fonction de la pression appliquée pour l'état anti-ferromagnétique (S = 0 en bleu) et l'état ferromagnétique (S = 8 en jaune). Ces calculs résultent de l'utilisation de deux approches pour le traitement des électrons de coeur des atomes de cuivre : le pseudo-potentiel NLCC (pentagrammes, lignes pointillées) et le pseudo-potentiel *semicore* (cercles, lignes solides)

Dans la Figure 8, les bandes interdites (dites "gap") correspondantes aux états α sont représentées pour le cas du pseudo-potentiel NLCC (pentagrammes) et *semicore* (cercles) en fonction de la pression. Avec ce dernier, le gap obtenu à pression nulle pour le système AF (S_0, symboles bleus dans la Figure 8) est de 1.20 eV à comparer avec 0.42 eV obtenu avec l'approche NLCC. L'évolution en fonction de la pression est similaire dans les deux cas pour les deux configurations magnétiques (symboles jaunes pour le cas ferromagnétique, S_8). Il est à noter que le système ferromagnétique montre une augmentation monotone dans le cas *semicore* en contraste avec les calculs NLCC. Compte tenu du fait que CuOHAc est un matériau antiferromagnétique et un isolant quand aucun stimulus extérieur n'est appliqué [4], nous estimons que l'évaluation des propriétés électroniques est également optimisée par l'approche *semicore*. De ce fait, nous utilisons cette description pour les atomes de cuivre dans le prochain chapitre dans lequel d'autres structures lamellaires à base de cuivre sont étudiées.

Chapitre 4

De nouvelles fonctionnalités dans les hybrides lamellaires

Dans ce chapitre, nous visons la maîtrise de l'architecture des matériaux hybrides multifonctionnels grâce à l'insertion de nouvelles molécules organiques (fluorène phosphonates) dans la structure de l'hydroxyde acétate de cuivre CuOHAc. Celles-ci sont destinées à remplacer les groupes acétate, conduisant à la stabilisation du nouveau composé lamellaire. Ainsi, l'objectif est d'appliquer les méthodes de dynamique moléculaire *ab initio* (FPMD) pour élaborer une approche dite d'"ingénierie moléculaire" ayant comme objectif de concevoir, construire et étudier des matériaux hybrides multifonctionnels. La porte est alors ouverte pour l'utilisation de ces composés dans de nombreuses applications telles que la catalyse [19], le photovoltaïque [20], les matériaux multifonctionnels [12] ou les milieux d'optique non linéaire [21].

4.1 Construction des structures atomiques stables

Dans le cadre de ce travail théorique, nous avons établi une collaboration avec l'équipe de recherche expérimentale du Dr. Guillaume Rogez à l'IPCMS afin de construire une approche combinée pour l'étude de ces matériaux hybrides. Les travaux récents de ce groupe ont pour but l'extension de l'utilisation des composés à base de molécules fluorènes afin de proposer de nouveaux hybrides lamellaires à base d'acides mono et diphosphoniques. Dans ces systèmes, diverses chaînes alkyle dans la position correspondante de l'unité fluorène sont envisagées (-H, -CH_3 ou -$(CH_2)_7CH_3$). L'idée est d'explorer des phénomènes magnéto-électriques dans les hydroxydes lamellaires simples de cuivre ou de cobalt (Cu-LSH ou Co-LSH). Rappelons que la synthèse des composés hybrides a été effectuée suivant une procédure très utilisée consistant à dissoudre un excès de la molécule organique dans de l'eau à un pH relativement élevé. Ensuite, on ajoute un volume d'éthanol équivalent avec les matériaux de départ $Cu_2(OH)_3(DS)$ (DS^- est le dodécylsulfate et DS_0^- est le dodécylsulfonate) [49].

Après analyse des diagrammes de diffraction aux rayons X sur des poudres de ces composés hybrides, le changement abrupt de leur espacement inter-lamellaire par rapport aux hydroxydes lamellaires de départ est en accord avec l'insertion des molécules de fluorène monophosphonique. Compte tenu de la longueur des acides fluorène monophosphoniques et de l'épaisseur des feuillets inorganiques, la distance interlamellaire obtenue pour le cas des hydroxydes fluorène monophosphoniques de cuivre (CuOHFP1) est cohérente avec un agencement en double couches organiques. Une éventuelle interpénétration selon l'angle d'inclinaison est aussi à considérer. Pour les hydroxydes fluorène diphosphoniques de cuivre (CuOHFP2), l'espace interlamellaire observé n'est pas cohérent avec un double greffage des molécules sur les couches inorganiques. Afin de résoudre cette divergence apparente et de déterminer l'agencement moléculaire des acides de fluorènes mono- et di-phosphoniques dans l'environnement interlamellaire, nous avons utilisé les méthodes FPMD.

Dans la suite, nous résumons les étapes clés de notre procédure. Ainsi, nous étudions :

- La compatibilité entre les paramètres de maille obtenus expérimentalement, la distance interlamellaire et l'interaction entre les molécules organiques ainsi que leur densité.
- Les conformations, les orientations et l'empilement possible des molécules de fluorènes phosphonates dans le but d'associer une composition spécifique à une structure atomique particulière.
- La nature des liaisons chimiques et en particulier à l'interface entre les parties organiques et inorganiques du système afin d'expliquer le rôle des conditions synthétiques expérimentales dans la définition de la structure résultante.
- Les comportements magnétiques attendus de ces composés, en utilisant comme référence les résultats obtenus dans l'étude de l'hydroxyde acétate de cuivre.
- Le rôle des molécules d'eau dans les cristaux. L'eau est un élément crucial dans de tels matériaux hybrides stratifiés, car sa présence stabilise les agencements des molécules organiques et influence la liaison chimique au voisinage des couches inorganiques.

Notre première étape est de partir du système d'hydroxyde acétate de cuivre et d'échanger les molécules d'acétate par des fluorènes phosphonates dans ce que nous désignons comme l'approche d'ingénierie moléculaire. Cette terminologie est justifiée par la méthodologie suivie "étape par étape", nécessaire à la construction, *in silico*, d'une structure réaliste sur la base de caractérisations expérimentales. Ce procédé exploite trois outils de simulations disponibles dans nos études FPMD. Un premier est la possibilité de fixer et libérer des fragments de la structure atomique considérée afin d'explorer l'espace des configurations de manière sélective. Deuxièmement, nous pouvons faire des simulations à température finie ce qui permet de vérifier la stabilité et les différentes positions atomiques caractéristiques de la structure d'équilibre du système. Troisièmement, on effectue des simulations de surface en exposant une surface de cuivre au vide d'un côté et à l'hydroxyde acétate de cuivre massif de l'autre afin d'analyser le phénomène de greffage des molécules organiques sur les couches métalliques.

En exploitant toutes ces méthodes, nous avons obtenu une structure du composé CuOHFP1, optimisée et caractérisée par une couche organique montrant les molécules de fluorènes monophosphoniques (FP1) inclinées et avec un certain degré d'interpénétration. Dans le cas du système CuOHFP2, nous avons rencontré un nouveau problème lié à la nature non compatible de la distance interlamellaire observée avec la structure modèle correspondante envisagée par les expérimentateurs. Grâce à des simulations test avec différents paramètres *c*, nous avons déduit qu'aucune structure anhydre n'est plausible au vu de la distance interlamellaire expérimentale (d_{EXP}=17.5 Å) proposée pour le cas de CuOHFP2.

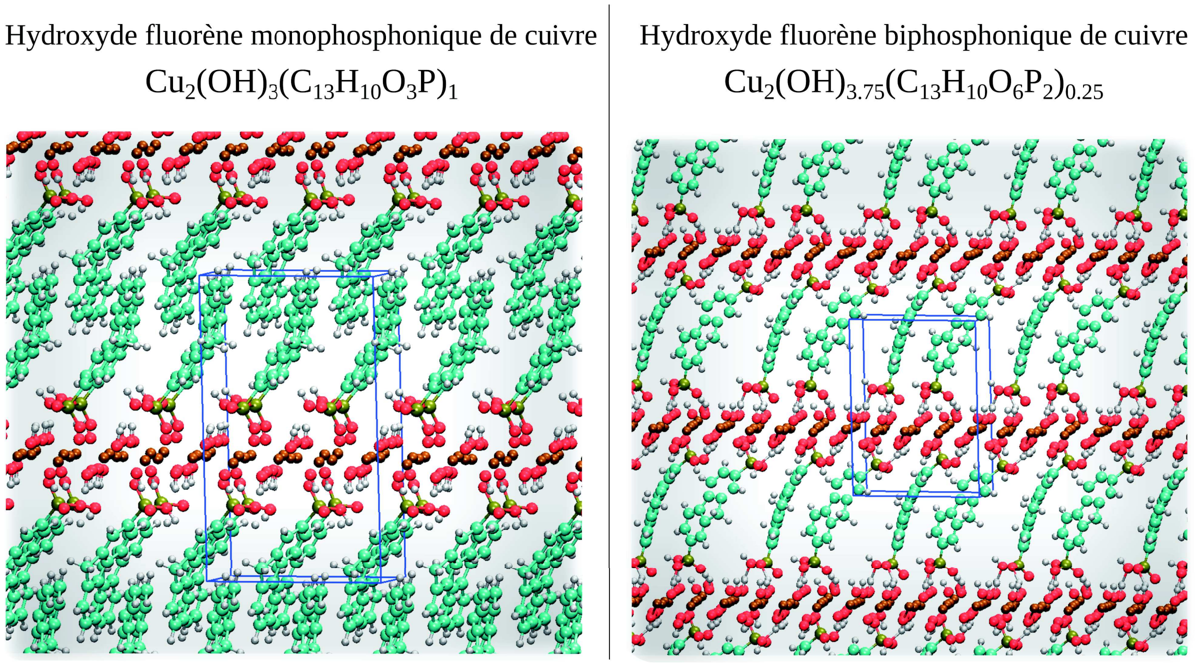

Hydroxyde fluorène monophosphonique de cuivre

$Cu_2(OH)_3(C_{13}H_{10}O_3P)_1$

Hydroxyde fluorène biphosphonique de cuivre

$Cu_2(OH)_{3.75}(C_{13}H_{10}O_6P_2)_{0.25}$

FIGURE 9 – Structures périodiques de deux matériaux étudiées dans ce projet, les deux systèmes hybrides sont l'hydroxyde fluorène monophosphoniques de cuivre (partie gauche) et l'hydroxyde fluorène diphosphonique de cuivre (partie droite). Celles-ci correspondent aux structures optimisées utilisées dans les simulations FPMD réalisées dans cette section

Sur le côté gauche de la Figure 9, nous présentons la structure optimisée de CuOHFP1 accompagnée de la composition chimique considérée. Sur le côté droit, le système CuOHFP2 est représenté avec une dimension de cellule primitive le long de la direction *c* qui diffère de 2 Å de l'expérience (d_{SIM} = 15.5 Å) mais représentant une structure anhydre optimisée pour ce système (à 0K). Ainsi, nous pouvons effectuer une analyse détaillée de l'effet des molécules d'eau sur la stabilité structurale de ces systèmes en tenant compte de trois teneurs en eau différentes $(H_2O)_y$ (y = 0, 0.5 et 1) notés respectivement, 0W, 0.5W et 1W. Pour le système CuOHFP1, la structure n'est pas modifiée et l'eau est incluse directement tandis que pour le système CuOHFP2, nous augmentons la distance entre couches à la valeur expérimentale (17.5 Å) et on utilise des molécules d'eau pour compenser le volume libre restant dans le système.

Du point de vue de la structure, on effectue une analyse basée sur la fonction de distribution de pairs (PdF) atomiques qui nous permet d'évaluer les différences obtenues lorsque les molécules d'eau sont considérées. Nous en incluons un certain nombre dans le système dans l'objectif de stabiliser la structure à température finie et, en particulier, stabiliser la liaison chimique entre les parties organiques et inorganiques. Dans la figure 10, nous présentons l'analyse PdF correspondante au cas du système CuOHFP1 pour les trois densités d'eau considérées, 0W, 0.5W et 1W correspondantes, respectivement, à l'inclusion de 0, 4 et 8 molécules d'eau dans la structure.

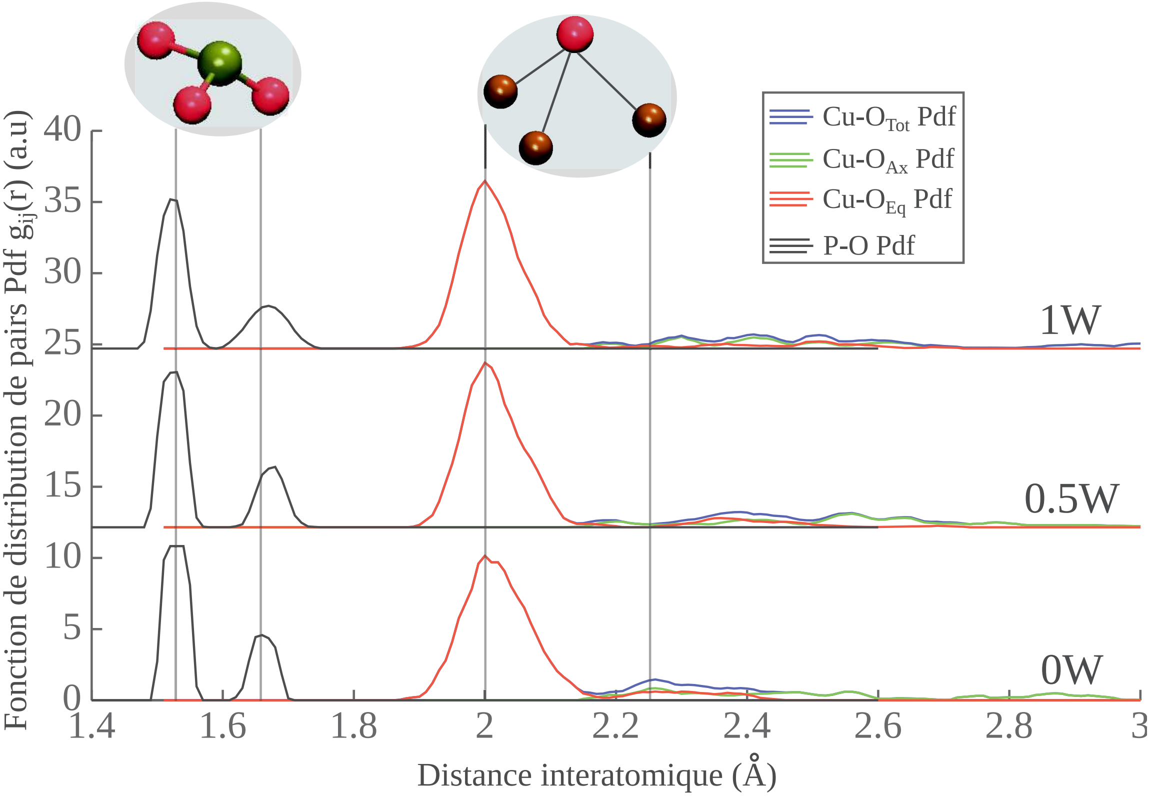

FIGURE 10 – Fonction de distribution de pairs pour différentes paires atomiques dans des structures d'hydroxyde fluorène monophosphonique de cuivre (bleus pour toutes les pairs Cu-O, vert pour les pairs Cu-OPO$_2$, rouge pour les pairs Cu-OH et noir pour P-O). Les lignes solides, à tirets et en pointillées correspondent à des systèmes à contenu d'eau différent (0W, 0.5W pour 4 molécules d'eau ou 1W pour 8 molécules d'eau). Les résultats pour les cas 0.5W et 1W sont rigidement décalées selon l'axe des ordonnées pour plus de clarté.

Comme prévu, la répartition des distances équatoriales correspondantes aux liaisons Cu-OH n'est pas influencée par la quantité d'eau considérée car seul un changement de forme négligeable et aucun changement de position ne sont observés pour le pic localisé autour de 2 Å (courbes rouges et bleues dans la Figure 10). Cependant, pour les distances axiales, correspondantes aux distances de Cu-O supérieures à 2,2 Å (courbes vertes et bleues), leurs répartitions changent en fonction du contenu d'eau. En particulier, l'effet de l'eau sur ces liaisons Cu-O(FP1) est d'augmenter la distance et de contraindre l'environnement local afin de résister aux mouvements thermiques imposés. L'analyse des liaisons PO (courbes noires dans la Figure 10) indique que les tétraèdres PO_3H^- sont légèrement déformés. Cela est visible dans le cas de la distance P-O la plus longue ($\simeq$ 1.65 Å) qui augmente en fonction de la teneur en eau. Cela s'explique par l'établissement du réseau de liaisons hydrogènes stabilisant ce groupe d'ancrage en attirant légèrement l'oxygène protoné vers la molécule d'eau la plus proche. Nous avons effectué des études similaires pour le cas CuOHFP2 pour les compositions suivantes : $Cu_2(OH)_{3.75}(C_{13}H_{10}O_6P_2)_{0.25}{\cdot}(H_2O)_y$ avec y= 0, 0.5, 1. Néanmoins, les résultats correspondants ne sont pas repris dans le cadre de ce résumé de thèse car les analyses de propriétés qui suivent sont principalement effectuées dans le cas CuOHFP1.

4.2 Propriétés magnétiques et influence de l'eau

Dans cette section, on s'intéresse aux propriétés magnétiques ainsi qu'au rôle joué par les molécules d'eau dans les structures LSH étudiées en se concentrant sur l'hydroxyde fluorène monophosphonique de cuivre. Plus précisément on se concentre sur la structure contenant la quantité maximum d'eau considérée jusqu'ici : le cas 1W.

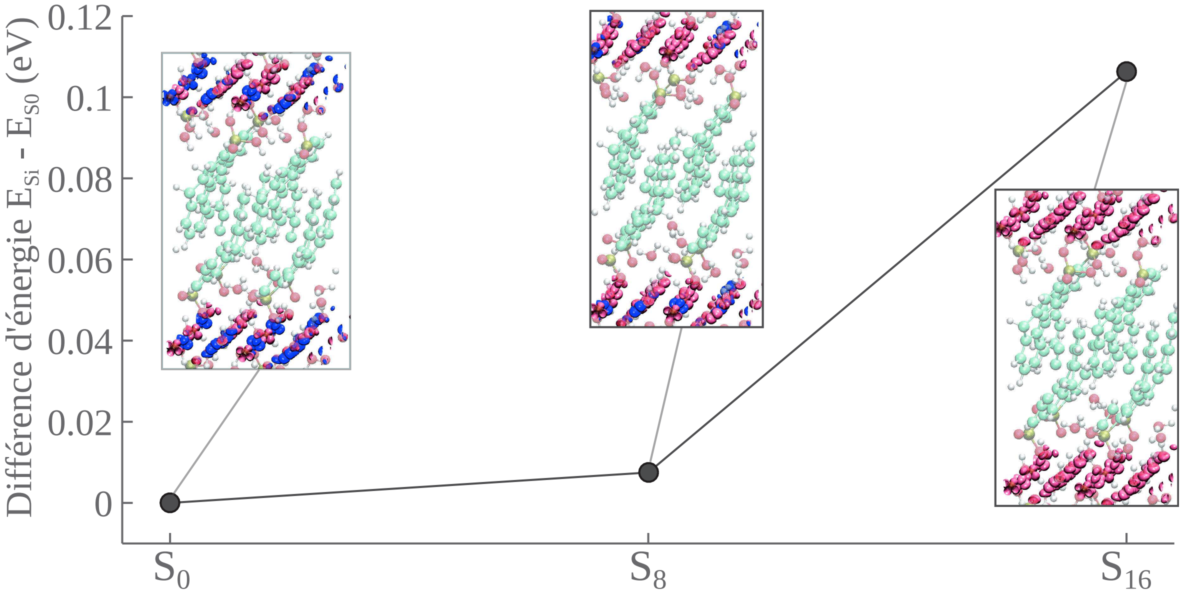

FIGURE 11 – Évaluation de l'énergie totale relative de deux états ferromagnétiques (S = 8 et S = 16) par rapport à l'état fondamental AF (S = 0) de l'hydroxyde fluorène monophosphonique de cuivre. La supercellule de simulation considérée est doublée dans la direction $\vec{c}$-(608 atomes dans la boîte) pour inclure deux couches d'hydroxyde de cuivre. Des représentations des structures atomiques correspondantes à chaque configuration magnétique mettent en évidence les différentes surfaces de densité de spin (↑ en bleu et ↓ en rose) obtenues pour ces systèmes

Pour ce qui est des propriétés magnétiques, nous construisons une cellule de simulation en doublant la taille dans la direction $\vec{c}$ pour contenir deux couches complètes du réseau inorganique, leurs environnements chimiques, l'eau ainsi que les molécules organiques de fluorènes phosphonate (FP) greffées aux deux couches. Nous calculons les densités de spin locales dans le système pour différents états magnétiques déjà considérés pour le système CuOHAc. Dans la Figure 11, les énergies totales du système antiferromagnétique (S = 0), du système entièrement ferromagnétique (S = 16) et une configuration intermédiaire (S = 8) sont évaluées et représentés comme des énergies relatives par rapport à l'état de base antiferromagnétique (AF). Ce système AF est le plus stable (l'énergie la plus basse). Les distributions locales de densité de spin sont représentées dans les trois cas comme des isosurfaces bleues pour le cas α et rose pour les densités de spin β. La densité de spin est principalement localisée autour des sites de cuivre dans tous les systèmes et pour cela le reste de la structure atomique est représenté avec un degré de transparence.

Ces résultats montrent que ce matériau est également anti-ferromagnétique à l'état fondamental du système massif. Néanmoins, le système S_8 n'est moins stable que de 0,007 eV par rapport au système S_0 tandis que la configuration S_{16} est clairement plus élevée en énergie (0,106 eV). La différence d'énergie observée pour le cas S_8 indique que l'on pourrait étudier davantage l'effet des stimuli externes (la pression) qui peuvent déclencher une compétition de stabilité entre l'état AF et le cas S_8 du système ferromagnétique.

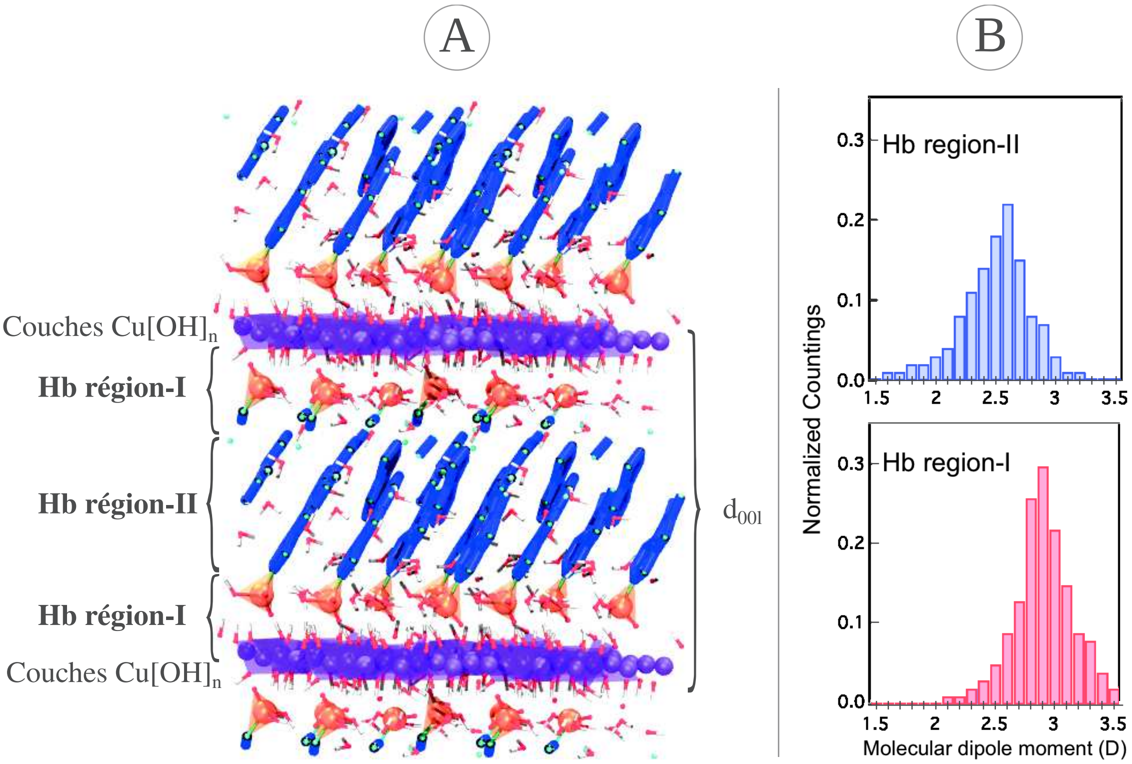

FIGURE 12 – **A)** Configuration typique de l'hydroxyde fluorène monophosphonique de cuivre obtenue via des simulations FPMD (la supercellule considérée est répliquée 2 × 2 × 2 le long de x, y et z pour plus de clarté). La distance interlamellaire (d_{00l}), les couches d'hydroxyde de cuivre ($Cu[OH]_n$) ainsi que les régions correspondantes aux type I et II de liaisons hydrogènes (H) sont également indiquées (voir texte). Couleurs : Cu en pourpre ; P en orange et PO_3 en polyèdres oranges ; C et squelette des groupes fluorène en bleu ; O en rouge ; H en blanc. **B)** Distributions normalisées du module des moments dipolaires moléculaires des molécules d'eau pour le même matériau CuOHFP1. Dans la partie interfaciale de l'espace interlamellaire, région I, correspond la distribution en bas de la figure (en rouge) et à la partie centrale de la structure, région II, correspond la distribution en haut de la figure (en bleu)

En parallèle à cette étude de propriétés magnétiques, nous avons également évalué les propriétés électriques des molécules d'eau dans la structure afin de bien caractériser l'interdépendance entre les propriétés, la structure et la teneur en eau. La figure 12-A montre une configuration stable typique du système CuOHFP1. Pour un tel système, l'acide fluorène monophosphonique se trouve chimiquement ancré dans la couche d'hydroxyde de cuivre par l'interaction de trois atomes de Cu et d'un atome d'oxygène du groupe phosphonate avec une distance d'équilibre variant de 0.26 à 0.32 nm. Plusieurs scénarios ont été explorés pour comprendre la chimie locale du groupe phosphonate monoprotonée (forme la plus stable PO_3H^-). Le système optimisé résulte d'une simulation à température finie (50K) pour environ 5 ps. On obtient alors les fragments de fluorène inclinés de manière homogène par rapport au plan d'hydroxyde de cuivre avec un angle de 66°, ce qui induit une interpénétration partielle des parties aromatiques. Dans cette figure (12-A), nous divisons l'espace interlamellaire en deux régions : (I) une première située à moins de 0.6 nm de la couche de cuivre et (II) une deuxième région à des distances supérieures à 0.6 nm des couches inorganique. Les réseaux de liaisons hydrogène dans les deux régions sont caractérisé par des propriétés différentes. Dans la région I, le réseau de liaisons hydrogènes est favorisé par l'implication de molécules d'eau, de groupes hydroxydes et de groupes phosphonates, alors que dans la région II, les liaisons H sont établis uniquement par les molécules d'eau. Cette différence peut être rendue plus quantitative en analysant le moment dipolaire électrique des molécules d'eau. La Figure 12-B montre les distributions de dipôles des molécules d'eau calculées en utilisant l'analyse des fonctions de Wannier [50]. Au centre de la couche organique (région II), les dipôles sont légèrement inférieurs par rapport aux molécules d'eau à proximité des couches d'hydroxyde de cuivre et des groupes phosphonates (I : 2.6 D, II : 2.9 D). Ceci est révélateur du fait que le champ électrique induit par les molécules environnantes augmente le moment dipolaire des molécules d'eau incluses dans l'environnement proche des couches inorganiques [51, 52, 53, 54, 55, 56].

Nous avons également considéré un autre système hybride lamellaire à base de cuivre : le 9H-fluorène-2-phosphonic acid $C_{13}H_9PO(OH)_2$ [57]. Ceci est un projet en cours dans lequel nous établissons un protocole de simulation FPMD nous permettant d'évaluer les spectres d'absorption de tout matériau hybride lamellaire dont la structure atomique exacte est connue.

Conclusions

Dans ce travail de thèse, nous traçons une voie pour l'exploration de la structure, des propriétés et des couplages magnéto-structuraux observés dans les matériaux hybrides lamellaires, principalement de type LSH. Nous avons effectué des simulations réalistes grâce à des méthodes FPMD permettant de compléter les observations expérimentales et de prédire des comportements inconnus dans plusieurs conditions de température et de pression.

Dans le cas de l'hydroxyde acétate de cuivre, nous avons construit notre boîte de simulation à partir de la caractérisation cristallographique expérimentale de Svarcova et al. [3] et nous démontrons la stabilité du système à température ambiante. Étant donné qu'un couplage magnéto-structural existe dans ce matériau, c'est-à-dire une transition magnétique induite par la pression [4], nous effectuons des compressions et extensions successives correspondantes aux déformations expérimentales observées sous pression. Une transition d'un état fondamental anti-ferromagnétique (S = 0) à un état ferromagnétique (F) se produit pour le système F de spin total S = 8. La région de transition obtenue (1.2 à 3.5 GPa) est en très bon accord avec la valeur expérimentale (1.2 GPa) confirmant la nature réaliste de ces simulations. Nous démontrons le rôle de la magnétisation des couches de cuivre dans l'apparition du ferromagnetisme dans le système sous pression [47]. Nous avons également effectué une analyse détaillée comparant l'utilisation des pseudo-potentiels dits NLCC et *semicore* visants à une meilleure description des électrons de coeur des métaux de transition (Cu^{2+}). Nous démontrons l'amélioration de la description des propriétés magnétiques et électroniques avec la description *semicore* et nous l'utilisons dans nos calculs.

A partir du réseau inorganique de ce composé, c'est-à-dire des couches d'hydroxyde de cuivre, nous avons inséré des molécules de fluorène monophosphonique et diphosphoniques pour construire de nouveaux matériaux hybrides, des hydroxydes fluorènes phosphonates de cuivre. Nous avons construit plusieurs configurations d'essai pour lesquelles nous avons établi un traitement approprié pour stabiliser la structure et aller vers l'étude des propriétés. Ainsi, nous avons obtenu des structures atomiques qui correspondent aux compositions et les teneurs en eau caractérisées expérimentalement. Nous avons effectué plusieurs études précises sur la protonation et la déprotonation des groupes phosphonates, le rôle des réseaux de liaisons hydrogènes établis par les molécules d'eau et l'influence du rapport de la densité des molécules organiques par rapport à la teneur en hydroxyde sur la stabilité du composé final. L'étude de l'insertion du système biphosphonique nous a amené à proposer de nouvelles structures cristallographiques qui correspondent mieux à la composition chimique et qui sont compatibles avec la distance interlamellaire expérimentale (17.5 Å).

Dans l'ensemble, l'application des méthodes FPMD ouvre de nouvelles possibilités d'élaborer, par la modélisation, des composés chimiques complexes et d'étudier leurs propriétés pour compléter, tester et aller au-delà des modèles largement utilisées dans le cadre de la chimie expérimentale.

Part II

PhD Thesis: english version

Ph.D. Thesis

Structural, electronic and magnetic properties of hybrid organic-inorganic layered materials: a first-principles molecular dynamics study

Ziyad Chaker

Thesis Director: Dr. Carlo Massobrio

Rapporteur 1: Professor Carla MOLTENI
Rapporteur 2: Doctor Florent BOUCHER
Reviewer 1: Doctor Vanessa PREVOT
Reviewer 2: Professor Vincent ROBERT
Reviewer 3: Doctor Guido ORI

Université de Strasbourg (Unistra)
Institut de Physique et de Chimie des Matériaux de Strasbourg, Université de Strasbourg
and CNRS UMR 7504, 23 rue du Loess, F-67034 Strasbourg Cedex 2, France

Academic years 2014/2017

Acknowledgments

I profoundly thank my PhD supervisor, Dr. Carlo Massobrio for supporting and managing me during these three beautiful years. Also, I sincerely thank Dr. Guido Ori that provided me daily unconditional support and made all this work possible. Pr. Mauro Boero, to whom I owe my deepest gratitude, will never stop astonishing me with his infinite knowledge. I also thank Dr. Guillaume Rogez and Quentin Evrard, for the fruitful collaboration that gave a realistic and experimental counterpart to this project. I am grateful to all IPCMS' members that provided me with an amazing productive environment and confronted me to the scientific diversity and performance necessary to envisage the reality of modern science. Thank you to the University of Strasbourg and in particular to the High Performance Computing center for the millions of calculation hours that made this project possible.

I would like to mention that my everyday life has been made compatible with such wonderful PhD adventure thanks to my perfect wife Karina, my mother Souad & my father Mohammed. Thank you to my wise sister Dr. Zayna Chaker that went through every obstacle by my side and to her husband Benjamin with whom discussions are always a pleasure.

*A huge "Thank you!" to my colleagues and friends, Meltem, Kubra, Elodie, Mathias the great (my favorite poker mate) and Etienne the compulsory. I also thank my Ukrainian soul mates Stazik and Ivan with whom D**A was an everyday pleasure. Thank you to all members of our reading group from other institutes than IPCMS (ISIS, IGBMC, CEA etc) and especially my friends Oussama, Artur and Mathieu who hosted us for these wonderful weekly meetings. Finally, thank you to Jean-Yves Runser, Maximillien Barbier, Thibault Chervy and Dr. Jérôme Hurst. We came from far together accompanied with long discussions on philosophy, science, politics etc... that constructed and polished my humanity to make me who I am. Thank you for existing.*

Notations

AF, F : anti-ferromagnetic, ferromagnetic
B3LYP : hybrid exchange-correlation functional
BLYP : exchange-correlation functional (Becke, Lee, Yang and Parr) [38, 39]
CASSCF : complete active space self-consistent field method
CPMD : Car-Parrinello molecular dynamics [2]
CuOFP : copper fluorene phosphonate
CuOHAc : copper hydroxide acetate, $Cu_2(OH)_3(CH_3COO)$
CuOHFP1 or 3a$\subset$Cu: copper hydroxide fluorene monophosphonic, $Cu_2(OH)_x(C_{13}H_{10}O_3P)_y$
CuOHFP2 or 6a$\subset$Cu: copper hydroxide fluorene biphosphonic, $Cu_2(OH)_x(C_{13}H_{10}O_6P_2)_y$
CuOHN : copper hydroxide nitrate, $Cu_2(OH)_3(NO_3)$
DDCI : difference-dedication configuration interaction
DFT : density functional theory
DoF : degrees of freedom
DOSY-NMR : diffusion-ordered spectroscopy - nuclear magnetic resonance
DSA : dynamical simulated annealing
DSC : differential scanning calorimetry
DTA : differential thermal analysis
EDX : energy-dispersive X-ray spectroscopy
ELF : electron localization function
FFT : fast Fourier transform
FPMD : first-principles molecular dynamics
FTIR : Fourier transform infra-red spectroscopy
GGA : generalized gradient approximation
HCTH : exchange correlation functional (Hamprecht, Cohen, Tozer and Handy [58])
HTH : Hay-Thibeault and Hoffmann model [59]
HTXRD : high temperature X-ray diffraction
KS : Kohn-Sham
LDA : local density approximation
LDH : layered double hydroxides
LSH : layered single hydroxides
MOF : metal-organic frameworks
NLCC : non linear core corrections
NMO : natural magnetic orbitals
PBE : exchange-correlation functional (Perdew, Burke and Ernzerhof [60])
PP : pseudo-potential
PW : plane waves
SCO : spin cross-over
SEM : scanning electron microscopy
SQUID : superconducting quantum interference device
TGA : thermogravimetric analysis
WFC : Wannier function centers
XAES : X-ray excited Auger electron spectroscopy
XPS : X-ray photoelectron spectrometry

Introduction

Since the dawn of civilization, survival ability and thus the need of mastery of nature are relevant order parameters to follow human evolution. The study of materials and their transformation is, in this context, a fundamental skill developed through our rich history. Nowadays, it allows us to synthesize complex materials with an outstanding level of control on the structure and the properties. In parallel with the active history of experimental achievements, the ability of creating suitable models explaining the phenomena observed led to very elegant and fundamentally simple theories such as classical and quantum mechanics. The combined approach of performing experiments while elaborating theories brought coherence, logics and understanding taking the place of "magic" recipes based on widespread trial and error procedures.

Animated by this ancestral instinct and equipped with first-principles molecular dynamics (FPMD) techniques, we perform systematic analyses of the structure as well as magnetic and electronic properties of a specific family of hybrid organic-inorganic systems. The interest in layered simple hydroxide (LSH) stems from the synergy obtained between the properties of organic and inorganic parts. We intend to establish the correct simulation protocols allowing to reproduce, *in silico*, the realistic properties of hybrid materials. This enable us to provide a rationale of experimental observations and then explore unknown features obtained under the effect of external stimuli. Experimentally, the synthesis of high quality layered hybrid materials is made possible by the new synthetic environments used in the so called "chimie douce" (soft chemistry) pioneered by Livage [23, 24] in 1988. Theoretically, our approach is based on Car-Parrinello Molecular Dynamics (CPMD) techniques [43, 2] developed in 1985 bringing together density functional theory (DFT) [61] and molecular dynamics (MD) [42]. Our strategy is two-fold: First, we elaborate the adequate simulation protocols to study copper hydroxide acetate, recognized as a prototypical system in the study of LSH materials. Then, we apply these well established recipes to more challenging systems for which many open issues on the atomic structure are addressed. On the one hand, we use first-principles molecular dynamics to optimize the structures and room temperature simulations to reproduce experimental conditions. On the other hand, we perform electronic structure calculations to compute local spin densities, density of states and the electronic structure of the material.

Overall, the aim of this PhD thesis is to present state-of-the-art achievements concerning the applications of first-principles molecular dynamics to the field of transition metal hydroxide hybrids. We elucidate the complex interplay between structural properties of such nanostructured materials and their magnetic character, both at the local (atomic) and bulk level. Considering different organic components (such as acetate and fluorene phosphonate), we show how external stimuli (pressure for instance) or different organic-inorganic interfacial chemistry can be used to tune the magnetic properties for the case of copper hydroxide-based hybrid materials [47, 36, 37, 7]. This work further demonstrates how theoretical modeling can be employed to make available an atomic-scale rationale for the tuning of the magnetic nature for such multi-functional materials.

Chapter 1

Layered hybrid materials

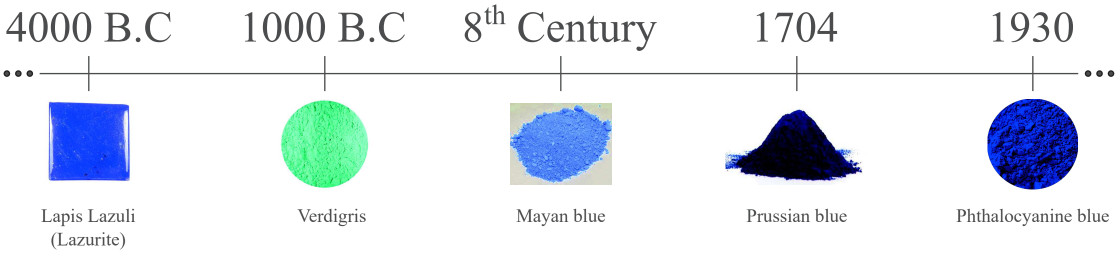

Figure 13 – From left to right: Lapis lazuli or lazurite, a natural alumino silicate of sodium and of calcium of chemical formula $(Na,Ca)_8Al_6Si_6O_{24}(S,SO_4,Cl)$, known since sumerian civilization and used for carvings and ornaments of statues; The "Verdigris" or copper hydroxide acetate, a green pigment obtained through the application of acetic acid (CH_3CO_2H) to copper plates, used in antiquity for protecting copper or bronze objects and as a fungicide agent; The Mayan blue is a truly man made hybrid organic-inorganic material, that is to say a natural blue "indigo" organic dye is embedded in channels of a clay mineral known as palygorskite. Such concept opened the route for Prussian or Phtalocyanine blue pigments that were designed for fundamental, industrial and artistic purposes [25].

Since the 4^{th} millenium B.C, a remarquable civilization, Sumer (actual Iraq), possessed already the great human potential for crafting tools of all kinds, statues and graphical representations of their everyday experience [62, 63]. The sumerians adapted the natural compounds at their disposal to improve their lifestyle and express their creativity. I will use this historical landmark as the starting point of the development of human ability to observe, understand and master the art of designing and producing specific materials. In Figure 13, I sketch the historical landmarks of "blue colored" materials used throughout the ages. In order to set the scene for the concepts introduced in this chapter, it could be useful to underline that there is a continous line connecting the past, i.e. the very early stages of process of the Lapis-lazuli, cited in Gilgameš' book (first book of humanity), and the present, i.e. the most recent studies on the structural properties of copper hydroxide acetate. The common denominator of these efforts is the need of knowledge and control of the environment, it is a powerful driving force for the intellectual evolution of the mankind.

This chapter is divided in two main sections:

- First, I will provide a detailed account of the nature and definition of organic-inorganic hybrid materials in both the fundamental and applied research fields. The introduction of the so-called "chimie douce" (soft chemistry) approach is of particular value since this innovative chemistry stimulated a strong interest in all hybrid materials experimentally accessible. The focus will be on the class of layered hybrids that are promising systems to obtain multi-functionality and fine control of the properties. Accordingly, the state-of-the-art of the experimental advances in synthesis, analysis and applications of such materials is proposed in the first section. It will become clear that specific open issues partially unsolved on the experimental side could be successfully addressed by relying on atomic-scale simulation approaches such as first-principles molecular dynamics (FPMD).

- The second section is an overview of the state-of-the-art theoretical accomplishments achieved in the area of structural, electronic and magnetic properties of hybrid materials. The treatment of external stimuli such as temperature or pressure will be of special interest. With the intention of bridging the gap between the communities of molecular magnetism and the one of solid state chemistry, I shall review briefly few concepts and results obtained for some prototypical magnetic molecular materials. Then, I invoke and discuss two representative reference systems such as copper hydroxide nitrate $Cu_2(OH)_3(NO_3)$ (CuOHN), and copper hydroxide acetate $Cu_2(OH)_3(CH_3COO)$, (CuOHAc). In particular, I will present an extended review of what has been already accomplished by the scientific community in this field over the last 15 year.

1.1 Experimental state-of-the-art

1.1.1 Introduction

In the quest for specific design and tunable properties of matter, a rejuvenated interest is, recently, observed for the study of hybrid organic-inorganic materials [5]. Several approaches are pursued in the search for more synergy between the structural building blocks present in metal-organic frameworks (MOF) as well as in hybrid layered materials. These classes of systems are two representative final targets of synthetic routes currently highly exploited to produce hybrid materials [6, 7]. Critical parameters in promoting multifunctionality in hybrid systems are the interfacial bonding between the inorganic and organic building blocks as well as the dimensionality of the functional network. Structural units with strong metal bonds with organic linkers are obtained in MOF materials combining various properties such as magnetism and chirality [8, 9] or ferroelectricity [10].

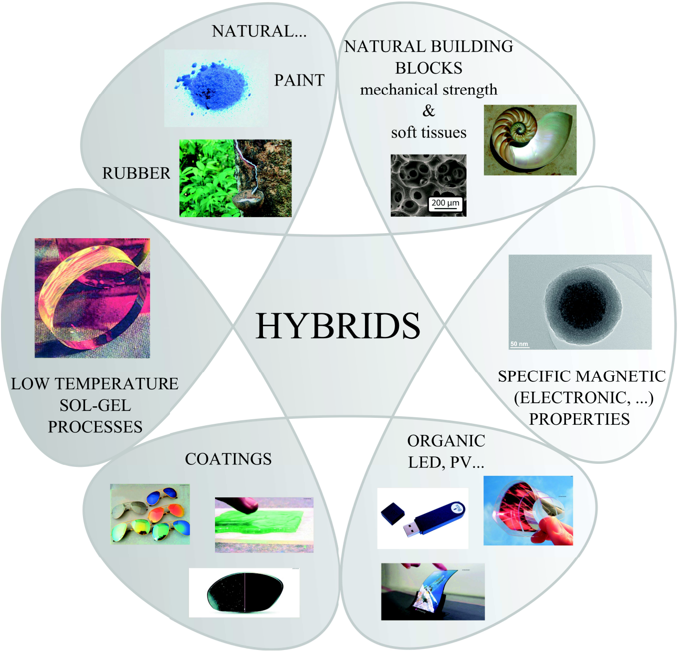

Figure 14 – Schematic overview of the omnipresence of organic-inorganic hybrid materials in our natural environment (mollusk shell, plants or in various minerals) as well as in fundamental research applications (core-shell nanoparticles and the glasses resulting from the variety of sol-gel processes developped) for industrial coating, memory storing devices, solar photovoltaic devices and nanoelectronics

However, when long-range cooperative interactions are sought after, the interfaces between the building blocks affect drastically the electronic and magnetic properties of the materials [12]. This fact has been recently highlighted in multiferroic systems by the use of neutron scattering experiments [11]. In the wide variety of layered materials explored in literature, the bond between the organic molecules and the inorganic network is weak which in turn affects the synergy of the electronic properties between the components [13, 14, 15, 16]. Through the hybridization of layered metal hydroxides, the new layered simple hydroxides (LSH) allow for strong bonds between the components since the anions are bound to the transition metal to form a crystal lattice [17].

A control of these hybrid materials through specific chemical synthesis methods allows for tunable magnetic interactions occurring by exchange mechanisms along metal-oxygen-metal bridges and leading to ferromagnetic, antiferromagnetic or ferrimagnetic behaviors of 2D and 3D type [7, 18]. Layered intercalation compounds find applications for catalysis purposes [19], photovoltaics [20], multifunctional materials [12] or as non linear optical media [21]. In Figure 14, we provide an overview of the diversity and applications of hybrid materials in the current research and technological context.

1.1.2 Experimental approaches

The first organic-inorganic compounds were obtained by intercalation chemistry from the insertion of organic compounds into certain layered solids. The field evolved considerably with the advent of soft inorganic chemistry processes called "Chimie Douce" [22]. The design strategies embedded in this method allow for molecular engineering of nanomaterials through the understanding of materials chemistry and processing. The sol-gel method is one of the possibilities of "soft" synthesis used in this framework. It allows for a good control of the chemical process used to synthesize a specific material (density, porosity, structure..). The general "Chimie Douce" concept is used referring to chemical conditions considered to be "mild" therefore involving reasonable temperature, pressure or pH conditions. This concept was pioneered by Livage [23, 24] and it was inspired by the biological world, especially by bio-mineralization processes. These methods lead to high quality glasses within particularly soft conditions opening the way for tremendous industrial applications. The controlled design of such hybrid compounds can be viewed as the evolution of the "trial and error" methods traditionally employed to achieve this type of materials.

As a broad concept, hybrid organic-inorganic materials can be defined as synthetic materials with organic and inorganic components intimately mixed, either homogeneous (miscible organic and inorganic compounds) or heterogeneous (phase separated). The development of soft inorganic chemistry processes is linked with the mild synthetic conditions in which the sol-gel process involves metal-organic precursors, low processing temperatures and versatility of colloidal state systems. This allows for a mixing of organic and inorganic components in *virtually* any ratio [25]. In the following, we sketch the basic principles of sol-gel methods insisting on definitions and few core concepts to highlight and emphasize specific strategies of hybrid materials chemistry. In sol-gel processes, typical precursors have the form $\mathrm{M(OR)}_n$, MX_n or $\mathrm{R'}\text{–}\mathrm{(OR)}_{n-1}$ where M, n, X and OR are, respectively, a metal center, its oxidation state and common "leaving groups" such as chloride or bromide anions. R' is any organic functional group anchored to the metallic center via a covalent bond (Si-C for example) or through complexing ligands, as in the case of $\mathrm{M} = \mathrm{Ti}, \mathrm{Zr}$. The sol-gel mechanism occurs through the connection of metallic centers with oxo- (or hydroxo-) bridges thereby generating metal-oxo (metal-hydroxo) polymers in solution.

Three common reactions are considered: *hydrolysis*, *oxolation* and *olation*.

- Hydroxyl-metal species are obtained by *hydrolysis* of an alkoxy group or the deprotonation of a water molecule attached to a metal center

  $$M - OR + H_2O \longrightarrow M - OH + ROH \tag{1.1}$$

  Through the reaction of the hydroxylated metal species with other metal centers, *condensation* reactions occur, an oligomer is thus formed as a result of the bridging of two or more metal centers.
- For *oxolation*, the condensation leads to the formation of an *oxo bridge* while water or alcohol molecules are eliminated

  $$M - OH + XO - M \longrightarrow M - O - M + X - OH \quad ; \quad X = (H, R) \tag{1.2}$$

- In the case of *olation*, metal centers (cations) may have a coordination higher than their valence, as in the case of Ti(IV), then an additive reaction takes place and a hydroxo bridge forms

  $$M - OH + XO - M \longrightarrow M - (OH) - M - OX \quad ; \quad X = (H, R) \tag{1.3}$$

The interplay and relative contribution of these three reactions impacts strongly the structure, morphology and connectivity of the final inorganic network. This occurs in most sol-gel processes by successive hydrolysis and condensation reactions [26]. The obtained hydroxo-oxo-polymers form a variety of structures such as branched system like dendrimers or compact clusters (for example organometallic clusters). The type of resulting structure depends strongly on intrinsic parameters (nature of metallic centers, lability..) or extrinsic conditions (solvent, water content, pH, catalysts..). Using methods to limit aggregation (spacers or tuning electrostatic interactions of the dispersed phase), the growth of these structures can be controlled and *sols* are obtained in the form of suspended colloids. An extensive growth or aggregation may occur up to macrosopic dimensions eventually trapping solvent molecules and smaller monomers to produce a *gel*. The precise control of the reactions 1.1 to 1.3 allows a tuning of size, shape or even miscibility of the inorganic compounds with the organic counterparts. In addition, functional precursors of the form R'-M(OR)$_{n-1}$ can also be used to modify the surface of inorganic entities enhancing the bio-compatibility of the system. Favored by the mild conditions characteristic of "Chimie Douce", sol-gel-derived species are suitable for further modification or functionalization with polymers, a variety of organic dyes or biomolecules. Such possibilities led to new fields of material research known as "sol-gel optics" and biohybrids [27, 28].

At this point, it is of interest to consider additional contributions to the methodologies for the design of transition-metal nanocomposites. These have been particularly inspiring when considering the study of phosphonate based systems that will be presented in detail within this PhD project [29, 30, 31].

In the 1990's, stemming from the experimental guidelines presented above, two main research directions were followed, exploiting different strategies to synthetize hybrids [64]. The first route consists in the synthesis of periodic mesoporous materials via sol-gel condensation. One of the pioneering works is the one of Inagaki et al. [65], in which the authors successfully synthesized an ordered benzene silica via a surfactant-assisted method. The second route concerns metal-organic frameworks (MOFs), considered as nanoporous crystalline hybrid coordination networks. Materials such as cyanide compounds or prussian blue-like structures attracted little interest until the middle of the 90's when several groups, as those of Robson and Yaghi [66, 67], started using rigid, polyfunctional molecules to bridge metallic cations or clusters into extended arrays with large amounts of voids. For the production of such robust systems, the idea was to engineer a "molecular scaffold" to connect the rigid organic components with non flexible inorganic structures or single metallic centers acting as joints. The choice of the length and functionalities of the organic units allows for a fine control of the size, chemical environment as well as void spaces within the architecture of the resulting hybrid compound. Similarly to the phosphonic groups case, metal phosphonates systems have been considered as layered inorganic networks and only later evolved toward organic-inorganic hybrids through the use of organic pillars [68]. In such layered structures, the orientation of the pillars is often perpendicular or quasi-perpendicular to the metallic layers in the interlamellar region [69]. Therefore, these organic pillars can be used to tune the interlayer distances of the final product, allowing exfoliation of the material into films [70].

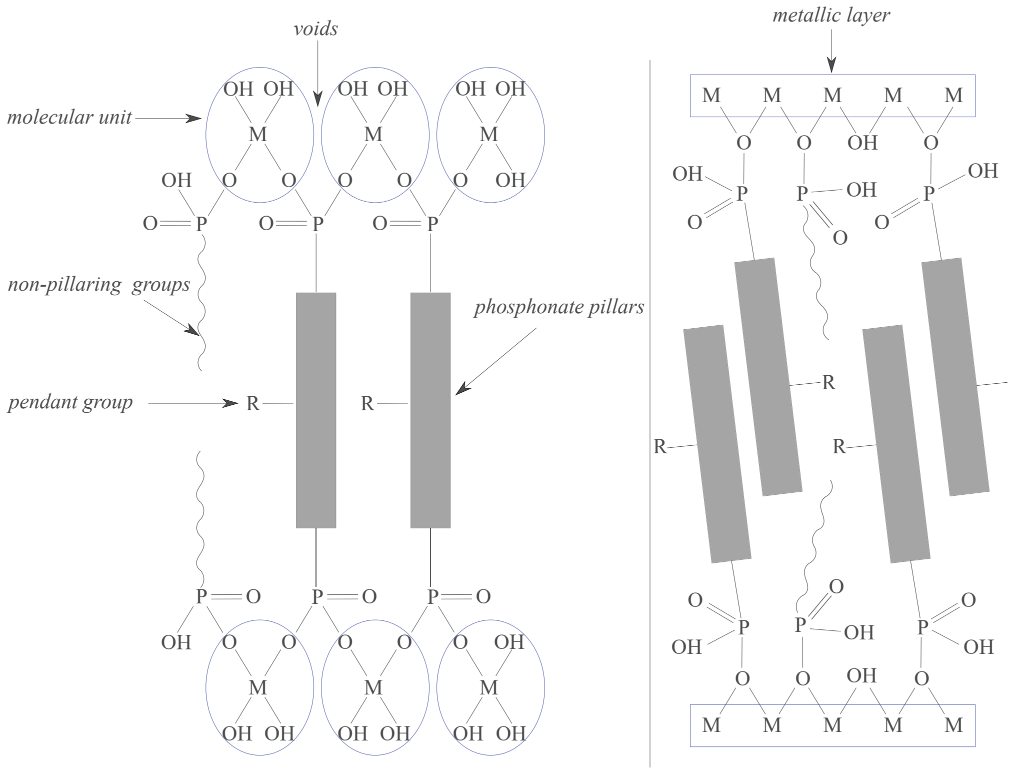

Figure 15 – Illustration of the structural differences between phosphonate based metal-organic frameworks (MOF) shown in the left part and hybrid layered materials (right part). *Figure inspired from Figure 2.3 of ref. [64]*

In Figure 15, we give a comprehensive scheme allowing us to highlight the differences between MOFs and layered hybrids in the case of metal phosphonate organic-inorganic hybrid materials. In view of the use of both "layered hybrid" and "MOF" terminology referring to separate types of materials, the differences between the two types need to be clarified. In fact, one encounters the ambiguous terminology of layered MOF materials in the recent work of Moreno et al. [71]. In their work, a family of stable layered MOF materials is obtained, based on ordered nickel cluster-type nanoribbons separated by organic species.

We consider three parameters that allow us to differentiate MOF from layered hybrids: porosity, the synthesis method as well as the nature of metal-organic bonds. The porosity is expected to be a parameter that can be controlled in MOF materials through the tunable amount and size of voids between molecular units (as exemplified in the left part of Figure 15). In the case of layered hybrids, cations are organized in packed layers (short metal-metal bonds) and form a surface on which the organic moieties are anchored (right part of Figure 15). Therefore, in this case, molecular units are hardly defined and the study is performed at the layer rather than at the single metallic center scale. In such hybrid layered systems, the porosity cannot be simply quantified and can just be expected if molecular spacers are used to separate the organic parts in a controlled way. In MOF materials, the metal centers are fully covalently linked with their coordination atoms (M-O solid lines in Figure 15) while in layered materials, these bonds have a much weaker covalent character and the same oxygen can coordinate few metallic sites ($\mathrm{M}\cdots\mathrm{O}$ dashed lines in Figure 15). In terms of synthesis method, MOFs are usually produced by hydrothermal or solvothermal techniques, with crystals slowly grown from a hot solution allowing the construction of the framework from bridging organic ligands. These ligands remain intact throughout the synthesis. Most often, MOF are described as 3D framework structures that exhibit porosity and/or guest exchange properties even if this definition does not encompass all compounds quoted in the literature [72]. In the case of layered hybrid materials, direct reaction, hydrothermal or exchange reactions can be used to obtain a crystalline compound [5].

An overall remark on the previous comparison between MOF and layered hybrids, is that the term "hybrid organic-inorganic material" is often used for MOFs even if this terminology mainly refers to sol-gel processes and ceramization. Thus, according to IUPAC recommendations, it is suitable to define "hybrid organic-inorganic materials" as "materials composed of an intimate mixture of inorganic components and organic components" [73]. Conversely, a complete name is given for characterizing MOFs which is "chemically bonded hybrid inorganic-organic coordination polymers". A more complete classification of hybrid materials and an explicit focus on layered metal hydroxides is performed in the next subsection.

Before performing this rigorous classification, we briefly review the characterization methods suitable for the study of hybrid materials. The main method to obtain the atomic structures of such systems is X-Ray diffraction (XRD) that can also be performed at high temperature (HTXRD). This technique is strongly dependent on the quality of the crystal. Fourier Transform Infrared Spectroscopy (FTIR) is a complementary technique allowing to observe the absorption spectrum of the system (vibration modes) with high sensitivity to the positions of hydrogen atoms. In addition, characterization is possible through methods such as scanning electron microscopy (SEM), useful to extract the samples surface topography and energy dispersive X-ray spectrometry (EDX) for the composition. Thermoanalytic techniques allow to get information on the exo- or endothermic nature of the transformations undergone by the system, a useful tool to identify the occurrence of glass transitions, crystallization, melting or sublimation. Examples of such techniques are DTA (Differential Thermal Analysis) and DSC (Differential Scanning Calorimetry) [3]. Due to the importance of the interfaces between organic and inorganic parts, more modern tools such as DOSY-NMR (Diffusion Ordered SpectroscopY-Nuclear Magnetic Resonance), are used in the context of pulsed field gradient methods to combine efficiently the high selectivity of NMR with the absence of any physical separation step. While standard NMR gives no information on the presence of functionalization species, grafted and free ligands can clearly be differentiated and quantified using DOSY-NMR experiments [25].

1.1.3 *Classification* of hybrid materials

Assuming the chemistry considerations introduced in the previous section, we can now classify hybrid materials based on all the related literature. A basic and broad classification of organic-inorganic materials includes the three main groups: intercalation compounds, organic derivatives of inorganic solids, and sol-gel hybrid materials (section 2.2 of ref [22]). However, these groups correspond to fields of research rather than to simple subsets of materials. Therefore, we do prefer to employ an alternative classification of hybrid materials relying on three main order parameters used in literature, namely, the dimensionality of the inorganic (and organic) networks, the nature of chemical bonds and the chemical pathways employed for the synthesis.

— Once the dimentionality of the inorganic (organic) components is considered (top left part of Figure 16), one can define a host and a guest phase in the system [20]. A formal way of quantifying this classification have been introduced by Cheetham and coworkers [32]. The metal-ligand-metal network dimensionality O^n and the inorganic framework counterpart I^n ($n = 0, 1, 2, 3$) are used to differentiate the various types of hybrid materials . The example of organochemistry is given to account for I^0O^0 type materials in view of the nature of the molecular complexes, that are virtually single inorganic units combined with organic molecules, not forming extended structures. The 3D nickel succinate structure is used to illustrate the I^3O^0 category due to the 3D nickel-oxygen framework decorated by organic groups. MOF materials are used for describing the other extreme category, I^0O^3 materials.

— When the nature of the interfaces, chemical bonds and interactions between inorganic and organic components are considered, a classification in two types of hybrid materials arises (top right part of Figure 16). Class I corresponds to all systems with no covalent bonding, only weak interactions (in terms of orbitals overlap) such as hydrogen bonding, π-π, weak electrostatic interactions and van der Waals contacts between the inorganic parts and organic moieties. In contrast, in Class II materials, at least a fraction of organic and inorganic components are linked through strong covalent, coordination or iono-covalent bonds [22]. However, these interactions can differ by the corresponding binding energy inducing

Classifications of hybrid materials by:

Dimensionality of inorg. (org.) components

Dimensionality of inorganic connectivity, I^n ($n = 0$ to 3)

Metal-organic-metal connectivity, O^n ($n = 0$ to 3)

	0	*1*	*2*	*3*
0	Molecular complexes	Hybrid inorg. chains	Hybrid inorg. layers	3D Inorg. hybrids
1	Chain coordination polymers	Mixed inorg.-org. layers	Molecular complexes	?
2	Layered coordination polymers	Mixed inorg.-org. 3D framework	?	?
3	3D coordination polymers	?	?	?

Types of interaction between inorg. and org. components

Class I	*Class II*
Weak interactions H-bonds van der Waals Electrostatic	Covalent bonds Coordination bonds Iono-covalent bonds Lewis acid-base bonds

Chemical pathways used for synthesis

Path A	*Path B*	*Path C*	*Path D*
Conventional sol-gel methods (hydrolysis/condensation) Hydrothermal synthesis Use of bridged precursors	Use of well-defined nanobuilding blocks (NBB) Assembling of NBB Dispersion of NBB	Self-assembling procedures combined to NBB approach Fabrication of templates by organic surfactants Use of bridged precursors	Integrative synthesis Micromolding methods Controlled phase separation phenomena

Figure 16 – Classification of hybrid organic-inorganic materials on the basis of three order parameters: the dimensionality of each component (I=inorganic, O=organic) in the top left part, the type of chemical bonding between the two parts in the top right table and the synthesis method (bottom part). The first table is adapted from Table 1 of ref. [32] while the two other tables are constructed based on the classifications proposed in refs. [22, 33]

an uncertainty in the classification. For example, H bonds interactions range in between 5 and 65 kJ·mol^{-1} while ionic bonds have energies in between 50 and 200 kJ·mol^{-1} [74].

— In the chemical pathways used to design hybrid materials, we can distinguish four main synthesis routes (bottom table of figure 16). **Path A** corresponds to syntheses via conventional sol-gel chemistry methods leading to amorphous hybrids through hydrolysis of organically modified metal alkoxides (or metal halides). Belong to this pathway also the so-called iono- and chalco-gels, where the inorganic network is made up of porous amorphous silica or chalcogenide and the organic part is made up of ionic liquids [75, 76, 77, 78]. It also encompasses: i) the exploitation of bridged precursors such as silsesquioxanes X_3Si-R'-SiX_3 (with R' an organic spacer and X = Cl,Br,OR) forming homogeneous molecular hybrids or

ii) hydrothermal syntheses in polar solvents in the presence of organic templates leading to MOF type materials. **Path B** consists of well defined assemblies of preformed objects or a dispersion of Nano-Building Blocks (NBB). NBBs can be clusters, functionalized nanoparticles, layered compounds (such as clays, layered simple/double hydroxides) able to intercalate organic compounds. **Path C** corresponds to self assembling procedures through templated growth of hybrid materials with controlled porosity, or periodically organised mesoporous hybrid silicas functionalized with organic compounds. One may combine self assembly approaches with the use of nanobuilding blocks allowing for a fine control of the assembling step. The previous synthesis paths lead to hybrid materials with crystallites of less than 500 Å size in at least one dimension. Combining A, B and C strategies, hierarchical complex architectures can be designed to obtain hybrid materials with specific structure to property relations [33]. **Path D** corresponds to integrative synthesis methods such as micro-molding using emulsion droplets, latex beads, or organogelators resulting in a fine control of the shape of complex objects up to the micron scale.

In view of all the possibilities offered in terms of design of hybrid materials, several applications from fundamental science to industrial products have been developed under the label of *functional hybrids* [22]. Hybrids with tunable mechanical properties, improved optical properties, good laser efficiencies and photostability, very fast photochromic response or pH sensors are revealing examples [79, 80, 81]. The one million Toshiba TV sets sold each year have screens coated with hybrids made of indigo organic dyes inserted in a SiO_2/ZrO_2 matrix. This is a striking demonstration of the immediate impact of the design of hierarchical hybrid systems on the industrial world, where conception and implementation of advanced materials is synonym of technological evolution. To further illustrate the wide impact of hybrid materials' concepts in the current technological context, we can mention bio-sensors. Indeed, such devices constitute a major biological as well as chemical tool for which the design and conception challenges are sometimes very similar to those encountered in hybrid materials case [82]. A bio-sensor is composed of two central components, the *biologically sensitive element* interacting selectively with another biological system and the *transducer* which transforms the chemical signal of interaction in a physical (often electrical or optical) signal more suitable for precise measurement and quantification. Therefore one can build a device able to track the change of concentration of any biological component provided a precise design of the "bioactive" (organic compounds) and the "physico-active" parts (often inorganic) of the device is available. The science of hybrid materials is involved in such issues since the study and control of interfaces between the organic and inorganic parts is unavoidable to achieve efficient properties.

In this specific situation, as in many others, it is highly desirable to perform a detailed study of the properties of hybrid materials by focusing on the origin and nature of their structural electronic and magnetic properties. Model systems are thus needed to provide insights on these properties. Layered metal hydroxide compounds are prototypical hybrid organic-inorganic materials. By referring to the criteria of the previous classification, copper hydroxide acetate fall within the category of I^2O^1, class I (or II) materials, synthesized via chemical pathways of type B. Such hybrids are made of 2D inorganic layers between which organic species are inserted making them an ideal subject of study both experimentally (well characterized single-crystal phases) and theoretically (atomic positions largely available and interesting electronic and magnetic properties). In addition, the functional aspect of the materials is an added value fostering the study of combinations of properties that cannot be reduced to the simple superposition of the isolated components behaviors.

1.1.4 Functionality and complexity in layered metal hydroxides

Layered insertion compounds are model systems for further ligand functionalization purposes through the use of versatile reactions. A first example is given by the interesting ferromagnetic or spin cross-over properties obtained for bimetallic oxalates (ox) systems of formula $A[M^{II}M^{III}(ox)_3]$ (with "A" a monovalent organic cation) at low temperature [83]. The inorganic framework of such materials often forms a honeycomb lattice in which the organic cations are replaced by the desired functional cations to design specific properties for the final product [5]. Layered double hydroxide (LDH) systems are another example, those anionic clays have a hydrotalcite-like structure and formula $[M^{II}_{1-x},M^{III}_{x}(OH)_2]^{x+}[A^{n-}_{x/n}](H_2O)_y$ with M^{II}=Mg,Co (or Ni,Zn..), M^{III}=Al,Cr,V,Ga,Rh..) with y an integer. The $[M(OH)_2]$ layers contain both tri and bivalent metal ions in octahedral sites, the positive charge of which is compensated by anionic species A^{n-} occupying the interlayer space [84, 85, 86]. Despite the tremendous number of exchange reactions offered by these systems, in general, the bond between organic and inorganic networks is weak (Class I materials) resulting in a low interaction between the components. Other methods favoring stronger interaction between inorganic and organic species have been developed by hybridization of LSH materials, $M_x(OH)_{2x-yn}(X^{n-}_y)$, the divalent metal being M(II) = Co, Cu, Ni, Mn, Zn and the anion X^{n-} = carboxylate, sulfate, sulfonate or phosphonate [12, 17].

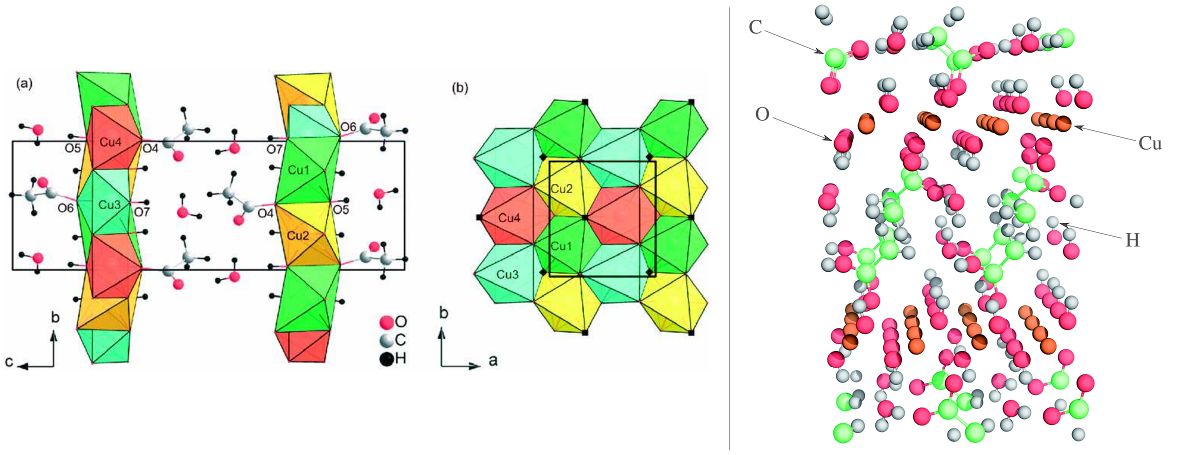

Figure 17 – Experimental (left part, a) side view and b) top view) and simulated (right part) structures of a prototypical layered simple hydroxide system: copper hydroxide acetate $Cu_2(OH)_3(CH_3COO)\cdot(H_2O)$. *The left part of the Figure is adapted from the experimental paper of Švarcova et al. [3]*

Basic LSH structures with general formula $M_2(OH)_3(X)$ ($X = NO_3$, CH_3CO_2, Cl) deriving from Bottalackite type systems are, in this work, the model systems to be considered. The second part of this chapter will be focused on exposing the state of the art of theoretical approaches used to study the properties and behaviors of such compounds. An example of the experimental single crystal structure of copper hydroxide acetate is provided in Figure 17 (a,b) [3] where one can also find an example of the simulated cell used in our work (right part of Figure 17). The crystal structure consists in a quasi-planar triangular array of octahedral M(II) ions separated by anions, in this case acetate groups CH_3COO^-, coordinating the metallic sites in the presence of water molecules. One assumes that each non hydroxyl anion (carboxylate, sulfate, phosphonate) is linked to three metal ions in a tetrahedral environment [34]. These different anchoring groups possibilities are exemplified in the schematic representation of Figure 18, in which the three chemical functionalities cited are represented [87, 49].

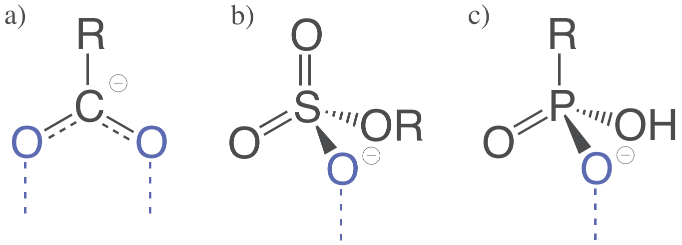

Figure 18 – Schematic representation of the chemical functionalities typically used to link the organic component to the inorganic metallic or metal hydroxide layers: a) carboxylate; b) sulfate; c) phosphonate. R represents the organic moiety (such as acetate, alkyl chain or fluorene) and in blue are highlighted the oxygen atoms, potentially, involved in the interaction with the metal ions through covalent, iono-covalent or weaker interactions [87, 49].

The short metal-metal bonds ($\simeq 3$ Å) result in effective magnetic interactions due to the exchange coupling along metal-oxygen-metal paths leading to ferromagnetic, antiferromagnetic or ferrimagnetic 2D behaviors. From the synthesis point of view, direct reactions of transition metal salts in aqueous solutions with alkaline agents result in the precipitation of hydroxide phases and are well adapted for small anions like chloride, nitrate or acetate. High quality crystalline powders are obtained and a full characterization of the crystal structure is possible. For larger and more complex anions, hydrothermal conditions and exposition to higher temperatures (100 to 250 °C), similar to the synthesis of MOF materials, are necessary to achieve good crystallization [12]. Therefore, by substituting a large variety of organic molecules via anionic exchange reactions, the interlamellar species can be used as pillars or bridges between the magnetic layers and achieve a control of interlayer interactions by tuning the size and electronic properties of the exchanged anions.

The chemical and structural possibilities offered by LSH materials allow for insertion-grafting of functional molecules within the layered inorganic-organic network. Various properties such as conductivity, luminescence, chirality, electro-activity and magnetism can thus be obtained [12]. However, the grafting of the organic species is not a straightforward process due to the difficulty of stabilizing the inserted species on host matrix surfaces in the mild synthesis conditions. Post-functionalization and *in situ* molecular synthesis can be used to achieve stabilization by pre-grafting single molecules providing adequate reaction sites for further building of the final compounds [88].

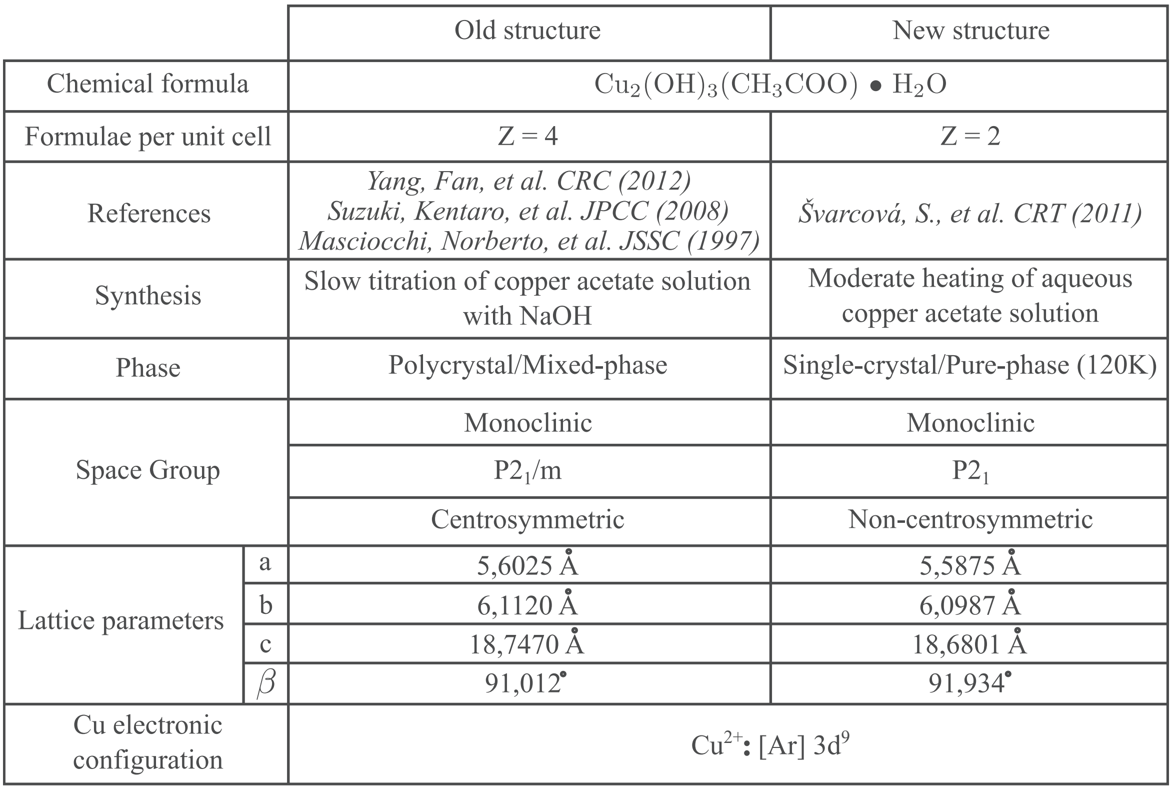

		Old structure	New structure
Chemical formula		$Cu_2(OH)_3(CH_3COO) \bullet H_2O$	
Formulae per unit cell		Z = 4	Z = 2
References		*Yang, Fan, et al. CRC (2012)* *Suzuki, Kentaro, et al. JPCC (2008)* *Masciocchi, Norberto, et al. JSSC (1997)*	*Švarcová, S., et al. CRT (2011)*
Synthesis		Slow titration of copper acetate solution with NaOH	Moderate heating of aqueous copper acetate solution
Phase		Polycrystal/Mixed-phase	Single-crystal/Pure-phase (120K)
Space Group		Monoclinic	Monoclinic
		$P2_1/m$	$P2_1$
		Centrosymmetric	Non-centrosymmetric
Lattice parameters	a	5,6025 Å	5,5875 Å
	b	6,1120 Å	6,0987 Å
	c	18,7470 Å	18,6801 Å
	β	91,012°	91,934°
Cu electronic configuration		Cu^{2+}: [Ar] $3d^9$	

Figure 19 – Comparative table of the experimental copper hydroxide acetate structure characterized by Masciocchi and coworkers in 1997 [89] and the one of Švarcova et al. in 2011 [3] *(details in the text)*

The problem most often encountered in hybrid organic-inorganic materials is the understanding of the structure of the final compound in terms of arrangement of the organic molecules within the interlayer space. On the other hand, the inorganic part of the system is a challenge in terms of nano-structuration, in particular for the organic parts anchoring sites. The different experimental methods used for the characterization do not always provide a clear picture for the relationship between the structure and the physical properties [12]. If we consider the case of the copper hydroxide acetate (CuOHAc) system, fourteen years went by between the first characterization of the material in 1997 by Masciocchi et al. [89] and the first elaboration of a single crystal [3]. Many characterization techniques used such as XRPD (X-Ray Powder Diffraction), XPS (X-ray Photoelectron Spectroscopy), XAES (X-ray Auger Electron Spectroscopy) or FTIR (Fourier Transform Infra Red) allowed Masciocchi et al. [89] to obtain a reasonable structural characterization of the system, later used to initiate theoretical works on this compound. Typically, in such systems, the resolution of hydrogen atoms and water molecules is a complicated issue, playing an important stabilization role in the structure through hydrogen bonds (H-bonds) networks. Many theoretical works presented in the next section were stimulated by the first available characterization of Masciocchi and coworkers, recently complemented by the work of Švarcova et al. in 2011 [3]. In the latter, the morphology and crystal phase control issues were solved by using a moderate heating method (60 °C) of copper acetate solution resulting in a single crystal phase obtained both at 120K and 293K. A full characterization of the systems allowed to obtain the complete set of atomic positions. A comparison between the structures obtained by Masciocchi [89] and Švarcova [3] is presented in Figure 19. Copper hydroxide acetate has also been investigated for its magneto-structural properties. Indeed, in 2008, Suzuki and coworkers [4] obtained a copper hydroxide acetate compound following Maschiocchi's [89] route of synthesis and characterization, and went further performing SQUID (Superconducting QUantum Interference Device) measurements. They were able to probe the magnetic properties at the 2D Cu^{II} layers scale and for the full compound (3D). By applying an isostatic pressure along the $\vec{c}$ direction of the crystal, the magnetization (M) versus applied magnetic field (H) is measured for both ambient (0.0001 GPa) and 1.2 GPa pressures. The comparison of these results highlighted an interesting pressure-induced magnetic transition in the system (Figure 20).

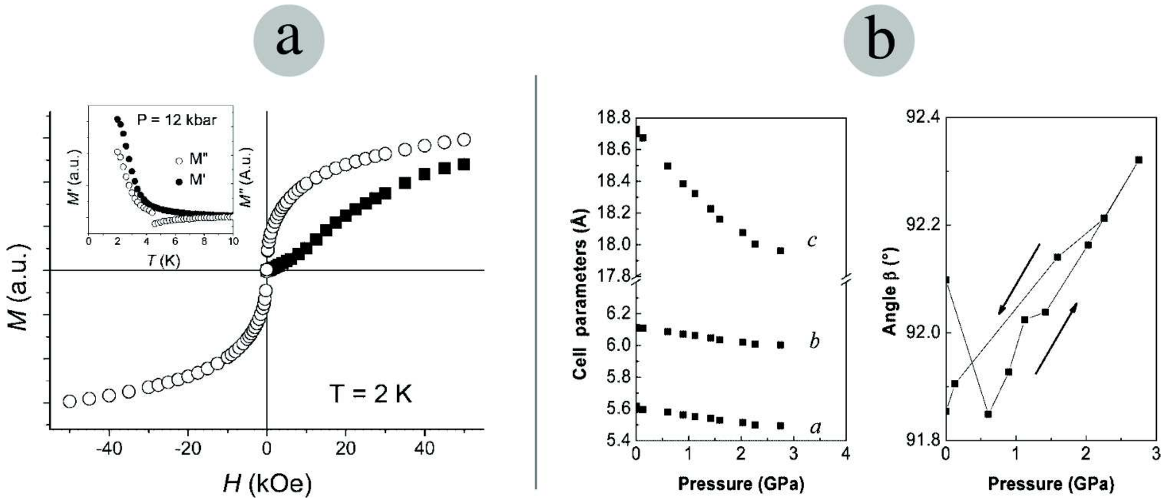

Figure 20 – a) Magnetization versus applied magnetic field for the CuOHAc compound under ambient pressure of 1 bar (squares) and 1.2 GPa pressure (circles). The inset shows the ac real (M') and imaginary components (M") of the magnetic susceptibility measured under the application of 1.2 GPa pressure (*Figure 5 of ref. [4]*), b) Evolution of the lattice parameters of the copper hydroxide acetate (CuOHAc) structure under application of an isostatic pressure along the $\vec{c}$ direction of the crystal (*Figure 6 of ref. [4]*)

The magnetization measured is related to the magnetic susceptibility χ used to characterize the output of magnetic measurements and defined as $\chi = \mathrm{dM}/\mathrm{dH}$ measured at $\mathrm{H} = 0$ [90]. The AC magnetic susceptibility measurement yields two quantities: the magnetic susceptibility χ, and the phase shift ϕ relative to the driving signal. Commonly, susceptibility is thought of as having an in-phase (or real) component χ' and an out-of phase (or imaginary) component χ''. Both representations are related as follows [91]

$$\begin{array}{ll} \chi' & = \chi cos(\phi) \\ \chi'' & = \chi sin(\phi) \end{array} \Leftrightarrow \begin{array}{ll} \chi & = \sqrt{\chi'^2 + \chi''^2} \\ \phi & = arctan\left(\frac{\chi''}{\chi'}\right) \end{array} \tag{1.4}$$

Therefore, the steep increase of the M(H) curve at low field, shown in Figure 20-a, is characteristic of a ferromagnetic behavior. This magnetic transition brings a 3D ferromagnetic-like ordering, confirmed by the out of phase signal observed in the AC susceptibility at 2 K. This pressure induced magnetic transition from an anti-ferromagnetic to a ferromagnetic state is interpreted as being due to the distortion of the inorganic network similar to the chemical pressure effect observed in long alkylcarboxylate systems [4]. The main difference between these two situations is the localization of the distortions in the long chains system while an homogeneous distortion is expected in the acetate system.

All these results and experimental investigations highlight the importance of control and precise monitoring of the electronic, magnetic and structural properties of hybrid compounds in order to achieve new and innovative multifunctional materials. It seems clear that there is a need of modeling and advanced simulation techniques in order to disentangle all the effects observed at different scales. More precisely, understanding the nature of chemical bonding between the organic and inorganic parts, investigating the magnetic properties at the atomic scale and simulating the effects of external stimuli such as pressure or temperature are challenges for the computational material science community that fit within this context. We follow this route using FPMD (first-principles molecular dynamics) methods, we focus on LSH systems to get insights on the characteristics of complex hybrid materials. In the next section, we present the theoretical state-of-the-art underlying our main project, through the review of previous approaches and the most recent results obtained in theoretical investigations of hybrid systems.

1.2 Theoretical state-of-the-art

1.2.1 Introduction

Through the previous section, we described the design of hybrid materials and the fine control of the structure and chemical bonding from an experimental science perspective. It is of interest to employ modeling methods to unravel the physics and chemistry involved in such systems. Depending on the type of issue, modeling methods can be "classical" (this being a very general definition) such as classical molecular dynamics (MD) or Monte Carlo techniques (MC). However, in most cases, to account explicitly for the nature of chemical bonding, one has to resort to quantum mechanical calculations as in the framework of quantum chemistry methods (QC) or density functional theory (DFT).

In this section, we discuss the interest of such techniques and their domain of validity. This will bring us to introduce the use of first-principles molecular dynamics (FPMD) that allows both the investigation of electronic and magnetic properties as well as the application of statistical physics methods to follow the atomic trajectories as a function of time. In the Figure 21, the diversity of models and systems are associated to give

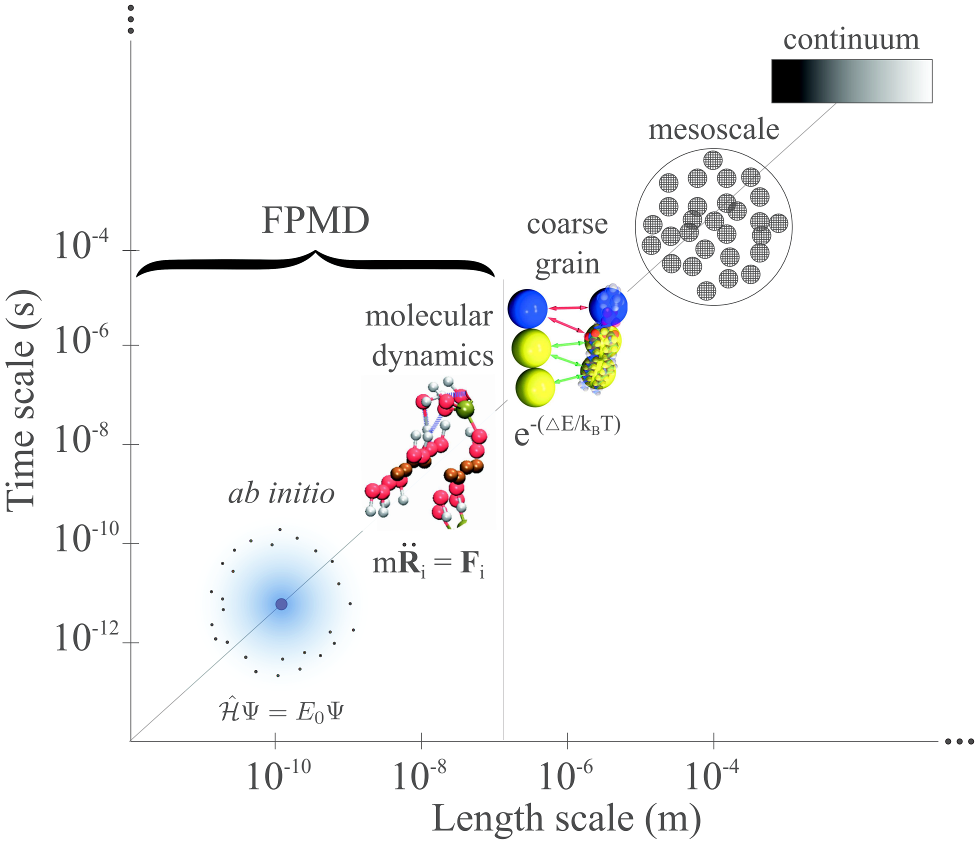

Figure 21 – Length and time scales corresponding to the different modeling methods. An enormous range of phenomena can be understood by simulation techniques. At the two extremes, these feature *ab initio* models for a quantum description to obtain electronic and atomic scale behavior and continuum-like heat equations modeling the thermal convection in earth's mantle. The main methods used in this project for describing both structural and electronic properties are first-principles molecular dynamics (FPMD) in which a quantum description of the electrons is coupled with the classical motion of the ions

a coherent picture of the purpose of modeling of materials. In the left bottom side we refer to techniques implementing quantum mechanical equations (Schrodinger-like equations), thereby allowing for a first-principles description. There are two notions of first-principles methods that are invoked in different communities, namely solid-state physicists and quantum chemists. For the first, DFT is first-principles, the applications being mostly oriented toward solids and periodic systems. A quantum chemist does not necessarily consider DFT as a first-principles method since he mostly seeks to benchmark and reproduce experimental data with the highest accuracy. As to the significance of first-principles as a general label denoting calculations not parametrized on experimrental data, there is a lack of consensus within the two above communities. As far as my work is concerned, first-principles is employed throughout this thesis as corresponding to density functional based calculations.

The need for precise optimization of structures and the inclusion of external fields such as temperature or pressure underscores the necessity of following explicitly the motion of the atomic degrees of freedom as a function of time. This is exactly what molecular dynamics does. When this technique employs interatomic forces calculated by accounting for a potential energy surface depending on the electronic structure, it becomes first-principles molecular dynamics. In view of the size of the simulation cell and the number of atoms ($\simeq$ 100 to 1000 atoms), FPMD is the ideal method to combine chemical accuracy and the realistic treatment of model systems intended to be the counterpart of experimental compounds. To this end, we use exclusively FPMD methods as implemented in the CPMD package [2] for the study of LSH systems. In what follows, some examples are given in this context referring to studies of the magnetic behavior of materials through first-principles techniques ([17]). We also focus on the model systems of interest for our work, copper hydroxide nitrate and copper hydroxide acetate.

To span the large spectrum of available literature on theoretical studies of hybrid materials, we first present in more detail the models used for understanding magnetism and other properties in such systems. Then, we consider more closely the potential impact of atomic-scale modeling on these investigations relying on specific examples justifying the choice of FPMD methods. The details concerning the exchange correlation functionals used (BLYP, B3LYP etc) are left for the next chapter.

1.2.2 Molecular magnetism models

The great variety of magnetic behaviors observed in transition metal complexes led to the construction of models aiming at describing magnetic interactions between the components. It has been recognized very early that such behaviors cannot be described by the sum of the magnetic properties of individual units [92]. In fact, the coupling of the electron spin of the different atoms or molecules requires the inclusion of exchange interactions effects. Since the first recognition of intramolecular magnetic coupling by Guha [93], many theoretical studies aimed at investigating the mechanism of exchange coupling and its relationship with the electronic structure of materials [94]. The study of the electronic structure of magnetically coupled systems is more challenging than the problem of chemical bonding in closed shell molecules. Exchange couplings effects have challenged many of the simplistic models previously used to understand molecular magnetism, showing their severe limitations [17].

The first and most widely used phenomenological model is based on the Heisenberg Hamiltonian. From the conceptual point of view, such model (in 1D) is not more complex than the problem of N cards, each colored red or blue, arranged in a ring, with a shuffler choosing two adjacent cards to switch. Indeed the transition matrix of such a situation is precisely the one corresponding to a Heisenberg Hamiltonian with the cards being half integer spin particles (electrons) and the color (red/blue) corresponding to their spin state (up/down) [95]. However, despite the simplicity in stating the problem, the solution may correspond to very complex situations and arrangements of the spins. In the case of magnetic copper(II) acetate compound (dimeric with four acetates bridging two Cu^{2+} sites), a broad maximum of the magnetic susceptibility is observed as a function of temperature while becoming negligible below 100K [96]. The Heisenberg Hamiltonian can, here, be used to model the exchange interaction between two paramagnetic centers

$$\hat{H} = -J\hat{S}_A.\hat{S}_B \tag{1.5}$$

where S_A and S_B (S_A=S_B=1/2 here) are the total spins on each metal ion and J is called the exchange coupling constant [94]. The idea consists in modeling nearest neighbors magnetic sites (A and B) interaction with the sign of J determining the magnetic configuration corresponding to the system under study (positive and negative J values for ↑↑ and ↓↑ configurations respectively). S_A and S_B cease to be good quantum numbers as soon as an interaction occurs between the two magnetic sites and the pair states need a total spin operator to be suitably described

$$\hat{S} = \hat{S}_A + \hat{S}_B \tag{1.6}$$

for which the corresponding eigenvalues involving the total spin are

$$E(S) = -\frac{J}{2}S(S+1) \tag{1.7}$$

For the two local doublet states found in copper(II) acetate, the last expression leads to a singlet (S=0) and a triplet (S=1) states separated by an energy gap

$$E_{Singlet} - E_{Triplet} = J \tag{1.8}$$

The goal of this section is to overview the models allowing a qualitative understanding of experiments in the area of molecular magnetism. We note that exchange coupling constants are not directly measured, since one obtains rather the magnetic susceptibility. Therefore, the model Hamiltonian is used to derive an expression for the temperature dependence of the magnetic susceptibility. Then, a fit to experimental data is performed with the exchange coupling constant being the fitting parameter [94]. In the Cu^{2+} dimer case, the application is straightforward while for more complex systems the task becomes intractable. The multiple possibilities are dealt with through several approximations on the nature of magnetic couplings and the paths by which such interactions can be mediated. Therefore, the coupling constants determined in this way may widely differ in particular in the case of complex hybrid materials.

A part from such phenomenological approach, many ideas on exchange interactions were inspired by the study of infinite solid lattices [97]. The introduction of the role of superexchange and the validity of the atomic orbital approximations fostered the realization that bridging atoms (such as oxygen) between metal ions with unpaired electrons determine the sign and magnitude of the exchange coupling. The quantum treatment of orbitals overlap between the ligands and metal *d* orbital brought to the construction of all kind of qualitative models [94, 98], from which, two widely used valence-only models are based on *orthogonal magnetic orbitals* and *natural magnetic orbitals* descriptions [59, 99]. We should emphasize that a main goal for such methods is to compute the exchange coupling parameter as defined, previously, in the Heisenberg model, identifying it to the singlet-triplet splitting (E_S - E_T). The first approach corresponds to Hay, Thibeault and Hoffmann proposition (HTH) [59] to treat magnetic interactions in dimeric systems ligand (L) metal (M) anion (X) of the type L_nM_a-X-M_bL_n (n = 3,4,5) with ligands being halogens and the anion, an acetate-like group. The authors consider d-like orbitals of two weakly interacting metal centers bridged by one or more atoms, each bearing an unpaired electron occupying $d_{x^2-y^2}$ orbitals. New orbitals are constructed from linear combinations of these as follows

$$\Phi_1 \simeq d^a_{x^2-y^2} + d^b_{x^2-y^2} \tag{1.9}$$

$$\Phi_2 \simeq d^a_{x^2-y^2} - d^b_{x^2-y^2} \tag{1.10}$$

with a and b corresponding to the two d^9 metals.

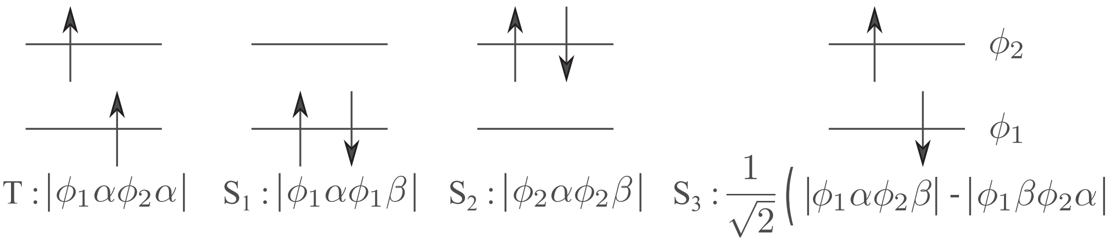

Figure 22 – The two possible electrons configuration: the Triplet (T) and Singlet (S) states corresponding to ϕ_1 and ϕ_2, the molecular orbitals constructed from the partially occupied $d_{x^2-y^2}$ orbitals of two metal centers forming a M$_a$-X-M$_b$ bridged system (X being the anion)

Four many-electron configurations are constructed as shown in Figure 22, the lowest energy triplet state being well represented by ψ_T while the corresponding singlet ground state is a mixture of S$_1$ and S$_2$ configurations:

$$\psi_S = \lambda_1\psi_{S_1} + \lambda_2\psi_{S_2} \tag{1.11}$$

In the noninteracting situation (metal centers too far apart), $|\lambda_1|$=$|\lambda_2|$ and if strong metal-metal bonds exist, $|\lambda_1|$»$|\lambda_2|$. In the original formulation of the HTH model, expectation values are calculated for the triplet (E$_T$) and singlet (E$_S$) states considering a Hamiltonian containing all kinetic, electron-nuclei (also with passive electrons) and nuclei-nuclei interactions ($\hat{h}$) as well as Coulomb ($\hat{J}$) and exchange ($\hat{K}$) interactions operators. S$_1$ and S$_2$ have the same spin and spatial symmetry. To obtain the lowest energy singlet, a 2x2 matrix is diagonalized with E$_{S1}$ and E$_{S2}$ on the diagonal and interactions between the two determinants in off-diagonal components. Using approximations on the relative amplitude of electrostatic and exchange interactions, a final expression of the HTH model for the singlet-triplet splitting is obtained

$$E_S - E_T = J = 2K_{ab} - \frac{(\epsilon_1 - \epsilon_2)^2}{J_{aa} - J_{ab}} \tag{1.12}$$

with ϵ_1 and ϵ_2 corresponding to the Restricted Hartree-Fock (RHF) energy operator for triplet state orbitals

$$\epsilon_1 = h_1 + J_{12} - K_{12} \tag{1.13}$$

$$\epsilon_2 = h_2 + J_{12} - K_{12} \tag{1.14}$$

Localized orthogonal molecular orbitals are also introduced to simplify the expression such that

$$\phi_a = \frac{1}{\sqrt{2}}(\phi_1 + \phi_2) \;\; ; \;\; \phi_b = \frac{1}{\sqrt{2}}(\phi_1 - \phi_2) \quad and \quad \langle\phi_a|\phi_b\rangle = 0 \tag{1.15}$$

Therefore, we have in the expression of the total J (eq. 1.12), a ferromagnetic J$_F$ contribution due to the first term (positive) and an anti-ferromagnetic J$_{AF}$ contribution from the second term (negative). Many limits of such model are described in literature such as the impossibility of treating intramolecular magnetism and the localization criterion, only valid when metal centers M$_a$ and M$_b$ are symmetry related (inversion for example). These shortcomings are discussed in the book of J. Miller and M. Drillon [17]. A more rigorous derivation of the model, as well as its extension to more than one unpaired electron on each metal atom, can be found in the chapter 4 of the book of Cohen et al. [100] (also exposing Kahn-Briat and McConnell's models).

The second example is the natural magnetic orbitals model (NMO) proposed by Girerd et al. [99]. This approach addresses some of the deficiencies of the HTH model, for M-X-M systems, by analyzing the relationship between electronic structure and exchange coupling. In this approximation, for the fragments M$_a$-X and M$_b$-X in their respective local ground states, two orbitals ϕ_a and ϕ_b (for the two metal centers M$_a$ and M$_b$) are defined as singly occupied partially delocalized toward their surrounding ligand. This partition of the system is the weak point of the approach due to the overestimated weight given to the bridging component orbitals [17]. The starting point of the NMO approach is a Heitler-London type wavefunction [101]

$$\Psi = \frac{1}{\sqrt{2(1 \pm S_{ab}^2)}}\left[\phi_a(1)\phi_b(2) \pm \phi_a(2)\phi_b(1)\right] \tag{1.16}$$

where the positive sign holds for the singlet and the negative sign for the triplet state. In addition, natural magnetic orbitals are by construction non-orthogonal and an overlap integral is defined

$$S_{ab} = \langle\phi_a|\phi_b\rangle \tag{1.17}$$

A singlet-triplet splitting is thus obtained from the two states defined by the wavefunction in equation 1.16 and is expressed as

$$E_S - E_T = J = 2k_{ab} + 4h_{ab}S_{ab} - 2S_{ab}^2\left(2h_{aa} + j_{ab}\right) \tag{1.18}$$

In this valence-only method (as in the HTH model), $\hat{h}$, $\hat{k}$ and $\hat{j}$ correspond to the one-electron Hamiltonian (containing kinetic energy of the electron and its interactions with nuclei and passive electrons), the exchange and coulomb terms respectively

$$h_{ab} = \langle\phi_a|\hat{h}|\phi_b\rangle \tag{1.19}$$

$$k_{ab} = \langle\phi_a(1)\phi_b(2)|r_{12}^{-1}|\phi_a(2)\phi_b(1)\rangle \tag{1.20}$$

$$j_{ab} = \langle\phi_a(1)\phi_b(2)|r_{12}^{-1}|\phi_a(1)\phi_b(2)\rangle \tag{1.21}$$

$$\tag{1.22}$$

Similarly to the expression obtained in the HTH model, the first term of 1.18 is always positive and thus represents a ferromagnetic contribution, while the second term is negative as S_{ab} and h_{ab} are of opposite sign. If the overlap integral measuring the non-orthogonality of the orbitals is small enough, the last term is neglected and we obtain

$$J = J_F + J_{AF} \simeq 2k_{ab} + 4h_{ab}S_{ab} \tag{1.23}$$

Note that the exchange coupling constant now crucially depends on S_{ab}. If this overlap vanishes, we have $J = 2k$ and a triplet ground state is to be expected. Therefore, in principle, if the S_{ab} term can be computed, the effect of different bridging anions on exchange interactions can be evaluated [17].

The two models briefly exposed in this section give an idea of the models and approximations used to qualitatively predict the nature and effect of magnetic interactions in polynuclear complexes. These were applied with some success as in the case of the (molecular) copper acetate model system. However, the nature of the approximations on orbitals overlap as well as their construction is making the model far from being quantitative. In chapter 7.4 of ref. [17], an overview of more quantitative approaches such as perturbation theory, variational methods and broken-symmetry functions is provided followed by the exposition of the possibilities of first-principles considerations. This last method is of special interest for us since it allows for the prediction of exchange coupling constants in complex systems through the use of specific exchange correlation functionals. At this point, we will detail the successes and limitations of the computation of exchange coupling parameters through first-principles methods. There will be a special emphasis on the importance of atomistic simulations in predicting good structural properties of complex materials, a necessary step for the computation of reliable electronic and magnetic properties of hybrid materials.

1.2.3 Atomic-scale modeling of materials

Atomic-scale modeling label encompasses (at least for the purpose of this work) all electronic structure calculations performed via density-functional theory as well as the use of molecular mechanics methods to optimize the corresponding structures. Historically, within density functional theory, the combination of a carefully chosen exchange-correlation part of the total energy and localized basis sets for the electronic orbitals has been the method of choice for computing exchange coupling constants in magnetic molecular materials. In contrast, plane waves form a complete and orthogonal basis set, more suited to allow for efficient structural optimization of unknown geometries. In this respect it is worth reviewing a paper in which, for molecular magnetic systems, was proposed a detailed comparison of localized orbitals and pseudopotential-plane wave basis sets in term of performance and accuracy in the determination of exchange coupling constants in complex molecular magnetic systems [102]. From this contribution one can conclude that, even though DFT is, in principle, less accurate than configuration interaction (CI) techniques, its efficiency in terms of computational cost is superior, since its reliability is quite high and large system sizes (hundreds of atoms) become accessible. Therefore, this route allows for the computational study of materials ranging from heterodinuclear molecules to large polynuclear compounds and complex solids [17]. The choice of the exchange-correlations functional affects importantly the quality and the performances of the DFT scheme used and the use of a manageable basis set allows to account adequately for the nature of the problem. However, in such approaches and for complex solid state systems, a complete characterization of the structure is necessary to compute reliable quantities. It is therefore mandatory to use periodic extension of the simulated systems, such as in the CRYSTAL package [103], in order to optimize the structure (relaxing the forces on the atoms) and thus obtain a fair determination of exchange coupling constants for periodic solids. If the starting systems (experimental structures) are close to local configuration minima, the localized basis sets schemes allow for structural optimizations but methods based on plane waves (PW) often enable more efficient implementation strategies that can handle the exploration of a large configuration space. The core idea behind PW usage is the exploitation of fast fourier transforms (FFT) for total energy and forces calculations simplified by the construction of plane waves (independent on ionic coordinates) [104].

The application of density functional methods using so called B3LYP functionals has led to a variety of studies focused on dinuclear compounds of type of hydroxo-bridged Cu(II) complexes. This "simple" magnetic system nevertheless exhibits, in a variety of molecular environments, ferro or anti-ferromagnetic behaviors which makes it ideal to design and check models of molecular magnetism. Crawford and coworkers [107] have proposed, in 1976, that a linear correlation exists between the observed exchange coupling constants and the $Cu\hat{O}Cu$ bridging angle θ (sketch in Figure 23). In the Figure 23-A, an example of a success of the use of the use of gaussian basis sets to describe magneto-structural coupling in Cu(II) hydroxo-bridged model system [105] is presented. A theoretical study of the dependence of the exchange parameter on the bridging angle (squares in Figure 23-A) shows that an optimized θ (with a corresponding out of plane angle τ) produces "J" values that are in good agreement with experimental findings (black circles). In addition, as shown in Figure 23-B, one can reproduce the linearity suggested in the HTH model (equation 1.12) between the exchange coupling constant and the energy difference between the Kohn-Sham single occupied molecular orbitals in the triplet state (SOMO) as introduced in the previous subsection (Figure 22). The applicability to periodic solids of the trends established above for molecular systems is questionable, due to the existence of a large number of exchange pathways. The role played by interlayer interactions and the occurrence of frustration effects prevents isolated molecular models to be considered for periodic materials [17] (such as $Cu_2(OH)_3NO_3$ presented in the next subsection). For such systems, provided the experimental atomic structure is known, DFT-PW methods can be used to extract exchange coupling constants from the study of a collection of microscopic spin configurations compatible with the total magnetic character of the system [102]. In addition, whenever experimentally well characterized structures are not available, the structural optimization is a mandatory prerequisite. In such context, first-principles molecular dynamics becomes a method of choice handling both structural and electronic degrees of freedom.

Therefore, it is also an adequate approach to extract information on the bonding properties and their evolution with temperature in many systems such as nanostructures or disordered materials. This fact is illustrated by the work performed by Matsubara

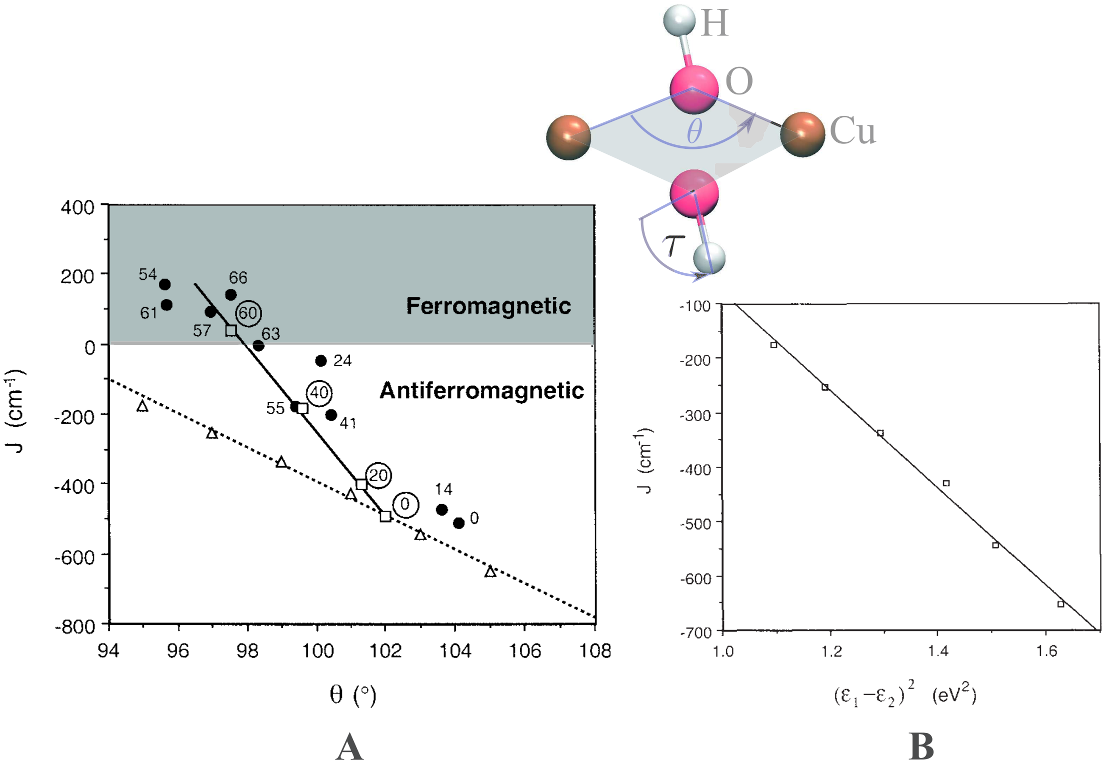

Figure 23 – A) Exchange coupling constants calculated by DFT-B3LYP methods for Cu(II) hydroxo-bridged compounds as function of $Cu\hat{O}Cu$ bridging angle θ. Black filled circles correspond to experimental values accompanied with the value of the τ angle for each structure [105]. Triangles correspond to the calculated values for the planar model ($\tau = 0$) fitted with a line (dotted line). The squares correspond to the calculated J values for the optimized θ at a fixed τ value (circled numbers). B) Singlet-triplet energy separation calculated with the same computational method for the Cu(II) hydroxo-bridged model with $\tau = 0$ as function of the square of the energy difference of Kohn-Sham calculated orbitals in the triplet state (as introduced in the HTH model equation 1.12). *A and B plots are adapted from refs. [17, 105, 106]*

and coworkers [108] on these two categories of materials through the study of disordered amorphous binary systems Ge_xSe_{1-x} (glasses) in particular for x = 0.20 and x = 0.33 and as a second model system, silicon-doped heterofullerenes. In the case of amorphous glasses (Ge_xSe_{1-x}), the authors use a practical tool in the study of disordered systems which is the partial pair distribution function (pdf) $g_{\alpha\beta}(r)$. It gives an account for the number of neighbors β of a certain atom type α for increasing radial distances, a quantity which reduces to three possibilities in the binary glass system: $g_{\alpha\alpha}$, $g_{\beta\beta}$ and $g_{\alpha\beta}$, with α=Ge and β=Se. An example of the comparative study of this function for $GeSe_2$ and $GeSe_4$ is presented in Figure 24-A. The pdf for the three possible atomic pairs in the system is shown, solid lines and dotted curves corresponding to $GeSe_4$ and $GeSe_2$ systems respectively. Much information can be obtained by the analysis of such structural data as the presence of Ge centered tetrahedra associated with the pattern of Ge-Se environment (dominant peak), the number of homopolar bonds Ge-Ge and the number of corner and

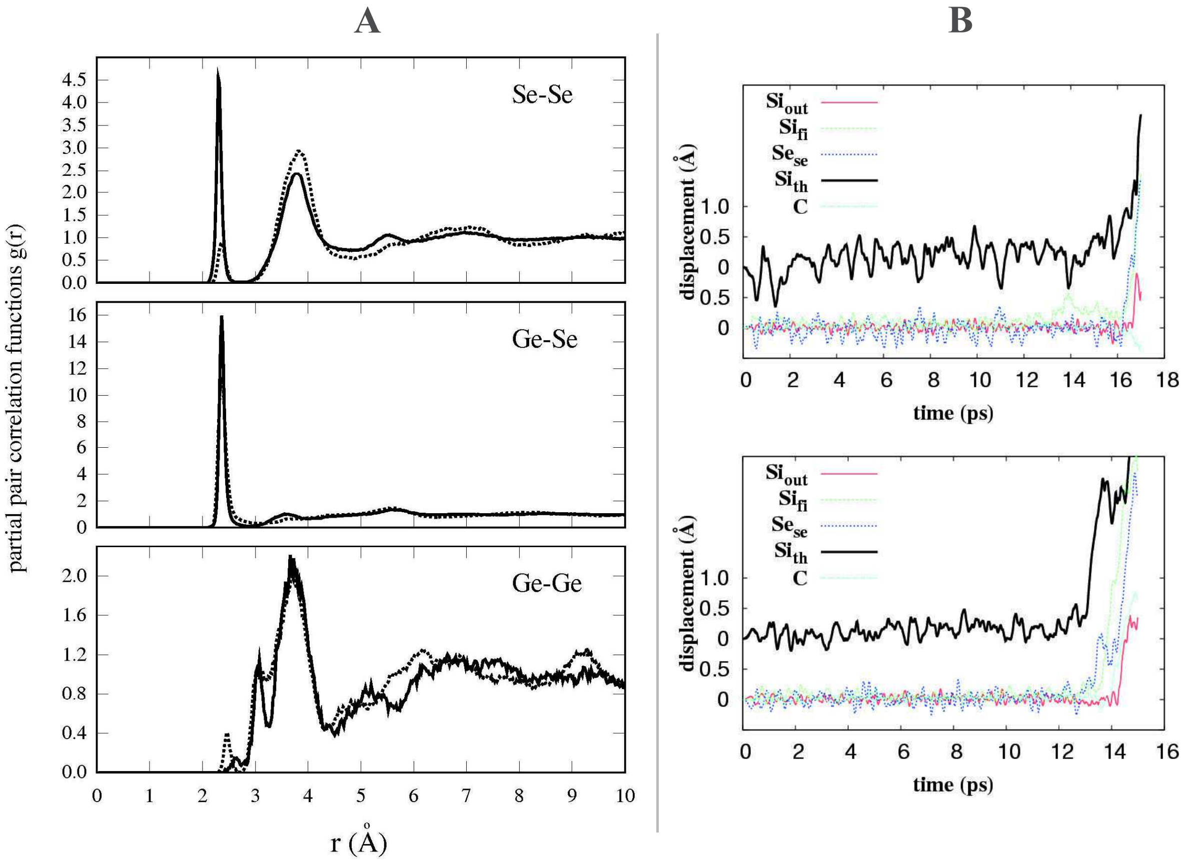

Figure 24 – A) Partial pair distribution function $g_{\alpha\beta}$ calculated for the amorphous Ge_xSe_{1-x} system for $x = 0.2$ (solid lines) and $x = 0.33$ (dotted lines) simulated by first-principles molecular dynamics (FPMD). B) Calculated Si and C atoms displacement evolution as function of time in Si-doped heterofullrenes systems $C_{30}Si_{30}$ simulated by FPMD methods. The top and bottom plots correspond to the positively and negatively charged systems respectively (See text). *These figures are adapted from figures 2, 4 and 5 of ref. [108]*

edge sharing tetrahedra. The second example is a study of the stability of Si-doped heterofullrene nanostructures by comparing first the neutral to the charged system and then two types of charged systems [108]. The results shown in Figure 24-B correspond to the temporal evolution of the deviation of the coordinates of Si and C atoms from their initial positions for the positively (top) and negatively (bottom) charged $C_{30}Si_{30}$ systems. In such configurations, Si atoms at the border with C atoms are noted Si_{out}, Si atoms in Si regions are labeled Si_{in} and such inner Si are split in first (Si_{fi}), second (Si_{se}) and third (Si_{th}) neighbors of the outer Si atoms. The authors observed a dynamical instability occurring after about 15 ps, and thus disentangle the interplay between structure and charges roles in the material.

The next subsection is a review of major results obtained on layered hybrid materials using FPMD methods both as a guide for optimizing the structural properties and the chemistry of the systems but also to push the predictive power of the method to investigate magnetic and electronic properties in these systems.

1.2.4 Application to hybrid compounds

To complete the state-of-the-art of theoretical results that are constituting the background of our project, we focus on three main studies, the first recalls the achievements of DFT-PW methods in studying molecular magnetic materials, then two pioneering works in the field of simulation of model hybrid materials, i.e copper hydroxide nitrate and copper hydroxide acetate.

Copper(II) acetate $Cu_2(CH_3CO_2^-)_2$		$Cu_2[(\mu\text{-}OH)_2(bipym)_2](NO_3)_2$		$[(dpt)Cu(\mu\text{-}Cl)_2Cu(dpt)](Cl)_2$	
Method	J (cm^{-1})	Method	J (cm^{-1})	Method	J (cm^{-1})
Experimental	-290	Experimental	+114	Experimental	+42.9
DDCI-2	-77	B3LYP	+113	B3LYP	+47.7
DDCI-3	-224	BLYP	+221	BLYP	+100
CASSCF	-24	BLYP-PW	+95	BLYP-PW	+61
CASPT2	-117				
UHF-spin-projection	-54				
$X\alpha$	-848				
SVWN	-1057				
B3LYP	-299				
BLYP	-779				
B3LYP pseudo	-346				
BLYP pseudo	-754				
PBE	-776				
PBE0	-237				
BLYP-PW	-518				
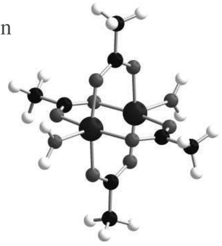		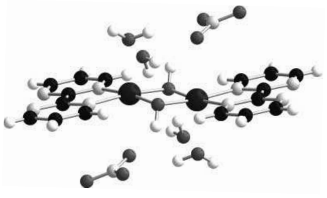 *bipym = bipyrimidine*		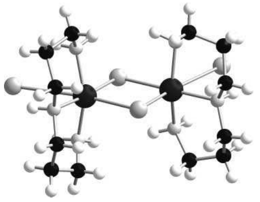 *dpt = dipropylenetriamine*	

Figure 25 – Compilation of the calculated and experimental exchange coupling constants obtained for 3 different compounds with several exchange-correlation functionals in the framework of first-principles calculations. The data of this Figure is collected from ref. [102], with the exception of the experimental value for the copper(II) acetate system corrected to match the one proposed by Güdel et al. [109]. The calculated coupling constant for the $[(dpt)Cu(\mu\text{-}Cl)_2Cu(dpt)]Cl_2$ with B3LYP functional comes from the work of Rodríguez and coworkers [110]

First, I present the work performed by Massobrio and Ruiz [102] in which the authors review the results obtained from DFT-PW methods compared to many other theoretical approaches in the computation of exchange coupling constants. In the case of Copper(II) acetate system, the experimental and calculated exchange coupling constants are reported in the leftmost column of the table in Figure 25. The experimental value (290 cm^{-1}) is the one obtained by Güdel and coworkers [109], the optimal performances are clearly obtained using the hybrid B3LYP functional (-299 cm^{-1}), close to the experimental value (-290 cm^{-1}). In this case the value obtained by BLYP-PW methods (-518 cm^{-1}) is deviating from the experimental one but is still better than the ones computed with the same BLYP functional but using all electron basis sets (-779 cm^{-1}) through "Gaussian" software [111] or using specific sets of pseudo-potentials (-754 cm^{-1}). However, we should note that the effect of localized basis sets usage is different in the case of B3LYP since $J^{BLYP-pseudo} > J^{BLYP}$ while $J^{B3LYP-pseudo} < J^{B3LYP}$. The use of other generalized gradient methods (GGA) such as the PBE functional with localized basis sets gives similar results to the BLYP case. However, other functionals including larger amounts of exact exchange such as PBE0, a free parameter hybrid functional, provide values (-237 cm^{-1}) less deviating from the experimental value. The absolute value of the exchange constant is underestimated rather than overestimated as it is the case for the other GGA methods considered [102]. The same observations are drawn in the case of the hydroxo-bridged Cu(II) dinuclear complex, $[Cu_2(\mu OH)_2(bipyrimidine)_2](NO_3)_2 \cdot (H_2O)_4$ (pictured in the second column of the table of Figure 25). For this system, the calculated structures correspond to the non-hydrated system as indicated in the header of the column. The experimental investigations of Giovanni De Munno and coworkers [112] on the hydrated bipyrimidine (bipym) compound led to the observation of a strong intramolecular ferromagnetic coupling of the order of 114 cm^{-1} for the singlet-triplet energy gap. The calculated exchange constants through different exchange-correlation functionals (BLYP, BLYP-PW and B3LYP) were obtained by Ruiz et al. [113] and found to be highly dependent on the amount of exact exchange included in the hybrid method. It is nevertheless interesting to see that the simpler BLYP functional associated with a plane waves basis ($J^{BLYP-PW} = 95$ cm^{-1}) still ensures an improvement of the calculated exchange constant upon the same calculation with localized bases using "Gaussian" package [111] ($J^{BLYP} = 221$ cm^{-1}). The third column, in Figure 25, corresponds to a similar study on the complex $[(dipropylenetriamine)Cu(\mu\text{-}Cl)_2Cu(dipropylenetriamine)]Cl_2$ as an interesting example of chloro-bridged dinuclear Cu(II) systems showing a smaller exchange constant. The experimental investigations were performed by Rodríguez et al. [114] and the authors observed, from magnetic susceptibility measurements, a ferromagnetic coupling between the two Cu(II) characterized by a small positive exchange constant (42.94 cm^{-1}). The calculations on this system using BLYP and B3LYP within a Gaussian framework (localized basis sets) have been performed in another work of Rodríguez and coworkers [110] in which the influence of bridging angles ($Cu\hat{X}Cu$) and the nature of the X anion (Cl in this case) on the exchange coupling constants were evaluated. For the $[(dpt)Cu(\mu\text{-}Cl)_2Cu(dpt)]Cl_2$ compound a value of 47.7 cm^{-1} is obtained which confirms that the hybrid B3LYP functional is very efficient even when localized basis sets are used. However, in the case of the BLYP calculation, the value obtained is closer to experiment for delocalized basis sets like plane waves ($J^{BLYP-PW} = 61$ cm^{-1} while $J^{BLYP-Gaussian} = 100$ cm^{-1}) [102].

One of the first applications of FPMD methods to hybrid layered materials concerned the study of structural, electron localization and magnetic properties of Copper Hydroxonitrate, $Cu_2(NO_3)(OH)_3$ (CuOHN), well characterized by X-ray diffraction (XRD) techniques. Massobrio and coworkers [115] used this material as a prototypical example of a layered solids characterized by a planar array of transition-metal ions. The objective of this article was to check the compatibility of experimental magnetic susceptibility measurements indicating an anti-ferromagnetic order at low temperatures [119] with the magnetic ground state calculated for the system. An unconstrained structural optimization have thus been performed on CuOHN compound using FPMD methods resulting in a very good agreement with experimental data. A deviation of about 4 to 5% in terms of angles and distances is obtaibed, except for the Cu-O (of NO_3^-) and O-N distances (higher deviation $\simeq 9\%$). Then the magnetic properties were investigated to explain the occurrence of an anti-ferromagnetic (AF) order. The authors found that the AF state (total spin $S = 0$) of the system took its origin from each Cu-layer (inorganic network) being

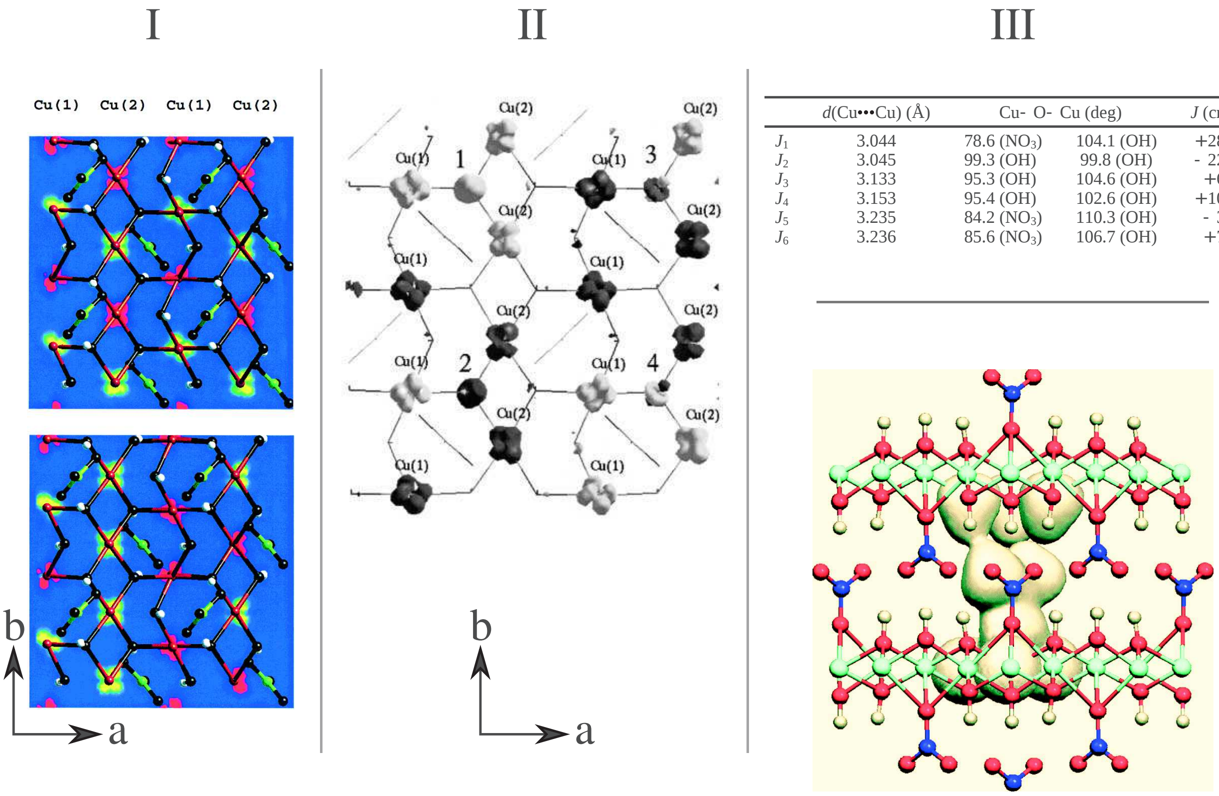

	d(Cu•••Cu) (Å)	Cu- O- Cu (deg)		J (cm^{-1})
J_1	3.044	78.6 (NO_3)	104.1 (OH)	+28.6
J_2	3.045	99.3 (OH)	99.8 (OH)	- 22.9
J_3	3.133	95.3 (OH)	104.6 (OH)	+6.9
J_4	3.153	95.4 (OH)	102.6 (OH)	+10.7
J_5	3.235	84.2 (NO_3)	110.3 (OH)	- 3.54
J_6	3.236	85.6 (NO_3)	106.7 (OH)	+7.9

Figure 26 – **I)** Two different (**a**,**b**) planes of the model used by Massobrio and coworkers [115] for the $Cu_2(NO_3)(OH)_3$ system. The contour slices correspond to values of spin densities ranging from -0.1 to 0.1 $|e|$ with positive and negative spin densities in red and green respectively. Spin density is localized around copper sites (brown spheres) while negligible amounts appear in the rest of the system. O atoms are black, N atoms are green and H atoms are white spheres (*adapted from Figure 3 of ref. [115]*). **II)** Spin density distribution in the (**a**,**b**) plane of copper hydroxide nitrate system highlighting non-negligible spin densities on oxygen sites. The solid surfaces correspond to majority (grey) and minority (black) spin density isosurfaces at 5.10^{-2} e/(bohr)^3. The labels Cu(1) and Cu(2) correspond to copper sites with different environments and 1, 2, 3 ,4 labels correspond to the oxygen bridges between specific copper sites (*adapted from Figure 2 of ref. [116]*). **III)** The table shows the exchange coupling constants J_i (i=1,..6) and structural parameters for the six exchange pathways identified in copper hydroxinitrate calculated using first-principles methods with the use of B3LYP exchange-correlation functional (*adapted from table 1 of ref. [117]*). The bottom part shows the total electron density isocontour at a value of 0.12 e.Å^{-3} for the $Cu_3 \cdots NO_3 \cdots (OH)_3$ fragment in the interlayer region of CuOHN system (*adapted from Figure 7 of ref. [118]*)

in an anti-ferromagnetic configuration resulting from parallel or anti-parallel alignment between the calculated spin densities (or its sign rather) located on copper sites. Indeed, the exploitation of density functional calculations together with the use of the electron localization function (ELF) allowed to highlight the strongly non-covalent nature of the chemical bonding among the three main molecular components (Cu^{2+}, OH^- and NO_3^-). Examples of molecular magnetism models (such as those exposed in previous sections) have been considered showing that the neglect of the interlayer couplings, the ruling out of the variations of spin distributions among the Cu layers as well as the uncertainties of the signs of exchange coupling constants made such approaches inapplicable to the case of copper hydroxonitrate. Therefore FPMD methods permitted a characterization at the atomic level of the spin densities and through a projection of this quantity in the (**a**,**b**) plane, the calculated distributions yielded an AF character on each (**a**,**b**) plane but differing from one plane to another (Figure 26-I) [115]. It appeared that no systematic correlation between the nature of the bridging groups could be used to reveal the nature of the magnetic properties due to the complexity and diversity of chemical environments of the Cu sites.

These observations were extended further in a second article in which the authors went on to describe the precise interactions involved in the stabilization of the magnetic structure of copper hydroxonitrate [116]. Indeed, they found that depending on the type of coordination of the Cu atoms, a non-negligible spin density can be found on the O atoms sites especially when neighboring Cu ions carry spin densities of the same sign (parallel spins). Moreover, they demonstrated that this situation appears only in the case of hydroxide linked oxygens (not NO_3^- oxygens) this being a possible explanation of the lack of clear correlation between the nature of the bridging group and the exchange interactions. In addition, the possibility of observing several microscopic spin structures all compatible with the total spin (S = 0) imposed on the system leads to the conclusion that many spin distributions yield the stable AF state of CuOHN system. The authors also noted that, regardless of specific differences in Cu sites environments, the inorganic layers formed by the periodic system introduce a correlation of all Cu centers for the system size considered. As shown in this system's spin densities (Figure 26-II), they established that the large spin densities obtained on the bridging oxygens were directly correlated with their three Cu neighbors. That is to say, the bridging atom holds a large positive (negative) spin if the three nearest neighbors bear a positive (negative) spin density. The route of this study of CuOHN compound led in 2006 to two papers from Ruiz et al. [117] and Pillet et al. [118] building a connection between the theoretical works on this material with experimentally accessible quantities. The results obtained are reported in the table of Figure 26-III. The authors exploit Monte Carlo techniques to evaluate an expression for the magnetic susceptibility that they use to fit experimental data readjusting the exchange coupling constants. This procedure uses values produced by first-principles calculations as a starting point for the Monte Carlo simulation yielding final magnetic susceptibility curves in good agreement with experimental data. Nevertheless, the exchange constants evaluated fall within the accuracy limits of the DFT plane-waves approach. This issue is quantified by the correspondence between thermal energy and the magnitude of some coupling constants obtained, the smallest one (J_6=2.0 cm^{-1}) being in terms of energy scales equivalent to a temperature as small as 2.77K. Pillet and coworkers [118] produced a map of a specific electron density in the interlayer region as shown in Figure 26-III where an isosurface of 0.12 $e{\cdot}Å^{-3}$ of the fragment $Cu_3 \cdots NO_3^- \cdots (OH)_3$ is plotted. This further shows that we are able to control the determination of the electronic and magnetic properties of complex materials that cannot be studied in the framework of phenomenological models.

First-principles molecular dynamics methods were also applied to copper hydroxide acetate $Cu_2(OH)_3(CH_3COO){\cdot}H_2O$ (CuOHAc). This work was motivated by many experimental investigations, for example, the study of electronic and structural properties of layered hybrid materials as a function of the inserted anions and depending on the length of the alkyl inserted through anion exchange reactions [34, 35]. The existence of a magneto-structural coupling in this compound has been directly shown in the work of Suzuki and coworkers [4] in which an external pressure was applied on copper hydroxide acetate system inducing the appearance of ferromagnetism in the system. These observations are the main motivation for the interest of Fan Yang et al. in the study of this material, by means of first-principles molecular dynamics methods to understand the origin of the pressure-induced magnetic behaviors [36, 37, 7]. The authors followed the lines of analysis established in the case of CuOHN system [36]. A dynamical annealing was first performed to obtain a stabilized structure starting from the incomplete set of atomic positions experimentally available at that time ([89]). Then a full study of the antiferromagnetic ground state of this system (total spin S = 0) have been performed [34]. From the structural point of view, the authors provide, in addition to the full set of distances, an analysis of the H-bonds network stabilizing the structure. The top image of Figure 27-I shows snapshots of two spin density distributions obtained, both for a global AF system, differing by 0.019 eV in total energy. The authors used this result as a quantification of the energy needed to convert one configuration into the other (the black arrows highlight the copper row on which this operation is applied) giving an estimation of the corresponding exchange coupling constant ($|J| \simeq 150 cm^{-1}$).

The table of Figure 27-I shows the spin density analysis results obtained for the CuOHAc system in order to confirm the location of non-negligible spin densities on oxygen bridging copper sites. In addition, a correlation is drawn between the magnitude and sign of the spin density located on copper centers with the distance and spin density of their oxygen neighbors. A distinction is made between the hydroxide linked (top part of table) and acetate linked oxygens (bottom part) to compare both behaviors. It is clear that the largest spin densities for O atoms (0.172 to 0.224 $|e|$) are found to correspond to a pair of Cu neighbors carrying spin densities of the same sign and at distances in the range 1.91 to 2.21 Å. The effect of the third Cu neighbor on the corresponding oxygen is reduced due to larger interatomic Cu-O distance. In 2012, a second article [37] has been published by the same authors addressing the effect of pressure on the system in the aim of reproducing the AF to F transition observed expermentally [4]. For this, two systems with total spin S = 0 (anti-ferromagnetic configuration) and S = 4 (ferromagnetic configuration) have been inspected at 0 GPa as well as at 3 GPa and 5 GPa of applied pressure, using BLYP and HCTH/120 (Hamprecht, Cohen, Tozer and Handy [58]) exchange-correlation functionals. These systems are represented in Figure 27-II, total energy differences E(S=4) - E(S=0) separating AF and F configurations obtained at 3 GPa of applied pressure are 0.715 eV (BLYP) and 0.215 eV (HCTH). Therefore, no magnetic transition was obtained but the clear diminution of the total energies difference between AF and F states indicated a possibility of describing this pressure effect through the use of FPMD method. It was the purpose of a last article [7], in 2014, that included more pressure values as well as an intermediary spin state (S=2). A pressure-induced magnetic transition is obtained since the total energy difference between S = 2 and S = 0 configurations changes sign when using the HCTH/120 functional and for a pressure

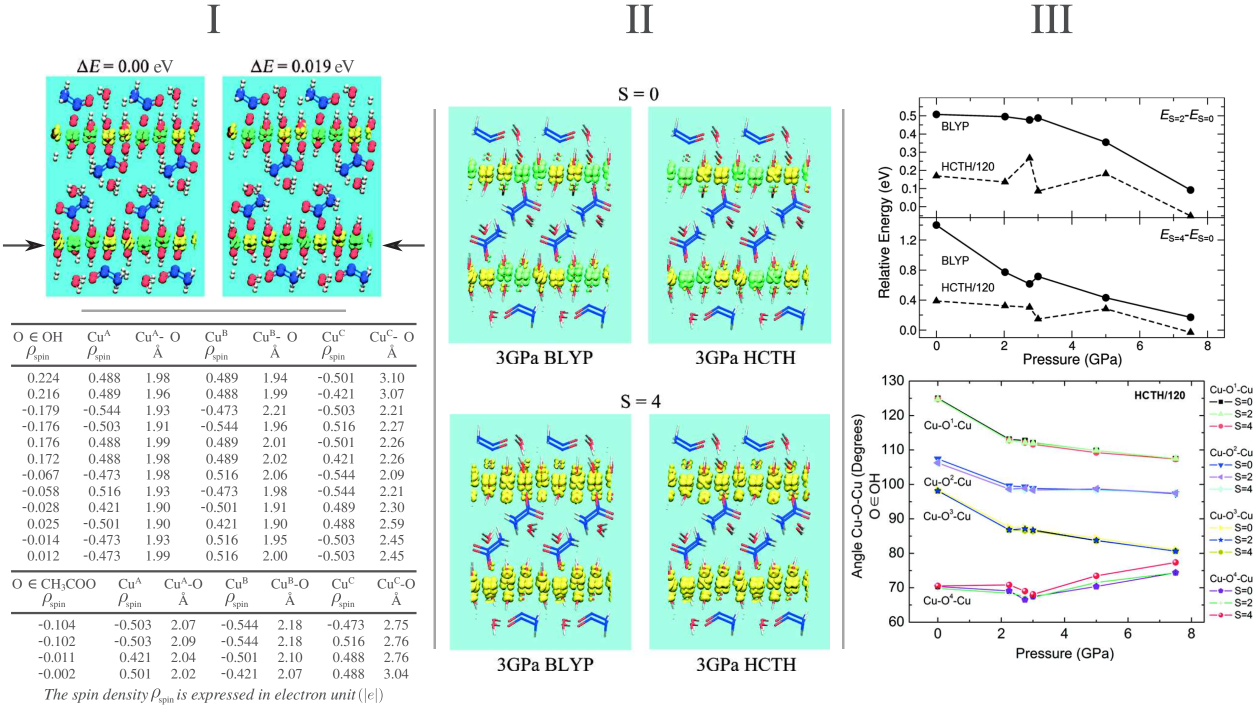

O ∈ OH ρ_{spin}	Cu^A ρ_{spin}	Cu^A- O Å	Cu^B ρ_{spin}	Cu^B- O Å	Cu^C ρ_{spin}	Cu^C- O Å
0.224	0.488	1.98	0.489	1.94	-0.501	3.10
0.216	0.489	1.96	0.488	1.99	-0.421	3.07
-0.179	-0.544	1.93	-0.473	2.21	-0.503	2.21
-0.176	-0.503	1.91	-0.544	1.96	0.516	2.27
0.176	0.488	1.99	0.489	2.01	-0.501	2.26
0.172	0.488	1.98	0.489	2.02	0.421	2.26
-0.067	-0.473	1.98	0.516	2.06	-0.544	2.09
-0.058	0.516	1.93	-0.473	1.98	-0.544	2.21
-0.028	0.421	1.90	-0.501	1.91	0.489	2.30
0.025	-0.501	1.90	0.421	1.90	0.488	2.59
-0.014	-0.473	1.93	0.516	1.95	-0.503	2.45
0.012	-0.473	1.99	0.516	2.00	-0.503	2.45

O ∈ CH_3COO ρ_{spin}	Cu^A ρ_{spin}	Cu^A-O Å	Cu^B ρ_{spin}	Cu^B-O Å	Cu^C ρ_{spin}	Cu^C-O Å
-0.104	-0.503	2.07	-0.544	2.18	-0.473	2.75
-0.102	-0.503	2.09	-0.544	2.18	0.516	2.76
-0.011	0.421	2.04	-0.501	2.10	0.488	2.76
-0.002	0.501	2.02	-0.421	2.07	0.488	3.04

The spin density ρ_{spin} is expressed in electron unit $(|e|)$

Figure 27 – **I)** Top part: Copper hydroxide acetate $Cu_2(OH)_3(CH_3COO){\cdot}H_2O$ (CuOHAc) optimized structure ([010] view) for the antiferromagnetic configuration (total spin S = 0) for the two spin density distributions resulting in the lowest total energies of the system. Cu atoms are brown, C in blue, O in red, H in white and the solid surfaces correspond to isosurfaces of spin density (α in green and β in yellow) at a value of ±0.03 e/Å^3 (*adapted from Figure 1 of ref. [36]*). Bottom part: Spin density values (ρ_{spin}) localized on the two types of oxygen atoms (see text) in correspondence with the spin density and distances of the three nearest neighbor copper centers Cu^A, Cu^B and Cu^C (*adapted from TABLE 4 of ref. [36]*). **II)** Spin density distribution for the CuOHAc system under 3 GPa of applied pressure calculated with BLYP (left) and HCTH (right) exchange correlation functionals and for two total spin states of the system, S = 0 (top) and S = 4 (bottom). α and β isospin surfaces are in light green and yellow respectively and the isosurfaces are plotted for spin density values of ± 0.01 e/Å^3 (*adapted from figures 2 and 3 of ref. [37]*). **III)** Top part: Relative total energies, with respect to the S = 0 AF configuration, of the S = 2 and S = 4 spin states of CuOHAc system as function of the applied pressure and for two exchange-correlation functionals: BLYP (solid line, filled circles) and HCTH/120 (dashed line, filled triangles). Bottom part: $Cu\hat{O}Cu$ angles as function of applied pressure for each oxygen (belonging to $CH_3CO_2^-$ group) bridging copper sites in CuOHAc structure. For clarity, CuO^iCu(i=1-4) curves are rigidly shifted along the y-axis (*the corresponding original Figure and numerical values are present in Figure 4 and Tables 2, 3 and 4 of ref. [7]*)

as large as 7.5 GPa, as shown in the top graphs of Figure 27-III. Besides, the structural analyses performed also showed an interesting change of slope around 3 GPa in the behavior of Cu-O distances and $Cu - \hat{O} - Cu$ angles. We report the evolution of these angles as function of pressure in Figure 27-III (bottom plot). These calculations were successful in proving the feasibility of the application of FPMD to study such complex behaviors. Nevertheless, simulations results are only in qualitative agreement with experimental data and many loopholes were left open such as the effect of the exchange functional used, the investigation of an extended range of pressure or the consideration of a larger simulation cell to access to more magnetic configurations.

The results quoted above are the essential prerequisite on which this project is constructed. In this context, our first objective is to perform a systematic study of magnetic and structural properties of copper hydroxide acetate system by exploiting an improved model system. Then, through the use of the protocols established for this hybrid, we focus on new systems never approached before via DFT calculations such as copper hydroxide (or oxide) fluorene phosphonate materials. To fully clarify the theoretical framework underlying this strategy, one needs to make explicit a series of concepts that are at very origin of any first-principles approach (and in particular of any first-principles MD application). This is the purpose of the next chapter that could be safely skipped if the reader is more willing to focus (with no further delays) on the main results obtained within this PhD thesis.

Chapter 2

First-Principles Molecular Dynamics (FPMD)

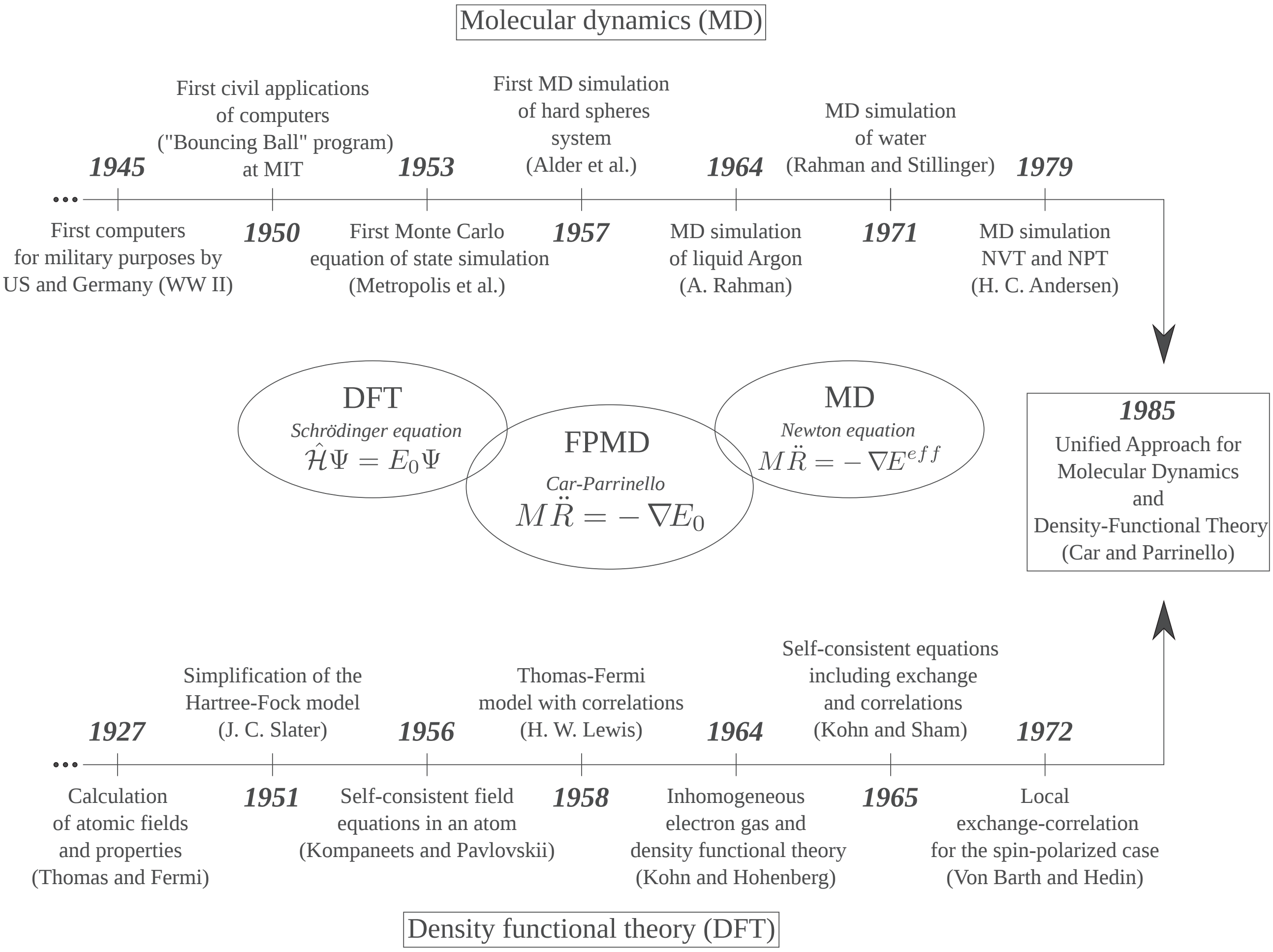

Figure 28 – A parallel history of molecular dynamics and density functional theory simulations is presented. The historical landmarks together with the corresponding concepts, dates and contributors are used to construct a background for the method introduced in this chapter: Car-Parrinello (or first-principles) molecular dynamics (CPMD) [43]. The central scheme highlights the main idea of this method combining classical equations of motion and a quantum mechanical description of the potential from which the classical forces are derived. The references corresponding to the articles cited are (MD) [120, 42, 121, 122, 123], (DFT) [124, 125, 126, 127, 128, 61, 129, 45]

This chapter aims at exposing the concepts behind the formulation of density functional theory as well as the construction of Car-Parrinello molecular dynamics. Particular care is exercised in the study of the different exchange correlation functionals, the basis set and the pseudopotentials compatible with the form of DFT proposed in the first section. Molecular dynamics methods are not exposed in detail since it is only a part of the methodology employed in this PhD project. However, the necessary milestones of this method are introduced in the second section (the Car-Parrinello molecular dynamics technique as implemented in the CPMD code [2]). An historical survey of the main contributions underlying basic computational science ideas is presented in Figure 28 with a focus on MD and DFT methods. The chapter is divided in two main sections:

- In the first section, we construct density functional theory (DFT) starting from the quantum, non-relativistic, time-independent Schrödinger equation by reminding where DFT comes from and what physics can be characterized through it. We propose two views of DFT, first as a many-body theory based on the minimization of an explicit energy functional and second as an effective single-body theory through the Kohn-Sham formulation that brings back into play single-particle orbitals. A special emphasis on exchange-correlation (XC) functionals is presented, highlighting the major reasons for the popularity of specific ones (see Chapter 1). Different basis sets are introduced and the plane waves are chosen as the best options to cope with periodic systems and to allow for a tractable calculation of forces. The idea and procedure of pseudo-potentials' construction are explained together with specific examples of so-called "semicore" and "NLCC" (non-linear core corrections) pseudopotentials (extensively used in this project).

- The second section develops the CPMD method that is a scheme combining DFT methods for electronic structure calculations and MD techniques for classical ions dynamics (central scheme in Figure 28). The development of the technique in the specific case of plane wave basis sets is accompanied by many insights on the implementation challenges and the main limits associated with it. The main differences with Ehrenfest and Born-Oppenheimer molecular dynamics are invoked and a derivation of the key quantities used in CPMD are presented (total energy, fictitious energy, forces). We also propose a "theoretical toolbox" containing the essential ingredients of the methods used in this project to produce and analyze the results of first-principles molecular dynamics. Electronic structure calculations allow to compute total energies, real space electron density, Kohn Sham orbitals as well as density of states, band structures and spin density projections. By using molecular dynamics, we can follow as a function of time and temperature the changes in the atomic positions and in the different crystal properties. We can also perform geometry optimizations and obtain many structural properties such as radial distribution functions, distances and angles. The Wannier functions analysis, through which the effect of electronic properties can be linked to structural aspects (localization of electrons wavefunctions) is also of central importance for our studies. In this framework, finite temperature simulations allow for an efficient mapping of the configuration space, this being a big step toward the reproduction of experimental conditions.

2.1 Density Functional Theory (DFT)

2.1.1 Introduction

The problem of studying hybrid materials at the atomic scale brings into play the quantum treatment of a large amount of atoms and molecules in a solid. For this purpose, as indicated in the Figure 28, one can trace back the tremendous development of electronic structure methods to the well-known work of Schrödinger in 1926 [130]. In this pioneering paper, Schrödinger proposes a new undulatory view of quantum mechanics based on a wave equation that has also a mechanistic character. A redefinition of the charge density is used and implemented within the framework of the known rules of electrodynamics. In fact, Schrödinger developed his theory by extending the methods used to demonstrate Fermat's geometrical optics as a limit of Huygens' wave mechanics when the dimensions of obstacles becomes comparable to the wavelength of the beam. From this beautiful reasoning based on Hamilton's principle and applied to electrons and atoms, the author was able to construct a fundamental wave equation, establishing an immediate parallel with the theory developed by Heisenberg, Born and Jordan. As a result of such construction, a linear equation, "Schrödinger equation", was born and became the central stone in most of today's electronic structure methods. A mathematical physics analysis of the similarities between the role played by Schrödinger equation in nonrelativistic quantum mechanics and the one played by Hamilton's laws of motion in nonrelativistic classical mechanics is detailed by T. Tao in ref. [131].

One should emphasize that since 1926, major advances in physics extended the quantum theory to the relativistic domain through Dirac's work [132] or Majorana's developments of a symmetric theory of electrons and positrons [133]. In fact, many other contributors made the theory of atoms and molecules more and more developed. One of the beauties of DFT is that one can implement it in a relativistic as well as a time-dependent manner using the same functional formalism but different equations [134]. However, we confine ourselves to the nonrelativistic time-independent problem, which in itself, contains enough intricacies related to the study of many electrons systems. The main stake in the straightforward use of Schrödinger equation is the many body problem treated through diagrammatic perturbation theory (Feynman diagrams and Green's functions) or using "configuration interaction" methods based on a systematic expansion in Slater determinants. Whereas such methods appear as the ultimate solution in the case of small systems (atoms or molecules), the computational power available today does not allow to consider them as a valuable option in the study of complex solids [135].

The problem of exposing the construction of DFT stems from the apparently ambiguous identity of this method. On the one hand, it is a many-body theory transferring all the information contained in the wavefuntion to a central quantity, the electron density via to Kohn-Hohenberg theorems [61]. On the other hand, it is implemented as a single-particle effective theory involving single particle orbitals within the Kohn-Sham approach [129]. The Kohn-Sham *ansatz* is at the heart of the latter distinction and therefore, it will be analyzed in detail [135]. Once sketched the main lines of the theory, the approximations used in the treatment of exchange and correlations phenomena are discussed since they are at the very essence of the so-called "art of making DFT working". Finally, we introduce the practical implementation methods of basis sets choices and pseudo-potentials construction.

2.1.2 Some elementary quantum mechanics

In quantum mechanics, all the information relative to a specific system is contained into one mathematical object: the wavefunction Ψ. As our objective is to treat systems of atoms, molecules and solids, the many-body character of the problem requires a first restriction, the Born-Oppenheimer approximation. The large difference in characteristic mass and speed between nuclei and electrons allows considering these two components as separated in their evolution time scales. Therefore, we consider the nuclear degrees of freedom, such as the crystal lattice in a solid, to be fully accounted for in the form of a potential operator $\hat{V}$ (with an energy $v(\vec{r})$) acting on the electrons so that the wavefunction depends only on electronic coordinates. We do not consider the spin degree of freedom, we will take it into account in the following sections when introducing the Hartree-Fock approximation. Therefore, the equation to be considered in this context is the quantum non-relativistic time-independent Schrödinger equation which, in the simplest case of a single electron in the potential $v(\vec{r})$, is written as

$$\hat{H}\Psi(\vec{r}) = \left(-\frac{\hbar^2\nabla^2}{2m} + v(\vec{r})\right)\Psi(\vec{r}) = \epsilon\Psi(\vec{r}) \tag{2.1}$$

with "m" the electron mass, "$\hbar$" the reduced Planck constant and "ϵ", the energy eigenvalues corresponding to the Hamiltonian operator $\hat{H}$. In view of the additive nature of both kinetic and potential terms, this expression becomes, for a many-body system

$$\left[\sum_{i=1}^{N} -\frac{\hbar^2\nabla_i^2}{2m} + \sum_{i=1}^{N} v(\vec{r}_i) + \sum_{i<j}^{N} \frac{q^2}{|\vec{r}_i - \vec{r}_j|}\right]\Psi(\vec{r}_1, ..., \vec{r}_N) = E\Psi(\vec{r}_1, ..., \vec{r}_N) \tag{2.2}$$

with "q" the electron charge and the Coulomb constant $(1/4\pi\epsilon_0)$ is equalized to unity. $\Psi(\vec{r}_1, ..., \vec{r}_N)$ the many-body wave function and the potential operator is explicitly given by

$$\hat{V} = \sum_{i=1}^{N} v(\vec{r}_i) = \sum_{i,k=1}^{N_e,N_k} \frac{qQ_k}{|\vec{r}_i - \vec{R}_k|} = \sum_{i,k=1}^{N_e,N_k} \frac{-e \cdot eZ_k}{|\vec{r}_i - \vec{R}_k|} \tag{2.3}$$

"N_e" and "N_k" correspond to the number of electrons and nuclei respectively. Besides, the Coulomb operator $\hat{U}$ and kinetic operator $\hat{T}$ are defined by

$$\hat{U} = \sum_{i<j}^{N_e} U(\vec{r}_i, \vec{r}_j) = \sum_{i<j}^{N_e} \frac{q^2}{|\vec{r}_i - \vec{r}_j|} \quad ; \quad \hat{T} = -\frac{\hbar^2}{2m}\sum_{i=1}^{N_e} \nabla_i^2 \tag{2.4}$$

In short, the Schrödinger equation plays the role of both Newton's laws and the energy conservation principle in classical mechanics, i.e., predicting the dynamical behavior of a system provided that a sufficient number of initial conditions are fixed. The two operators of equation (2.4) are referred to as "universal" in contrast with the "non-universal" potential operator (Eq. 2.3) that is system dependent. However, all the complexity is contained in the electron-electron interaction operator $\hat{U}$ that differentiates the single body quantum mechanics of Eq. (2.1) from the many-body problem exemplified by Eq. (2.2). These observations lead to a general variational formulation of the problem that becomes the search for the ground state wavefunction and the ground state energy corresponding to a certain system. This minimum of energy depends *a priori* only on the number of electrons and the given nuclei potential resulting in an energy functional E[N$_e$,$v(\vec{r})$] [136]. We will now establish this variational method as an equivalent to the problem of solving the Schrödinger equation (SE) (2.2).

The state of a physical system is characterized by a ket $|\Psi\rangle$, solution of the Schrödinger equation (SE) (2.2), using the corresponding Hamiltonian operator $\hat{H}$. In quantum mechanics, the average of many measurements on the energy is calculated as

$$E[\Psi] = \frac{\langle\Psi|\hat{H}|\Psi\rangle}{\langle\Psi|\Psi\rangle} = \frac{\langle\Psi|\hat{H}|\Psi\rangle}{\int \Psi^{*}\Psi d\vec{r}} \tag{2.5}$$

At this point, the variational procedure becomes clear, since the ground state energy is the lowest possible energy state for the system, the following energy minimum principle is deduced

$$E[\Psi] \geqslant E_0 \quad \Leftrightarrow \quad E_0 = \underset{\Psi}{min}\,(E[\Psi]) \tag{2.6}$$

The full minimization of the functional E[Ψ] with respect to all N-electrons wavefunctions gives access to the true ground state energy E$_0$ and wavefunction Ψ_0. In fact, every eigenstate $|\Psi\rangle$ of $\hat{H}$ is an extremum of the functional E[Ψ] and thus one may replace the solution of the SE equation through matrix diagonalization by the variational principle

$$\delta E[\Psi] = 0 \tag{2.7}$$

If one wishes to ensure the automatic normalization of the wavefunctions, a Lagrange multiplier (E) is considered and the principle becomes

$$\delta\left[\langle\Psi|\hat{H}|\Psi\rangle - E\langle\Psi|\Psi\rangle\right] = 0 \tag{2.8}$$

We recall that the orthogonalization of the wavefunctions ensures that these are a complete basis set compatible, through the superposition principle, with the linear hermitian Hamiltonian operator of the system. This condition results in the well-known quantum measurement that fixes the system in a unique state, thereby assigning a null probability for all the other eigenstates. The property of normalization of the wavefunction is introduced with respect to the condition that the probability of finding an electron integrated over all space ($\int|\Psi(\vec{r})|^2 d\vec{r}$) is normalized to unity.

At this point, the choice of the form of the wavefunction is the condition to use the variational principle in order to establish a self-consistent procedure leading to the energy ground state of the system. The first approximation is the Hartree approximation proposing the following form of the wavefunction

$$\Psi_H(\vec{r_1}, ..., \vec{r_N}) = \phi_1(\vec{r_1})\phi_2(\vec{r_2})...\phi_N(\vec{r_N}) \tag{2.9}$$

with "$\phi_p(\vec{r_i})$", the p^{th} single electron orbital occupied by the i^{th} electron. However, we consider particles that are electrons. Electrons are indistinguishable fermions with half-integer spin and therefore, according to the spin-statistics theorem, the Pauli principle requires the anti-symmetry of the corresponding wavefunctions. Indeed, according to this exclusion principle, *two or more identical fermions cannot occupy the same state.* The spin degree of freedom, although not considered hitherto, ensures the coherence of the theory exposed since it is responsible for this fundamental anti-symmetry constrain. Therefore, we consider a new set of coordinates for the i^{th} electron, $\vec{x}_i = \{\vec{r_i}, \vec{\sigma}(s_i)\}$ encompassing both a spatial component labeled with the particle index i and a spin part ($\mathrm{s}_i=\pm 1/2$ for electrons) with $\vec{\sigma}(s_i)$ equal to ($\alpha(\mathrm{s}_i)$,$\beta(\mathrm{s}_i)$) for (↑,↓) spin states. We assume that space and spin coordinates are separable and we write the Hartree-Fock (HF) many-body wavefunction as a Slater determinant formed of new spin orbitals $\chi_p(\vec{x}_i) = \phi_p(\vec{r_i})\vec{\sigma}(s_i)$. Thus, we have

$$\begin{aligned}\Psi_{HF}(\vec{x}_1, ..., \vec{x}_N) &= \frac{1}{\sqrt{N!}}\begin{vmatrix}\chi_1(\vec{x}_1) & \dots & \chi_N(\vec{x}_1)\\ \vdots & \ddots & \vdots \\ \chi_1(\vec{x}_N) & \dots & \chi_N(\vec{x}_N)\end{vmatrix}\\ &= \frac{1}{\sqrt{N!}}\begin{vmatrix}\phi_1(\vec{r}_1)\alpha(s_1) & \phi_1(\vec{r}_1)\beta(s_1) & \dots & \phi_{N/2}(\vec{r}_1)\alpha(s_1) & \phi_{N/2}(\vec{r}_1)\beta(s_1)\\ \vdots & & \ddots & & \vdots\\ \phi_1(\vec{r}_N)\alpha(s_N) & \phi_1(\vec{r}_N)\beta(s_N) & \dots & \phi_{N/2}(\vec{r}_N)\alpha(s_N) & \phi_{N/2}(\vec{r}_N)\beta(s_N)\end{vmatrix}\end{aligned} \tag{2.10}$$

where ($1/\sqrt{N!}$) is a normalization constant and the N orbitals are decomposed in N/2 orbitals of each spin type. The Hartree-Fock approximation is the method by which the orthonormal orbitals χ_p are found so that they minimize the energy functional E[Ψ] of equation (2.5) for this form of Ψ_{HF}. In the framework of this HF approximation, two main variants are used, the restricted HF (RHF) and the unrestricted HF (UHF) approximations. The first corresponds to the study of closed shells systems with an even number of electrons. The wavefunction construction does not allow the spatial part of the single-particle α-spin orbital ($\phi_p(\vec{r_i})$) to be different from the one corresponding to the β-spin orbital of the same particle. This case is exemplified by the Slater determinant components shown in equations (2.10). In contrast, when the number of electrons is odd, the standard HF scheme becomes the UHF method. In the latter, spatial parts of spin-orbitals for α-spin and those for β-spin are allowed to be different. The first component of the second column of the determinant (2.10) thus becomes $\widetilde{\phi}_1(\vec{r}_1)\beta(s_1)$ with $\widetilde{\phi}_1 \neq \phi_1$. The orthogonality between the wavefunctions is preserved but an increased number of orbitals results in an additional implementation difficulty. In the quest for more accuracy, the problem of correlation energy is often introduced in the framework of the Hartree-Fock approach. In fact, the correlation energy is a pure many-body effect often defined as the energy error of HF approximation

$$E^{Corr} = E^{Tot} - E^{HF} \tag{2.11}$$

where E^{Tot} corresponds to the total energy of the real system. The associated physical quantum phenomena are the collective fluctuations of the electrons between the recognized ground state and virtual energy levels of the energy spectrum. A straightforward extension of the single determinant wavefunction is the so-called "multi-configurations" method that involves linear mixing of many determinants (the "configuration interactions" method, CI). However, despite the success of such method in increasing the accuracy of *ab initio* calculations, it is known that the wavefunction of real interacting electrons system is never a single or a simple combination of determinants [136]. To complete this description of essential concepts for the construction of DFT, we introduce the central quantity of this theory, the electron density ($n(\vec{r}_1)$) based on the wavefunction constructed so far. The number of electrons per unit volume, occupying a given state, corresponds to the electron density for that state

$$n(\vec{r}_1) = N \int \dots \int |\Psi(\vec{x}_1, ..., \vec{x}_N)|^2 ds_1 d\vec{x}_2 ... d\vec{x}_N \tag{2.12}$$

where the number N corresponds to the number of electrons in the system. The expression (2.12) indicates that the electron density is not a functional but rather a simple non-negative function of three variables (spatial ones), fulfilling the condition that its integral over the entire space matches the exact number of electrons in the system

$$\int n(\vec{r}) d\vec{r} = N \tag{2.13}$$

At this point, the electron density is a key observable that can be distinguished from all other physical quantities since it can be used to obtain the total energy, the particle number, the potential or, in fact, any other observable for a real system. The ground state electron density is the core object of the theorems of Kohn and Hohenberg [61], developed in the next subsection.

2.1.3 DFT: effective or many-body theory

Nowadays, DFT is either presented as a many-body theory including formally many-body effects or as a single-particle effective theory when referring to the Kohn-Sham approach. First, we construct the "general many-body" DFT method through the presentation of Kohn-Hohenberg theorems in order to establish the standard background of the theory and its inherent limits (N & v- representability). Then, we construct the Kohn-Sham (KS) equations and the single-particle orbitals that allow DFT to be a practical and efficient method for the calculation of electronic properties of materials.

Density functional theory is based on two important theorems established in 1964 by Pierre Hohenberg and Walter Kohn (HK) [61] and on the definition of the HK universal functional (F_{HK}). The **first HK theorem** can be stated as follows [136]:

"The unique external potential $v(\vec{r})$ is determined, within a trivial additive constant, by the electron density $n(\vec{r})$"

In other words, the external potential is a unique functional of $n(\vec{r})$ and $v(\vec{r})$ fixes the Hamiltonian (as shown in the previous subsection). This leads to the full many particle ground state as unique functional of n($\vec{r}$). Therefore, the nondegenerate ground state (GS) wavefunction is a unique functional of the GS density ($\Psi_0(\vec{r}_1, ..., \vec{r}_N)$=$\Psi[n_0(\vec{r})]$). These statements form the essence of the first HK theorem and results in the possibility of evaluating the expectation value of any observable $\hat{O}$ (Hermitian operator) as a functional of $n_0(\vec{r})$

$$O_0 = O[n_0] \tag{2.14}$$

$$= \langle \Psi[n_0] | \hat{O} | \Psi[n_0] \rangle \tag{2.15}$$

This theorem shows that the electron density n($\vec{r}$) determines the fundamental quantities, the potential energy functional and the electron number N (from equation 2.13). Thus, all the ground state properties and in particular the total energy can be expressed as a density functional composed of electron-ion (V[n]), kinetic (T[n]) and electron-electron (U[n]) contributions. We do not consider the classical ion-ion interactions and the kinetic ionic energy as we focus, for now, on the electronic problem in Born-Oppenheimer approximation. The total energy is then written as

$$E[n] = V[n] + T[n] + U[n] \tag{2.16}$$

The potential functional is formed by the interaction of the ionic potential with the electron density rather than point charges as described in equation (2.3):

$$V[n] = \int n(\vec{r}) v(\vec{r}) d\vec{r} \tag{2.17}$$

The kinetic and electron-electron (e-e) interaction functionals form the famous Hohenberg-Kohn (HK) functional

$$\begin{aligned} F_{HK} &= T[n] + U[n] \qquad (2.18) \\ &= T[n] + (J[n] + K[n]) \\ &= T[n] + \left(\frac{1}{2} \iint \frac{n(\vec{r})n(\vec{r'})}{|\vec{r} - \vec{r'}|} d\vec{r} d\vec{r'} + K[n] \right) \end{aligned}$$

We note in this last expression that we decomposed the e-e interaction into a classical coulomb part (J[n]) and a non-classical part. The term denoted K encompasses all self-interaction corrections (SIC), exchange interactions and other correlation effects for which density functional forms are not exact. The kinetic term (T[n]) is left unmodified in (2.18) since such functional is not known explicitly, in particular, the quantum-correlations contributions due to this electrons kinetic energy. The HK functional is the *Holy Grail* of density functional theory since the knowledge of its exact form lead to the exact solution of Schrödinger equation. In addition, F$_{HK}$ is a *universal functional*, completely independent on the system under study and valid both for the simplest isolated Hydrogen atom and for the complex DNA strands. Density functional theory is thus the art of approximating this functional for atoms, molecules and solids since its exact explicit expression is unknown.

The **second HK theorem** completes the DFT description by establishing a minimum principle analogous to the one of Hartree-Fock theory (equation 1.6) but this time, relying on the electron density rather than the wavefunction. It can be stated as follows

"The $F_{HK}[\tilde{n}]$ functional gives the energy minimum (ground state) if and only if the trial density $\tilde{n}$ coincides with the correct ground state density n_0"

This is the variational principle

$$E_0 \leqslant E[\tilde{n}] = V[\tilde{n}] + F_{HK}[\tilde{n}] \tag{2.19}$$

This expression completes the development of DFT as a formal many-body theory and the complete procedure can be summarized in four points:

- Provided ionic positions and charges (potential v($\vec{r}$)), all the properties of the defined system are determined by the ground state density.
- The total energy functional E[n] is constructed as the sum of the universal functional F_{HK}[n] and the potential energy functional of equation (2.17). E[$\tilde{n}$] is minimal if and only if $\tilde{n} \equiv n_0$, the ground state density.
- The variational principle applies only on the ground state of the system and the same approach cannot be extended to excited states.
- The ultimate goal of DFT is to obtain an explicit expression of F_{HK}[n].

Beyond the issues of non-uniqueness of the potential that do not affect actual implementations of DFT, there exist two main representability problems in the density functional formulation, the **N and v-representability** of densities. We will briefly review these two questions

1. Given an arbitrary function $\tilde{n}(\vec{r})$, what guarantees that it can be represented in the form (2.12), a density function arising from antisymmetric wavefunctions?
2. Given a density function that can be written in the form (2.12), what guarantees that this density is a ground state density of a local potential v($\vec{r}$)?

The first problem (N-representability) is solved for single-particle (Kohn-Sham approach) densities since any nonnegative function can be written from a set of antisymmetric functions in the form (2.12). For the second issue, the first HK theorem does not exclude the possibility that for a certain density function, there exist no associated external potential. However, it is known that in "discretized" systems, every density is "ensemble v-representable". A local potential v($\vec{r}$), with a degenerate ground state ($\{E_0^i\}_{i=1,..,l}$), can always be found such that the associated density $n_0(\vec{r})$ can be written as a linear combination of the densities ($\{n_0^i(\vec{r})\}_{i=1,..,l}$) corresponding to each of these "l" degenerate ground states. In view of the intimate connection of v-representability to the Kohn-Sham *ansatz* (explained thereafter), we distinguish the interacting and non-interacting v-representability. Every interacting ensemble v-representable density is also non-interacting ensemble v-representable. However, as mentioned, only in discrete problems, all densities are interacting ensemble v-representable. This restriction informs us that it is not known whether ensemble-representable densities may be non-interacting pure-state representable, i.e., written as a single determinant, or not. A more complete introduction of these two problems is performed by Klaus Capelle in ref. [135].

From the first postulate of quantum mechanics, we deduce that the wavefunction contains all the system's information in a pure state at 0K and the finite temperature counterpart is the density matrix. The problem of 3N space variables in this case makes the search for such objects unfeasible for realistic systems. Two routes are often considered to reduce the problem, Green's functions and reduced density matrices. The former

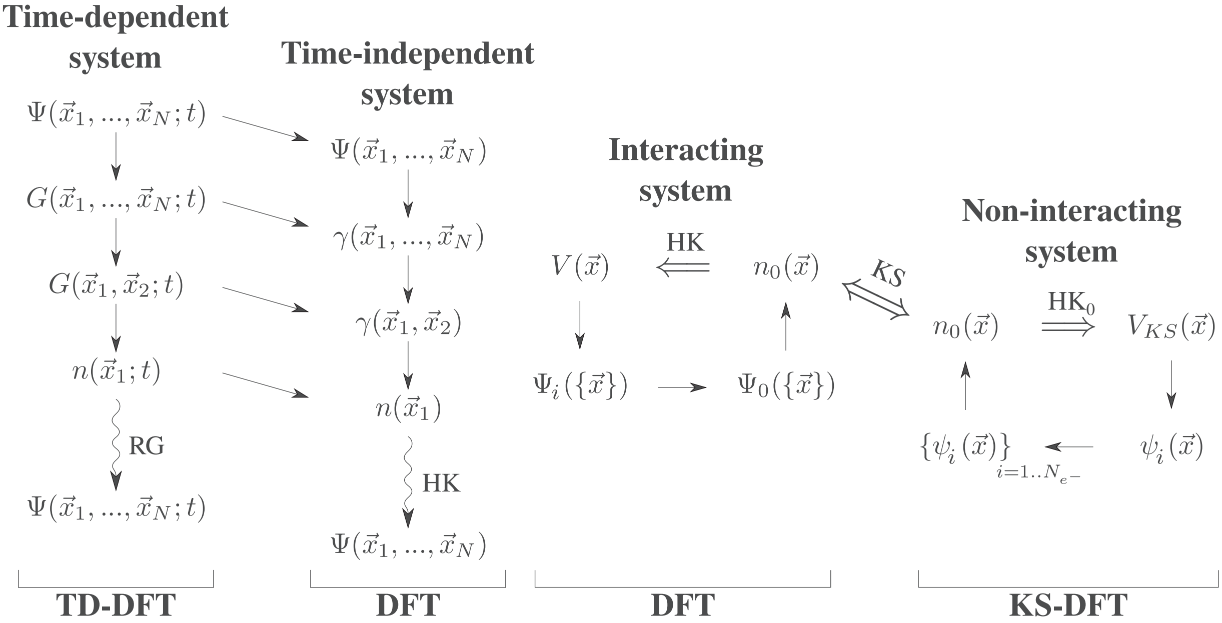

Figure 29 – The left part distinguishes the time-dependent (TD-DFT) from the time-independent density functional theory (DFT). The many-body wavefunction information is built into Green's functions in the former and in density matrices in the latter. The reduction procedure is performed by integrating out degrees of freedom from the N-body Green's function and density matrix to the pair quantities and finally to the ordinary charge density "n". In the DFT framework, the Hohenberg-Kohn (HK) theorem and its generalization, the Runge-Gross (RG) theorem, are used to ensure that all implicit wavefunction information is contained in "n". The right part highlights the Kohn-Sham (KS) *ansatz*, the mapping established between the ground state density n_0 of the interacting system and the non-interacting one. The KS arrow establishes this connection so that, in principle, all properties of the many-body problem are determined by the independent-particle Kohn-Sham problem. The HK_0 arrow corresponds to the HK theorem applied to a non-interacting system. *This Figure is constructed from Figure 7.1 of ref. [137] and Figure 1 of ref. [135]*

is suitable in time dependent cases (TD-DFT) as shown in Figure 29 and will not be considered. The latter, however, is of central importance since the HK theorems suggest that, in the ground state, the charge density is equivalent to the N variables wavefunction. In fact, through the procedure shown in Figure 29 (time-independent DFT), we have only integrated out explicit information from the many-body wavefunction to the charge density "n". Since, implicitly, all information is still contained in "n", practical DFT consists in getting such implicit information out, once the density is obtained. The right part of Figure 29 refers to the Kohn-Sham procedure, that we detail hereafter. The main idea is to perform a mapping between the many-body interacting system and the non-interacting one. A reduction of complexity is operated and we restrict ourselves to the computation of the non-interacting ground state density. This is the extension of the v-representability discussed for the HK theorems to non-interacting systems that gives clues on the validity of the Kohn-Sham *ansatz* (KS arrow in Figure 29). To clarify these considerations, we introduce the pair density matrix [138], and then expose briefly the Thomas-Fermi procedure [124, 125] in order to straightforwardly construct the Kohn-Sham equations [129].

It is possible to extend the definition (2.12) of the electron density to the two-particle case, i.e., to the probability of finding two electrons of spin s_1 and s_2 simultaneously in two volume elements $d\vec{r}_1$ and $d\vec{r}_2$. This information is contained in the pair density denoted $\gamma(\vec{x}_1, \vec{x}_2)$ (Figure 29), defined as

$$\gamma(\vec{x}_1, \vec{x}_2) = N(N-1) \int \dots \int |\Psi(\vec{x}_1, ..., \vec{x}_N)|^2 d\vec{x}_3 ... d\vec{x}_N \tag{2.20}$$

To underline its importance, we mention that all the electronic correlation information is contained in this quantity. In non-interacting systems (NI) this density becomes the simple product of the single particle densities

$$\gamma^{NI}(\vec{x}_1, \vec{x}_2) = \frac{N-1}{N} n(\vec{x}_1) n(\vec{x}_2) \tag{2.21}$$

Using the two previous expressions, we can write a more general expression of the pair density including a new "exchange-correlation (xc) hole" function.

$$\gamma(\vec{x}_1, \vec{x}_2) = \gamma^{NI} + n(\vec{x}_1) h_{xc}(\vec{x}_1; \vec{x}_2) \tag{2.22}$$

This is a pair density in which h_{xc} is a mathematical function describing the differences between the interacting and non-interacting systems. A part of correlations included in h_{xc} correspond to exchange effects due to the Pauli principle depending on the spin of the particles. A second correlation contribution accounts for the balance between the Coulomb energy gain and the kinetic energy cost when two electrons of different spins are separated in space. The xc-hole is a way to picture the effects of both Coulomb and exchange correlations on the electron distribution of an atom or a molecule. Therefore, each electron "A" is accompanied by its xc-hole which, through its particular form, excludes electrons with the same spin close to the electron A and determines the probable position of electrons of different spins in the neighborhood of electron A. At this point, we can apply these considerations to rewrite the electron-electron interaction introduced in equation (2.16) and isolate the pair density contributions.

$$\begin{aligned} U[\gamma] &= \frac{1}{2} \iint \frac{\gamma(\vec{x}_1, \vec{x}_2)}{|\vec{r}_1 - \vec{r}_2|} d\vec{r}_1 d\vec{r}_2 \qquad (2.23) \\ &= \frac{1}{2} \iint \frac{n(\vec{x}_1) n(\vec{x}_2)}{|\vec{r}_1 - \vec{r}_2|} d\vec{r}_1 d\vec{r}_2 + \frac{1}{2} \iint \frac{n(\vec{x}_1) h_{xc}(\vec{x}_1; \vec{x}_2)}{|\vec{r}_1 - \vec{r}_2|} d\vec{r}_1 d\vec{r}_2 \\ &= J[n] + \frac{1}{2} \iint \frac{n(\vec{x}_1) h_{xc}(\vec{x}_1; \vec{x}_2)}{|\vec{r}_1 - \vec{r}_2|} d\vec{r}_1 d\vec{r}_2 \end{aligned}$$

While the first term corresponds to the classical Coulomb interaction, including the self-interaction error (SIE), the second represents the interaction between the charge density (including spin) and the xc-hole. This term thus includes SIE corrections, exchange effects and other quantum many-body correlations that may be relevant in the system (non-local effects). One further distinguishes the Fermi hole, affecting electrons of the same spin and consequence of Pauli principle $h_X^{\sigma_1=\sigma_2}(\vec{r}_1;\vec{r}_2)$ from the Coulomb hole $h_C^{\sigma_1,\sigma_2}(\vec{r}_1;\vec{r}_2)$ resulting from electrostatic interaction between all electrons regardless to the spin. Using these expressions, the universal Hohenberg-Kohn functional (2.18) can be written as:

$$\begin{aligned} F_{HK}[n] =& T[n] + J[n] + \frac{1}{2}\iint \frac{n(\vec{x}_1)h_X^{\sigma_1=\sigma_2}(\vec{r}_1,s_1;\vec{r}_2,s_1)}{|\vec{r}_1-\vec{r}_2|}d\vec{r}_1 d\vec{r}_2 \\ &+ \frac{1}{2}\iint \frac{n(\vec{x}_1)h_C^{\sigma_1,\sigma_2}(\vec{r}_1,s_1;\vec{r}_2,s_2)}{|\vec{r}_1-\vec{r}_2|}d\vec{r}_1 d\vec{r}_2 \\ &= T[n] + J[n] + E_{xc}[n] \end{aligned} \tag{2.24}$$

This xc-hole formulation is an intuitive approach to the problem and therefore is presented to help introduce the following considerations. In what follows we do not consider the spin anymore. The spin will be again taken into account in the next subsection in which a straightforward generalization to the spin-dependent problem will be considered.

The last term to be investigated is the kinetic energy functional (T[n]). In 1926 and 1927, Thomas and Fermi (TF) [124, 125] were the first to use the charge density rather than the wavefunction and to propose an expression of the kinetic energy functional based on the homogeneous electron gas (subscript "hg") situation. The idea is to decompose the inhomogeneous interacting system into small cells of constant density n_{hg} and constant potential v_{hg}, and evaluate T[n] as the sum of kinetic contributions from each homogeneous electron gas cell [135]. This is a first example of local density approximation (LDA) in which the kinetic energy functional of an inhomogeneous electron gaz is obtained by approximating, locally, $n(\vec{r}) \simeq n_{hg}$. The TF kinetic energy functional is then

$$\begin{aligned} T_{TF}[n] &= \frac{3}{10}\hbar^2(3\pi^2)^{2/3}\int n(\vec{r})^{5/3}d\vec{r} \\ &= C_F\hbar^2\int n(\vec{r})^{5/3}d\vec{r} \end{aligned} \tag{2.25}$$

This unrealistic but instructive procedure led Kohn and Sham to propose that the main contribution to the kinetic energy is the one computed in an Hartree-Fock approach as the first sum in (2.2). The idea is to focus on calculating T_s[n] (the single-particle functional) exactly using a particular set of single-particle orbitals (from now on $\phi_i(\vec{r})$ are these KS orbitals) reproducing the correct interacting system's density in the form (2.12). These mathematical objects should contain the real system information making the computation of the non-interacting kinetic energy component exact. For this purpose, Kohn and Sham first decompose T[n] as a sum of the single particle (subscript s) term and the correlation (subscript c) one. Then, using the single-particle KS orbitals, T_s is computed as follows

$$\begin{aligned} T[n] &= T_s[n] + T_c[n] \\ &= -\frac{\hbar^2}{2m}\sum_{i=1}^{N}\int \phi_i^*(\vec{r})\nabla^2\phi_i(\vec{r})d\vec{r} + T_c[n] \end{aligned} \tag{2.26}$$

The self-consistency appears already when one realizes that, as a consequence of the first HK theorem and in the ground state, $\phi_i(\vec{r})$ are functionals of $n(\vec{r})$ and thus T$_s$ is an explicit orbital functional and an implicit density functional T$_s$[n] = T$_s$[$\{\phi_i[n]\}$] [135]. Therefore, using equations (2.16), (2.24) and (2.26), the exact Kohn-Sham energy functional is written as

$$\begin{aligned} E[n] &= T[n] + J[n] + E_{xc}[n] + V[n] \\ &= T_s[\{\phi_i[n]\}] + J[n] + \Big((T[n] - T_s[\{\phi_i[n]\}]) + (U[n] - J[n]) \Big) + V[n] \end{aligned} \tag{2.27}$$

The scheme suggested by Kohn and Sham for the minimization of this functional (similar to 2.7) is

$$\begin{aligned} 0 &= \frac{\delta E[n]}{\delta n(\vec{r})} \\ &= \frac{\delta T_s[n]}{\delta n(\vec{r})} + \frac{\delta V[n]}{\delta n(\vec{r})} + \frac{\delta J[n]}{\delta n(\vec{r})} + \frac{\delta E_{xc}[n]}{\delta n(\vec{r})} \\ &= \frac{\delta T_s[n]}{\delta n(\vec{r})} + v(\vec{r}) + v_H(\vec{r}) + v_{xc}(\vec{r}) \end{aligned} \tag{2.28}$$

with v($\vec{r}$), the external potential (from 2.17), v$_H$ the Hartree potential and v$_{xc}$ is the exchange potential calculated explicitly once E$_{xc}$ is approximated. The Kohn-Sham procedure consists in an identification of equation (2.28) with the non-interacting particles system for which the minimum principle reads

$$\begin{aligned} 0 &= \frac{\delta E_s[n]}{n(\vec{r})} \\ &= \frac{\delta T_s[n]}{\delta n(\vec{r})} + v_s(\vec{r}) \end{aligned} \tag{2.29}$$

in which only the external potential v$_s$($\vec{r}$) is to be considered. The density (n$_s$) solving this equation can thus be identified to the interacting system density n($\vec{r}$) if the potential v$_s$ is chosen to be

$$v_s(\vec{r}) = v(\vec{r}) + v_H(\vec{r}) + v_{xc}(\vec{r}) \tag{2.30}$$

We can therefore calculate the density of the many-body system in a potential v($\vec{r}$) by solving the Schrödinger equations of a non-interacting (single-particle) alternative system in a potential v$_s$($\vec{r}$)

$$\left(-\frac{\hbar^2 \nabla^2}{2m} + v_s(\vec{r}) \right) \phi_i(\vec{r}) = \epsilon_i \phi_i(\vec{r}) \tag{2.31}$$

The $\phi_i(\vec{r})$ solutions of these equations are the same than those used in the definition of T$_s$[n] in (2.26) and thus yield the original interacting system density

$$n(\vec{r}) \equiv n_s(\vec{r}) = \sum_{i=1}^{N} f_i |\phi_i(\vec{r})|^2 \tag{2.32}$$

with f_i the occupation number of the ith orbital. These last three equations are the so-called **Kohn-Sham equations** replacing the HK energy density functional minimization by the problem of solving the Schrödinger equation for a non-interacting system. One starts with an initial guess n($\vec{r}$) and computes the corresponding potential v$_s$($\vec{r}$). Then, the differential equations (2.31) can be solved for the $\phi_i(\vec{r})$ and the new density constructed from (2.32).

The density functional theory framework is now set and the next subsections will complement this overview with the development of the relevant exchange-correlation functionals as well as the basis set and pseudo-potentials considered in this project.

2.1.4 Exchange and correlations

First, we bring back the spin into our treatment in the framework of the local spin density (LSD) approach in which the full Kohn-Sham method is still valid. The objective is to use a functional allowing to determine magnetic properties using a spin-polarized electron density. Taking back the notations described in the Hartree-Fock method, we consider two spin states σ=(↑, ↓) and we denote the corresponding densities with superscripts α and β for those two states respectively. The spin degree of freedom (s_i) of each particle is either α or β and only collinear spin configurations are considered. We thus define the new densities for each spin state, in the same form than previously (2.12) keeping the $\vec{x} = (\vec{r}, s)$ notation

$$\begin{aligned} n^{\alpha}(\vec{r}_1) &= N^{\alpha} \int \dots \int |\Psi(\vec{r}_1, \alpha, \dots, \vec{x}_N)| d\vec{x}_2 \dots d\vec{x}_N \\ n^{\beta}(\vec{r}_1) &= N^{\beta} \int \dots \int |\Psi(\vec{r}_1, \beta, \dots, \vec{x}_N)| d\vec{x}_2 \dots d\vec{x}_N \end{aligned} \tag{2.33}$$

with N$^{\alpha}$ and N$^{\beta}$ corresponding to the number of α (↑) and β (↓) occupied spin-orbitals respectively, the sum of which equals the total electron number "N" in the system. In the case of the Kohn-Sham approach (2.32), the density originates from the KS single-particle spin-orbitals and therefore can be written as

$$\begin{aligned} n^{\alpha}(\vec{r}) &= \sum_{i=1}^{N^{\alpha}} |\phi_i^{\alpha}(\vec{r})|^2 \\ n^{\beta}(\vec{r}) &= \sum_{i=1}^{N^{\beta}} |\phi_i^{\beta}(\vec{r})|^2 \end{aligned} \tag{2.34}$$

The total electron density n($\vec{r}$) is defined as the sum of both densities and now a spin density "$\rho(\vec{r})$" (or spin polarization) can be defined

$$\begin{aligned} n(\vec{r}) &= n^{\alpha}(\vec{r}) + n^{\beta}(\vec{r}) \\ \rho(\vec{r}) &= \frac{n^{\alpha}(\vec{r}) - n^{\beta}(\vec{r})}{n(\vec{r})} \end{aligned} \tag{2.35}$$

where we normalized the spin density to the total density. We can now briefly introduce the different approximations to the exchange-correlation (xc) functional (E$_{xc}$[n]) starting from the Hartree formalism in which E$_{xc}$=0 up to the hybrid functionals accounting for the non-local character of xc phenomena. This is the so-called "**Jacob's ladder of DFT**" that we will climb step by step in the following in the case of spin-dependent density functional theory. We review in more details the local density approximation (LDA) and then introduce the functional that we will use for our investigations (BLYP), as well as an example of hybrid functional (B3LYP) considered in this work.

- The 1st step: **LDA**

  The local density approximation (LDA or LSD if the spin is included) refers to the approaches of KS-DFT [129] in which one considers that the exchange-correlation (xc) functional (E$_{xc}$[n$^{\alpha}$,n$^{\beta}$]) depends only on the value of the electron density at each homogeneous electron gas (hg) cell of the TF model. In this context, the xc functional takes the form

$$E_{xc}^{LSD}[n^{\alpha},n^{\beta}] = \int n(\vec{r})\epsilon_{xc}^{hg}([n^{\alpha},n^{\beta}];\vec{r})d\vec{r} \tag{2.36}$$
$$= \int f_{xc}(n;\vec{r})d\vec{r}$$

  ϵ_{xc}^{hg} is the exchange-correlation energy and f$_{xc}$ the corresponding energy per particle (energy density). This formulation considers a homogeneous electron gas with uniform spin densities n$^{\alpha}$($\vec{r}$)=n$^{\alpha}_{hg}$ and n$^{\beta}$($\vec{r}$)=n$^{\beta}_{hg}$ for which the energy density is accurately known and parametrized [139]. In this context, an example of the form of the exchange function ϵ_x is the one proposed by Von Barth and Hedin [45]

$$\epsilon_x^{LDA}(n,\rho) = \epsilon(n,0) + \left(\frac{(1+\rho)^{4/3}+(1-\rho)^{4/3}-2}{2^{4/3}-2}\right)(\epsilon_x(n,1)-\epsilon_x(n,0)) \tag{2.37}$$

  The exact form of the correlation functional for a uniform electron gas is not known but, in the framework of the random phase approximation (RPA), Perdew and Wang [140] proposed a simple analytic representation of the correlation energy for this system [141]

$$\epsilon_c^{LDA}[n] = -A\int n(1+\alpha_1\tilde{\rho})\cdot\ln\left(1+\frac{1}{A(\beta_1\tilde{\rho}^{1/2}+\beta_2\tilde{\rho}+\beta_3\tilde{\rho}^{3/2}+\beta_4\tilde{\rho}^2)}\right)d\vec{r} \tag{2.38}$$

  In this expression, the high and low density limits are implemented giving this parametric construction (including the spin polarization ρ dependency). The density parameter $\tilde{\rho}$=$(3/4\pi\rho)^{1/3}$ and A, α_1, β_1, β_2, β_3 and β_4 are fixed parameters. The local density approximation is always the first choice because it only approximates the lowest total energy contributions, the exchange energy (few percents of total energy) and correlation energy (around 10 percent of exchange energy). However, within LDA, band gaps are underestimated by up to 2 eV [142]. Atomization energies are also a weak point of LDA that tends to overestimate this quantity, it is clearly shown by Perdew and Schmidt in table 1 of ref. [140]. One can possibly use Green's functions in a perturbation method to take into account excitation and improve the band gap and electron-hole pair formation.

— The 2^{nd} step: **GGA**

The objective of the generalized gradient approximation (GGA) is to use a semi-local functional depending on the density and its gradient to account for the non-homogeneity of the real system density. Keeping the same notations already used for the LDA exchange-correlation term (2.36), we can write the gradient corrected energy as [140]

$$E_{xc}^{GGA}[n^{\alpha}, n^{\beta}] = \int n(\vec{r})\epsilon_{xc}^{GGA}([n^{\alpha}, n^{\beta}, \nabla n^{\alpha}, \nabla n^{\beta}]; \vec{r})d\vec{r} \tag{2.39}$$

We introduce the main *xc* functional used in this project (BLYP) which is due to Becke [38] for the exchange part and to Lee, Yang and Parr (LYP) [39] for the correlation energy formula. For the exchange part, the expression proposed by Becke was designed to reproduce the 1/r asymptotic behavior of the exchange energy density. He writes the exchange energy as

$$\epsilon_x^B(n^{\alpha}, n^{\beta}) = \epsilon_x^{LDA} - C_B \cdot \sum_{\sigma=\alpha,\beta} \int (n^{\sigma})^{4/3} \frac{(x^{\sigma})^2}{(1 + 6 \cdot C_B \cdot x^{\sigma} sinh^{-1}(x^{\sigma}))} d^3r \tag{2.40}$$

and introduces the dimensionless ratio x$^{\sigma}$ with $\sigma = \{\alpha, \beta\}$

$$x^{\sigma} = \frac{|\nabla n^{\sigma}|}{(n^{\sigma})^{4/3}} \tag{2.41}$$

where C$_B$ is a constant parametrizing this semi-empirical expression of the exchange energy functional.
In the article of Lee, Yang and Parr [39], the authors propose an expression for the correlation energy involving the density and the local kinetic energy density. For its construction, a local "Weizsacker" kinetic energy density (t$_W(\vec{r})$), a function (named $\gamma(\vec{r})$ in their paper) and the Thomas-Fermi constant (C$_F$) of equation (2.25), are invoked

$$t_W^{\sigma=\alpha,\beta}(\vec{r}) = \frac{1}{8}\frac{|\nabla n^{\sigma}(\vec{r})|^2}{n^{\sigma}(\vec{r})} - \frac{1}{8}\nabla^2 n^{\sigma}(\vec{r}) \quad ; \quad \gamma(\vec{r}) = 2\left(1 - \frac{(n^{\alpha}(\vec{r}))^2 + (n^{\beta}(\vec{r}))^2}{n^2(\vec{r})}\right) \tag{2.42}$$

The correlation functional is then written as [39]

$$\begin{aligned}\epsilon_c^{LYP} =& - a_0 \int \frac{\gamma(\vec{r})}{1 + a_1 n^{-1/3}} \Big[n + 2a_2 n^{-5/3} \Big(2^{2/3} C_F (n^{\alpha})^{8/3} + 2^{2/3} C_F (n^{\beta})^{8/3} \\ &- n t_W + \frac{1}{9}(n^{\alpha} t_W^{\alpha} + n^{\beta} t_W^{\beta}) + \frac{1}{18}(n^{\alpha}\nabla^2 n^{\alpha} + n^{\beta}\nabla^2 n^{\beta}) \Big) e^{-a_3 n^{-1/3}} \Big] d\vec{r}\end{aligned} \tag{2.43}$$

with a$_0$=0.014918, a$_1$=0.132, a$_2$=0.2533 and a$_3$=0.349, four fixed parameters. The atomization energy improvement and the good description of all structural properties make GGA methods very popular and, in particular, BLYP is one of the best performing.

— The 3^{rd} step: **MGGA**

Meta generalized gradient approximations can make use of the Laplacians Δn^{α} and Δn^{β}. Let us note that the Kohn-Sham (KS) single-particle kinetic energy densities are implicit functionals of n^{α} and n^{β} like the KS orbitals from which they are constructed. By accounting for the self-correlation correction, one ensures that only one of the two spin densities (n^{α} or n^{β}) is nonzero in a region of space where correlation energy should vanish [140]. The corresponding single-particle kinetic energy is of the form

$$\tau^{\sigma}(\vec{r}) = \frac{1}{8}\frac{|\nabla n^{\sigma}(\vec{r})|}{n^{\sigma}(\vec{r})} \tag{2.44}$$

A meta-GGA xc correlation functional is therefore written as

$$E_{xc}^{MGGA}[n^{\alpha}, n^{\beta}] = \int n(\vec{r})\epsilon_{xc}^{MGGA}([n^{\alpha}, n^{\beta}, \nabla n^{\alpha}, \nabla n^{\beta}, \tau^{\alpha}, \tau^{\beta}, \Delta n^{\alpha}, \Delta n^{\beta}]; \vec{r})d\vec{r} \tag{2.45}$$

This approximation is the highest step of the Jacob's ladder which avoids full nonlocality and the corresponding computational cost. It is, in fact, a fully nonlocal functional of the density but a semi-local functional of the orbitals so that the KS self-consistent procedure is not far from the GGA requirements. One can include higher orders in the density gradients expansion to improve the description of the exchange in slowly-varying density systems [140]. We did not employ any MGGA in this project.

— The 4^{th} step: **Hybrid functionals**

The objective of hybrid functionals is to include a portion of the exact Hartree-Fock (HF) exchange term, in order to correct the "self-interaction" error and account for the highly nonlocal character of exchange interactions. The exact exchange term is written as follows [141]

$$\epsilon_x^{HF}(\vec{r}) = -\sum_{k,l=1}^{N^{\alpha},N^{\beta}} \int \frac{\phi_k(\vec{r})\phi_l(\vec{r'})\phi_k^*(\vec{r'})\phi_l^*(\vec{r})}{|\vec{r}-\vec{r'}|}d\vec{r'} \tag{2.46}$$

and constructed from the Kohn-Sham orbitals. The general form of such hybrid functional is

$$E_{xc}^{hybrid} = E_{xc}^{GGA} + a(\epsilon_x^{exact} - \epsilon_x^{GGA}) \quad with \quad a \simeq 0.25, \tag{2.47}$$

the parameter "a" being fitted to experimental atomization energies. The most popular hybrid functional in quantum chemistry is the Becke 3-parameter, Lee Yang and Parr (B3LYP) [140] functional fitted originally to a set of atomization energies, proton affinities and ionization potentials. The B3LYP functional is written with the 3 parameters a_0=-0.20, a_1=0.72 and a_c=0.81

$$\begin{aligned} E_{xc}^{B3LYP} &= \epsilon_x^{LDA} + a_0(\epsilon_x^{HF} - \epsilon_x^{LDA}) + a_1(\epsilon_x^{GGA} - \epsilon_x^{LDA}) \\ &+ \epsilon_c^{LDA} + a_2(\epsilon_c^{GGA} - \epsilon_c^{LDA}) \end{aligned} \tag{2.48}$$

There are more advanced approaches, introducing more accurate evaluations of the correlation energy involving not only occupied orbitals but also the unoccupied ones through Slater determinants of the KS non-interacting N-particle system [140]. We will not introduce this last step approaches as they deserve much care and do not enter within the scope of our project.

2.1.5 Representation and pseudo-potentials

The prerequisite for this section is the construction of the matrix representation of Kohn-Sham formulation of DFT that is developed in Appendix A. We now introduce two fundamental tools, plane waves (PW) basis set and pseudo-potentials (PP) [143, 144, 142] that are used in the implementation of the CPMD code [2] used in this thesis work.

To solve the Kohn-Sham equations (2.31), one needs to choose an arbitrary basis set functions $\{\chi_l(\vec{r})\}$ to perform a linear expansion of the Kohn-Sham orbitals

$$\phi_i(\vec{r}) = \sum_{l=1}^{p} C_{li}\chi_l(\vec{r}) \tag{2.49}$$

the elements C_{li} being the expansion coefficients. We will use plane waves as a representation basis of our KS orbitals bringing into play the Fourier transform in conjunction with a periodicity of the system in the real space. Plane waves are, by construction, an orthonormal basis set, independent of atomic positions and naturally periodic. In this work, only periodic systems are considered. The $\vec{k}$-space is the space in which the Fourier transform (FT) of a spatial function is represented. Therefore, the Bravais lattice of the direct space is characterized by the Wigner-Seitz cell matrix $\boldsymbol{h} = \left[\vec{a}, \vec{b}, \vec{c}\right]$. Any direct lattice vector $\vec{L}$ can be written as a linear combination of these three vectors. Similarly the reciprocal lattice box (first Brillouin zone) is characterized by the matrix $\boldsymbol{h'} = \left[\vec{a'}, \vec{b'}, \vec{c'}\right]$ and any reciprocal lattice vector $\vec{g}$ can be written as a linear combination of these three vectors. In this context, the first Brillouin zone (BZ) is our main focus. The Bloch theorem applying for such periodic systems implies that the wavefunction associated with a vector $\vec{k}$ lying in the first BZ is a plane wave $\chi_{\vec{k}} = e^{i\,\vec{k}\cdot\vec{r}}$ characterized by the wave vector $\vec{k}$ and spatially modulated by a periodic function $u_{\vec{k}}(\vec{r})$

$$\phi_{j,\vec{k}} = e^{i\,\vec{k}\cdot\vec{r}} u_{j,\vec{k}}(\vec{r}) \quad ; \quad u_{j,\vec{k}}(\vec{r}+\vec{L}) = u_{j,\vec{k}}(\vec{r}) \tag{2.50}$$

with $u_{j,\vec{k}}(\vec{r})$ invariant by translation in direct space by $\vec{L}$. This periodicity allows for a decomposition of this function in Fourier series

$$u_{j,\vec{k}}(\vec{r}) = \sum_{\{\vec{g}\}} c_{j,\vec{k}}(\vec{g})\, e^{i\,\vec{g}\cdot\vec{r}} \tag{2.51}$$

with $\{\vec{g}\}$ the ensemble of reciprocal lattice vectors so that the wavefunction can be written as

$$\phi_{j,\vec{k}} = \sum_{\{\vec{g}\}} c_{j,\vec{k}}(\vec{g})\, e^{i\,(\vec{k}+\vec{g})\cdot\vec{r}} \tag{2.52}$$

Plugging this wavefunction in the Kohn-Sham equations (2.31), we obtain

$$\sum_{\{\vec{g}\}} \left(\frac{1}{2}|\vec{k}+\vec{g}|^2 + v_s(\vec{r}) \right) c_{j,\vec{k}}(\vec{g})|\vec{k}+\vec{g}\rangle = \epsilon_{j,\vec{k}} \sum_{\{\vec{g}\}} c_{j,\vec{k}}(\vec{g})|\vec{k}+\vec{g}\rangle \tag{2.53}$$

where we introduced a *bra-ket* notation for the plane wave $\left(|\vec{k}+\vec{g}\rangle = e^{i\,(\vec{k}+\vec{g})\cdot\vec{r}}\right)$ in the last expression. Considering another reciprocal space vector $\vec{g'}$, we project (2.53) on the *bra* $\langle\vec{k}+\vec{g'}|$ and use the orthonormality of the plane waves $\left(\langle\vec{g}|\vec{g'}\rangle = \delta_{\vec{g},\vec{g'}}\right)$ to obtain

$$\begin{aligned} \sum_{\{\vec{g}\}} \frac{1}{2}|\vec{k}+\vec{g}|^2 c_{j,\vec{k}}(\vec{g})\,\delta_{\vec{g},\vec{g'}} + \sum_{\{\vec{g}\}} \langle\vec{k}+\vec{g'}|v_s(\vec{r})|\vec{k}+\vec{g}\rangle c_{j,\vec{k}}(\vec{g}) &= \epsilon_{j,\vec{k}} \sum_{\{\vec{g}\}} c_{j,\vec{k}}(\vec{g})\,\delta_{\vec{g},\vec{g'}} \qquad (2.54) \\ \iff \frac{1}{2}|\vec{k}+\vec{g'}|^2 c_{j,\vec{k}}(\vec{g'}) + \sum_{\{\vec{g}\}} \left(\int d^3r\, v_s(\vec{r}) e^{i(\vec{g}-\vec{g'})\cdot\vec{r}} \right) c_{j,\vec{k}}(\vec{g}) &= \epsilon_{j,\vec{k}}\, c_{j,\vec{k}}(\vec{g'}) \\ \iff \frac{1}{2}|\vec{k}+\vec{g'}|^2 c_{j,\vec{k}}(\vec{g'}) + \left(\sum_{\{\vec{g}\}} \tilde{v}_s(\vec{g}-\vec{g'}) c_{j,\vec{k}}(\vec{g}) \right) &= \epsilon_{j,\vec{k}}\, c_{j,\vec{k}}(\vec{g'}) \end{aligned}$$

and the term between brackets in the left had side, involving the KS potential is nothing but the Fourier transform of $v_s(\vec{r})$ that we denoted with a tilde symbol $\tilde{v}_s(\vec{g}-\vec{g'})$. We thus construct the Kohn-Sham Hamiltonian matrix for the plane wave with wave-vector $\vec{k}$ that we denote $\boldsymbol{H}_{\vec{k}}^{PW}(\vec{g},\vec{g'})$ from which we can write the KS equations as an diagonalization problem

$$\begin{aligned} \boldsymbol{H}_{\vec{k}}^{PW}(\vec{g},\vec{g'}) &= \frac{1}{2}|\vec{k}+\vec{g'}|^2 \delta_{\vec{g},\vec{g'}} + \tilde{v}_s(\vec{g}-\vec{g'}) \qquad (2.55) \\ \sum_{\{\vec{g}\}} \boldsymbol{H}_{\vec{k}}^{PW}(\vec{g},\vec{g'}) c_{j,\vec{k}}(\vec{g}) &= \epsilon_{j,\vec{k}}\, c_{j,\vec{k}}(\vec{g'}) \end{aligned}$$

Plane waves turn out to be a suitable basis for our problem and the Kohn-Sham method is simplified by the possibility of using fast Fourier transforms (FFT) techniques for the computation of the potential elements. Another important aspect is the control of the size of the basis, the number of elements and thus the cut-off energy. Indeed, a simple way used to cut-off the plane wave expansion of the periodic wavefunction (2.52) is given by the largest reciprocal lattice vector $\vec{\kappa} = \vec{g} - \vec{g'}$ defined from the cut-off energy

$$E_{Cut}^{PW} = \frac{1}{2}\vec{\kappa}_{max}^2 \tag{2.56}$$

The advantages exposed are accompanied by the corresponding limits of such delocalized basis. Many plane waves are necessary to describe the electron density $n(\vec{r})$ around atomic sites ($\simeq 10^8$ plane waves for 0.01Å spatial resolution) and therefore the sizes of the Hamiltonian matrices (2.55) to be diagonalized become intractable. The situation is paradoxical since these "core" electrons that need so many plane waves to be represented do not participate much to the interatomic bonding. Therefore this basis set is not adequate for "all electrons" (AE) calculations. In such approach, core electrons, valence and conduction electrons are treated on the same footing. In our case, to retain the efficiency of plane waves we associate to each atom a "pseudo-potential" allowing us to avoid the treatment of core electrons. The fundamental idea is to reproduce the wavefunction and the potential of an AE calculation for a distance superior to a cut-off radius (r_c) from the nuclei positions. The frozen core approximation and "pseudisation" are the two steps of the construction of the combined plane wave and pseudo-potential (PP) approach. We follow the scheme designed by Troullier and Martins [46] for constructing norm-conserving pseudo-potentials. This construction starts by assuming a spherical screening approximation and considering the self-consistent solution of the single particle radial Kohn-Sham equation

$$\left[-\frac{1}{2}\frac{d^2}{dr^2} + \frac{l(l+1)}{2r^2} + V[n,r]\right] rR_l(r) = \epsilon_l R_l(r) \tag{2.57}$$

dependent on the orbital moment "l" and "R_l" the radial part of the wavefunction considered. The different steps and core ideas of the pseudo-potential approach are sketched

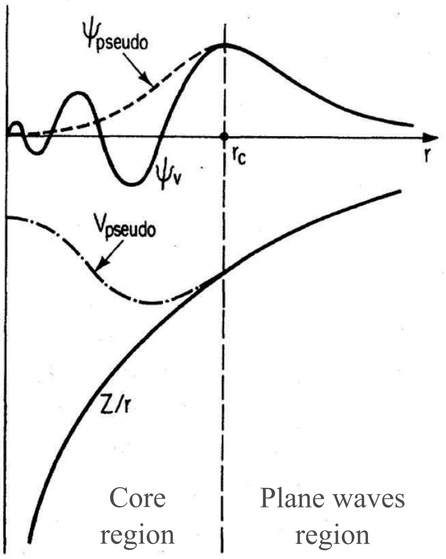

1) Construction of the radial pseudo- (PP) wavefunction

$|\vec{r}| > r_c$

$$R_l^{PP}(r) \simeq R_l^{AE}(r)$$

$|\vec{r}| < r_c$

$$\int r^2 \left|R_l^{PP}(r)\right|^2 d^3r = \int r^2 \left|R_l^{PP}(r)\right|^2 d^3r$$

2) Construction of the screened pseudo-potential

$$V_l^{PP}(r) = \epsilon_l - \frac{l(l+1)}{2r^2} + \frac{1}{2rR_l^{PP}(r)}\frac{d^2}{dr^2}\left(rR_l^{PP}(r)\right)$$

3) "Unscreen" the potential to obtain an ionic pseudo-potential

$$V_{ion,l}^{PP}(r) = V_l^{PP}(r) - V_H^{PP}(r) - V_{xc}^{PP}(r)$$

Figure 30 – Construction of the Pseudo-wavefunction and the pseudo-potential sketched from the development performed in ref. [142]. The pseudo-wavefunction (superscript PP) should accurately match the all-electron wavefunction (superscript AE) far from the nuclei ($r > r_c$). The norm-conserving condition is imposed in the "core" region ($r < r_c$). The screened pseudo-potential is then constructed by inversion of the radial equation (2.57). The final step is to subtract the Hartree potential and exchange-correlation pseudo-potential contribution to take only into account the nucleus and core electrons states with no participation to interatomic interactions

in the Figure 30. The recipe of Troullier and Martins [46] writes the radial part of the wavefunction in the core region for $r < r_c$ (Figure 30) as

$$R_l^{PP}(r) = r^{l+1}e^{p(r)} \qquad with \qquad p(r) = b_0 + \sum_{i=2}^{n} b_i r^i \tag{2.58}$$

where the b_1 coefficient is not considered in order to avoid the singularity of the screened pseudo-potential V_l^{PP} at r=0. The coefficients b_i are determined respecting the norm-conserving condition and the smoothness requirements. The optimization of smoothness for the wavefunction and its derivatives (m=0,..,4) and the potential depends on the conditions imposed at the cut-off radius r_c and at the nuclei positions (r=0) [46]

$$\left.\frac{d^m R_l(r)}{dr^m}\right|_{r=r_c^-} = \left.\frac{d^m R_l(r)}{dr^m}\right|_{r=r_c^+} \qquad ; \qquad \left.\frac{dR_l(r)}{dr}\right|_{r=0} = 0 \tag{2.59}$$

The eigenvalues that are obtained by the pseudo-potential procedure ϵ_l^{PP} have to match the valence all electrons system eigenenergies ϵ_l^{AE}. An important consequence of the pseudo-potential generation is highlighted by the angular momentum (l) subscripts. This means that each l-dependent wavefunction will see a different potential so that the ionic pseudo-potential operator can be separated into a local and a "non-local" parts [46]

$$\hat{V}_{ion}^{PP}(r) = V_{ion,local}^{PP}(r) + \sum_{l}^{l_{max}} V_{semilocal,l}(r)\hat{P}_l, \tag{2.60}$$
$$V_{semilocal,l}(r) = V_{ion,l}^{PP}(r) - V_{ion,local}^{PP}(r)$$

The non-local potential is, in reality, semi-local for the angular momentum l and the operator $\hat{P}_l$ projects out the l^{th} angular momentum component from the wavefunction. The local potential is constructed so that, for all angular momentum channels higher than l_{max}, the atomic scattering is still adequately reproduced. The Kleiman and Bylander [145] procedure allows to transform the semi-local potential $V_{semilocal,l}(r)$ into a non-local form using the atomic reference pseudo-wavefunction $\phi_l^{PP,0}$ (superscript "0" indicate nodeless pseudo-wavefunctions for which the inversion of KS equation is possible) including the angular momentum component for which the potential was computed

$$V_{nonlocal,l}^{KB} = \frac{|V_{semilocal,l}(r)\phi_l^{PP,0}(r)\rangle\langle\phi_l^{PP,0}(r)V_{semilocal,l}(r)|}{\langle\phi_l^{PP,0}(r)|V_{semilocal,l}(r)|\phi_l^{PP,0}(r)\rangle} \tag{2.61}$$

We will come back to the exact form of the "non-local" contribution to the pseudo-potential in the next section, while developing the formulation of the Car-Parrinello molecular dynamics. The main problem encountered by this pseudo-potential procedure is the possible overlap (especially in transition metals) between the valence states (d-orbitals) and the "core states" (s and p orbitals). In such situation the unscreening procedure cannot be effectively performed since the xc potential is not linear and therefore the contribution from the valence states is not fully canceled in the 3^{th} step of the construction (Figure 30). The frozen core approximation (core electrons chemically inert) cannot hold. Two solutions have been considered here, the "non-linear" core corrections (NLCC) proposed by Louie et al. [40] and the "semicore" approach proposed by Reis and coworkers [41]. In the case of the NLCC approach, one includes, in the 3^{rd} step in Figure 30, not only the valence electron density ($n_v(\vec{r})$) but also the core electron density $n_c(\vec{r})$. The ionic pseudo-potential is thus written as [40]

$$V_{ion,l}^{NLCC}(\vec{r}) = V_l^{PP}(\vec{r}) - V_H^{PP}[n_v(\vec{r})] - V_{xc}[n_v(\vec{r}) + n_c(\vec{r})] \tag{2.62}$$

so that the total exchange-correlation potential including the nonlinear core-valence term is subtracted from the neutral potential. In such configuration, errors may occur due to inaccuracies in the computation of the valence charge density inside the core region. The effect of the core charge have to be treated as a perturbation leading to minor changes in the total energy.

To solve this problem, Louie et al. highlight the fact that the core charge has an effect only when it is comparable in magnitude with the valence charge. The full core charge density is thus replaced by a partial core charge density matching the true density beyond a radius r_0 and arbitrary from 0 to r_0. A spherical Bessel function have been chosen for this core charge density thus defined

$$n_c^{partial}(r) = \begin{cases} Asin(Br)/r & if \;\; r < r_0 \\ n_c(r) & if \;\; r > r_0 \end{cases} \tag{2.63}$$

with A and B determined by the value of $n_c(r)$ and its gradient at $r = r_0$. This NLCC approach is used in our study of copper hydroxide acetate system in the next chapter.

The "semicore" solution will also be used and confronted to the NLCC calculations to highlight the main differences of the two methods. In 2003, Reis and coworkers [41] proposed a way of construction for norm-conserving pseudo-potentials including semicore states. The idea is to include in the first-principle calculation states corresponding to the region of overlap between core states and valence states. For a given angular momentum l, Reis et al. propose a new distinction between the states for which there will be a single pseudo-wavefunction (in which case the Troullier-Martins scheme is applied) and the states for which there will be more than one pseudo-wavefunction. The latter are treated as "semicore states". For the $3d$-Cu case, the $3s$ and $3p$ are the semicore states. For each $l < 2$, the pseudo-potential is used to provide nodeless pseudo-wavefunctions $\phi_{l<2}^{PP,0}(r)$ matching the "semicore" orbitals for $r \geq r_c$, the cut-off radius. For the same l values, additional single-node pseudo-wavefunctions $\phi_{l<2}^{PP,1}(r)$ matching the valence orbitals for the same region ($r \geq r_c$) are included in the calculation. In the case of the nodeless pseudo-wavefunction $R_l^{PP,0}$, it is constructed following the Troullier and Martins scheme

$$l < 2, \quad R_l^{PP,0} = \begin{cases} R_l^{AE,semi}(r) & if \;\; r \geq r_c \\ r^l e^{q(r)} & if \;\; r \leq r_c \end{cases} \tag{2.64}$$

$$l \geq 2, \quad R_l^{PP,0} = \begin{cases} R_l^{AE,v}(r) & if \;\; r \geq r_c \\ r^l e^{p(r)} & if \;\; r \leq r_c \end{cases}$$

$$p(r) = b_0 + b_2 r^2 + b_4 r^4 + b_6 r^6 + b_8 r^8 + b_{10} r^{10} + b_{12} r^{12}$$
$$q(r) = w_0 + w_2 r^2 + w_4 r^4 + w_6 r^6 + w_8 r^8 + w_{10} r^{10} + w_{12} r^{12} + w_{14} r^{14} + w_{16} r^{16} + w_{18} r^{18}$$

with $R_l^{AE,semi}(r)$, the inner-shell (semicore) and $r_l^{AE,v}(r)$, the outer-shell (valence) all electron (AE) wavefunctions. The conditions of norm-conservation and eigenvalues developed in the previous considerations are applicable to the nodeless wavefunction $R_l^{PP,0}$.

The variational freedom introduced by the three additional polynomial coefficients w$_i$ is accompanied by three conditions applying to the single-node valence pseudo-orbitals R$_l^{PP,1}$

$$For \;\; l < 2, \;\; we \;\; have \;\; \begin{cases} R_l^{PP,1}(r_c) = R_l^{AE,v}(r_c) \\ \int\limits_0^{r_c} |R_l^{PP,1}(r_c)|^2 r^2 dr = \int\limits_0^{r_c} |R_l^{AE,v}(r_c)|^2 r^2 dr \\ \epsilon_l^{PP,1} = \epsilon_l^{AE,v} \end{cases} \tag{2.65}$$

Therefore, the semicore states inclusion goes along with an increased computational cost (for the single-node elements) since they tend to be very localized and hard inducing, in plane waves implementations, high Fourier components computations and thus higher energy cut-offs.

The most important characteristics of a pseudo-potential are transferability, cut-off requirement and the domain of validity. This last element means that the pseudo-potentials with NLCC or semicore approaches have been tested extensively on a certain type of atoms, molecules and environments. Therefore, preliminary to any plane waves calculation, the pseudo-potential have to be chosen according to the system and the properties that will be investigated.

2.2 Car-Parrinello Molecular Dynamics (CPMD)

Introduction

Molecular dynamics is a method introduced by Alder and Wainwright in the late 1950's for the study of phase transition phenomena in the case of hard sphere systems [42]. It is an approach developed to study a system of interacting particles by creating a model system as close as possible to the real system and simulate its behavior for a sufficient length of time to study the properties of interest. The objects described by molecular dynamics can be atoms, molecules or polymers, these are considered as point-like particles and represented as classical (deterministic) particles with well-defined positions and velocities. We consider a system of N$_I$ atoms with the corresponding position variables $\vec{R}_I$=(x$_I$,y$_I$,z$_I$) and I = 1,..,N$_I$. These particles interact via a given function of the positions, the potential V($\vec{r}$). The forces $\vec{f}_I$ applied on the particles are therefore the gradients of this potential,

$$\vec{f}_I = \frac{\partial V(\vec{R}_I)}{\partial \vec{R}_I} \tag{2.66}$$

the expression of this 3N$_I$ dimensional function $\vec{f}_I$ is called a force field. One includes all necessary forms of interaction functions in the potential such as bond streching or bending, Coulomb or even van der Waals interactions because they can be represented as analytical parameter-dependent functions of $\vec{R}_I$. The parameters of the system under study, within the force field considered, can be either taken from fits to experiments or extracted from ab-initio calculations. In this project, we use the first-principles molecular dynamics (FPMD) formulation introduced by Roberto Car and Michele Parrinello in 1985 [43] and implemented in the CPMD code [2]. This approach was developed for the study of structural, electronic and thermodynamic properties of solid state systems. The fundamental idea is to combine atomic motions and trajectories used in the molecular dynamics classical methods (MD) with the first-principles techniques for electronic structure calculations. The linker between the two methods is the interaction potential, approximated and empirically chosen in standard MD while directly expressed in terms of the electronic structure properties in the CPMD case [104]. Car-Parrinello molecular dynamics approach couples the electrons and ions subsystems via a calculation of the forces, due to electrons, applied on the ions "on the fly" [43]. Therefore, it is based on an interatomic potential which is parameter-free, derived from first-principles, with no experimental input and the forces are computed using state-of-the-art DFT calculations.

In this section, we construct the interatomic potential using the previous KS-DFT ideas in order to describe the parameter space in which one can perform first-principles molecular dynamics. This method is then applied to liquid water systems or copper hydroxide acetate to exemplify the predictive power and typical outputs of such simulations.

2.2.1 Construction of the first-principles potential

The first step in the construction of the CPMD method is the determination of the interatomic potential from first-principles. For a system of N_I atoms, the density functional (DF) framework informs us that the total energy for an atomic configuration $\{\vec{R}_I\}$ is a functional of the electronic density $\mathrm{n}(\vec{r})$ parametrized by the ionic positions $\mathrm{E}[n(\vec{r}), \{\vec{R}_I\}]$. For this construction we do not consider the spin degree of freedom since its introduction may be performed in the same way than the one described in the previous section. The electronic density is thus defined in terms of the $\mathrm{N}_e/2$ doubly occupied single-particle Kohn-Sham orbitals $\phi_i(\vec{r})$

$$n(\vec{r}) = 2 \sum_{i=1}^{N_e/2=Occ} |\phi_i(\vec{r})|^2 \tag{2.67}$$

with $\vec{r}$, the electronic space variable and the sum running over all occupied orbitals. We assume that the electronic gap is much larger than the characteristic energy of ionic motion, as it holds for most semiconductors and insulators. In the case of metallic systems, the situation is more delicate and one can still proceed provided the characteristic plasma frequency of the metal is much larger than the typical ionic thermal energies. An additional assumption is that ionic motion can be described classically, which is the general paradigm of molecular dynamics methods. In this context, the desired interaction potential corresponding to our atomic system and derived *ab initio* (AI) can be written as

$$V^{AI}\Big(\{\vec{R}_I\}\Big) = \langle \Psi_0(\vec{r}) | \hat{H} | \Psi_0(\vec{r}) \rangle \tag{2.68}$$

where $\hat{H}$ is the Hamiltonian of the system in the fixed ionic configuration $\{\vec{R}_I\}$ and $\Psi_0(\vec{r})$ is the ground state wavefunction. The total energy functional (2.16) has thus to be evaluated through the variational parameters that are the ionic positions as well as the Kohn-Sham orbitals $\{\phi_i\}$

$$E[\{\phi_i\},\{\vec{R}_I\}] = 2\sum_{i=1}^{Occ}\int \phi_i^*(\vec{r})\Big(-\frac{1}{2}\nabla^2\Big)\phi_i(\vec{r})d\vec{r} + \int V_{ext}(\vec{r}-\vec{R}_I)n(\vec{r})d\vec{r} \qquad (2.69)$$
$$+\frac{1}{2}\int \frac{n(\vec{r})n(\vec{r'})}{|\vec{r}-\vec{r'}|}d\vec{r}d\vec{r'} + E_{xc}[n] + \frac{1}{2}\sum_{I\neq J}\frac{Z_I Z_J}{|\vec{R}_I-\vec{R}_J|}$$

where V$_{ext}$ is the total nuclei electrostatic potential felt by the electrons, Z$_I$ are the nuclear charges and E$_{xc}$ is the exchange correlation energy functional encompassing all many-body effects in the system. The first-principles atomic interaction potential sought for can thus be written as

$$V^{AI}\Big(\{\vec{R}_I\}\Big) = \min_{\{\phi_i\}} E\Big[\{\phi_i\},\{\vec{R}_I\}\Big] \qquad (2.70)$$

for which the Kohn-Sham eigenvalues equations can be applied. The approach adopted by Car and Parrinello [43] is quite different since they do not rely on KS equations. They use the electronic ground state sought for in (2.6) determining the instantaneous energy minimum of the system and defined as the atomic interaction potential $V^{AI}\Big(\{\vec{R}_I\}\Big)$ used in the MD procedure. The method is to perform the minimization of the total energy functional by applying the simulated annealing (SA) concept introduced by Kirkpatrick, Gelatt and Vecchi in 1983 [44]. This approach permits the minimization of an objective function O($\{\beta\}$) relative to the corresponding parameter space $\{\beta\}$. This is achieved through successive generation of the $\{\beta\}$ with a Boltzman-type probability distribution ($\simeq e^{-O(\{\beta\})/T}$) via a Monte Carlo procedure using the metropolis algorithm. The state providing the lowest value of O(β) is reached when the temperature (T) tends to 0. The objective function in the context of the electronic structure calculation is the energy functional (2.69). In practice a Kohn-Sham calculation is still performed in the CPMD code [2] to get the Kohn-Sham orbitals of the initial atomic configuration considered but these orbitals become a tool to perform fictitious electron dynamics during the MD procedure. This approach will be used at a later step to construct the CPMD scheme. For now, we consider the $\{\phi_i\}$'s as fictitious classical dynamical variables in the space of electronic degrees of freedom of the system. For a given nuclei configuration $\{\vec{R}_I\}$, first order canonical dynamics can be generated for the fictitious electronic system and used to map the potential function via a steepest descent procedure (gradient method). The optimization method makes use of the calculation of the gradients of the total energy with respect to the fictitious classical electrons and leads to the minimum of the total energy

$$\dot{\phi}_i(\vec{r},t) = -\frac{1}{2}\frac{\delta E[\{\phi_i(\vec{r})\}]}{\delta\phi_i^*(\vec{r},t)} \qquad (2.71)$$

where the time derivative is performed with respect to the fictitious time introduced for the classical dynamics of the $\{\phi_i(\vec{r})\}'s$. We define the corresponding KS Hamiltonian as

$$H = -\frac{1}{2}\nabla^2 + V_{ext}(\vec{r}) + V_H(\vec{r}) + V_{xc}(\vec{r}) \qquad (2.72)$$

where V$_H(\vec{r})$ is the Hartree potential and V$_{xc}$, the exchange-correlation potential

$$V_{xc} = \frac{\delta E_{xc}[n]}{\delta n(\vec{r})} \tag{2.73}$$

and the associated KS equations

$$H\phi_i(\vec{r}) = \epsilon_i \phi_i(\vec{r}) \tag{2.74}$$

The form of the Hamiltonian indicates a nonlinear dependence on the single particle orbitals $\phi_i(\vec{r})$. This results in the non-linearity of the fictitious dynamics (2.71). We establish the correspondence between the KS formulation and the fictitious dynamics through the following relation

$$\frac{\delta E[\{\phi_i(\vec{r})\}]}{\delta \phi_i^*(\vec{r}, t)} = 2H\phi_i(\vec{r}, t) \tag{2.75}$$

and completed by adding the orthonormality constraint on the $\phi_i(\vec{r})$ functions

$$\int \phi_i^*(\vec{r})\phi_j(\vec{r})d\vec{r} = \delta_{ij} \tag{2.76}$$

The problem is now of minimizing self-consistently the total energy (2.69) without having to perform any explicit diagonalization. The steepest descent procedure is only a first guess and there exist very efficient conjugate gradients (CG) methods associated to pre-conditioning techniques that allow to achieve the minimization objective [104]. Therefore, one can efficiently calculate the ab initio potential V^{AI} (2.68) from which the forces on the ions can be derived through the application of the Hellmann-Feynman theorem [146], the extension of the classical electrostatic theorem to the quantum problem. It can be stated as follows [147]: it provided the quantum Hamiltonian H(λ) with eigenvalues $\epsilon_i(\lambda)$ and eigenvectors $\phi_i(\lambda)$, all dependent on the parameter λ, one can define the generalized force F$_\lambda$. It is equivalent to evaluate F$_\lambda$ it as the derivative of the eigenvalues or as the expectation values of the Hamiltonian derivative with respect to this parameter

$$\frac{\partial \epsilon_i(\lambda)}{\partial \lambda} = \langle \phi_i(\lambda)| \frac{\partial H(\lambda)}{\partial \lambda} \phi_i(\lambda) \rangle, \tag{2.77}$$

assuming the differentiability of ϵ_i, H and ϕ_i with respect to the parameter λ. We take λ to be the space coordinate $\vec{R}_I$ of the nucleus "I" and we assume that no external fields are present. The force on the Ith ion due to other nuclei and electrons can be computed from the other nuclei locations and the electronic charge density as it is done in electrostatics [147]. We can therefore construct the two equations of motion that will govern the dynamics of the electronic and ionic fictitious dynamics allowing for an efficient optimization of the atomic structure of our system

$$\begin{aligned} \bar{\mu}_i \dot{\phi}_i(\vec{r}, t) &= -\frac{1}{2}\frac{\delta E}{\delta \phi_i^*(\vec{r}, t)} + constraints \\ \bar{M}_I \dot{\vec{R}}_I(t) &= -\frac{\partial E}{\partial \vec{R}_I(t)} \end{aligned} \tag{2.78}$$

where $\bar{\mu}_i$ and $\bar{M}_I$ are the corresponding inertia coefficients ("masses") introduced to account for the timescales differences between the ionic $\vec{R}_I$ and electronic $\phi_i(\vec{r})$ degrees of freedom. Therefore, the SD trajectory is generated through the variation of the $\phi_i(\vec{r},t)$ for a fixed nuclei configuration. This procedure leads toward a single minimum of the energy surface E$[\{\phi_i(\vec{r},t)\}]$ that coincides with a local minimum of the Born-Oppenheimer potential energy surface V^{AI} (2.70). Therefore, the local minima of the energy surface explored through equations (2.78) are also the minima of the interaction potential. The task of following a trajectory on the fictitious E$[\{\phi_i(\vec{r},t)\}]$ surface while controlling the relative relaxation rates of electrons and ions is therefore possible through the use of optimal "mass" parameters for the ionic and electronic subsystems. In consequence, the perfect self-consistency required for each atomic configuration (at each step) in conventional gradient methods, is avoided and replaced by the possibility to ensure that the ionic and electronic motions are adiabatically separated through the adjustment of the "mass" parameters. This dynamical minimization approach allows treating fairly large systems with a simultaneous relaxation of the ionic and electronic degrees of freedom. The severe limitation is that the optimization remain local and global optimization procedures have to be considered to map efficiently all the minima of a complex system. We discuss the possibility of achieving such result in the next subsection, in which the global optimization is based on statistical mechanics methods together with the possibility of performing DFT-based MD simulations.

2.2.2 Molecular dynamics in the electron-ion parameter space

We can now exploit the computational scheme developed in the previous subsection to establish the second-order differential equations corresponding to Newtonian dynamics in the density functional (DF) parameter space. We consider the time-dependent parameters $\phi_i(\vec{r},t)$ and $\vec{R}_I(t)$ and write the Lagrangian of the Car-Parrinello scheme for this parametric system

$$\begin{aligned} L_{CP} =& 2\sum_{i=1}^{Occ}\int \mu \left|\dot{\phi}_i(\vec{r},t)\right|^2 d\vec{r} + \frac{1}{2}\sum_I M_I \dot{\vec{R}}_I^2 - E[\{\phi_i\},\vec{R}_I] \\ &+ 2\sum_{ij}\Lambda_{ij}\left(\int \phi_i^*(\vec{r},t)\phi_j(\vec{r},t)d\vec{r} - \delta_{ij}\right) + \sum_\nu \frac{1}{2}\mu_\nu \dot{\alpha}_\nu^2 \end{aligned} \tag{2.79}$$

where we dropped the subscript of the fictive mass $\mu_i = \mu$ considered the same for all electronic degrees of freedom. The mass M$_I$ is the real physical masses of the ions considered in the system. We remind that the fictive mass μ is non-physical and controls only the time-step of the classical electrons dynamics. An optimal value is chosen according to the adiabatic separation of the real ionic motion from the fictive electron motion and it is chosen to allow for the largest time-step possible. Typical values range from $\mu_{min} \simeq 300\,a.u$ (300m$_e$) to $\mu_{max} \simeq 1000\,a.u$ for an integration step of Δt=3 to 10 a.u (1a.u $\simeq$ 0.024fs). The second term of the Lagrangian corresponds to the ionic classical kinetic energy K_I. The third term is the total energy functional E$[\{\phi_i\},\vec{R}_I]$ corresponding to the potential energy surface V$^{AI}\left(\{\vec{R}_I\}\right)$ of the system even if at first sight, the two are not equivalent but related through equation (2.70). The fourth term of the CP Lagrangian corresponds to the orthonormality constraint (2.76) imposed for the electronic functions $\phi_i(\vec{r},t)$ and Λ_{ij} the corresponding Lagrange multipliers. The last term is present in the Lagrangian proposed by Car and Parrinello [43] and accounts for additional fictitious degrees of freedom that can be, for example, the "masses" of a temperature reservoir or constraints on the volume of the cell. Recalling the simulated annealing (SA) method of Kirkpatrick, Gelatt and Vecchi[44] in the present context, the total energy functional E$[\{\phi_i\},\vec{R}_I]$ is thus the objective function. The variational parameters are the coefficients of the expansion of the KS orbitals in the adequate basis $\{c_{j,\vec{k}}\}$ (2.49), the ionic positions $\{\vec{R}_I\}$ and possibly the $\{\alpha_\nu\}$. The SA procedure followed in the CP method is based on MD rather than on the metropolis Monte Carlo method. These methods allow not only for minimization toward 0 temperature but also for finite temperature simulations through making the parameters $\{\alpha_\nu\}$ become dynamical variables, $\alpha_\nu(t)$. We will come back on this point while exposing the Nosé-Hoover thermostat implementation.

From the CP Lagrangian (2.79), we can apply the following Euler-Lagrange equations

$$\begin{aligned}\frac{\delta L_{CP}}{\delta\phi_i(\vec{r},t)} - \frac{d}{dt}\left(\frac{\delta L_{CP}}{\delta\dot{\phi}_i(\vec{r},t)}\right) &= 0 \\ \frac{\delta L_{CP}}{\delta\vec{R}_I(t)} - \frac{d}{dt}\left(\frac{\delta L_{CP}}{\delta\dot{\vec{R}}_I(t)}\right) &= 0\end{aligned} \tag{2.80}$$

from which we obtain the corresponding equations of motion for the coupled electrons-ions system

$$\begin{aligned}\mu\ddot{\phi}_i(\vec{r},t) &= -\frac{1}{2}\frac{\delta E[\{\phi_i\},\{\vec{R}_I\}]}{\delta\phi_i^*(\vec{r},t)} + \sum_j \Lambda_{ij}\phi_j(\vec{r},t) \\ M_I\ddot{\vec{R}}_I &= -\frac{\partial E}{\partial\vec{R}_I(t)}\end{aligned} \tag{2.81}$$

These two equations of motion allow performing MD based statistical mechanics simulations. In terms of equilibrium properties, the total classical kinetic energy at equilibrium can be evaluated resulting from meaningful temporal averages

$$K_{Tot}^{classical} = K = K_e + K_I \quad ; \quad \langle K\rangle \simeq \langle K\rangle_t \tag{2.82}$$

and to define the classical system's temperature as its kinetic energy normalized by the number of degrees of freedom (DoF).

$$T_{system} \propto \frac{\langle K\rangle}{\#DoF} \tag{2.83}$$

Therefore the control of the variations of the ionic and electronic velocities allows for finite temperature dynamics and to perform annealing or quenching processes through simultaneous relaxation of both nuclear and electronic DoF. We are using a global optimization method that enables an efficient exploration of the configuration space that leads generally to the global minimum of the parametric energy surface E $[\{\phi_i\}, \vec{R}_I]$ considered. However, this total energy of the fictitious system coincide with the Born-Oppenheimer potential energy surface V^{AI} (defined in 2.68) only if E$[\{\phi_i\}, \vec{R}_I]$ is at an instantaneous minimum. The correct classical dynamical equations for the nuclei are

$$M_I \ddot{\vec{R}}_I = -\frac{\partial V^{AI}(\vec{R}_I)}{\partial \vec{R}_I} \tag{2.84}$$

Therefore, we still have to demonstrate how such Newtonian dynamics (2.81) can be used to generate Born-Oppenheimer trajectories for the nuclei and perform the so-called first-principles molecular dynamics (FPMD). This is a crucial point for the Car-Parrinello technique, the parameter of "fictive mass" μ and the initial conditions $\{\phi_i(\vec{r},0)\}$,$\{\dot{\phi}_i(\vec{r},0)\}$ are chosen so that a clear time-scale separation between electronic (fast) and ionic (slow) DoF occurs. In this configuration, once the first electronic calculation is performed, the nuclei are propagated from the Born-Oppenheimer surface (BO) on which nuclear trajectories initially lie in BOMD methods. In constrast, in the CPMD scheme, the system's energy will stay close to the BO surface as long as the electronic and nuclear DoF remain weakly coupled, i.e initial conditions choice prohibiting energy transfer between the two subsystems. The deviation from the BO surface occurs after times very large compared to the MD time step or even compared to MD observation time [104] and is demonstrated to be bound from above [148]. The result is that the electrons follow adiabatically the ionic motion remaining close to the BO surface so that these "classical adiabatic dynamics" allow computing meaningful temporal averages from such a metastable situation.

In the last subsection of this chapter, we will expose the practical aspects of the use of such scheme to produce many different electronic and structural properties. We illustrate this development by actual CPMD simulations of model systems studied.

2.2.3 Thermodynamical and electronic properties

We briefly overview the various electronic and thermodynamic properties that can be investigated within first-principles molecular dynamics methods. We consider two model systems that will be used to illustrate the properties obtained from CPMD calculations.

The first example is a cubic simulation cell with an edge length of 9.86 Å containing 32 water molecules $(H_2O)_{32}$ with the characteristic density if liquid water at room temperature (left part of Figure 31). The second example is the prototypical hybrid material that we study in the next chapter, copper hydroxide acetate $[Cu_2(OH)_3(CH_3COO) \bullet (H_2O)]_{16}$ (right part of Figure 31). This simulation cell contains 16 formula units which corresponds to 288 atoms. The lattice parameter and the atomic structure that will be used in this chapter and the next are those of the experimental work of Švarcová and coworkers [3]. In this contribution, the authors synthesized a single-crystal structure ideal for the full characterization of the crystal structure and therefore adequate for a first-principles molecular dynamics study.

The Nosé-Hoover thermostat

The methods to achieve thermodynamical control of systems simulated by MD approaches are pioneered by Rahman, Andersen, Parrinello, Nosé and Hoover [122, 123,

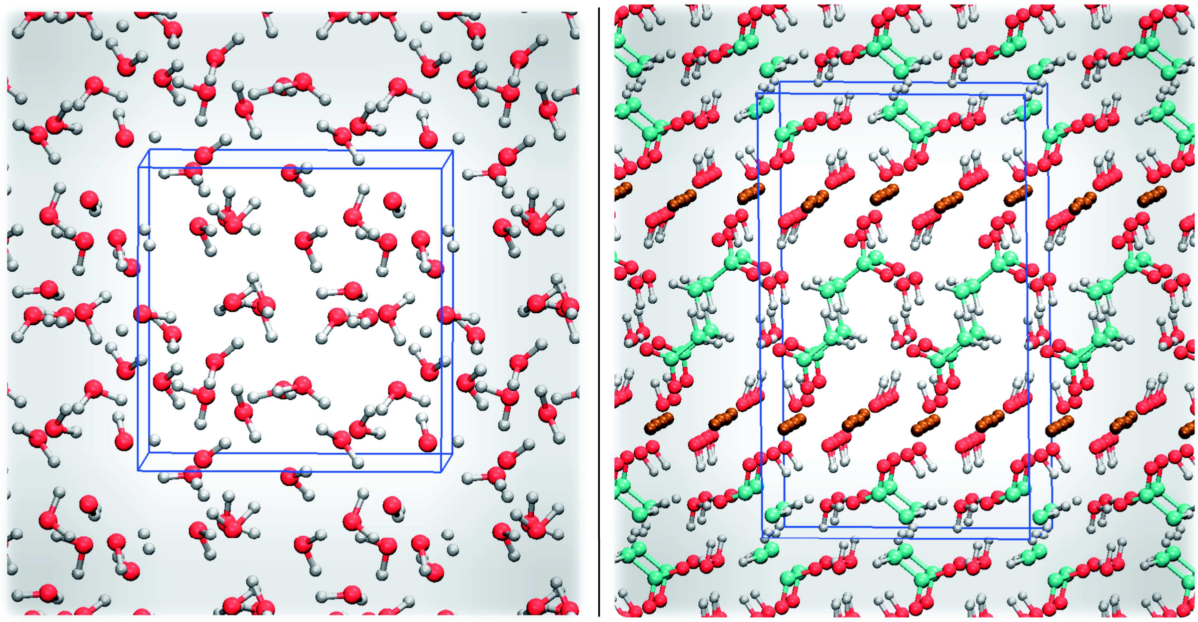

Figure 31 – Two model systems used to exemplify the possibilities of Car-Parrinello molecular dynamics methods in predicting electronic and structural properties of materials. **Left part:** liquid water simulated through a system of 32 (H_2O) molecules in a cubic cell of edge length 9.86 Å. **Right part:** the simulation supercell of the organic-inorganic hybrid copper hydroxide acetate material $[Cu_2(OH)_3(CH_3COO) \bullet (H_2O)]_{16}$ (CuOHAc). Both systems are represented with a shaded area surrounding the simulation cells (blue boxes) highlighting the periodic boundary condition considered in the three directions.

149, 150, 151]. Here, we will sketch the fundamental idea of this method relying on the CPMD Lagrangian introduced in the previous section. In statistical mechanics, the temperature of a system of N_I particles (ions) at positions $\vec{R}_I$(t) is defined with respect to the time average of the kinetic energy of of the system

$$\left\langle K_I \right\rangle = \left\langle \sum_{I=1}^{N_I} \frac{M_I \dot{\vec{R}}_I^2}{2} \right\rangle_t = \frac{3}{2} N_I k_B T \tag{2.85}$$

where K_I and M_I are the ionic kinetic energy and ionic masses respectively and k_B is the Boltzmann constant. The above equivalence holds true in the thermodynamic limit so that a heat reservoir is in contact with the ionic system providing a temperature bath (thermostat). This objective can be reached through the introduction of a scaling variable "s" which is acting on the velocities and therefore on the momenta of the ions $\vec{p}_I = M_I \dot{\vec{R}}_I$. This gives rise to a friction force $\vec{F}_I = -s\vec{p}_I$ acting on the ion "I" leading the system to heat up if s>0 or cool down if s<0. However, the direct rescaling of the velocities by fixing a target temperature T leads to fixing the kinetic energy of the system (from 2.85). This in turn affects the Hamiltonian energy (E_{HAM}) conservation. As an alternative, the stochastic method changes the scaling algorithm in a way that enforces the targeted canonical distribution as prescribed by Andersen [123]. Nosé [150] and Hoover [151] proposed to treat the problem differently, namely, through the introduction of the thermostat system into the CP Lagrangian. Therefore, the thermostat problem is accounted for by the inclusion of a single additional degree of freedom leading to still deterministic dynamical equations. The idea is therefore to be able to describe a canonical ensemble (NVT) through microcanonical ensemble calculations (NVE). For this purpose, one has to include this new degree of freedom ("s") in the Lagrangian L$_{CP}$ of equation (2.79). Therefore, the thermostat system has its own dynamical variable $s(t)$ and a fictitious mass Q ensuring the time scaling of the motion of $s(t)$ with respect to the motion of ionic positions $\vec{R}_I(t)$. The associated potential is given by the Boltzmann canonical term $(3N_I)k_BTln(s)$ and the extended Car-Parrinello-Nosé-Hoover (constructed from refs. [43, 152]) Lagrangian L$_{CP-NH}$ can be written, after dropping the constraints α_ν term,

$$\begin{aligned} L_{CP-NH} =& 2\sum_{i=1}^{Occ}\int \mu\left|\dot{\phi}_i(\vec{r})\right|^2 d\vec{r} + \frac{1}{2}\sum_{I}^{N_I} M_I s^2\dot{\vec{R}}_I^2 - E[\{\phi_i\},\vec{R}_I] \\ &+ 2\sum_{ij}\Lambda_{ij}\left(\int \phi_i^*(\vec{r})\phi_j(\vec{r})d\vec{r} - \delta_{ij}\right) \\ &+ \frac{1}{2}Q\dot{s}^2 - (3N_I+1)k_BTln(s) \end{aligned} \tag{2.86}$$

Using a Legendre transformation, we define the corresponding momenta for the classical ionic and thermostat velocities

$$\begin{aligned} \vec{p}_I &= \nabla_{\dot{\vec{R}}_I} L_{CP-NH} = M_I s^2 \dot{\vec{R}}_I \\ p_s &= \frac{\partial L}{\partial \dot{s}} \end{aligned} \tag{2.87}$$

as well as the momenta p$_e$ and p$_e^*$ for the classical electronic DoF velocities $\dot{\phi}_i$ which are unaffected by the thermostat

$$\begin{aligned} p_e &= \frac{\delta L_{CP}}{\delta \dot{\phi}_i^*(\vec{r})} = \mu\dot{\phi}_i(\vec{r}) \\ p_e^* &= \frac{\delta L_{CP}}{\delta \dot{\phi}_i(\vec{r})} = \mu\dot{\phi}_i^*(\vec{r}) \end{aligned} \tag{2.88}$$

We can now write the extended Hamiltonian for the electronic, ionic and thermostat system

$$\begin{aligned} H_{CP-NH} =& \sum_{i}^{N_e}\int \frac{p_e(\vec{r})p_e^*(\vec{r})}{\mu}d\vec{r} + \sum_{I}^{N_I}\frac{(\vec{p}_I)^2}{2s^2M_I} + V^{AI}\left(\{\vec{R}_I\}\right) \\ &+ 2\sum_{ij}\Lambda_{ij}\left(\int \phi_i^*(\vec{r})\phi_j(\vec{r})d\vec{r} - \delta_{ij}\right) \\ &+ \frac{p_s^2}{2Q} + (3N_I+1)k_BTln(s) \end{aligned} \tag{2.89}$$

where Q is an inertial coefficient associated to the heat bath introduced. Using Hamilton equations for each variables and their momenta in H$_{CP-NH}$ or equivalently the Euler-Lagrange equations associated with the Lagrangian L$_{CP-NH}$, we obtain the final set of equations of motion

$$\begin{aligned}
\mu\ddot{\phi}_i(\vec{r},t) &= -\frac{1}{2}\frac{\delta E[\{\phi_i\},\{\vec{R}_I\}]}{\delta\phi_i^*(\vec{r},t)} + \sum_j \Lambda_{ij}\phi_j(\vec{r},t) \qquad (2.90)\\
M_I\ddot{\vec{R}}_I(t) &= \frac{1}{s(t)^2}\nabla_{\vec{R}_I(t)}E[\{\phi_i\},\{\vec{R}_I\}] - 2\frac{\dot{s}(t)}{s(t)}M_I\dot{\vec{R}}_I(t)\\
Q\ddot{s}(t) &= \frac{1}{s}\left[s^2(t)\sum_I^{N_I} M_I\dot{\vec{R}}_I^2(t) - (3N+1)k_BT\right]
\end{aligned}$$

that encompass all the dynamical scheme of the Car-Parrinello method including the Nosé-Hoover thermostat. We note that a new conserved quantity has to be defined for the (ionic+thermostat) subsystem characterized by the Hamiltonian H$_{I,th}$

$$H_{I,th} = \sum_I^{N_I}\frac{(\vec{p}_I)^2}{2s^2M_I} + V^{AI}\left(\{\vec{R}_I\}\right) + \frac{p_s^2}{2Q} + (3N_I+1)k_BTln(s) \qquad (2.91)$$

so that the energy conservation can be written as

$$\frac{dH_{I,th}}{dt} = \sum_I\left(\frac{\partial H_{I,th}}{\partial\vec{p}_I}\dot{\vec{p}}_I + \frac{\partial H_{I,th}}{\vec{R}_I}\dot{\vec{R}}_I\right) + \frac{\partial H_{I,th}}{\partial p_s}\dot{p}_s + \frac{\partial H_{I,th}}{\partial s}\dot{s} = 0 \qquad (2.92)$$

The two important parameters that have to be fixed in order to perform the finite temperature simulations are the thermostat mass "Q" and the target temperature T. Luckily, one can define a frequency for the thermostat deduced from the thermostat equation of motion (third equation 2.94)

$$\omega_{th} = \sqrt{\frac{2(3N+1)k_BT}{Q\langle s\rangle^2}} \qquad (2.93)$$

Therefore, the preliminary work is to evaluate the lowest ionic vibration mode in the system to be studied and fix the frequency of the thermostat in order to ensure a controlled coupling with the ionic subsystem. Finally, the same technique can be applied to impose a thermostat on the fictitious electronic degrees of freedom so that both ionic and the fictitious electronic subsystems' temperatures remain under control.

Energy decomposition

Our first task is to perform a typical simulation of the liquid water system invoked earlier. We apply a thermal treatment that is characteristic of the protocols followed for all the materials studied in this project. Typically, we first perform the famous dynamical simulated annealing (DSA) of Car and Parrinello [43]. Then, we perform a free molecular dynamics run (without imposing any temperature or annealing) before heating the system up to room temperature in a further step.

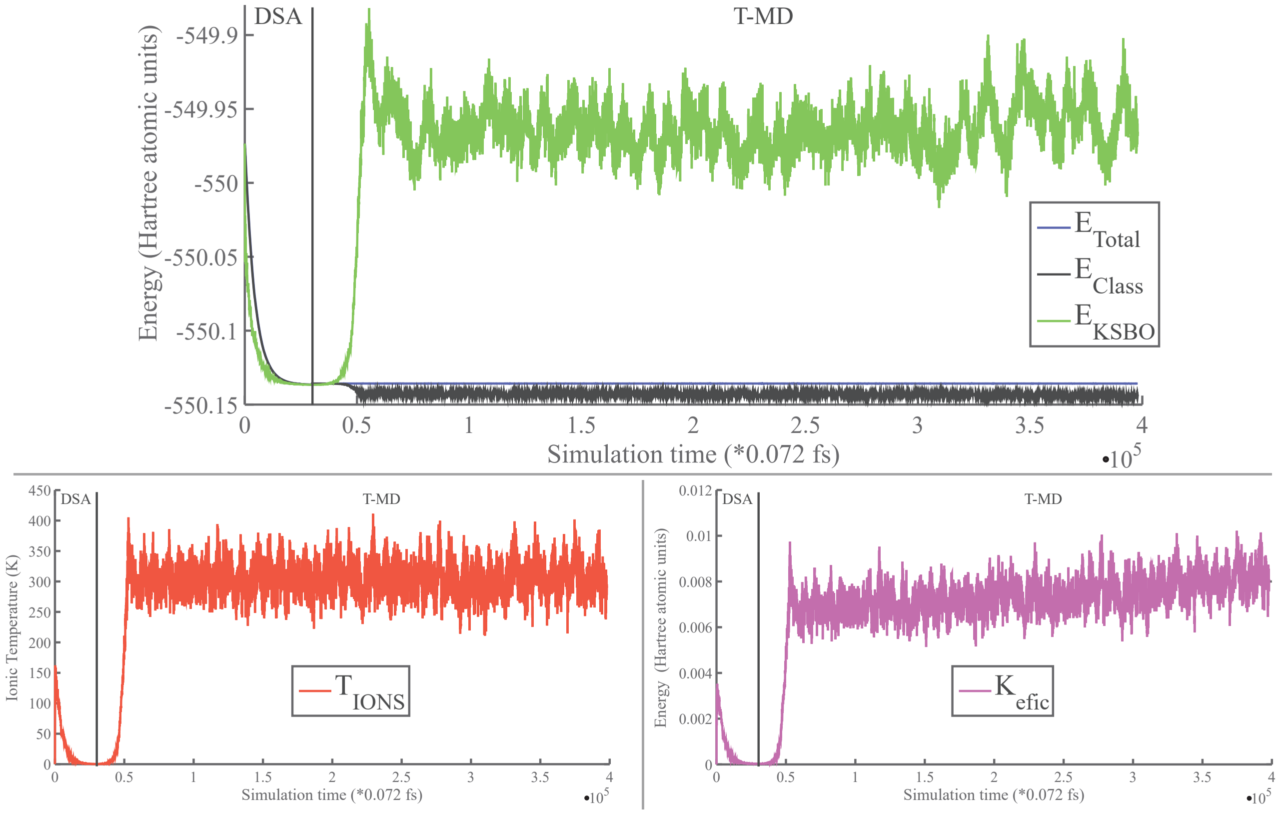

Figure 32 – Characteristic energies obtained from a CPMD run for a liquid water system (32 molecules and periodic boundary conditions). The first zone (left of dashed line) corresponds to the dynamical simulated annealing region (DSA) and the second (right part) corresponds to the finite temperature MD (T-MD) in which the system is brought to room temperature. In this case the Nosé-Hoover thermostat is applied to maintain the system at 300 K. The conserved Hamiltonian energy (blue line), total CPMD classical energy (black) and the Kohn-Sham potential energy computed from DFT (green) are represented in the top plot. In the bottom part, the ionic temperature (red) and the fictitious energy of the classical electrons (pink) are represented

We decompose the total energy of the system into the different contributions analyzing their origin and their magnitudes. In Figure 32, we show the behaviors of the main quantities to be analyzed in a CPMD run. These results correspond to a CPMD trajectory producing, first, 2.1 ps of DSA and then 26.6 ps of finite temperature molecular dynamics (T-MD) of the liquid water system at room temperature. In the top part of Figure 32, we show the evolution as function of time of the total energy of the system (Hamiltonian energy E_{HAM}) in blue. In the annealing region, the total energy is minimized with respect to both ionic and electronic degrees of freedom and then it is a constant of motion during the finite temperature molecular dynamics region (T-MD). The Kohn-Sham energy (E_{KSBO}) obtained from DFT assimilated to its instantaneous minimum (BO surface) at each MD step is shown in green. This corresponds to the system's potential energy (V^{AI} in the Hamiltonian 2.89). It is as well minimized in the DSA region with an oscillatory behavior characteristic of the annealing process. The minimization is ensured by the friction force applied. In the T-MD region, this potential energy is driven by the Nosé-Hoover thermostat procedure to bring the system at room temperature. The corresponding temperature evolution as a function of time is shown in the bottom left part of Figure 32. To maintain the system at room temperature, we control the coupling between electronic and ionic degrees of freedom (or the adiabatic character of the classical dynamics). Such classical dynamics are considered adiabatic and thus "physically correct" as long as the fictitious energy (K_{efic}) of the classical electronic degrees of freedom remains small and that no significant trends are observed after an MD observation time. Such requirements are met in this situation as highlighted by the bottom right plot in Figure 32. Indeed, the fictitious energy remains 5 orders of magnitude lower than the other energy contributions and does not show a significant drift after about 30 ps simulation time.

Electron localization

Many methods of electron localization allow for a transformation of the electron density data into a local information so that one can characterize the chemical bonding or perform dipole calculations in an efficient way. All of these methods can be spin sensitive in the sense that one can discriminate between local positive (n^{α}) spin density or local negative spin density (n^{β}). The electron localization function (ELF) introduced by Becke in 1990 [153] is an example of such a method. It is a measure of the probability of finding an electron in the space neighboring a reference electron located at a certain point. It is evaluated through the ratio of the electron kinetic energy density calculated from DFT and the uniform electron gaz counterpart. A second example is the Bader analysis introduced by Richard Bader [154] in which a partitioning of space is performed into subsystems separated by zero-flux density surfaces (no electron flow). The third example is the Wannier functions method introduced by Gregory Wannier in 1937 [50] and that will be the main tool used in this project for the investigation of chemical bonding or dipole dynamics calculations. This approach have also been refined and implemented largely and is today widely used [155]. While both ELF and Bader methods are based on the charge density, the Wannier functions are formulated in terms of orbitals and therefore will be detailed here within the framework of the CPMD method. We consider the KS orbitals at the Γ point ($\vec{k} = \vec{0}$), $\phi_i(\vec{r})$ and use them in the original definition given by Wannier in order to determine the Wannier centers w_i

$$w_i(\vec{r}, s) = \prod_{p=0}^{\infty} e^{\mathbf{A}^{(p)}} \cdot \phi_i(\vec{r}, s) \tag{2.94}$$

where $\mathbf{A}$ is an anti-Hermitian matrix. This is done through an iterative procedure [156], minimizing the spread Ω [157] of these Wannier functions defined as

$$\Omega = \sum_n \Omega_n = \sum_n \left(\langle w_n | (\vec{r})^2 | w_n \rangle - \langle w_n | \vec{r} | w_n \rangle^2 \right) \tag{2.95}$$

Since the Wannier functions are a complete ensemble of orthogonal functions, they are thus given by a unitary transformation of the Kohn-Sham orbitals

$$|w_n\rangle = \sum_i U_{in} |\phi_i^{KS}\rangle \tag{2.96}$$

so that the Wannier function centers corresponding to the center of mass of the new Wannier orbitals is written as

$$\langle r_{\nu,n}\rangle = -\frac{1}{g_\nu} Im\left(log\langle w_n|e^{-ig_\nu \cdot r_\nu}|w_n\rangle\right) \qquad ; \qquad \nu = x, y, z \tag{2.97}$$

where $g_\nu = 2\pi/L_\nu$ is defined with respect to the cell dimensions L_ν.

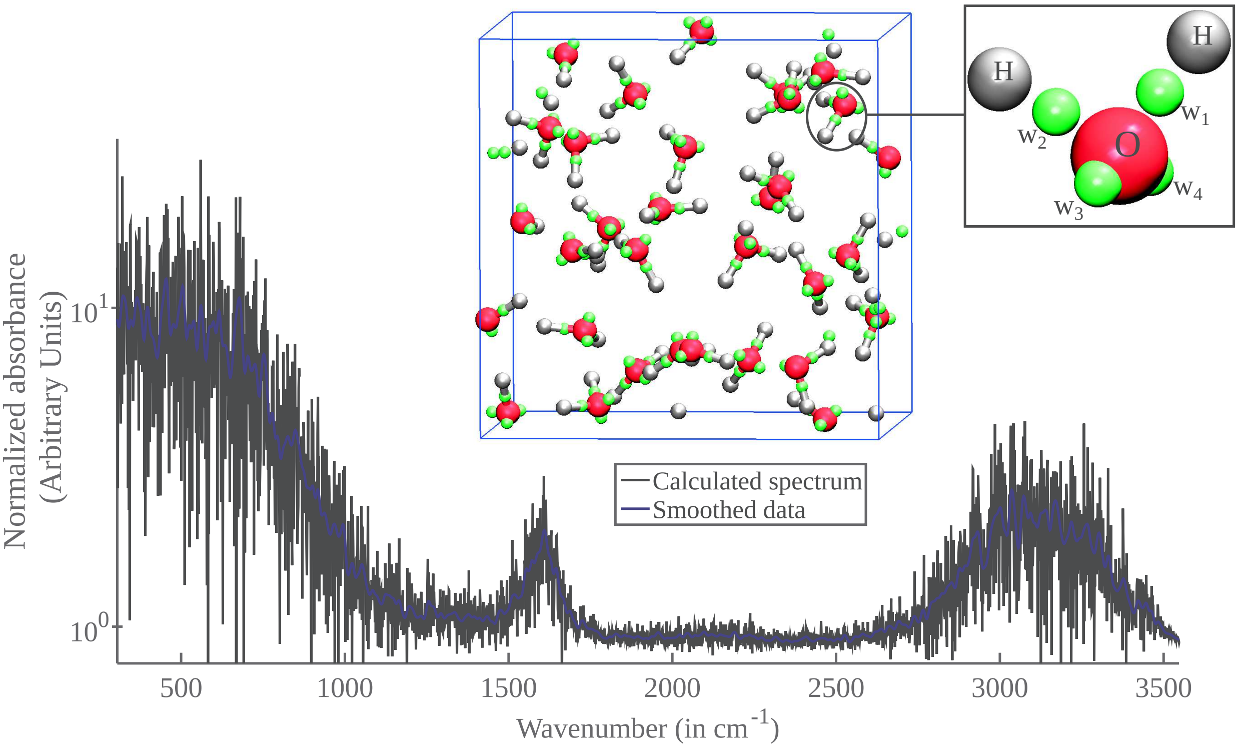

Figure 33 – Computed InfraRed (IR) spectrum of liquid water and the corresponding smoothed data obtained through a Fourier Transform (FT) of the time-autocorrelation function of the dipoles along the CPMD dynamics. This normalized spectrum is obtained from the simulation of a water system of 32 H_2O molecules (pictured in the top part) and applying periodic boundary conditions. The dipoles are computed through the Wannier functions centers (green spheres), an electron localization method, and are highlighted for a single water molecule in the inset (top right). The system is stabilized at room temperature (300K) for about 20 ps in order to achieve the resolution desired in the frequency domain

The Wannier centers locations (green spheres) are represented in Figure 33 in which one can distinguish the individual water molecule, the two bonding Wannier centers (w_1,w_2) and the lone pairs (w_3,w_4). Provided the atomic charges Z_I, the ionic positions $\vec{R}_I$ and the Wannier centers $\vec{r}_n$, one can then compute the dipole of the simulated cell summing all the individual contributions to the dipole so that

$$\vec{D} = \vec{D}_{ion} + \vec{D}_e = \sum_I Z_I \vec{R}_I - \sum_n 2 \cdot e \cdot \vec{r}_n \tag{2.98}$$

Therefore, we are able to compute the total dipole of our water system for each MD step all along the room temperature trajectory. From this set of data, we compute the time auto-correlation function (acf) of the signal D_{Cell}(t) acquired. By applying a Fourier transform, we obtained the computed IR spectrum for liquid water shown in Figure 33. The characteristic frequencies of the bending ($\simeq 1650$ cm^{-1}) and stretching (>3000 cm^{-1}) modes of liquid water are recovered. This result confirms that the MD simulation length considered gives a sufficient resolution in the frequency domain and that the time step of the dynamics is small enough to allow the exploration of high frequency modes.

In this work, we include van der Waals corrections according to the DFT-D2 method proposed by Grimme et al. [158]. The authors proposed a correction to the total self-consistent Kohn-Sham energy calculated from DFT (E_{KS}) in the form

$$E_{DFT-D} = E_{KS} + E_{disp} \tag{2.99}$$

where they introduce an empirical dispersion correction accounting for the van der Waals interactions effects for a system of N_I atoms

$$E_{disp} = -s_6 \sum_{I=1}^{N_I-1} \sum_{J=I+1}^{N_I} \frac{C_6^{IJ}}{R_{IJ}^6} f_{dmp}(R_{IJ}) \tag{2.100}$$

C_6^{ij} are the dispersion coefficients corresponding to the "IJ" atomic pair, s_6 is a global scaling factor that depends on the *xc*-functional used in the DFT calculations and $R_I J$ is the interatomic distance. A damping function f_{dmp} is introduced to avoid the singularities for small distances

$$f_{dmp}(R_{IJ}) = \frac{1}{1 + e^{-d_6(R_{IJ}/R_r - 1)}} \tag{2.101}$$

where R_r is the sum of atomic vdW radii and d_6 an additional empirical constant. This correction improves the results obtained in many FPMD simulations [155] and will be used in order to increase the quality of the structural optimizations performed in this project. Finally a first-principles scheme to calculate the C_6^{IJ} have been proposed by T. Ikeda and M. Boero [159] in which the Wannier functions are used to calculate these, hitherto empirical vdW, coefficients.

The spin density

In the case of the magnetic properties, one can rely on the formalism introduced by Von Barth and Hedin [45] of the LSD approximation detailed in the precedent section [160]. The spin degree of freedom is introduced *ad hoc* in the sense that one does not treat the rigorous problem of relativistic quantum Dirac equation. To include the spin, we employ a two-component representation for the wavefunction [161] which in our case are the Kohn-Sham spin orbitals

$$\phi(\vec{r}) = \begin{pmatrix} \phi^\alpha(\vec{r}) \\ \phi^\beta(\vec{r}) \end{pmatrix} \tag{2.102}$$

In the framework of the CPMD method, we consider only collinear magnetism. It is not possible to fix local atomic magnetic moment with such a method but rather, one can fix the spin multiplicity $M = 2S + 1$ with S the total spin value for the simulation cell considered. It is simply a measure of the degeneracy of the electronic wavefunctions, i.e. those that differ only by their spin orientation. Taking back the definitions (2.34), we write the condition on the total number of electrons N_e

$$N_e = N^\alpha + N^\beta = \int n^\alpha(\vec{r})d^3r + \int n^\beta(\vec{r})d^3r \tag{2.103}$$

where N^α and N^β are, respectively, the number of ↑ or ↓ spins in the system. We therefore fix a condition on the difference between the number of α and β states so that we get a net total spin fixed "S"

$$\begin{aligned} S &= N_\alpha - N_\beta \\ &= \int n^\alpha(\vec{r})d^3r - \int n^\beta(\vec{r})d^3r \\ &= \frac{M-1}{2} \end{aligned} \tag{2.104}$$

Therefore, the minimization of the electron-ion system energy in the CPMD scheme (DSA) may include such constrain on the total spin of the system, affecting in particular the DFT total energy functional (2.69) that provides the potential energy in the Car-Parrinello Lagrangian. Indeed, as long as no magnetic fields are considered, it is only the exchange-correlation potential that can have different values for the two spin directions. The potentials are thus written as

$$\begin{aligned} V_{xc}^\alpha &= \frac{\delta E_{xc}[n^\alpha, n^\beta]}{\delta n^\alpha(\vec{r})} \\ V_{xc}^\beta &= \frac{\delta E_{xc}[n^\alpha, n^\beta]}{\delta n^\beta(\vec{r})} \end{aligned} \tag{2.105}$$

where E_{xc} is the exchange correlation energy defined within the adequate (GGA) level of approximation (2.39).

As an example of such spin density calculations, we represent the simulation cell of copper hydroxide acetate system containing 32 copper atoms organized in the two layers highlighted in Figure 34. Two magnetic configurations are represented through the isosurfaces of spin density (α-spin density in blue and β spin density in pink). In the anti-ferromagnetic (AF) configuration, the spin densities located in the neighborhood of Cu atoms give rise to a specific arrangement of ↑ and ↓ spins so that the $S = 0$ constraint on the total spin is respected. In the ferromagnetic state (F) shown in the right part of Figure 34, only one spin value is present among all the system respecting the imposed constraint of $S = 16$.

The pressure

The last concept to be introduced is the static pressure applied on the systems that we

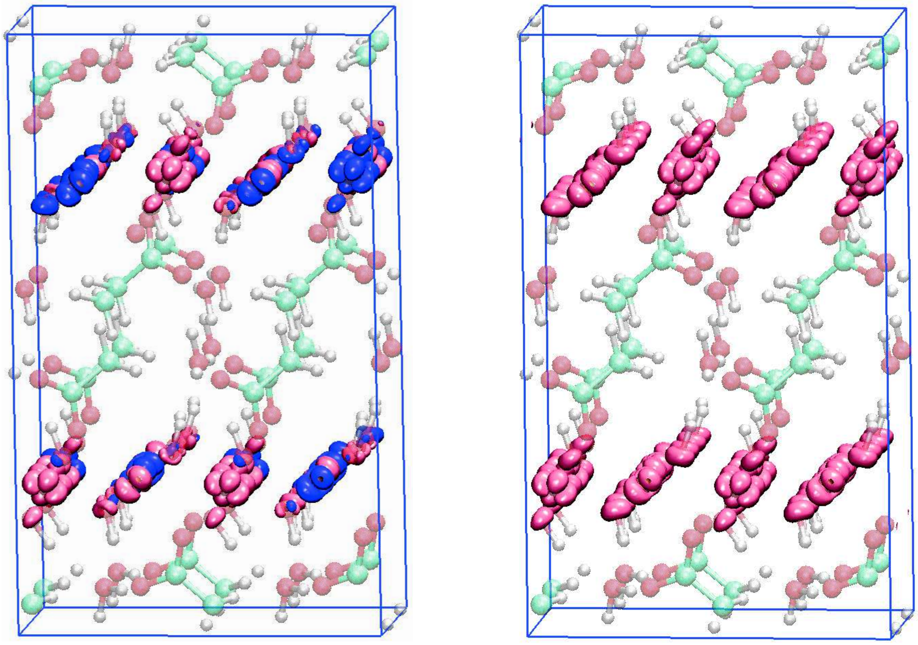

Anti-Ferromagnetic
S = 0 , M = 1

Ferromagnetic
S = 16 , M = 33

Figure 34 – Copper hydroxide acetate model systems in both the antiferromagnetic state (left part) and the fully ferromagnetic state (right part) constructed and simulated through first-principles molecular dynamics methods. The spin density isosurfaces for α-states (blue) and β-states (pink) are highlighted. The organic parts, water and hydroxide molecules are transparent for the clarity of the Figure

studied through FPMD methods. We compute the pressure P applied on the system as the derivative of the total energy E_{Ham} with respect to the volume of the simulation cell V_{Cell}

$$P = -\frac{\partial E_{Ham}}{\partial V_{Cell}} \tag{2.106}$$

This pressure is applied following two different protocols. In the first we apply an isotropic pressure to seek for the structural ground state of the system by changing the lattice parameters. The second (anisotropic pressure) is detailed in the next chapter. In the isotropic case, we have to deal with a 6 dimensional space characterizing the crystal structure of a system ($\vec{a}_1$,$\vec{a}_2$,$\vec{a}_3$,α,β,γ), in which one has to minimize the total energy. We choose to restrain the problem taking into account the symmetries of the system and decoupling the ($\vec{a}_1$, $\vec{a}_2$ and $\vec{a}_3$) lattice vectors from the crystal's primitive cell angles (α, β and γ). We preserve the crystal symmetry by performing an isotropic reduction of the norm of the lattice parameters ($\vec{a}_1$, $\vec{a}_2$ and $\vec{a}_3$) so that the ratios between the lattice parameters remain unchanged during the compression. An increase of these lattice parameters simulates an extension of the cell in the three directions. Each step of this procedure provides a new atomic structure to study and for which we perform an optimization via simulated annealing.

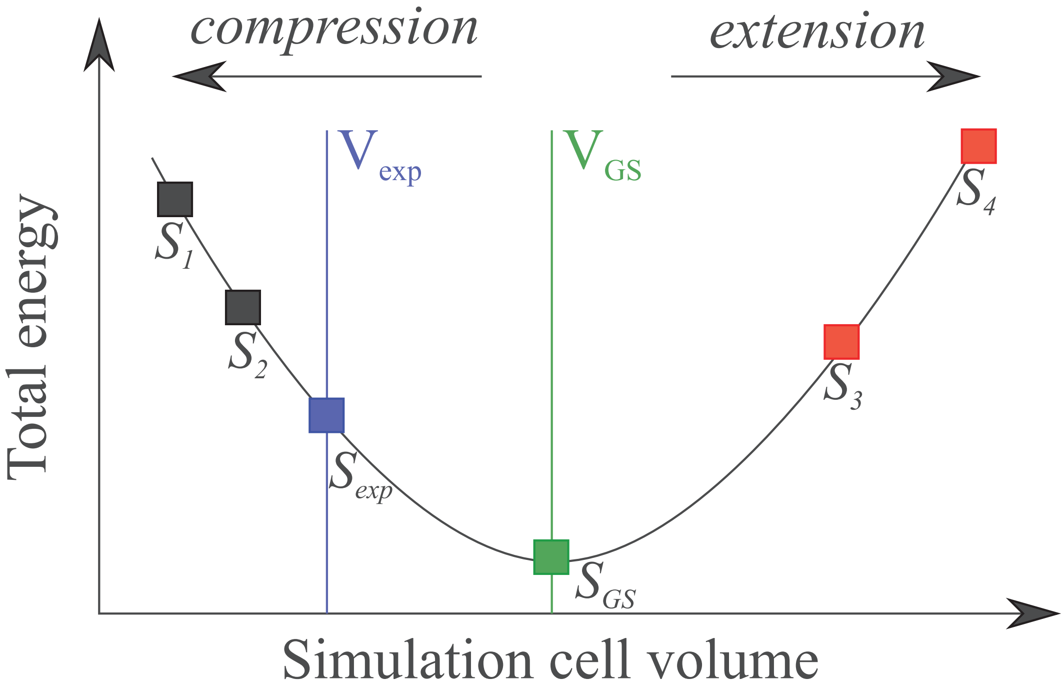

Figure 35 – Schematic representation of the evaluation procedure of the pressure applied on the simulated systems for the search of the structural ground state (P=0GPa). The total energy of the experimental system (S_{exp}) is the initial system, it is then compressed (systems S_1 and S_2) or expanded (systems S_3 and S_4) in the search of the optimized relaxed system (S_{GS}). Through an evaluation of the derivative of energy vs cell volume curve, we obtain an estimation of the pressure applied on the system (*see text*)

Therefore, we generate a set of systems with different calculated volumes in the space of the ($\vec{a}$, $\vec{a}_2$ and $\vec{a}_3$) parameters and obtain the behavior sketched in Figure 35. Two volumes are highlighted in the Figure and two opposite transformations (compression and extension). V_{exp} is the experimental system's cell volume (from XRD data) and V_{GS} is the structural ground state obtained through the compression procedure. The two systems S_1 and S_2 are at lower volume (positive pressures) compared to the experimental system. Conversely the systems S_3 and S_4 are the extended system with higher volumes than the experimental one. These type of "negative pressure" systems will be used only to obtain the structural ground state of the system (S_{GS}). In a second step, we vary the β angle keeping the ground state lattice parameters (corresponding to the system S_{GS}) obtained from the first step as well as the α and γ angles fixed. Finally, we obtain the β parameter that minimizes the total energy of the system.

In practice, the compression or extensions of the atomic structures are performed by normalizing all the atomic positions to a unity cell and then performing the isotropic transformations of the lattice parameter.

$$\begin{aligned}
\vec{a}_1^{\pm}(S_i) &= \vec{a}_1(S_0) \pm C \cdot \vec{a}_1(S_0) \\
\vec{a}_2^{\pm}(S_i) &= \vec{a}_2(S_0) \pm C \cdot \vec{a}_2(S_0) \\
\vec{a}_3^{\pm}(S_i) &= \vec{a}_3(S_0) \pm C \cdot \vec{a}_3(S_0)
\end{aligned} \tag{2.107}$$

where $S_i^{\pm}$ are the systems under the effect of positive (+) or negative (-) pressures with respect to the initial system S_0 and C is the percentage by which one reduces or increases the lattice parameters.

For clarity, the following chapters of results start by a figure summarizing the main lines of the subject followed by an abstract mentioning the core results obtained and a chapter outline

Chapter 3

Copper Hydroxide Acetate (CuOHAc)

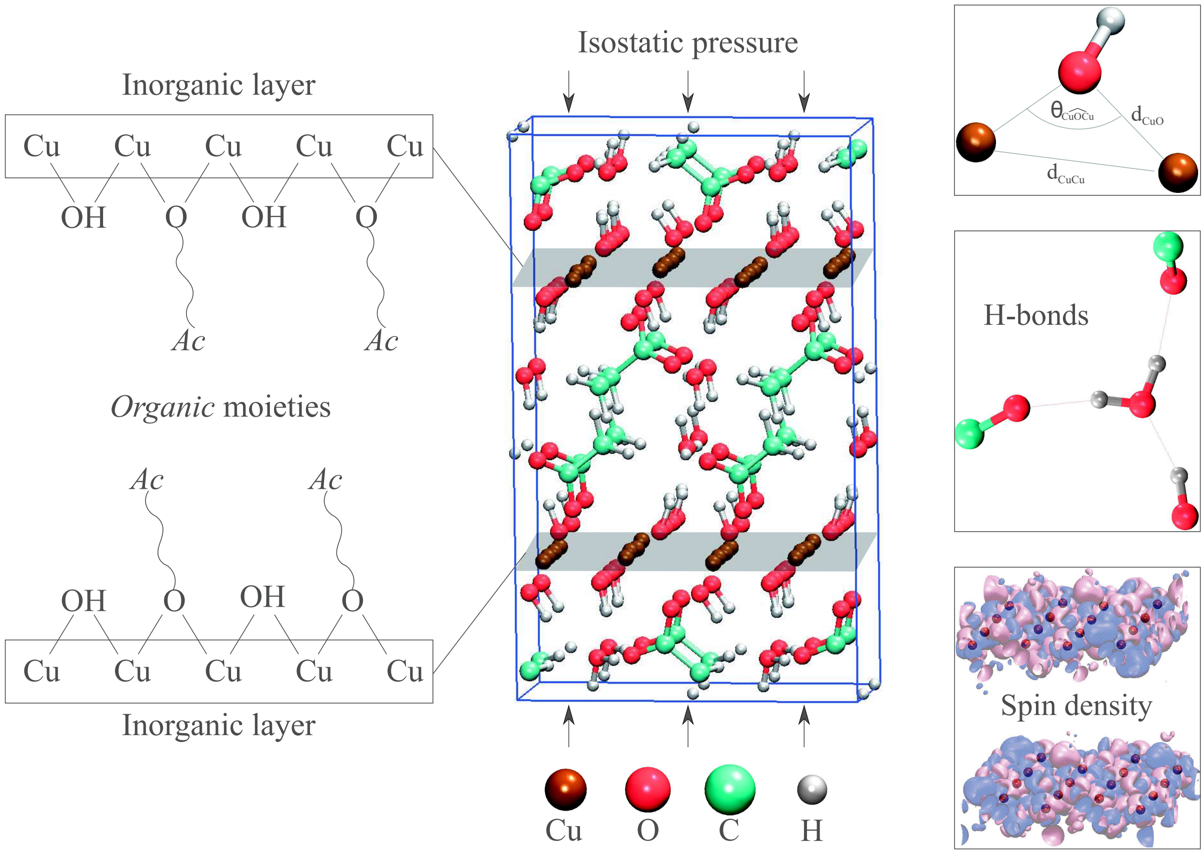

Figure 36 – Overview of our FPMD study of copper hydroxide acetate (CuOHAc). In the left part, a schematic representation of CuOHAc structure is proposed, highlighting the inorganic part (the two Cu layers) and the organic part (the interlayer acetate moieties). The dashed lines indicate the chemical bonding between the two components. In the central part, the corresponding simulation cell considered in our studies is represented. Water molecules are included in the structure since we study the hydrated form of this compound $Cu_2(OH)_3(CH_3COO)\cdot H_2O$. The black arrows indicate that we perform calculations applying an isostatic pressure, compressing the structure in the $\vec{c}$ crystallographic direction. In the right part, examples of the various properties investigated are given interatomic distances (d_{AB}), angles ($\theta_{A\hat{B}C}$), H-bonds and magnetic behaviors (spin density)

Abstract

The hybrid organic-inorganic material $Cu_2(OH)_3(CH_3COO).H_2O$ (CuOHAc) have been studied in terms of structural, magnetic and electronic properties by using first-principles molecular dynamics (FPMD[2]) calculations. A substantial improvement of the simulated magneto-structural response of this material is obtained, when comparing with the previous theoretical results [36, 7]. Spin densities are analyzed both on copper and oxygen sites to achieve a global description of magnetism in the layers and in the bulk. The detailed analysis of the atomic structure, the influence of pressure and the role of water molecules are detailed to understand the relation between magnetic and structural properties of copper hydroxide acetate. A transition from an anti-ferromagnetic to a weak ferromagnetic state is obtained through the application of pressure in the range 1.20 to 3.5 GPa. In view of the good agreement with the experimental findings (1.2 GPa [4]), we present the simulation protocol necessary to determine the pressure induced changes in such layered hybrid material.

3.1 Introduction and computational details

Organic-inorganic layered systems are a class of hybrid materials in which several types of organic chains can be inserted within the inorganic host architecture. Particular interest has been devoted to copper hydroxide acetate $Cu_2(OH)_3(CH_3COO){\cdot}H_2O$ abbreviated as CuOHAc. This system belongs to the family of $Cu_2(OH)_3X$ transition metal layered compounds where X is an exchangeable anion. Widespread interest stems from its tunable magnetic properties, strongly dependent on the nature of the interlayer organic spacers. Through FPMD, we simulate the effect of the external pressure on the microscopic structure of CuOHAc system. An X-ray powder diffraction study has led to a good characterization of the crystallographic structure of this material [89], making possible a set of previous theoretical investigations [36, 37, 7]. The aim of these studies was to identify a transition from an anti-ferromagnetic (AF) to a ferromagnetic (F) ground state when an external isostatic pressure is applied on the system as observed in experiments [4, 5, 12].

This work is a step further in the same direction, since we take advantage of a newly characterized CuOHAc single crystal structure. Svarcova et al [3] demonstrated that the structure of $Cu_2(OH)_3(CH_3COO){\cdot}H_2O$ could be solved in the non-centrosymmetric space group $P2_1$, in contrast with the centrosymmetric space group $P2_1/m$ originally suggested by Masciocchi et al [89]. Once the structure is optimized, we perform density of states and spin density calculations to have access to the electronic and magnetic properties. In contrast with the previous theoretical studies, we show that the pressure induced magnetic transition is observed only for an intermediate value of the total spin on the system. We shed light on a mechanism, based on the evaluation of the in-layer 2D magnetizations (copper layers) driving the promotion of the global ferromagnetic character observed for CuOHAc system when external pressure is applied. A full structural analysis is performed as a function of pressure indicating local changes in the chemical environments of the magnetic sites, favoring the 3D ferromagnetic behavior. Relevant Cu-O bond distances, $Cu\hat{O}Cu$ angles as well as Cu-Cu in-layer distances are correlated to give a precise picture of structural rearrangements in the system as function of pressure. Finally, estimations of the material's electronic gap are presented to corroborate the electronic structure analyses performed.

In the framework of first-principles molecular dynamics approach (CPMD package [2]), we use Kohn-Sham spin density functional theory (DFT) in the generalized gradient approximation due to Becke [38] for the exchange part and Lee, Yang and Parr [39] (BLYP) for the correlation functional. Valence electrons are treated explicitly while core-valence interaction is accounted for through norm conserving pseudo-potentials generated following the scheme of Trouiller and Martin [46]. In addition, non-linear core corrections [40] (NLCC) are included (introduced in the precedent chapter). The simulation cell used contains 288 atoms (32 Cu, 96 O, 32 C, and 128 H), and periodic boundary conditions are applied in the three directions. Such supercell is the result of doubling the primitive cell of 72 atoms along x and y directions. The new lattice parameters are therefore $a = 11.1552$ Å, $b = 12.1466$ Å, $c = 18.5134$ Å and $\beta = 91.802$ °. The wave functions are expanded at the Γ point of the supercell and a plane wave basis set is used with an energy cutoff of 90 Ry. As explained in the second chapter, a constraint on the total spin state (S) can be applied so that we can fix the total spin during the DFT calculations. We study four different magnetic states characterized by total spin values S = 0 and S = 16 for the limiting anti-ferromagnetic and ferromagnetic states respectively as well as two intermediary cases with S = 8 and S = 12.

Following previous investigations [37, 7], we used a randomization procedure applied on the starting wavefunctions (electronic degrees of freedom) in order to produce different spin topologies corresponding to distinct electronic ground states. For these multiple minima configurations, one obtains different values of the local in-layer spin Σ (where Σ=0 refers to the AF-in and Σ ≠0 to the F-in intralayer magnetic character) corresponding to an identical total spin S. The exploration of the multiple minima landscape and spin topology analysis is performed systematically in the relevant pressure range (0 to 8 GPa). The methods employed for the pressure application are detailed, for the isotropic case, in chapter 2 and will be used to identify the structural ground state of our system. For each system considered, the pressure is computed by fitting the total energy E_{Ham} of the system as a function of the volume V of the simulation cell following the definition P_{ext} = -$\partial E/\partial V$. In addition, a second procedure, taking into account experimental measurements of the pressure-induced lattice parameters changes, is introduced to allow for comparisons of our simulations to experimental results.

3.2 Pressure-induced magnetic transition

Our theoretical investigation is based on the experimental atomic structure provided by Svarcova et al. [3]. The main differences with the previously synthesized structures [89] are: the synthesis procedure, the new set of lattice parameters given for two different temperatures and most importantly a new space group assignation. Therefore we focus, at first, on the crystal structure determined from single-crystal X-ray diffraction data, characterized both at 120K and 293K. We employ the Nosé-Hoover thermostat [150, 151], to reproduce the experimental temperature conditions. We could confirm the stability of the structure simulated at finite temperature through the comparison between experimental and simulated Cu-O distances. We present, in the main plot of Figure 37, a comparison between Cu-O distances of a system based on the characterizations provided at 120K (Svar$_{120K}$ in blue) and at 293K (Svar$_{293K}$ in red). The dashed line and black diamonds are the experimental distances. The exact deviations (in percentage of the distances) are in the form of a bar plot showing the six distances from each Cu site to his neighboring oxygen octahedron. These data are averaged over the replicas (the 4 copies of the 72 atoms original system) providing the error bars represented in the inset. Concerning the simulated data for both temperatures, 293K and 120K, we obtain an overall deviation of simulated points from the experimental reference of about $\simeq$ 2.5%, which ensures that the structure used is a good starting point for studying the material properties.

In Figure 37, we note two groups of points, localized around 2.0 Å characteristic of hydroxide linked oxygen atoms and another population in between 2.3 and 2.45 Å, mostly representative of acetate linked oxygens. In addition, we note that simulated data corre-

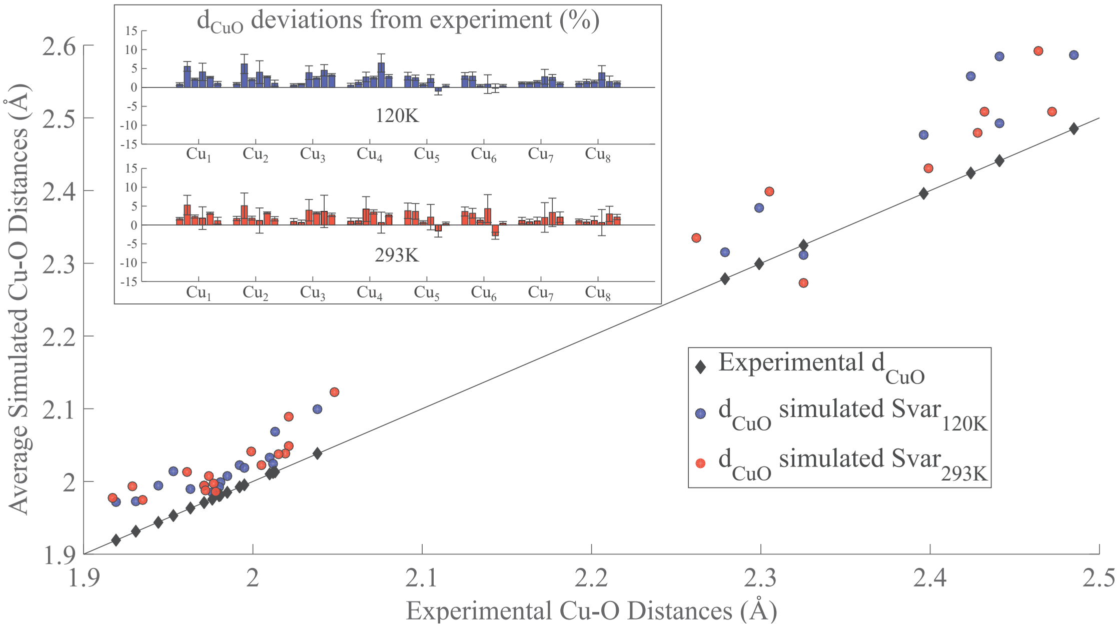

Figure 37 – Simulated Cu-O distances compared to experimental ones (black diamonds and dashed line) for finite temperature molecular dynamics calculations (red squares for 293K and blue circles for 120K). The inset shows the detailed distances deviations from experimental values for both systems.

sponding to the T=120K structure present slightly smaller deviations from experimenst than the system at 293K. In the inset of Figure 37, we report the detailed deviation from the corresponding experimental values (in percent), accompanied by the error bars of the averages performed from the replicas. Based on the comparison between the standard deviations (SD) calculated for both systems ($SD_{120K} \simeq 0.88\%$ and $SD_{293K} \simeq 1.51\%$), we choose to perform all the following investigations according to the lattice parameters corresponding to the T=120K structure.

The main purpose of this work being the study of the magnetic properties as function of external pressure, the first step is to obtain a system with no mechanical constraints on the volume (at $P_{computed} = 0$ GPa). To obtain the equation of state for CuOHAc system, we perform a total energy analysis as a function of different values of the lattice parameters ($\vec{a}$, $\vec{b}$, $\vec{c}$, β). This is achieved by performing contractions and expansions of the system from the initial experimental structure. We choose to conserve the symmetry of the system through this procedure, keeping the cell parameters ratios (b/a and c/a) constant and the angle β fixed at its experimental value (main plot in Figure 38). In a second step, the optimal lattice parameters $\vec{a}$, $\vec{b}$ and $\vec{c}$ (corresponding to V_{opt}) are fixed while the β angle is optimized separately (inset in Figure 38). Thus, we obtain the total energy of the system, evaluated as a function of the volume corresponding to different β-angles of the simulation cell. Each of the points appearing in the main plot (Figure 38) is obtained after 7.7 ps of relaxation of the structure. The systems are damped to temperatures lower than 0.01K which ensures stable structures. We note that the optimal lattice parameters and β angle values are identical for the ferromagnetic (S=16) and antiferromagnetic (S=0) configurations considered in this process. An optimized structure

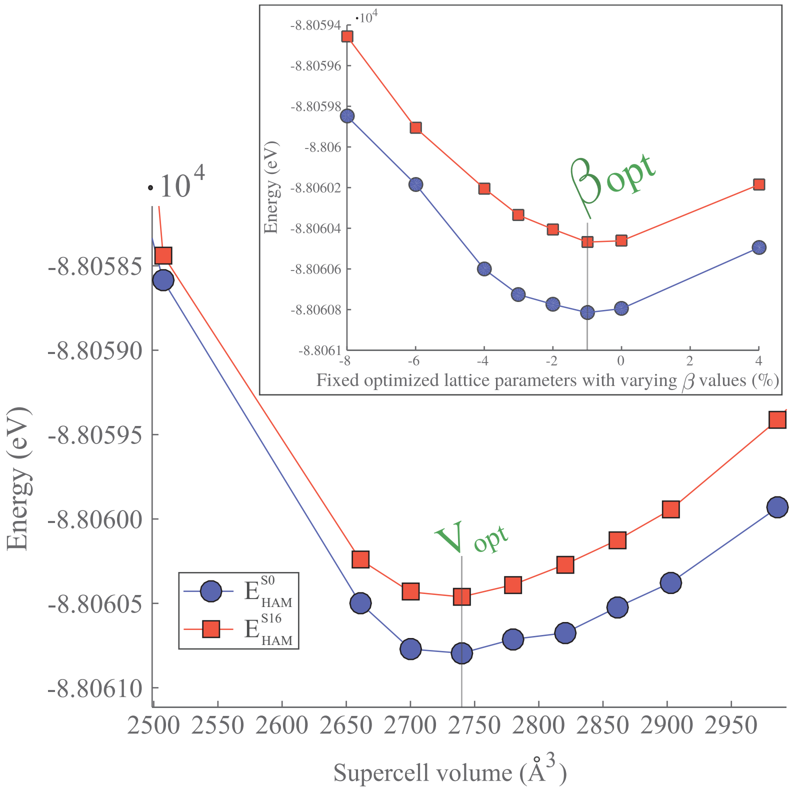

Figure 38 – **Main plot**: copper hydroxide acetate total energy computed as a function of the volume of the primitive cell considered for extremal magnetic configurations (AF–S_0 and F–S_{16}). Red squares and blue circles correspond respectively to the ferromagnetic ($S=16$) and anti-ferromagnetic ($S=0$) configurations. **Inset**: total energy as function of the β angle lattice parameter for both AF (blue circles) and F (red squares) states

being obtained, the application of pressure on the system is performed by following the deformations observed in experiments as indicated in Figure 39. The top part of the Figure shows the lattice parameters obtained by Suzuki et al. [4] when isostatic pressure is applied on the crystalline CuOHAc system. The bottom part corresponds to the actual parameters used in our simulations with a supercell expanded twice in the $\vec{a}$ and $\vec{b}$ directions. Through this procedure, we use experimental data to extract coefficients of contraction of the lattice parameters to study the effect of pressure on the system. Therefore, in the rest of this project, the initial structure considered is the one proposed by Svarcova [3] and coworkers but the pressure effects are based on an extrapolation, to high pressures range, of the deformations of the lattice observed by Suzuki et al. [4].

In addition to the AF (S_0) and F (S_{16}) configurations, two intermediary magnetic states of CuOHAc system are considered with total spin $S = 8$ (S_8) and $S = 12$ (S_{12}). However, the structural optimization is not affected by the choice of the magnetic configuration. Thus, similar optimized simulation cells have been used for evaluating the relative stability of different magnetic configurations. In the framework of FPMD studies, this optimization process has to be accompanied by a suitable choice of the simulation cell, being a trade-off between the number of atoms to be included and the computational resources available. In our case, the choice of the supercell size is guided by previous studies highlighting the interest of the use of an expanded cell for the analysis of different

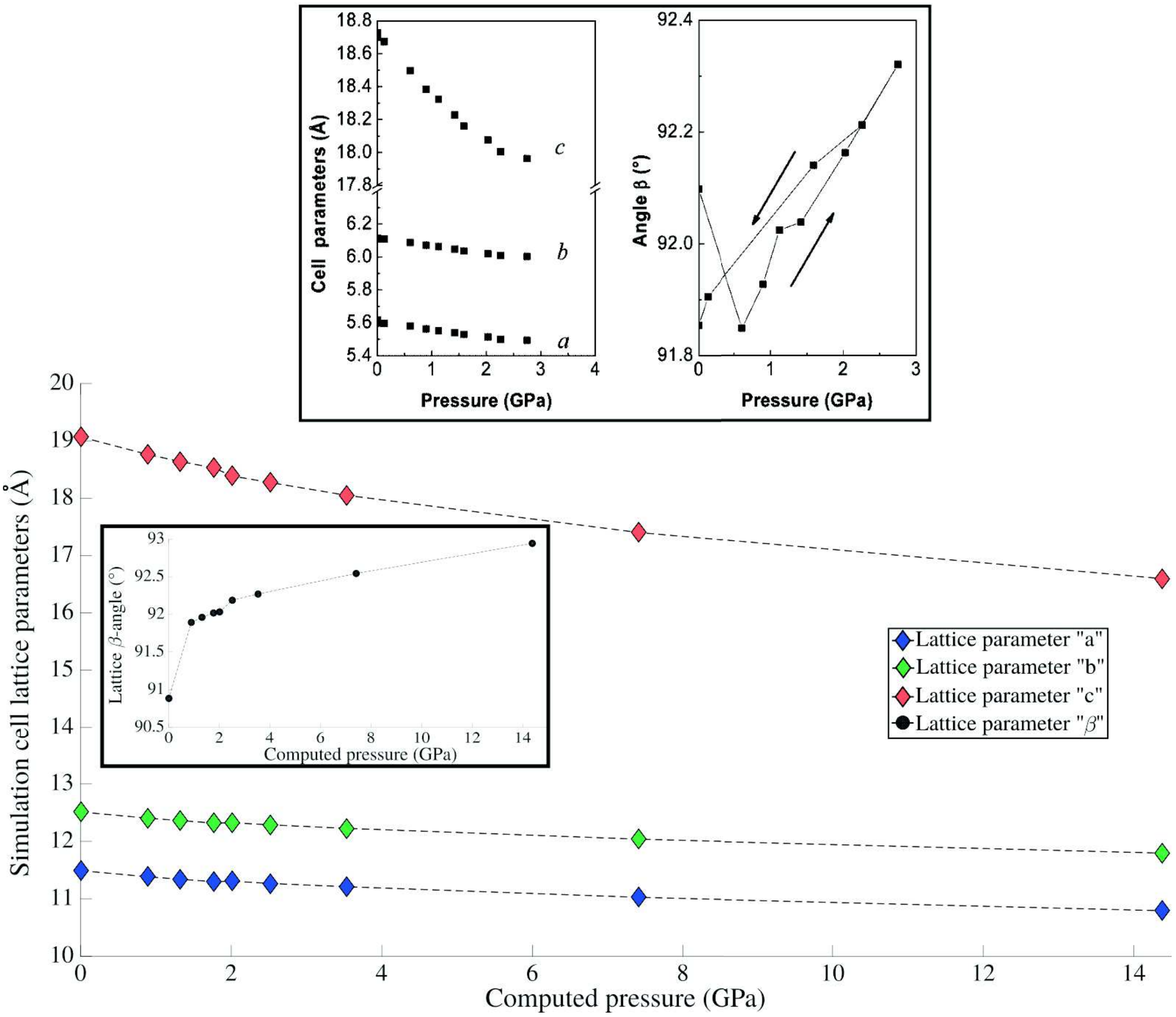

Figure 39 – **Top part:** Experimental cell deformations under application of pressure on copper hydroxide acetate compound *adapted from [4]*. **Bottom part:** Simulated supercell lattice parameters used for the purpose of our study of CuOHAc system. *Crystallographic data from [3]*

magnetic orders [7, 36]. Through the minimization of the total energy of the system within the DFT scheme, we compute the electronic ground state for different sizes of the system. We, thus, obtain an energy versus supercell volume curve presented in the inset of Figure 40 in which we identify the structural ground state of the material corresponding to the 0 pressure system at a volume of 2741 Å^3. For the rest of this work, we study only systems with cell volumes smaller than this structural ground state, that is, positive pressure effects. Our interest in the four magnetic configurations considered stems from the nature of the magnetic transition under pressure found experimentally [4] which indicated the appearance of a weak ferromagnetic behavior rather that a full ferromagnetic one. Through FPMD simulations, we quantified the total energy difference (relative stability) of the different magnetic states of this compound. In the main plot of Figure 40, we represent these energy differences $\Delta E_{i,j} = E(S_i, P_j) - E(S_0, P_j)$ with respect to the pure AF configuration (dashed line), as a function of pressure. We observe that both the fully ferromagnetic configuration (red squares) and the intermediary one with total spin S_{12} (green diamonds) remain less stable systems, relative to the AF configuration, for the entire pressure range studied. Remarkably, from 1.2 to 3.5 GPa, we see a clear competition between the AF configuration and the S_8 one (yellow pentagrams in Figure 40). In addition, at higher pressures, the material's ground state becomes permanently associated with this weak ferromagnetic behavior as observed in Figure 40 for $P > 3$ GPa. Error bars are produced from the randomization procedure applied on the initial electronic orbitals. Seventeen systems are produced with the same relaxed atomic structure enabling an exploration of the various spin topologies compatible with a fixed total spin of the simulation cell. From Figure 40, we see that the fully spin polarized structure (red squares) converges always to the same minimum energy (tiny error bars). In contrast, the abundance of spin distributions allowed by the spin state S=8 (or S=12) make the procedure to converge to values that can be found to lay within 0.05 eV. A detailed analysis of the S_0 and S_8 configurations and the identification of the most stable spin topologies are therefore necessary steps to understand the origin of this pressure induced magnetic transition. This route is also fostered by the fact that the half spin polarized system S_8 shows a simulated transition pressure in a range (1.2 to 3.5 GPa) close to the experimental value 1.2 GPa reported by Suzuki et al. [4].

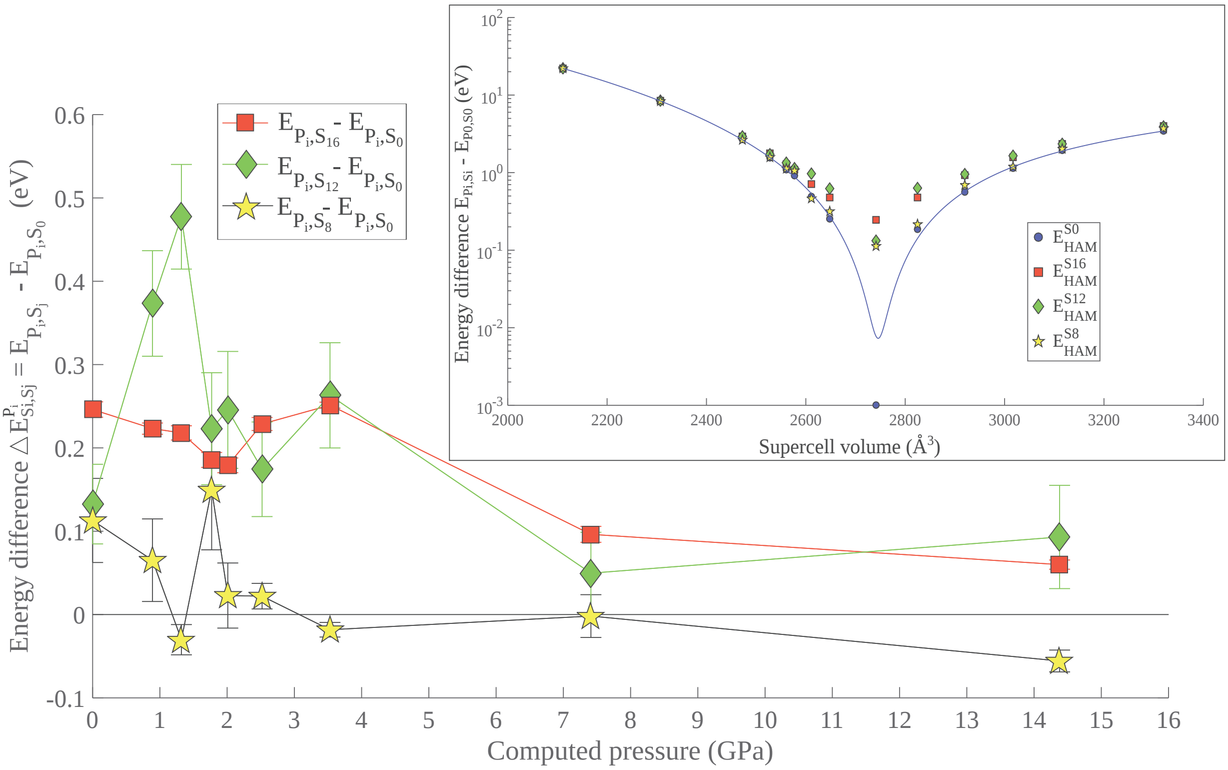

Figure 40 – Relative stability of the two intermediary magnetic states (S=8 and S=12) and the fully ferromagnetic systems (S=16) compared to the Anti-Ferromagnetic (dashed line) ground state (S=0). *Inset*: Equation of state of the structures considered $E_{tot}(V_{SuperCell})$

Our results are compared to the calculations performed by Fan Yang et al. [7] within the BLYP *xc*-functional framework and based on the Masciocchi characterizations of the CuOHAc structure [89] in the following table (Figure 41). This table highlights the systems studied in the present work. The computed pressures are evaluated through the fit of the energy vs volume, that provides an estimation of the pressure vs volume equation of state corresponding to this system (Appendix B Figure 82).

	Previous works *Masciocchi, N., et al. JSSC (1997)* *Yang, F., et al. JPCC (2014)*			Present work *Švarcová, S., et al. CRT (2011)* *Chaker, Z., et al. BJNANO (2017)*		
$P_{exp.}$ (GPa)	$P_{comp.}$ (GPa)	$\triangle E^{P_i}_{S_2,S_0}$ (eV)	$\triangle E^{P_i}_{S_4,S_0}$ (eV)	$P_{comp.}$ (GPa)	$\triangle E^{P_i}_{S_8,S_0}$ (eV)	$\triangle E^{P_i}_{S_{16},S_0}$ (eV)
0,00	0,18	0,51	1,40	0,00	0,11	0,25
				0,89	0,06	0,22
				1,32	-0,03	0,22
2,03	3,32	0,50	0,77	1,77	0,14	0,19
2,75	3,42	0,48	0,62	2,01	0,02	0,18
3,00	3,60	0,49	0,71	2,52	0,02	0,23
5,00	4,35	0,35	0,43	3,53	-0,02	0,25
7,50	5,80	0,09	0,17	7,41	-0,01	0,10
				14,38	-0,06	0,06

Figure 41 – Comparative table of the energetics properties obtained in the present work with previous FPMD studies performed within the BLYP framework [7] relying on the copper hydroxide acetate characterization performed by Masciocchi et al. [89]. The experimental pressure (P_{exp}), the computed one (P_{comp}) and the energy of two ferromagnetic states (E_{S_2}, E_{S4} in previous papers and E_{S8}, E_{S16} in the present work) relative to the AF ground state energy (E_{S0}) are reported. Negative values $\Delta E^{Pi}_{Si,Sj}$ correspond to magnetic configurations becoming more stable that the AF reference system.

The competition between the intermediate magnetic state (S=8) and the antiferromagnetic (S=0) configuration appears clearly in the table, in which the energy difference takes positive and negative signs alternatively in between 1.32 to 2.52 GPa of applied pressure. If one continues compressing the system ($P > 3$GPa), the stable ferromagnetic S_8 configuration is stabilized even more. The question arises on the origin of such phenomenon knowing that the atomic structure of these systems is relaxed. In particular, we would like to understand how the deformations of the organic parts and the compression of the Cu layers participates in stabilizing the 3D ferromagnetic character of the system. Therefore, in the next section, we investigate the magneto-structural properties of copper hydroxide acetate in detail. We choose to first investigate in the structural deformations in order to describe the various local environments within the cell. Then, we highlight eventual correlations between the structural analysis and the spin density analysis in order to propose a mechanism underlying the pressure-induced magnetic transition.

3.3 Magneto-structural couplings

3.3.1 Structural properties

As shown by the cell pictured in Figure 36 based on the experimental structure [3], the tilting of the distorted oxygen octahedra surrounding the copper sites favors a threefold coordination of these oxygens. This fact makes redundant a structural analysis based on copper sites, because of double counting. We rather focus on the oxygen atoms shared and analyze the tetrahedra they form with their three copper nearest neighbors. A full set of these structural data as function of pressure is provided in Figures 83, 84, 85 and 86 of Appendix B. The analyses of copper-oxygen bonds (Cu-O) and copper-oxygen-copper angles ($Cu\hat{O}Cu$) as a function of pressure are summarized here through the use of an averaging procedure to reduce the amount of data to be considered. Our supercell contains

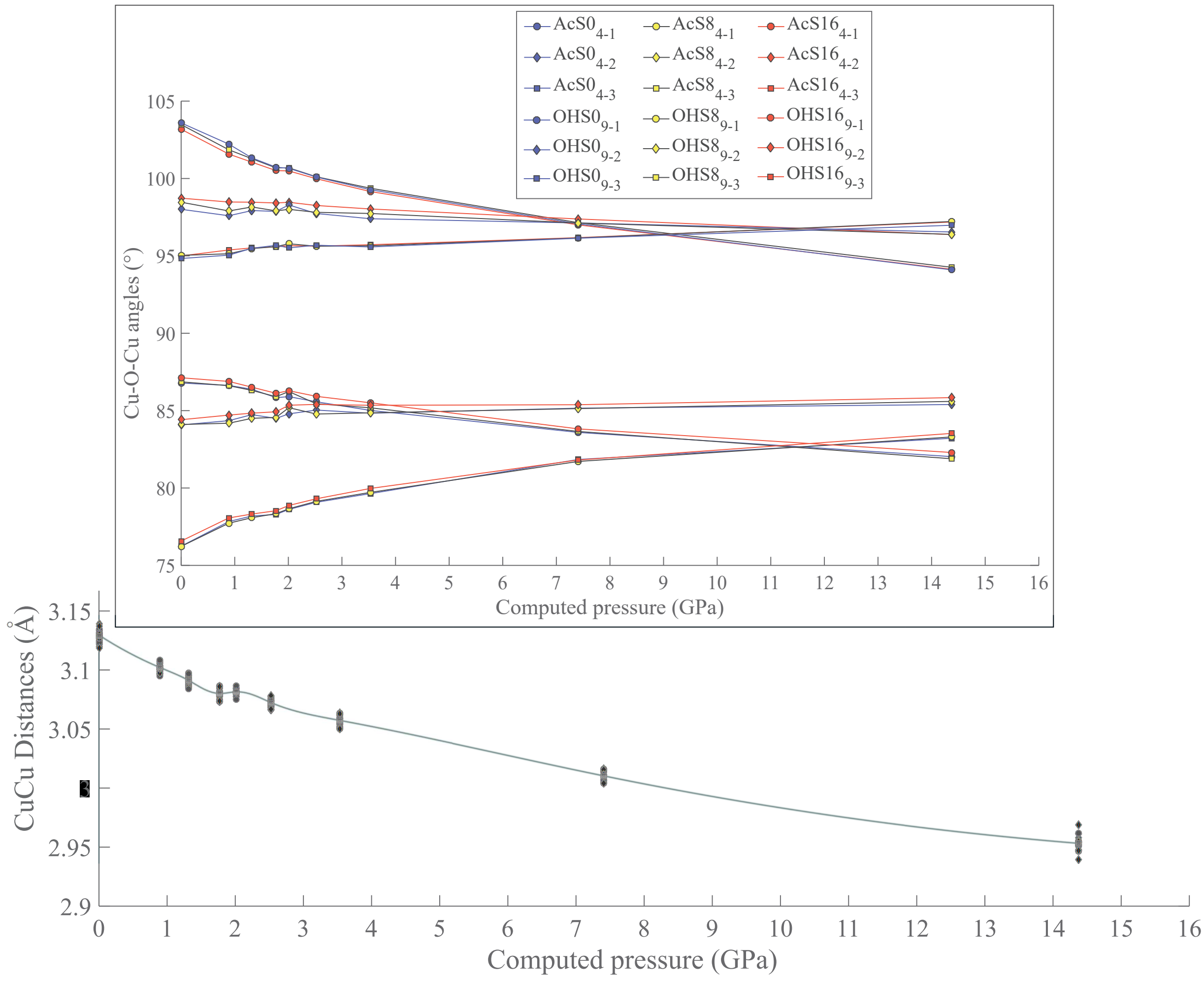

Figure 42 – **Top plot:** Evolution of the $Cu\hat{O}Cu$ as a function of pressure of the 3Cu-coordinated oxygen atoms linked to acetate molecules (solid lines) and hydroxide molecules (dashed lines) for three magnetic states: S_0 (blue circles), S_8 (yellow diamonds), S_{16} (red squares) for copper hydroxide acetate system. **Bottom plot:** evolution of the corresponding Cu-Cu distances as function of pressure

288 atoms from which 96 are oxygens, 64 from these are coordinating the copper layers

and the remaining 32 are contained within acetate or water molecules. Then, 16 out of the 64 coordination ones are linked to acetate molecules and 48 to hydroxide groups, evenly distributed among the two copper layers. Using the fact that our simulation cell contains 4 replicas of the primitive cell (72 atoms), we average the structural information on the replicas and thus obtain 4 O atoms linked to acetate molecules (OAc) and 12 are linked to hydroxide molecules (OH). Then, we select the angles and distances showing the strongest variations under pressure application and we converge to the choice of the specific structural data shown in the Figure 42. In this figure, we show $Cu\hat{O}Cu$ angles variations as function of pressure, with the corresponding Cu-O distances provided in Figure 87 of Appendix B. These local rearrangements of the copper hydroxide layers do not depend on the magnetic state considered since we observe very similar, if not identical, structural behaviors for all magnetic CuOHAc systems. The S_{12} system is omitted since its structure shows the same changes as the S_8 case. In terms of $Cu\hat{O}Cu$ angles, we observe that the acetate molecules are mostly affected by the pressure (top part of Figure 42) and the same in the case of Cu-O(acetate) distances ($\Delta_{CuO} \sim 0.4$ Å), while smaller deformations are obtained in the case of hydroxide linked oxygens (up to 0.2 Å). We note a change of slope in the transition region (1.5 to 3 GPa), related to critical distances reached between neighboring copper sites ($d_{CuO} \simeq 2.32$ Å and $d_{CuO} \simeq 2.03$ Å, Figure 87).

The corresponding variations in the Cu-Cu distances as a function of pressure are presented in the bottom plot of Figure 42. We report the full set of in-layer Cu-Cu distances in Figure 88 of Appendix B. A clear tendency of reduction of these distances is observed with a visible change of slope correlated to the one obtained for Cu-O-Cu angles between 1.5 and 3 GPa. The black line highlights this fact, knowing that we used a guide-to-the-eye fit performed on a representative set of Cu-Cu distances. These averaged distances take values in between 3.15 Å (low pressure) and 2.97 Å (high pressure). When compared to previous experimental work of Suzuki et al.[4] (3.25 Å to 3.1 Å), a good agreement is found.

To complete this picture, in the table 90 of supplementary materials, we picked up two specific oxygen atoms (O_{81}-hydroxide and O_{79}-acetate) in the structure. As a function of pressure, we observe a diminution of the Cu-O(hydroxide)-Cu angle, accompanied by a decrease of the associated Cu-Cu distance, while the Cu-O(hydroxide) distances remain unchanged. Interestingly, an increase of the Cu-O(acetate)-Cu angle is obtained. This is associated with an important decrease of Cu-O(acetate) distances and a decrease of Cu-Cu distances. This situation is explained by the deformation of the corresponding distorted CuO_6 octahedron in the sense of a reduction of the axial distance Cu-O between the inorganic layer and the "anchoring" oxygen of the acetate group.

To summarize the outputs of this structural study, we show that acetate and hydroxide molecules are highly affected by the pressure perturbing the inorganic network in a way that favors ferromagnetic behaviors for the copper layers. The abrupt changes visible on all set of structural data as a function of pressure indicate a correlation, in the transition pressure range, between the deformation of the chemical environments of the two copper hydroxide layers and the magnetic interactions. To elucidate the link between Cu layers perturbation by pressure and the ferromagnetic behavior promotion, we went on to study the local spin density distributions in the system, characteristic of each pressured system.

3.3.2 Magnetic properties

We use the local spin density analysis to understand the origin of the structural and energetic properties observed in the magnetic transition pressure range. In order to understand the promotion of 3D ferromagnetism, we analyze the local Cu spin densities and a variety of spin topologies are obtained for each pressure and for each total spin value imposed on the primitive cell. Since a randomization of initial conditions for electronic degrees of freedom is considered, many spin topologies are found to correspond to local minima close to the electronic ground state for a given pressure value. An overview of the early results relative to this analysis have been published in a peer-reviewed journal [47] and are completed in this section. Nevertheless, a summarizing Figure of the main results of this investigation of spin density distributions as function of pressure, is provided in Appendix B (Figure 91).

In Figure 43, we show the difference between the two copper layers magnetization ($\Delta\Sigma^S_{l_1 l_2}$=$\Sigma^S_{l_1} - \Sigma^S_{l_2}$), quantifying the 3D ferrimagnetic character in the system. In fact, if the two layers show identical magnetization amplitude with opposite sign, then $\Delta\Sigma^S_{l_1 l_2}$=0 with $\Sigma^S_{l_1} = -\Sigma^S_{l_2}$ and a 3D anti-ferromagnetic (AF) configuration is obtained. In contrast, with equal finite spin polarization ($\Sigma^S_{l_1} = \Sigma^S_{l_2} \neq 0$) and $\Delta\Sigma^S_{l_1 l_2}$=0, 3D ferromagnetism is obtained. In the intermediate configuration, both layer sustain different finite magnetization values $\Sigma^S_{l_1} \neq \Sigma^S_{l_2}$ resulting in a ferrimagnetic configuration (WF).

Three pressure ranges are considered, showing distinct magnetic behaviors. From 0 to 1 GPa, there is the region in which the AF case is clearly the most stable configuration. Nevertheless, both the AF (S_0) and the WF (S_8) systems tend toward a nonzero equal magnetization among the two layers of the simulation cell. An increase of pressure allows a redistribution of spin density favoring AF interactions within the layers and thus characterized by a decrease of $\Delta\Sigma^S_{l_1,l_2}$. The competition for stability starts at 1.2 GPa (in region II). We see, at first, an increase of the inter-layer spin polarization ($\Delta\Sigma^S_{l_1,l_2}$) in the S_0 case while for the S_8 system, it remains close to 0. At 2 GPa, a drop of this 3D spin polarization of the S_0 system is observed but followed by a final increase and a high spin polarization value is obtained at 3.5 and 7.5 GPa (Figure 43- region II and III). For the S_8 system in region II, an increase of the unbalance between the two layers magnetizations is immediately followed by a decrease and a stabilization of a spin density distribution favoring 3D ferromagnetism. This is characterized by the establishment of similar Σ_{IN} among the two copper layers. The opposite behavior observed for the S=8 and S=0 magnetic configurations (S_0 and S_8) is consistent with the competition for stability observed between the two systems, in the energies analysis (Figure 40) within the transition region.

Many spin topologies are obtained for each of the systems considered in the plot of Figure 43. We included, in the top part of Figure 43, snapshots of the spin density distributions of α-states (blue solid surfaces around copper sites) and β-states (green solid surfaces) obtained from the randomizations procedures. We only focus on the system of lowest total energy at each pressure value (Figure 40) and choose the spin configurations that are most often found at this pressure. In the first region (top Figure 43-I), the S_0 systems analyzed show mostly finite magnetizations within copper layers but of opposite sign for both layers as pictured in the example denoted S0-a. In the AF to F transition region (II), we picture the four dominant distributions obtained for the S_0 and S_8 sys-

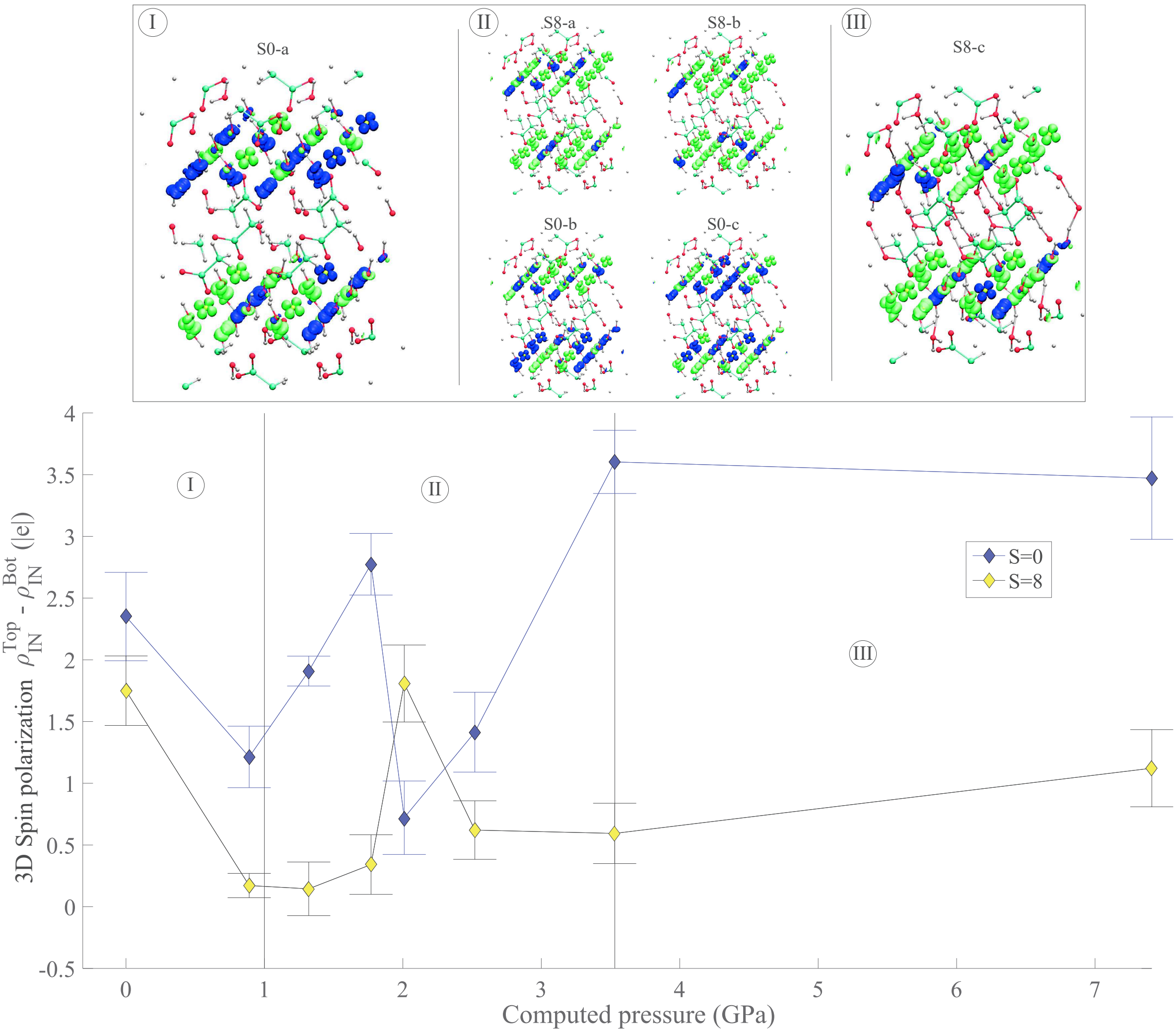

Figure 43 – **Top part:** Isosurfaces of spin density (±0.03 |e|) of α-spin (blue) and β-spin (green) of copper hydroxide acetate material in different pressure regions (I: 0 to 1 GPa, II: 1 to 3.5 GPa and III: 3 to 7.5 GPa). **Bottom part:** Differences in in-layer magnetizations ($\Delta\Sigma^{S}_{l_1 l_2}$) between the top and bottom Cu-layers in CuOHAc structure as a function of pressure for the antiferromagnet system (S = 0 in blue) and for the S = 8 system in yellow symbols.

tems since a competition between the two systems occurs. In the cases S8-a and S8-b, we obtain respectively the highest and lowest values of $\Delta\Sigma^{S}_{l_1 l_2}$ considered in the graph as function of pressure (Figure 43-bottom part). In the same scheme, we show spin density configurations corresponding to the high (S0-b) and low (S0-c) in-layer spin polarizations obtained for the S_0 system. As the total energy of the S_8 system gets lower and the transition occurs, the S_8 system stabilizes in a configuration favoring similar values of copper layers magnetizations in the primitive cell (case S8-c in Figure 43).

The two magnetic configurations, characteristic of low pressure CuOHAc anti-ferromagnetic and high pressure ferromagnetic characters, are considered in more details. We focus on the analysis of oxygen atoms coordinating copper layers and the spin density eventually

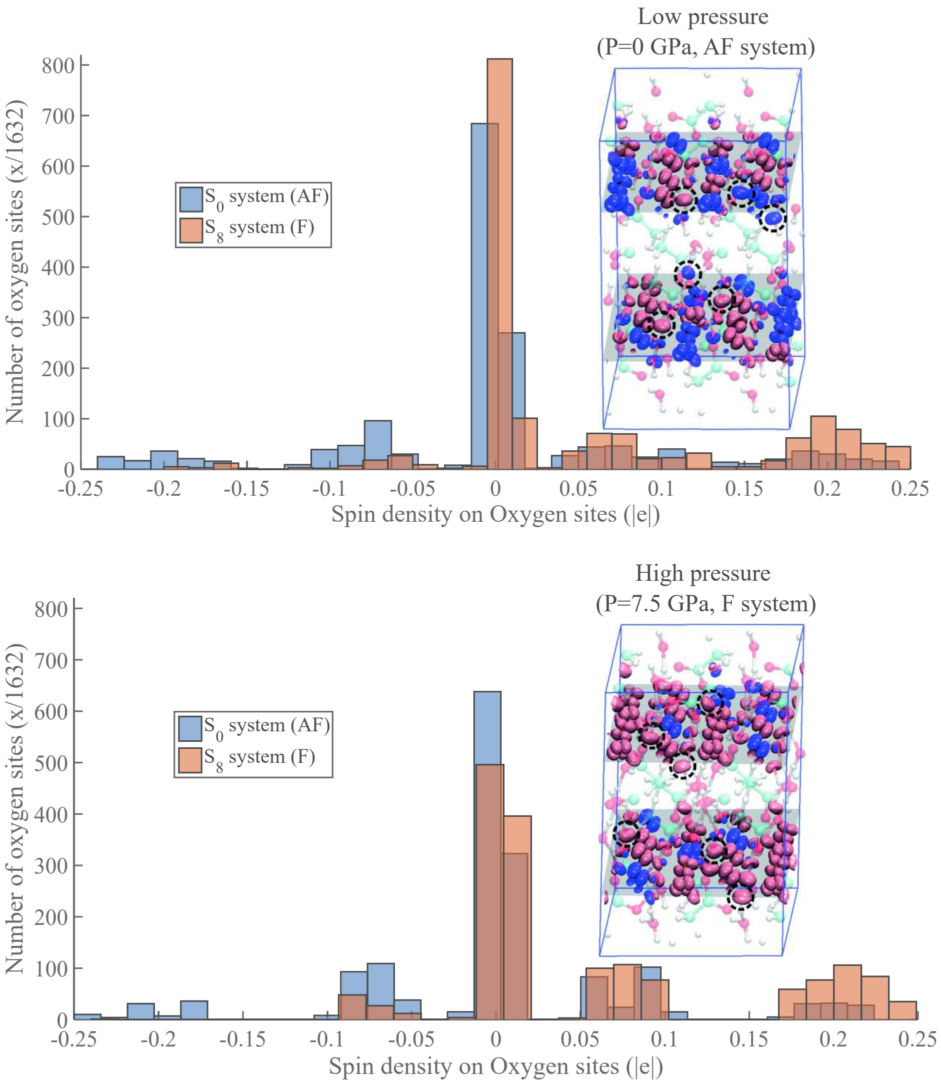

Figure 44 – Histogram representation of the 1632 oxygen atoms considered in the 17 spin configurations obtained for the low pressure (P = 0 GPa, the top bar plot) and the high pressure (P = 7.5 GPa, the bottom bar plot) copper hydroxide acetate systems. The two magnetic states considered are the anti-ferromagnetic one AF with total spin S=0 (blue bars) and the ferromagnetic one identified to be the most stable at high pressures, the S=8 system (red bars). These data are accompanied by snapshots of the corresponding simulation cells, highlighting the specific oxygen sites with the highest values of local spin density

present on these sites. A correlation can be drawn between structural deformations and the magnetic transition observed through the observation that the presence of spin density on oxygen sites is fostered by the application of pressure on the system. In Figure 44, we report the spin density (in electron units |e|) results obtained from the projection on oxygen atomic orbitals. As mentioned earlier, for the two pressure systems selected (0 pressure and high pressure 7.5 GPa), 17 randomized initial conditions are considered in the wavefunctions optimization. Therefore, including all oxygens of the structures (96) corresponding to the 17 configurations considered leads to statistics on 1632 oxygen atoms. This is performed for the AF case (S=0), in blue bars in Figure 44, and for the ferromagnetic case (S=8) in light red. Focusing on the top (low pressure) bar plot, we observe that a majority of oxygen atoms do not participate to the spin polarization of the system (main peak at 0 |e|). Two differences with the F configuration (S=8) are highlighted. First, there is a majority of α spin polarization in the latter, this being consistent with the total spin constraint imposed on the system. We also see that the number of oxygen atoms sustaining a large spin polarization ($\simeq 0.2$ |e|) is more important in the S=8 case. The bottom bar plot in Figure 44 shows the same result for the high pressure systems. The main output is that the central peak (at 0 spin polarization) is reduced in the S=8 case even more than in the AF state so that more spin density is obtained on the oxygen sites in the system. In addition, in this semi-quantitative analysis, we represent in both pressure conditions a snapshot of the CuOHAc structure with the corresponding spin density isosurfaces at 0.02 |e|. Besides, the majority of spin densities observed to be on copper sites (shaded planes), and it is clearly visible that no spin density is obtained on the acetate linked oxygen atoms. All the spin polarized oxygens instead correspond to the hydroxide molecules coordinating the copper layer. The condition that three copper neighbors of an oxygen, having all three the same spin polarization induce a share of spin density with this oxygen atoms is highlighted by dashed circles in both low and high pressure structures snapshots. These results are representative of the magnetic behavior of the copper hydroxide layers in CuOHAc. When pressure is applied on the system, a share of spin density is established between copper sites and their closest oxygen environment which are the oxygens of hydroxide molecules. The reduction of Cu-O distances in the systems favors this phenomenon. Such deformations are favoring specific patterns of exchange interactions resulting in trigonally arranged Cu-sites showing the same spin density sign (α or β spin density) and inducing the spin polarization of neighboring oxygen sites.

3.3.3 Electronic properties

Our first-principles calculations allow us to compute the electronic density of states (DOS) of the electronic ground state of the material at different pressures. Despite the well-known systematic underestimation of the band gap from DFT-GGA methods [48], we propose to focus on the band gap variation as a function of pressure for the two magnetic configurations relevant for our study, namely S_0 and S_8. In Figure 45 (bottom part), the bang gap of the material is evaluated for each pressure system and averaged over the 17 realizations obtained from the randomization procedure, resulting in the error bars reported. We obtain the highest values of band gap at high pressures and important variations in the transition pressure range for both S_0 and S_8 systems. The S_8 configuration stabilizes at a larger band gap value than the AF system at high pressures indicating that the pressure-induced magnetic transition is accompanied by the increase of the insulating character of the material. The stable state of CuOHAc is S_0 at low pressure and S_8 at high pressures. The density of states realizations for both situations are pictured in the top part of Figure 45. The insets are highlighting the bang gap region in order to visualize the effects of pressure on the localization of the highest occupied and lowest unoccupied states. The eigenvalues range (0.8 eV) is identical in both insets to facilitate the comparison. In addition, the symmetric nature of the up and down density of states

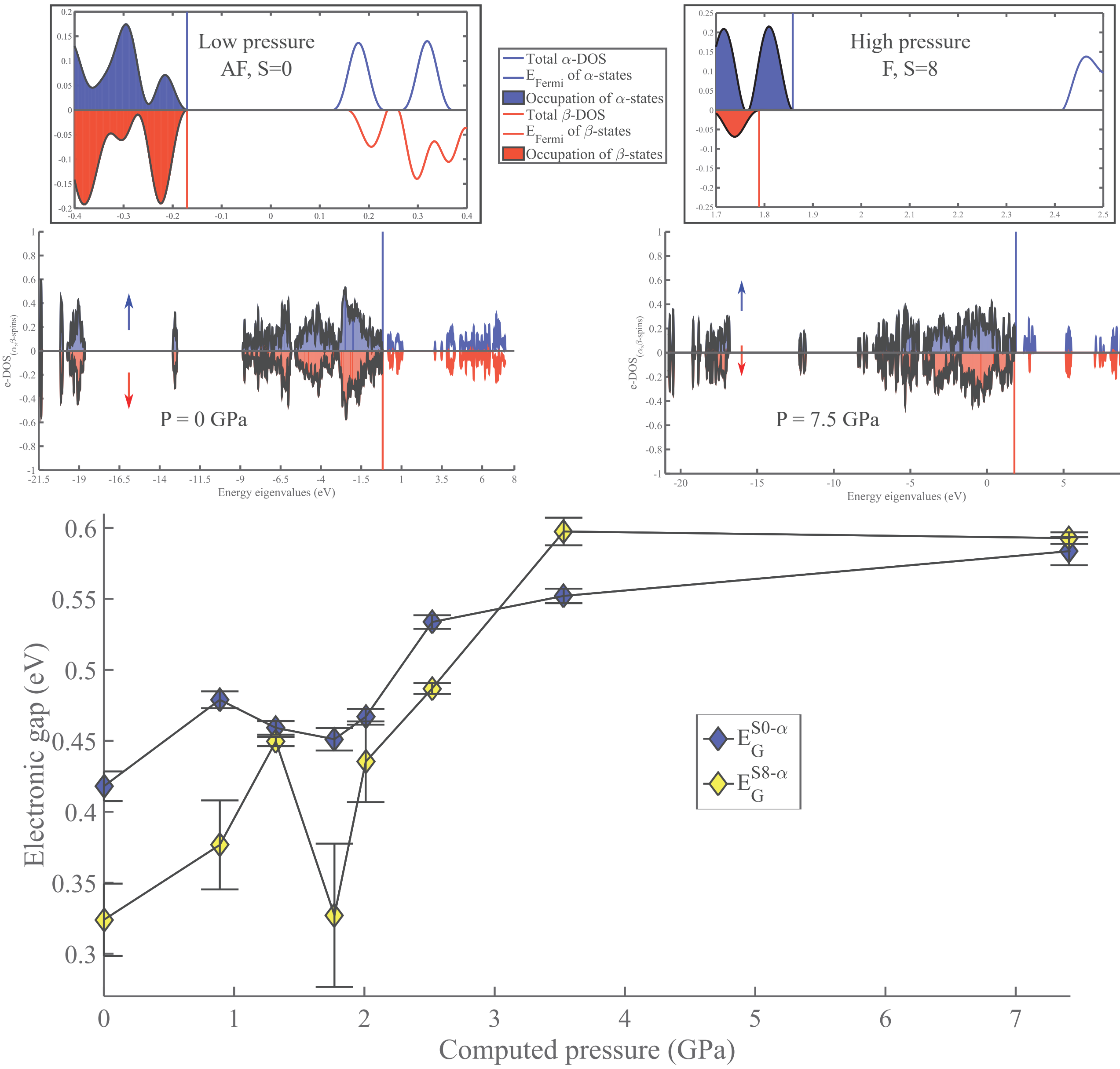

Figure 45 – **Top part:** density of states (DOS) computed for the S_0 system at low pressures (left) and the S_8 system at high pressure (right).α- and β-DOS are represented respectively in blue and red colors. Insets are providing a zoom on the electronic band gap region in an eigenvalues range of 0.8 eV in both cases. **Bottom part:** Computed electronic band gap as a function of pressure for the antiferromagnetic system (S = 0) and the half spin polarized system (S = 8)

in the antiferromagnetic case S_0P_{Low} contrasts with the non-symmetric shifts observed in the half spin polarized system S_8P_{High} density of states. Finally, the non-monotonic variations of the band gap of the material obtained for the S_8 and S_0 configurations from 1 to 3 GPa (Figure 45) goes in the same line than the changes highlighted in the spin density and structural studies. The effect of pressure is visible at the level of density of state analysis. In Appendix B, we report the full set of gap values for both α and β states as a function of pressure and multiplicity in Figures 92 and 93.

New basis sets have recently been proposed to enhance the description of the electronic band gap through ab-initio calculations especially for semiconductors and insulators [162]. However, within the PW basis approach, an improvement of the electronic gap determination requires complementary electronic structure calculations with better performing exchange-correlations functionals. In view of the lack of experimental counterparts on the electronic properties on CuOHAc system and the extreme computational cost of hybrid *xc*-functionals, we bound ourselves to the framework of BLYP calculations employed hitherto. The next section is devoted to several statistical studies and discussions of computational considerations that highlight interesting details concerning the calculations performed on CuOHAc hybrid material.

3.4 Statistics and discussions

3.4.1 Detailed analysis

In the early steps of our study of CuOHAc material, we performed a simulated annealing to optimize all the structures considered. In terms of the wavefunction calculation, our convergence criterion on the total energy is fixed to 10^{-5}Ha for all our calculations. But for the structural convergence, we consider the temperature that has to become negligible (T<0.1K) with sufficiently low ionic forces. In Figure 46, we report the histogram of the resulting forces on all the atoms of the 0 pressure (P_0) CuOHAc structure in the AF state (S_0) at the end of the simulated annealing process. We fixed the convergence criterion for the structural optimization to 10^{-3}Ha/a_0 with a_0 the Bohr atomic unit of distance. The optimized structure obtained is characterized by low forces (Figure 46) on

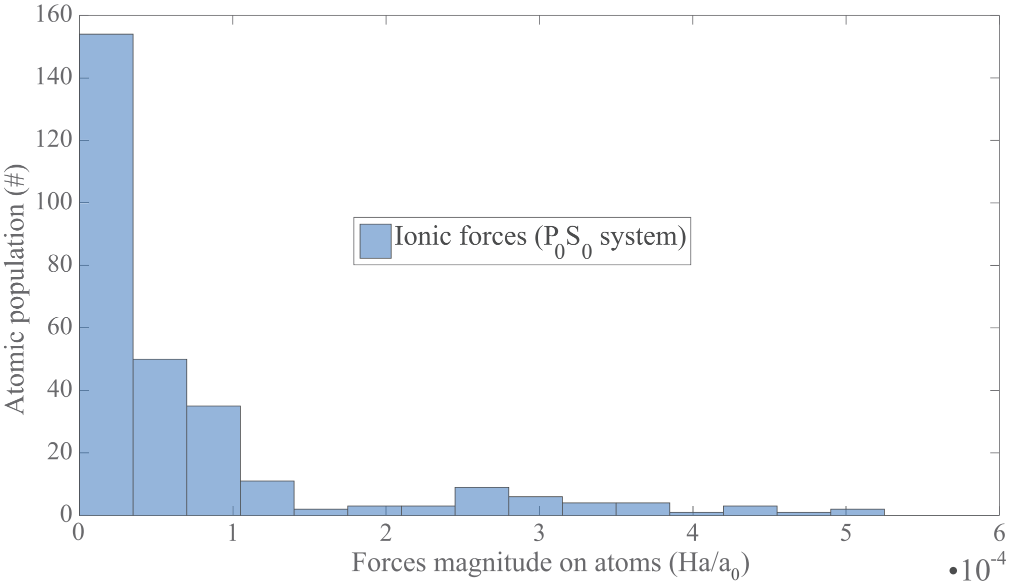

Figure 46 – Histogram of the ionic forces obtained on the 288 atoms of the optimized structure of copper hydroxide acetate system at 0 pressure in the anti-ferromagnetic ground state. a_0 corresponds to the Bohr atomic unit of distance

all the ions, even though the distribution enables a distinction between lighter atoms (H, O and C) characterized by the lowest forces ($<10^{-4}$Ha/a_0) and more heavy atoms (Cu) with forces slightly superior ($10^{-3}>F_{Cu}>2\cdot10^{-4}$Ha/$a_0$).

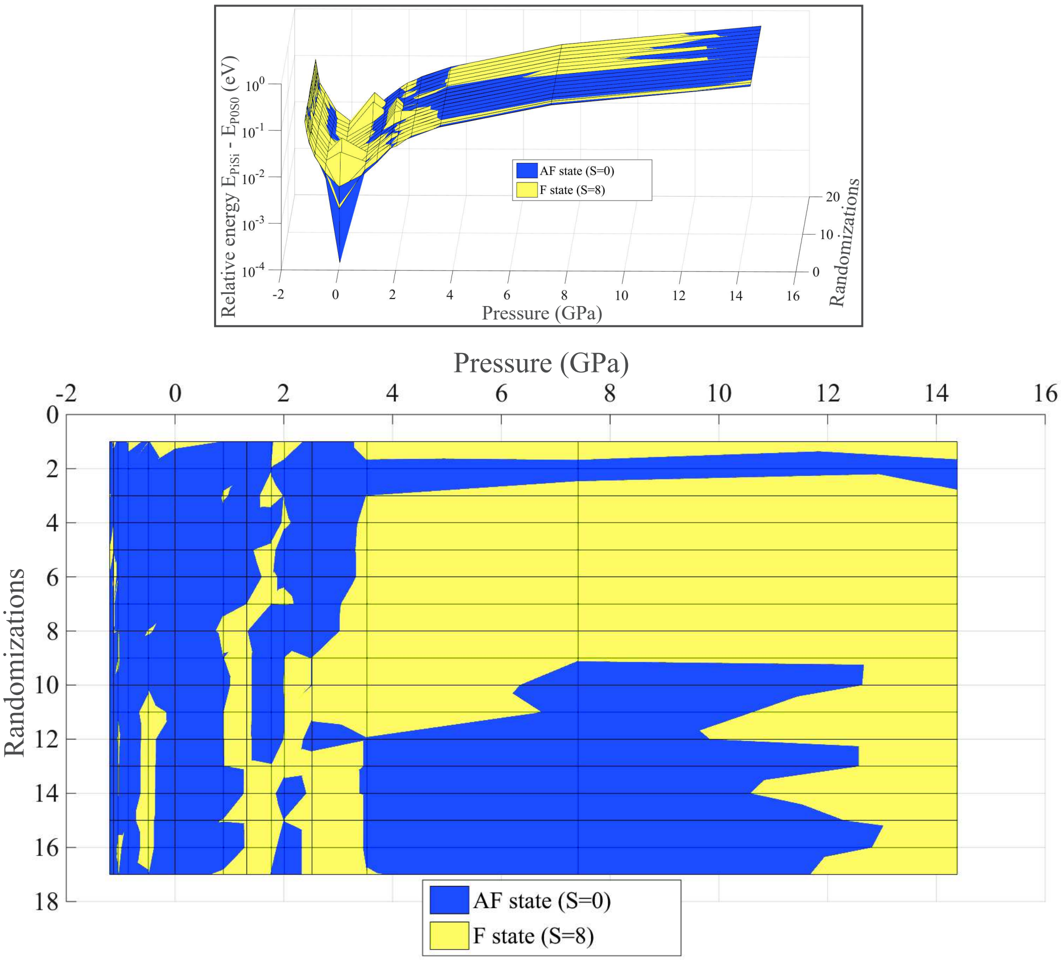

Figure 47 – **Top part:** 3D representation of relative stability (in terms of energy) of the two relevant magnetic states of copper hydroxide acetate system (antiferromagnetic in blue and ferromagnetic in yellow) as function of pressure. The third dimension corresponds to the multiple minima obtained through the randomization of initial electronic degrees of freedom. **Bottom part:** projection of the 3D map on a 2D space in which all the blue parts indicate the regions where the AF (S=0) state is the most stable and the yellow parts, the regions in which ferromagnetic (S=8) systems obtained at lower total energy than the AF state

As we mentioned earlier, once the structural optimization is performed, a randomization procedure is applied on electronic degrees of freedom so that different magnetic states can be explored within a total cell magnetization fixed at the beginning of the calculation. Despite the advantage of clarity in averaging the data as presented in the previous sections, there are interesting supplementary conclusions that one can draw through a more detailed analysis. The data gathered on such material through this FPMD study are 3 dimensional, one has to consider, the pressure, the total magnetization constraint and the various spin configurations obtained within each system at fixed total spin (multiplicity) and fixed pressure. We focus only on the two magnetic configurations competing for stability, the AF state (S=0) and the half spin polarized system (S=8). For these systems, we obtain the 3D surface reported in the Figure 47-(inset) with the computed pressure, in the x-axis, the randomized initial states labeled from 1 to 17 in the y-axis and the relative energy with respect to the AF 0-pressure system in the z-axis. The projection on the xy-plane of such surface is performed in Figure 47-(main plot), exemplifying a procedure to construct a magnetic phase diagram of the system as a function of pressure on the base of all the CuOHAc systems considered. If one includes the negative pressures (extended systems), the anti-ferromagnetic configuration (S=0) in blue is most stable up to the region of 1 GPa of applied pressure in which, from all the randomized systems, an important number of ferromagnetic systems (S=8 in yellow) become more stable than the original AF configurations. An interesting feature is that even if in average, at high pressures, the ferromagnetic state is more stable than the AF one, there are few situations in which the AF state is still obtained as a ground state. The blue region between 4 and 10 GPa attests this fact.

Once this picture of the magnetic transition is obtained, we use the pair distribution function (pdf) to characterize the effect of pressure on CuOHAc system. Indeed, despite the analysis performed on the different distances and angles in the system, this pdf allows to follow the effect of pressure on particular pairs of atoms. Considering the copper-oxygen pair, we first report the $g_{CuO}(|r|)$ obtained for copper hydroxide acetate structure at 0 pressure in Figure 48. This distribution is obtained from a FPMD simulation at room temperature of 5 ps, the error bars represent the standard deviations corresponding to the trajectory average. The main peak observed around 2.05 Å is characteristic of the oxygen

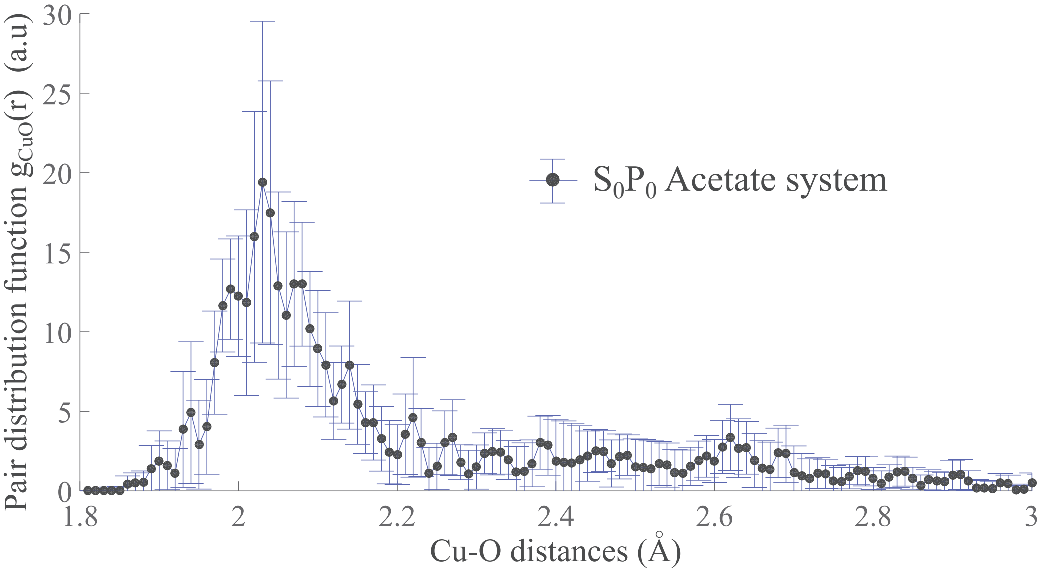

Figure 48 – Atomic pair distribution function g(r) computed for the copper-oxygen pair in the case of copper hydroxide acetate structure. The data are averaged from a molecular dynamics trajectory of 5 ps at 300K resulting in the error bars exposed (standard deviations)

of hydroxide molecules coordinating copper sites. The second population of acetate linked oxygen atoms is poorly localized around one specific distance because the temperature of the system allows for significant thermal vibrations. Nevertheless, the coordination of the copper layer by the organic moieties is maintained (Cu-OAc distances lower than 2.8 Å) and with it, the stability of the system. To highlight the effect of pressure on the system, we damped the structure to obtain the geometry at 0K and we performed this pdf analysis on the different structures obtained at each positive pressure considered. The results are reported in Figure 49. The black dashed line is an indicator giving access to the position of the first peak while the pressure is applied on the system. The shift toward shorter Cu-O distances is a visible characteristic of the deformations of the oxygen octahedra in the system. There is also an increase of the magnitude of this first peak when pressure is applied indicating that the distances to these equatorial oxygens of OH molecules becomes similar. Nevertheless, the shape of this peak being conserved, the geometrical distribution of hydroxide molecules in the system is not much affected by pressure. This is not the case for organic molecules coordinating the Cu layers for which more disorder is induced by pressure so that no clear trend, except an overall diminution of Cu-OAc distances, can be drawn.

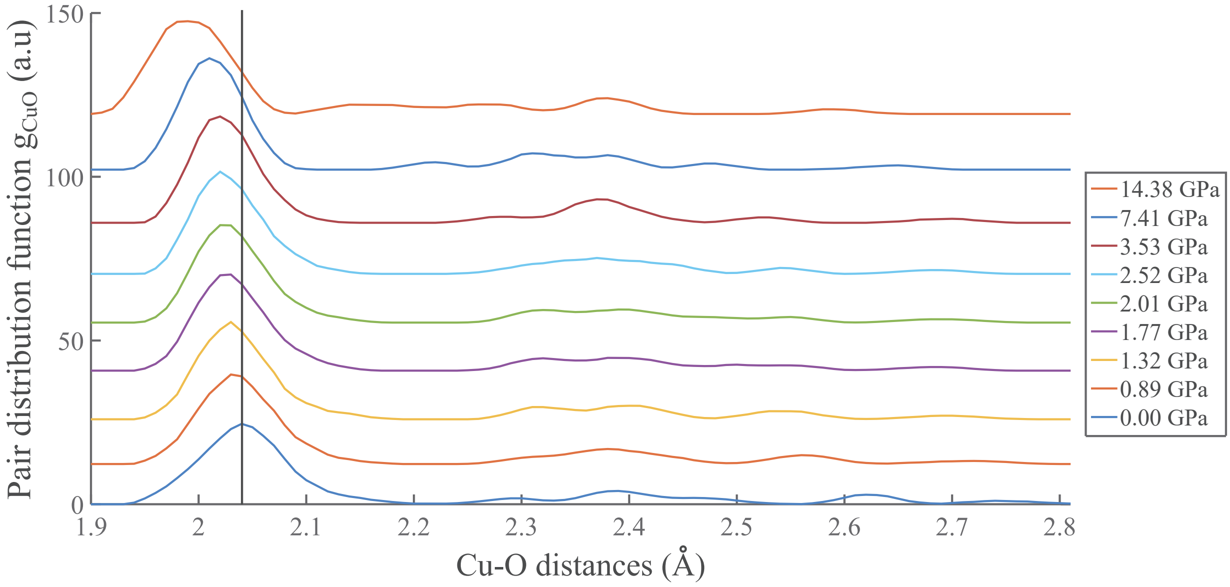

Figure 49 – Pair distribution function of the copper-oxygen pair in copper hydroxide acetate system, obtained for different values of pressure applied on the system. The different curves for increasing pressure values are rigidly shifted in the y-axis to highlight the evolution of Cu-O distances distribution

Another interesting structural feature investigated through radial distribution functions is the occurrence of hydrogen bonds and in particular between the double bonded oxygen of acetate molecules with hydrogen atoms of water molecules. To analyze the precise configurations of H-bonds present in our system, we can rely on the Wannier function analysis providing the maximally-localized Wannier orbitals surrounding each atom.

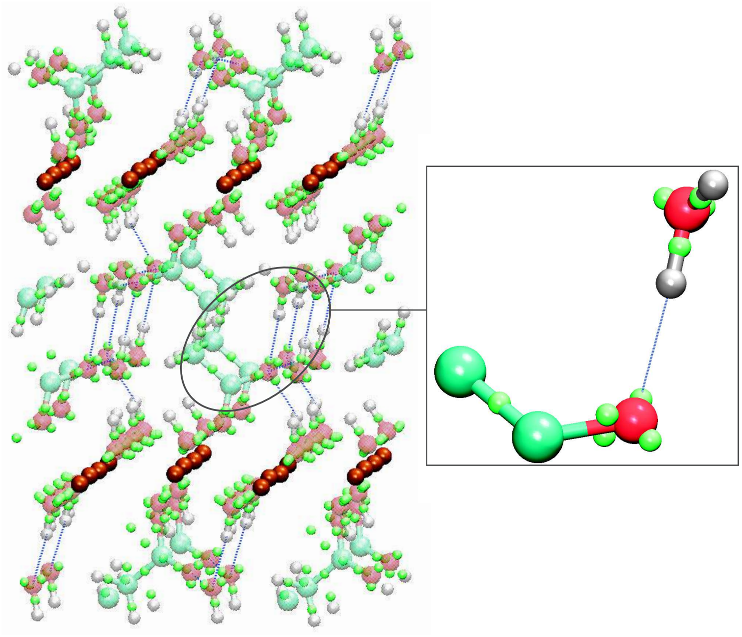

Figure 50 – CuOHAc structure resulting from a Wannier functions analysis. We obtain four Wannier functions centers (WFC) per oxygen atom and we highlight the hydrogen bonds (H-bonds in blue dotted lines) establishing between water molecules and acetate (or hydroxide) molecules. In the inset, we highlight the particular H-bonds identified between the double bonded oxygen of acetate molecules and hydrogen atoms of water molecules

In Figure 50, we highlight such Wannier functions centers (WFC) in green spheres, hydrogen bonds in blue dotted lines and we give a zoom of the region of interest. We observe that in the case of hydrogen bonding, the WFC of the lone pairs of the double bonded oxygen atoms (O_{db}) linked to acetate molecules point toward the hydrogen atom of a water molecules. Such configuration is observed among all the system with a distribution of $O_{db} \cdots H_{wat}$. The system shown in Figure 50 corresponds to the CuOHAc structure at 0 applied pressure. In this configuration most of the H-bonds are found for oxygen-hydrogen distances ranging in between 1.8 to 2 Å. This structural tool is of particular interest if one analyzes the chemical bonding properties of organic and inorganic parts in hybrid materials. We report the evolution of the $O_{db} \cdots H_{wat}$ as a function of pressure in Figure 51. Through these results, we can highlight the effect of pressure on the interlayer region made of acetate and water molecules. At zero pressure, we have two main peaks at 1.78 and 1.92 Å, characteristic of the order of magnitude of distance at which H-bonds are usually observed. An isolated peak is also present at larger distances and it corresponds to the H-bond that occurs at a larger distance. However, the more the pressure is applied, the more the two main peaks are shifted toward lower distances indicating the compression of the structure. Interestingly, the two peaks observed at zero pressure become more numerous peaks as pressure increases. This behavior indicates that water molecules are playing an increasingly important role in stabilizing the chemical bond between the organic part (acetate) and the inorganic one (Cu layers). For high pressures, water molecules are constraining the local environment of the acetate molecule

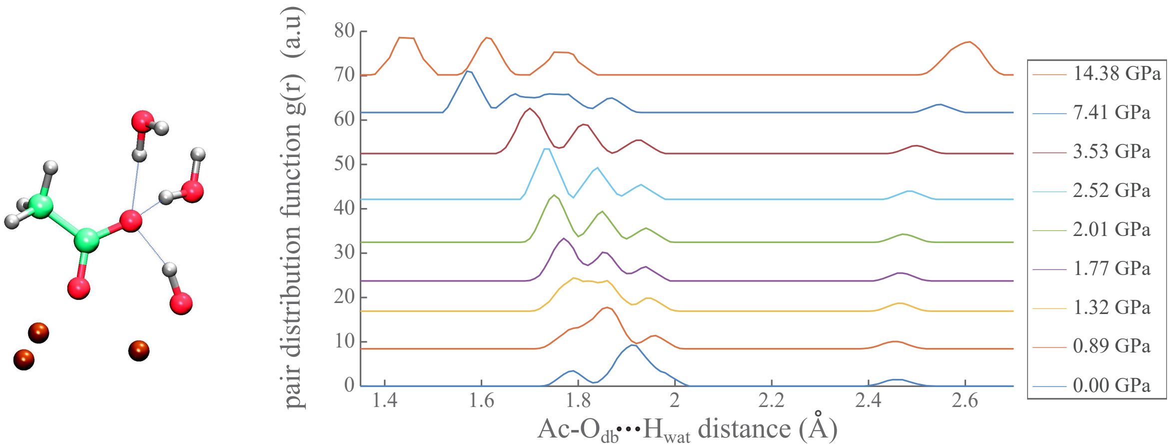

Figure 51 – Evolution of the hydrogen bonds involving water molecules and the double bonded oxygen of acetate molecules as a function of pressure applied on this copper hydroxide acetate system. The local atomic environment characteristic of such H-bonds is schematized in the left part of the figure

and result in a stable structure despite the large deformations identified with respect to the structural ground state at 0 pressure.

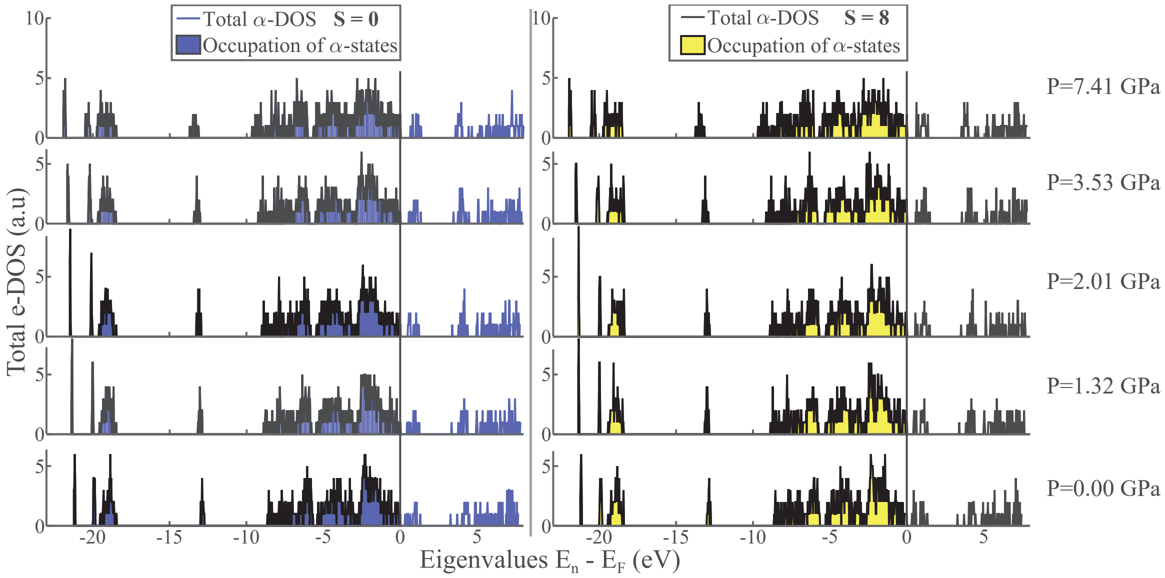

Figure 52 – Electronic α-states density of states (DOS) computed for copper hydroxide acetate system for increasing values of external applied pressure. The energy eigenvalues are computed relative to the Fermi levels (black dashed line) of each CuOHAc structure considered. Both the anti-ferromagnetic state (blue) and the ferromagnetic state (yellow) of this system are represented

Finally, we computed the electronic density of states (eDOS) for each of the studied systems. Therefore, 612 eDOS data sets (17×9×4) were obtained, from which we selected the relevant magnetic configurations (S=0 and S=8) to analyze the corresponding band gaps (Figure 45 in the previous section). Such results can be complemented by an example of eDOS obtained for the two magnetic states considered and for different pressure values. In Figure 52, we report the evolution of electronic density of states of the S_0 and S_8 systems as function of pressure. Slight changes in shape and magnitude of the eDOS occur as a function of pressure for both systems (S_0 in blue and S_8 in yellow) accompanied by a change of the band gap of the system highlighted by the energy difference between the first unoccupied state and the Fermi level (black dashed lines). Overall, pressure does not affect much the electronic density of states of the system despite the increase of the band gaps and the slight fluctuations of the Fermi levels observed for all the structures considered. The detailed electronic band gap results for both α- and β- states are presented in Appendix B (Figures 92 and 93).

3.4.2 NLCC and *semicore* pseudo-potentials

In the second chapter, we detailed the construction of two different pseudo-potentials (PP) designed to solve the problem of core and valence states overlap in the frozen core approximation. In this section, we investigate some similarities and differences between these two solutions applied to the copper ions used in the framework of our FPMD simulations of CuOHAc system. Applying the same procedures to both non-linear core corrected (NLCC) and semicore (semi) pseudo-potentials for Cu atoms, we first note higher forces obtained with the semicore treatment clearly visible through the population of Cu atoms in green ($>8\cdot10^{-4}$ Ha.a_0^{-1}) in Figure 53. We did not pursue further

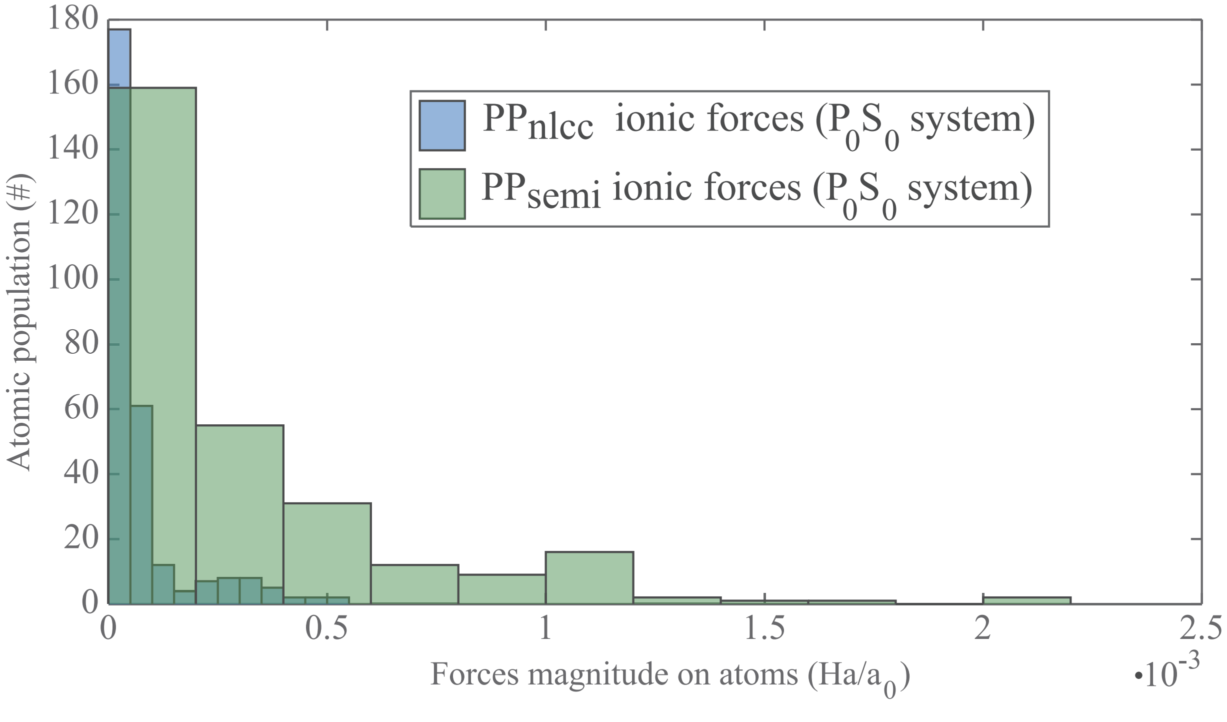

Figure 53 – Histogram of ionic forces corresponding to the 288 atoms of the copper hydroxide acetate structure studied with two different PP used for describing copper ions: the semi-core PP (green) and NLCC (blue). The system considered is the anti-ferromagnetic ground state of CuOHAc system at 0 pressure

a more extended temporal annealing (with the aim of reducing these forces) since our intent was to keep the same length for the two cases when seeking to relax the atomic and electronic structures. Since the PP change affects mainly electronic properties of Cu atoms, the final structure are very similar as expected in terms of distances and angles. However, the differences are more pronounced in the evaluation of the total energy of the system. For CuOHAc material, we report the relative stability between the total energy of the ferromagnetic (S=8 in yellow) state and AF (S=0, the blue dashed line) configuration as a function of pressure in Figure 54. The previous results obtained with NLCC PP (pentagram symbols) are compared with the new results obtained with the semicore PP (circles), all results are given with the error bars obtained from the randomizations applied on the initial wavefunctions. We observe the same overall behavior as a function of pressure, the magnetic transition lies in the same range from 1.5 to 3.5 GPa.

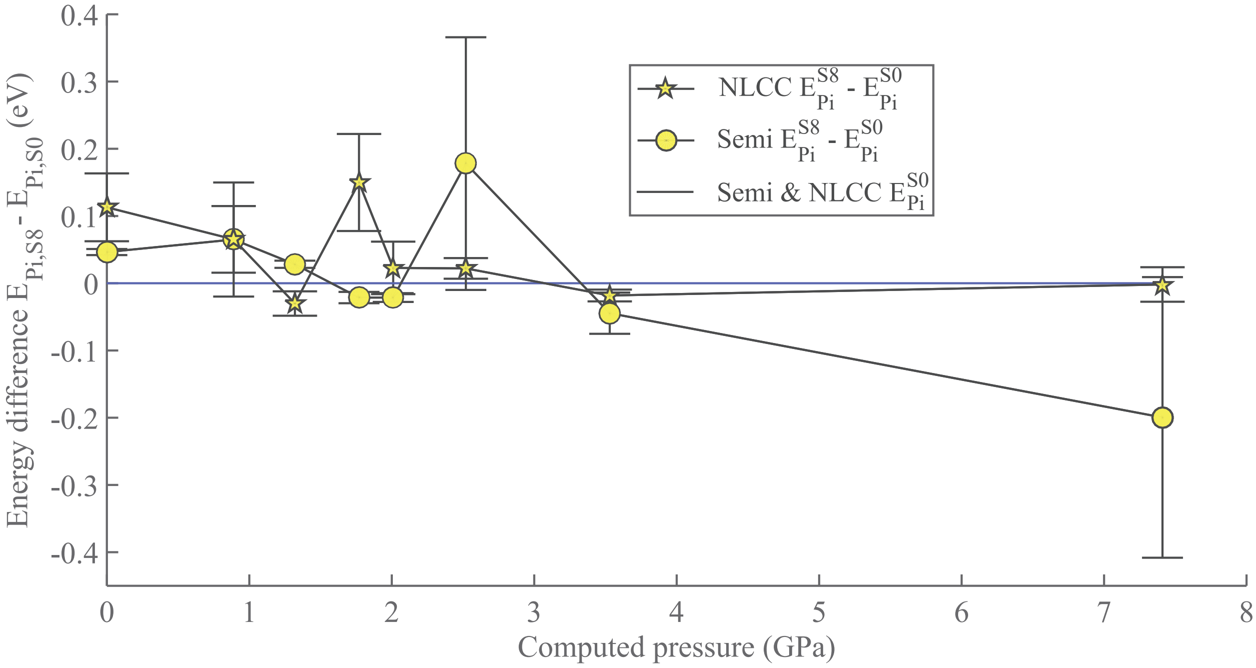

Figure 54 – Comparison between the results of copper hydroxide acetate system total energy evolution as function of pressure for the calculations performed with NLCC (pentagram symbols) and with the semicore (circles) methods for the description of copper cores pseudo-potentials. The energies are evaluated relative to the anti-ferromagnetic ground state of CuOHAc system at each pressure value (blue dashed line)

In the new semicore calculations, the competition between the AF and F states is reproduced and the S=8 system stabilizes at high pressures with a difference between the AF and F states of -0.2 eV. Besides, the total energy of the S=8 system at 1 GPa obtained at exactly 0.06 eV from the AF system's energy for both pseudo-potentials, confirming that the structures used in both calculations are very similar. The PP choice does not affect drastically the relative stability of the different magnetic systems. This fact is immediately softened by the two systems studied around 2 GPa for which results differing by as much as 0.2 eV were obtained from NLCC to semicore calculations within the magnetic transition region. We make the choice of conserving the semicore approach for the rest of this work. In terms of structural and total energy versus pressure description, much similarity is observed with the NLCC approach. However, in terms of electronic and magnetic properties, it is clear that the semicore Cu pseudo-potentials provide a better quality in the description of the core-valence interactions. An interesting difference in spin density distribution characterizes the two methods. In fact, when one projects the total spin density on atomic sites, one finds most of the spin density localized on Cu atoms. The histograms shown in Figure 55 highlights the fact that a higher local spin density value ($\simeq$0.6 |e|) is found when using the semicore approach comparing to the NLCC calculation ($\simeq$0.48 |e|).

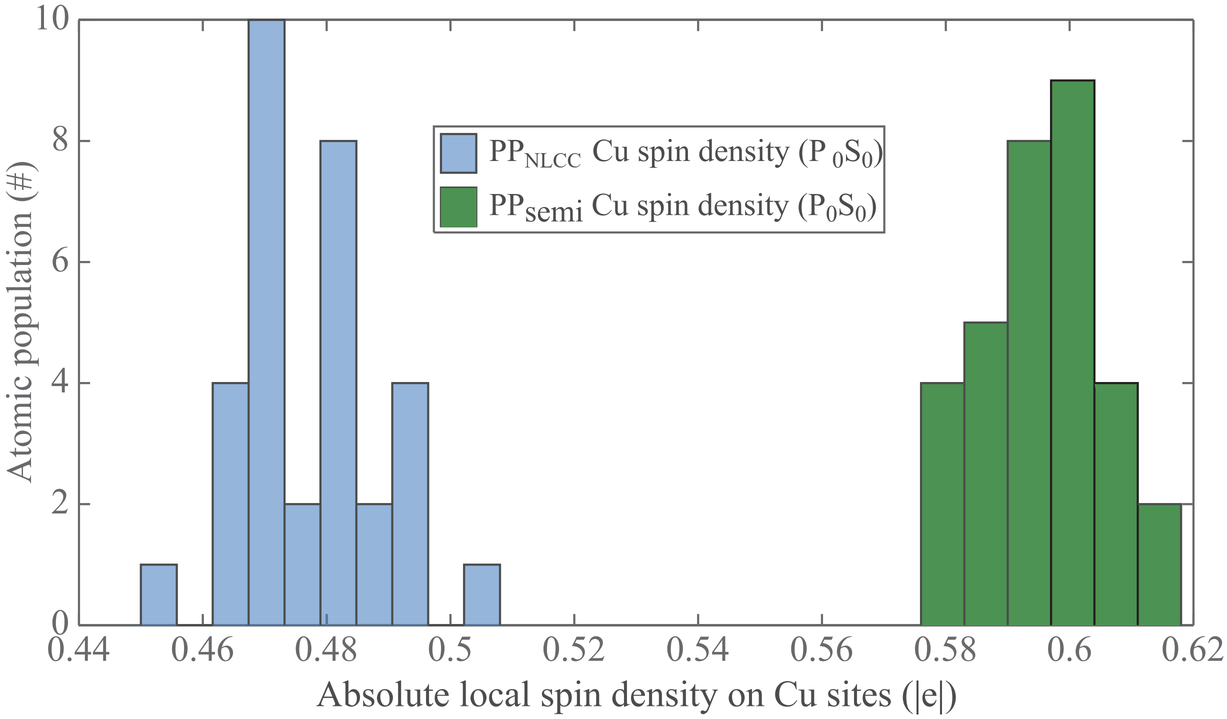

Figure 55 – Histogram of local spin density obtained on copper ions sites in copper hydroxide acetate structure when using non-linear core corrections (NLCC) approach (blue) or the semicore method (green) for the description of Cu core electrons. The systems analyzed correspond to the AF ground state of copper hydroxide acetate system at 0 pressure

We report in Figure 56 the variation of the 3D spin polarization of the system as a function of pressure indicating similar qualitative trends for semicore (filled circles) and NLCC calculations (dashed lines). In the anti-ferromagnetic configuration of the system (S=0 in blue), the same variations are observed in the magnetic transition region with higher values of spin polarization due to the enhancement of Cu local spin density with the inclusion of the semicore states. For the ferromagnetic (S=8 in black lines and yellow symbols) configuration, an important oscillation of this 3D polarization is obtained between 1 to 3 GPa correlated to the magnetic transition. This indicates a larger magnetic response of the system with respect to pressure application than the one observed in NLCC calculations (black dashed line). In addition, the semicore calculations show an enhancement of the behavior previously described at high pressures. This corresponds to the fact that the ferromagnetic system stabilizes an identical in-layer spin polarization (Σ_{IN}) among the two layers while the AF system sustains large in layer magnetization differences between the two Cu layers.

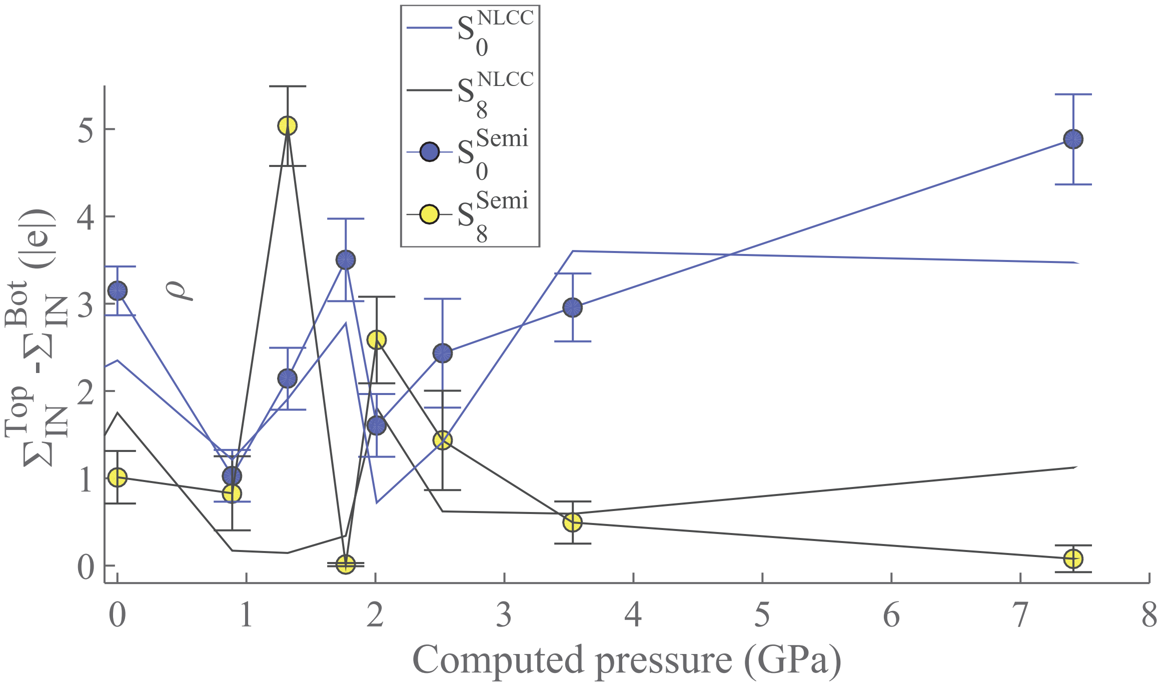

Figure 56 – In-layer magnetizations ($\Sigma_{IN}^{l_1,l_2}$) computed for copper layers (l_1,l_2) in CuOHAc system as function of the pressure applied. Both the antiferromagnetic (S = 0 in blue) and ferromagnetic (S = 8 in yellow) states are considered in the framework of NLCC (dashed lines) and semicore (solid lines) descriptions of the core electrons of copper

These results can be summarized by noting that qualitative agreement is obtained with previous NLCC calculations. Nevertheless, using this semicore description, the local spin density values on copper sites are higher and the relative stability between the magnetic states is more pronounced.

In terms of electronic properties, the semicore pseudo-potential allows for a much better description of the insulator character of this material. In Figure 57, we report the electronic α-states band gap that is obtained using NLCC pseudo-potential for copper (pentagrams) and semicore (filled circles) as a function of pressure. The band gap obtained at 0 pressure for the AF system is 1.20 eV to be compared with 0.42 eV obtained with the NLCC approach. The evolution as a function of pressure is similar in both cases for both magnetic configurations (AF in blue and F in yellow), even though the ferromagnetic system shows a monotonic increase in contrast with the NLCC calculations. Considering the fact that CuOHAc is antiferromagnetic and an insulator when no stress is applied [4], we consider the band gap obtained using the semicore approach to be better suited to describe our CuOHAc structure.

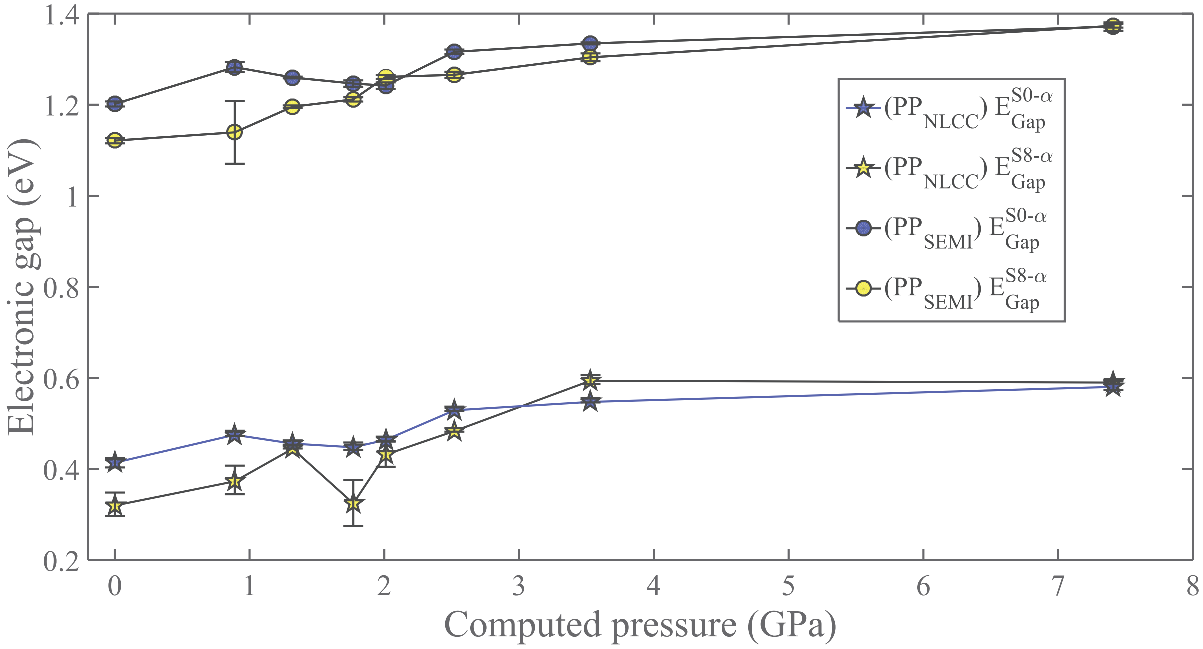

Figure 57 – Evolution of the electronic band gap of CuOHAc system as function of pressure for both the anti-ferromagnetic state (S=0 in blue) and ferromagnetic state (S=8 in yellow). The calculations using the NLCC pseudo-potential for the description of Cu atomic cores (pentagrams, dashed lines) are compared to those performed with the semicore pseudo-potential approach (circles, solid lines)

3.4.3 Discussion

Along with the detailed study of the CuOHAc material, we intended to obtain, at each step of this chapter, an insight on the way by which one can approach hybrid materials through the use of FPMD simulations. In what follows, we provide general considerations by referring to similar studies devoted to hybrid materials. The methods and understanding obtained during the CuOHAc material properties investigation will be exploited to better understand current open issue and previous work done in this field. The pressure-induced magnetic transition explored here is observed in other families of hybrid materials and it is interesting to relate these works to ours in order to position this study with respect to the state-of-the-art. Hybrid transition metal oxides are a family of materials with structural properties allowing for a great variety of interesting functionalities. These are associated with the presence of iono-covalent bonds between the organic parts and the cation centers. In the case of hybrid metal-organic framework perovskites, spin cross-over (SCO) phenomena and the interplay between magnetic and elastic interactions [163] are widely observed and studied. In the case of SCO hybrid materials, the molecular structure leads most often to a switch from a high spin state (HS) to a low spin state(LS) under the application of external pressure. Sometimes the inner couplings are difficult to disentangle [164, 165]. These situations are therefore very similar to the issues of magneto-structural properties in hybrid materials we have investigated in this thesis. DFT-based calculations performed by Banerjee et al. [6] provide a good example of the recent first-principles studies of SCO materials. Two specific Fe-based MOF perovskites, dimethylammonium iron formate (DMAFeF), $[CH_3NH_2CH_3][Fe(HCOO)_3]$ and hydroxylammonium iron formate, $[NH_3OH][Fe(HCOO)_3]$ (HAFeF) have been considered. The structures are represented in Appendix B-Figure 94. The authors focus on the study of the spin transition between a high spin state (S=2) and a low spin state (S=0) driven by the application of hydrostatic pressure. Pressure induced spin transition and the effects of cooperativity in DMAFeF and HAFeF hybrid perovskites has been studied through the computation of the density of states of both materials, and the projection on the orbitals of interest (mainly Fe *d states*). The authors prepared their initial structure through an analysis of the energy versus volume curves obtained for the two systems as reported in Figure 58-(I).

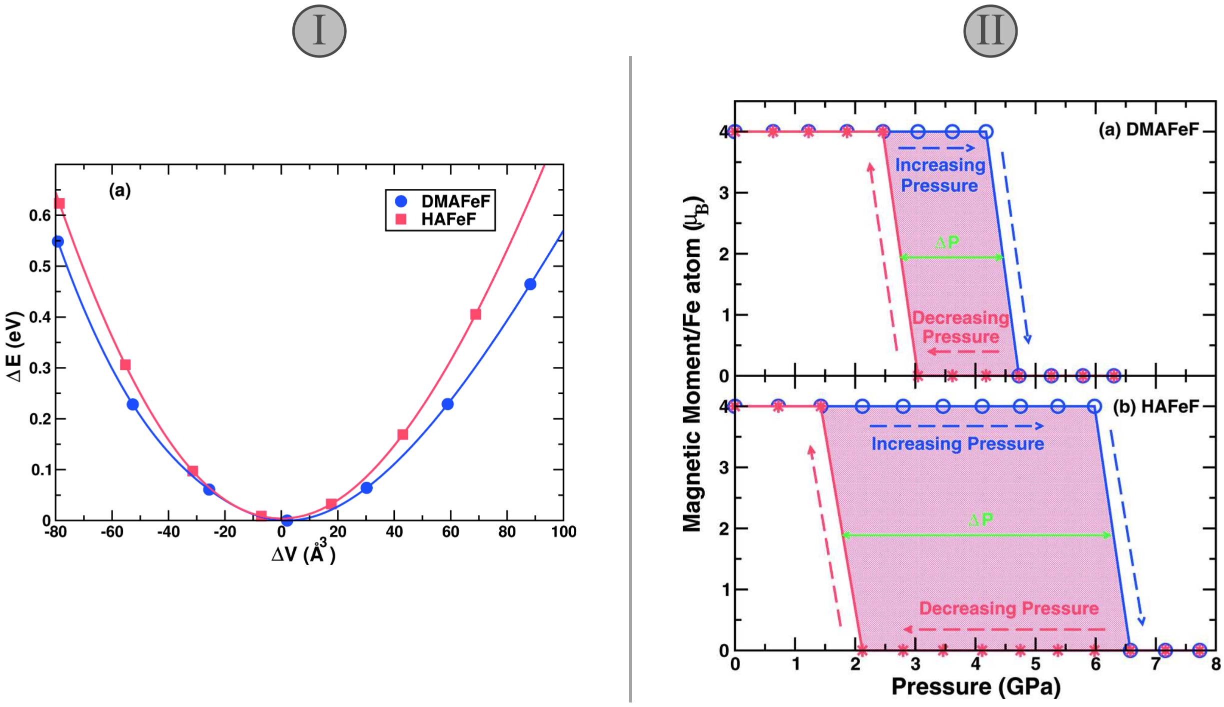

Figure 58 – **I** Energy as a function of volume for the two compounds considered in ref. [6]. **II:** computed magnetic moment per Fe atom as a function of increasing (blue) and decreasing (red) pressure for both DMAFeF (a) and HAFeF systems (b). *Data published by H. Banerjee et al. [6]*

This work is complemented by the critical pressure values at which the spin transition can be characterized for both materials. Therefore, compressions and expansions of the simulated cell by steps of about 0.6 to 0.7 GPa are performed starting from the ground state identified in their static structural study (Figure 58-I). It is more in terms of magnetic properties that this work is an adequate parallel to our own investigation. In Figure 58-(II), the spin crossover phenomenon is observed as a switch from a HS (high spin) state of iron sites to a LS (low spin) state at a critical pressure of 4.7 GPa for DMAFeF denoted $P_c^{DMA}\uparrow$ and 6.6 GPa ($P_c^{HA}\uparrow$) for HAFeF. A similar procedure is followed for the decreasing pressure path and new transition (LS→HS) pressures are obtained. As a result, one obtains M(P) hysteresis curves as in Figure 58-(II) with a 2.2 GPa width for DMAFeF and 5.2 GPa for HAFeF. This is a signature of the fact that the nature of the cation used (DMA or HA) has a strong impact on the spin-switching properties. In addition, the authors ([6]) use a model based on the interplay and competition between elastic and magnetic interactions [163, 166] to give a microscopic understanding of their results. They conclude that the main driving force for cooperativity in these metal-organic frameworks is a spin dependent lattice effect. This arises from the distribution of size and shapes of FeO_6 octahedra as well as the contribution of magnetic exchange interactions between iron sites.

In the case of our copper hydroxide acetate study, the magnetic moment of Cu atoms is 4 times lower than the one of iron and the magnetism has to be treated at the transition metal layers scale. In CuOHAc structure, the copper layers and the organic units are organized in a lamellar fashion excluding the treatment of transition metal units as independent. In contrast, the MOF structures are molecular systems with well-defined molecular units and the magnetic properties are investigated at the scale of the iron oxide units on which the magnetic transition is observed. Our approach insists on the need for first-principles molecular dynamics [2] as an efficient method to treat the structural optimization of hybrid layered materials. Such treatment allows to obtain a structural ground state of the systems considered and thus the exploration of many magnetic configurations allowed by the use of a large enough simulation cell. Therefore, both systems' types can be investigated using such methods and the fundamental differences between the magnetic behaviors of the two systems can be studied.

Chapter 4

Novel Functional Layered Single Copper Hydroxides

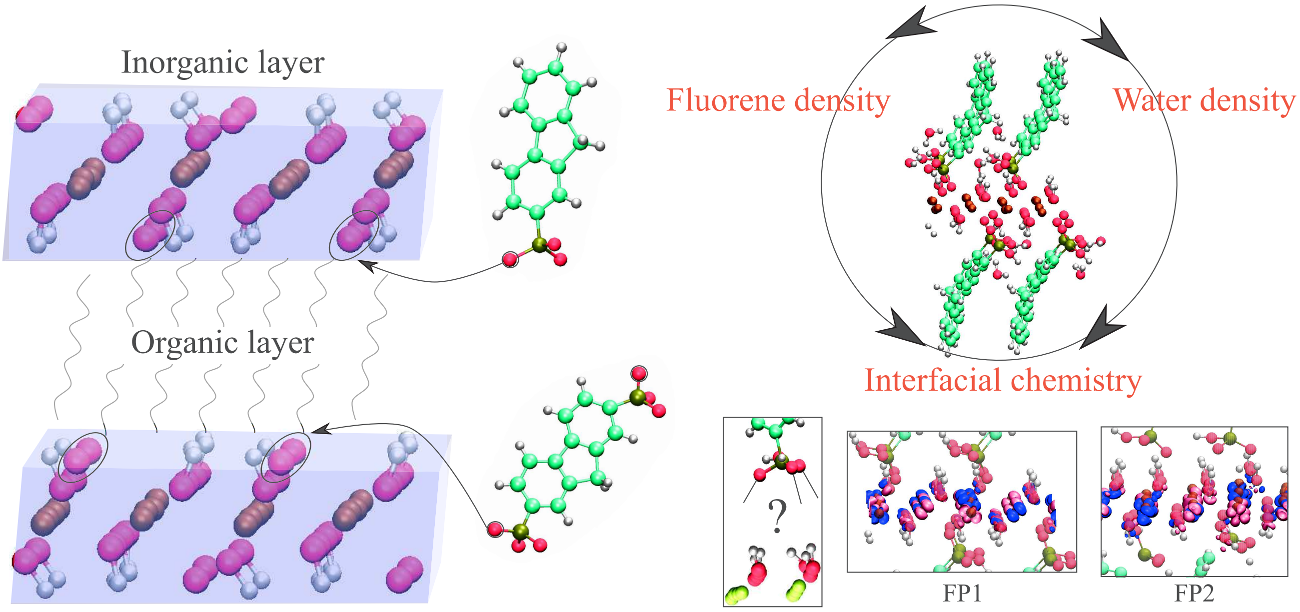

Figure 59 – Overview of the "molecular engineering" approach followed for the construction of phosphonate based hybrid lamellar materials and the study of the associated properties. On the left part, the copper hydroxide acetate framework is shown highlighting the two copper hydroxide layers and the organic molecules anchoring sites (Oxygen sites surrounded by black ellipses). In the top right part, we schematize the specific interdependence between water and fluorene phosphonate molecules densities, having a critical influence on the chemical bonding between the organic and inorganic parts in the system. The first inset is a representation of the specific problematic of anchoring of the $(PO_3H)^-$ group to the copper hydroxide layers. The last two insets (bottom right) indicate the difference of magnetic (spin density) distribution obtained in two different systems, i.e. the copper hydroxide fluorene monophosphonic (CuOHFP1) and the copper hydroxide fluorene biphosphonic (CuOHFP2), in the interfacial region

Abstract

In the quest for specific design and tunable properties of matter, a rapid growth is observed in the study of multifunctional hybrid materials over the past decade [5]. Critical parameters in promoting multifunctionality in hybrid systems are the chemical bonds between the components as well as the dimensionality of the functional network. Structural units having strong metal bonds with organic linkers are obtained in the metal-organic framework (MOF) materials already invoked in this thesis, combining various properties such as magnetism and chirality [8, 9] or ferroelectricity [10]. In this chapter, we aim at having a control of the architecture of multifunctional hybrid materials through the insertion of new organic molecules (fluorene phosphonates) in the CuOHAc structure. These are intended to replace the acetate moieties leading to the stabilization of the new compound. Thus, the goal is to apply first-principles molecular dynamics (FPMD) methods to elaborate a "molecular engineering" approach to design, construct and study multifunctional hybrid materials. A protocol of simulation is proposed to construct plausible crystal structures with very few starting information, e.g without the availability of the full set of atomic coordinates. Critical parameters such as the crystal lattice, the organic molecules conformations within the interlayer space and the chemical bonding properties of the phosphonate group to the inorganic network are investigated. The interplay between these parameters is shown in the case of specific compositions selected as suitable starting points in the search of stable final configurations. This procedure allows stabilizing final structures that match the chemical compositions obtained experimentally. **In this way, our "molecular engineering" approach is the method of choice conferring atomic scale simulation the power of predicting and producing realistic structures that complete experimental structural data quite often limited to interlayer distances and chemical compositions**. The route is thus opened for the design and use of these layered insertion compounds in many applications such as catalysis [19], photovoltaics [20], multifunctional materials [12] or as non-linear optical media [21].

4.1 Introduction

The present chapter extends the modeling approach proposed and discussed in the previous part in the frame of an ongoing collaboration with the IPCMS experimental team working on hybrid layered single hydroxide (LSH) systems. In particular, this theoretical and experimental joint effort aims at the study of copper- and cobalt-based LSH functionalized with novel organic sub-networks.

Organic-inorganic hybrid materials can be considered as promising systems to obtain multiferroic and magnetoelectric materials in which electric and magnetic orders can coexist. This route can present advantages with respect to traditional solid state chemistry approaches, in terms of synthesis and possibility to modulate rather easily the structures and properties. Compared to nanostructured composite materials, hybrid layered materials, where the two sub-networks responsible for the magnetic and electric properties are deeply connected, are more likely to feature magneto-electric coupling. In layered hybrid materials weak bonds between sub-networks can limit the synergy between the properties. An alternative approach relies on the insertion and grafting of functional organic molecules into magnetic layered transition-metal hydroxides $\mathrm{M}_x(\mathrm{OH})_{2x-ny}(\mathrm{X}^{n-})_y$ (M(II) = Co or Cu and X^- = carboxylate, sulfate or sulfonate anion). The X^{n-} anion located in the interlayer space may be substituted by a large variety of molecules via anionic exchange reactions. Whereas various organic molecules and coordination complexes bearing carboxylic or sulphonic acid anchoring functions have been successfully inserted into these LSH, phosphonic acid anchoring groups have never been used. As to the related compounds layered double hydroxides, $[\mathrm{M}^{2+}_{1-x}\mathrm{M}^{3+}_x(\mathrm{OH})_2]^{x+}(\mathrm{X}^{n-})_{x/n}\cdot(\mathrm{H_2O})_m$ without anchoring of X^- anions onto the layers, only a few papers on the intercalation of molecules bearing phosphonic acids have been reported (see Figure 60) [87]. Phosphonic acids, due to their coordination properties, are widely employed to prepare crystalline hybrid materials that are studied for their porosity, ionic conduction, magnetic or fluorescent properties or for their bactericidal effects.

Over the recent years, efforts were made on the use of rigid phosphonic acids for the solvothermal one-pot synthesis of hybrid compounds, with the aim to assess the consequences of this rigidity on the topology of the obtained systems. The rigidity results from a direct connection of the phosphonic acid on an aromatic or hetero-aromatic ring acting as a rigid molecular platform. When low symmetrical phosphonic acid compounds like 3-phosphonobenzoic acid (which features an aromatic ring with pro-chiral faces) are reacted with copper salts in solvothermal conditions, non-centrosymmetric crystals are obtained. Interestingly, non-centrosymmetric crystals can also be produced with biphosphonic acid as organic precursors. These well-established results motivated the study of biphosphonic acids as precursors of hybrid materials. The choice of the rigid platform is another important parameter. In this respect, fluorene stands as an interesting rigid platform in which the presence of the 5-membered ring breaks the symmetry of the compound.

Recent experimental work within IPCMS has targeted the extension of the use of fluorene-based compounds proposing novel mono and biphosphonic acids, with various alkyl chains in the corresponding position of the fluorene unit (-H, $-\mathrm{CH_3}$ or $-(\mathrm{CH_2})_7\mathrm{CH_3}$) (figure 60). The idea is to explore the potential occurrence of magneto-electric phenomena into Cu-

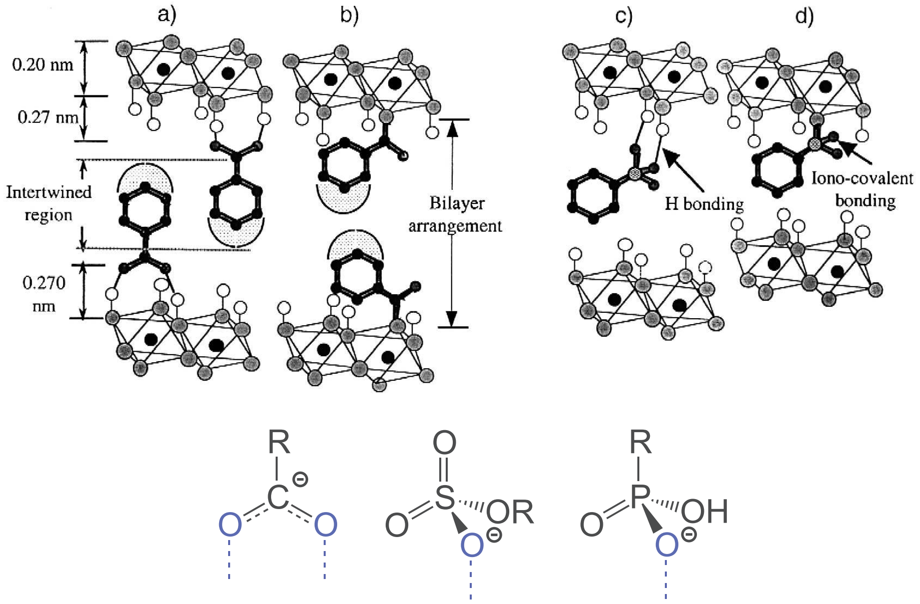

Figure 60 – Interlamellar arrangement of a prototypical LDH with (a) benzoate, (b) grafted benzoate, (c) benzenephosphonate or benzene sulfonate, and (d) grafted benzenephosphonate or benzene sulfonate. *Image adapted from scheme 2 of ref.* [87]

LSH. Within this context, it is useful to consider in the following the synthesis, characterization, structural modeling, magnetic and dielectric properties of new layered hybrid compounds which will be referred to as $A \subset M$, where A is the mono- or di-phosphonic acid fluorene and M denotes Cu hydroxide layers. To be noted that the experimental work has been also devoted to LSH hybrids based on Co hydroxide layers. However, the modeling work that will be presented within this manuscript is uniquely centered on Cu-based LSH. This choice is driven by the fact that at the moment the precise structure of the inorganic layers for layered Co hydroxide is still unknown due to static disorder of the $Co(OH)_2$ inorganic layers.

To make the connections with experiments, we recall that the synthesis of the hybrid compounds was carried out following a generally used procedure consisting in dissolving an excess of the organic molecule in water at relatively high pH; then an equivalent volume of ethanol is added along with the starting materials $Cu_2(OH)_3(DS)$ (DS^- is dodecylsulfate and DS_0^- is dodecylsulfonate) [49]. Such kind of preintercalation strategy is often used for the functionalization of layered materials. It consists in prefunctionalizing the starting compound by a molecule which is further removed to allow the insertion of the desired species. In the case of LSH, the IPCMS team has developed the prefunctionalization by DS^- or DS_0^- which is very efficient to allow the insertion-grafting of bulky or fragile molecules. The temperatures and durations of the reactions performed with preintercalated compounds $Cu_2(OH)_3(DS)$ were adapted to obtain single-phase materials, while optimizing the crystallinity and avoiding the formation of oxides. Through the analysis of the powder X-ray diffraction patterns of the synthesized hybrid compounds, the abrupt change of their inter-lamellar spacing with respect to the starting hydroxides is in agreement with the insertion of the fluorene phosphonic acid molecules. Considering the length of the fluorene monophosphonic acids and the thickness of the inorganic

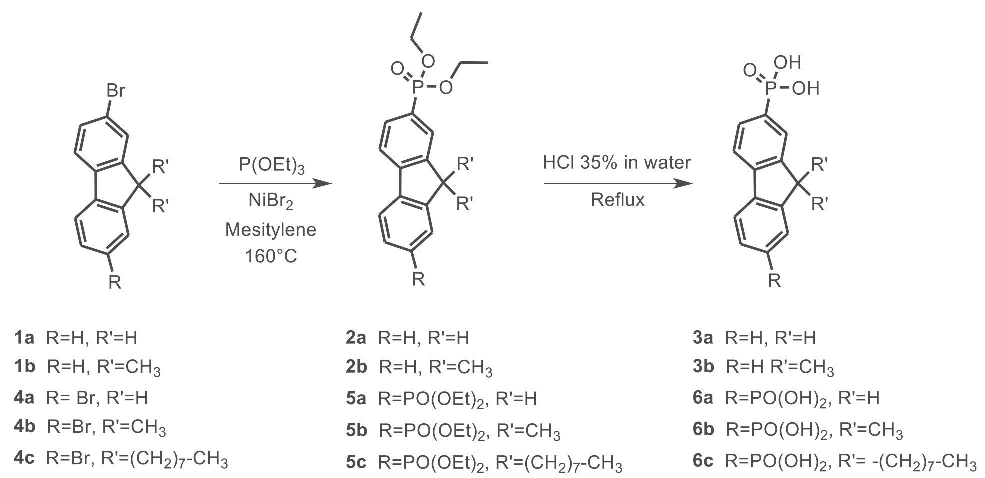

Figure 61 – Synthesis of the fluorenyl mono and biphosphonic acids used to produce novel fluorene mono- and biphosphonic acids.

sheets, the interlamellar spacing of the Cu-based hybrid compounds obtained with fluorene monophosphonic acids (FP1: **3a** in Figure 61) is coherent with a double layer arrangement of the molecules, with some possible interpenetration depending on the inclination angle. For the fluorene biphosphonic acids (FP2: **6a** in Figure 61), the observed interlamellar spacing obtained for Cu-based compounds is not coherent with a bi-grafting of the molecules onto the inorganic layers. In order to solve this apparent discrepancy and to shed light on the molecular arrangement of fluorene mono- and di-phosphonic acids in the interlayer environment for such systems we made use of FPMD simulations. This computational tool allowed us to unveil the interlayer chemical arrangements for **3a⊂Cu** and **6a⊂Cu**, providing support to the picture of **3a** and **6a** in copper hydroxide, a detail elusive to experimental probes.

Therefore, the two specific materials of interest in this chapter are copper hydroxide systems functionalized with fluorene (mono-) and (bi-)phosphonic acids. The resulting compounds are not fully characterized (missing atomic positions) since the quality of the crystals does not allow for precise XRD measurements. Nevertheless, two compositions are estimated for each material: $Cu_2(OH)_{4-x}(C_{13}H_{10}O_3P)_x{\cdot}(H_2O)_y$ (x=0.31, y=0.5 to 2) for **3a⊂Cu** and $Cu_2(OH)_{4-x}(C_{13}H_{10}O_6P_2)_x{\cdot}(H_2O)_y$ (x=0.23, y=2.5 to 3.5) for **6a⊂Cu**.

We list in the following, the key steps that we consider in order to provide a rigorous study of these hybrid materials through first-principles molecular dynamics methods. We provide insights on:

- The compatibility between the lattice parameters obtained experimentally, the interlayer distance and the interplay between organic molecules and hydroxide molecules densities.
- The conformations, orientations and possible stacking of the fluorene phosphonate molecules within the interlayer space in the aim of associating a specific composition to a particular atomic structure.
- Chemical bonding properties especially at the interface between the organic and inorganic parts of the system so that the role of the experimental synthetic conditions in defining the resulting structure can be explained.

— The magnetic behaviors expected from such compounds, using as a reference the results obtained in the study of copper hydroxide acetate.

— The role of water molecules in the crystals. In fact, water is a crucial component in such layered hybrid materials since its presence constrains the spatial arrangements of the organic parts and influences the chemical bonding in the vicinity of inorganic layers.

This chapter is divided in three main sections in which FPMD methods are used to elaborate and characterize fluorene phosphonate (FP)-based hybrid materials. **It has to be understood that our methodology has been the object of a "back and forth" exchange of information with the experimentalists that have put to good use our results by providing in turn the validation of certain of our assumptions.** The combined experimental-theoretical strategy established and employed in this work is summarized in the following scheme.

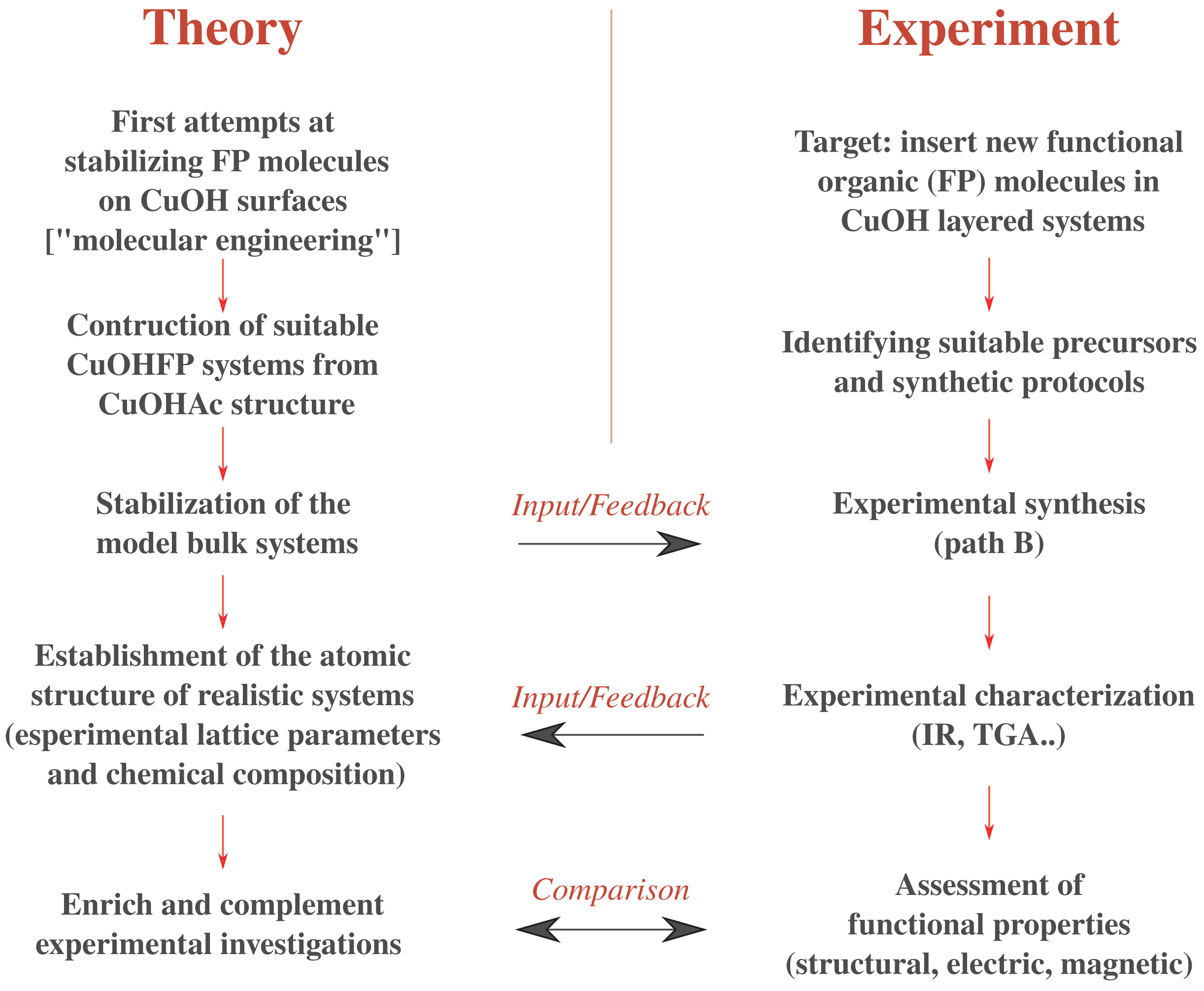

The first part details the construction and stabilization of copper hydroxide fluorene phosphonate (CuOHFP) compounds. In particular, we focus on the construction of structures starting from the Cu hydroxide framework of copper hydroxide acetate (CuOHAc) in order to obtain a stable insertion of the fluorene monophosphonic (FP1) molecules. Once the critical parameters are identified, different trial crystal structures are considered for the copper hydroxide fluorene biphosphonic (CuOHFP2) case to obtain the most realistic initial atomic structure compatible with the chemical composition provided experimentally. In a second section, we analyze the optimized model systems based on the ideal simulated structures constructed. We perform a detailed structural analysis to characterize the distribution of interatomic distances and the effect of different water contents on the final structure. We also evaluate the corresponding magnetic and electronic properties highlighting the effect of water content on these properties. We then consider higher water densities to fill all the free volume within the simulated cell, thereby stabilizing the crystal structure without perturbing the characteristic properties of the system. This allows us, in the third part, to move from the ideal systems considered to structures closely matching the experimental systems synthesized. In particular, for the CuOHFP1 system, we highlight the fundamental role of water molecules in stabilizing the low density of organic molecules in the experimental system. For the CuOHFP2 system, we propose alternative stable structures compatible with the experimental interlayer distance, chemical composition and water content insisting on the role of hydrogen bonding networks in the stability of the final structure. These studies are then enriched by additional FPMD room temperature simulations allowing the assessment of simulated infra-red (IR) spectra of a new copper fluorene phosphonate hybrid system containing FP1 molecules.

4.2 Molecular engineering approach

In this section, we apply FPMD simulations and the protocols developed in the previous chapters to construct a crystal structure that matches (and complements) the experimental characterizations of the synthesized phosphonate based materials. Since no single-crystal is obtained experimentally, we do not have access to the exact crystal structure. We therefore rely on the copper hydroxide system and exchange the acetate molecules by fluorene phosphonate ones in what we refer to as "molecular engineering approach". This terminology is justified by the step-by-step methodology necessary to construct, *in silico*, a realistic structure on the basis of structural experimental characterizations. We focus on the FP1 compound in first instance. We apply the thermostat techniques in conjunction with the molecular dynamics simulations to perform finite temperature simulations, necessary for the tests of structural stability.

We start by a detailed study of the anchoring properties of the organic molecules within the interlayer space of the Cu hydroxide lamellar structure considered. Such analysis is enabled by the various possibilities of fixing and freeing individual atoms or entire fragments of the structure during an FPMD simulation. We cut the Cu hydroxide cell to create a slab of CuOHAc structure representative of the bulk part while the second side of the Cu hydroxide layer is in contact with vacuum and represent the surface (snapshots in Figure 62). Since periodic boundary conditions are used in our method, we consider 10 Å of vacuum in the c-direction of the crystal cell so that the interactions of the surface with the images are minimized. After the elimination of the acetate molecules from the surface, we replace them by FP1 molecules grafted at the very same atomic sites where the acetate molecules were anchored. This procedure simulate a surface coverage by the new functional organic molecules, identical to the one obtained in the CuOHAc case.

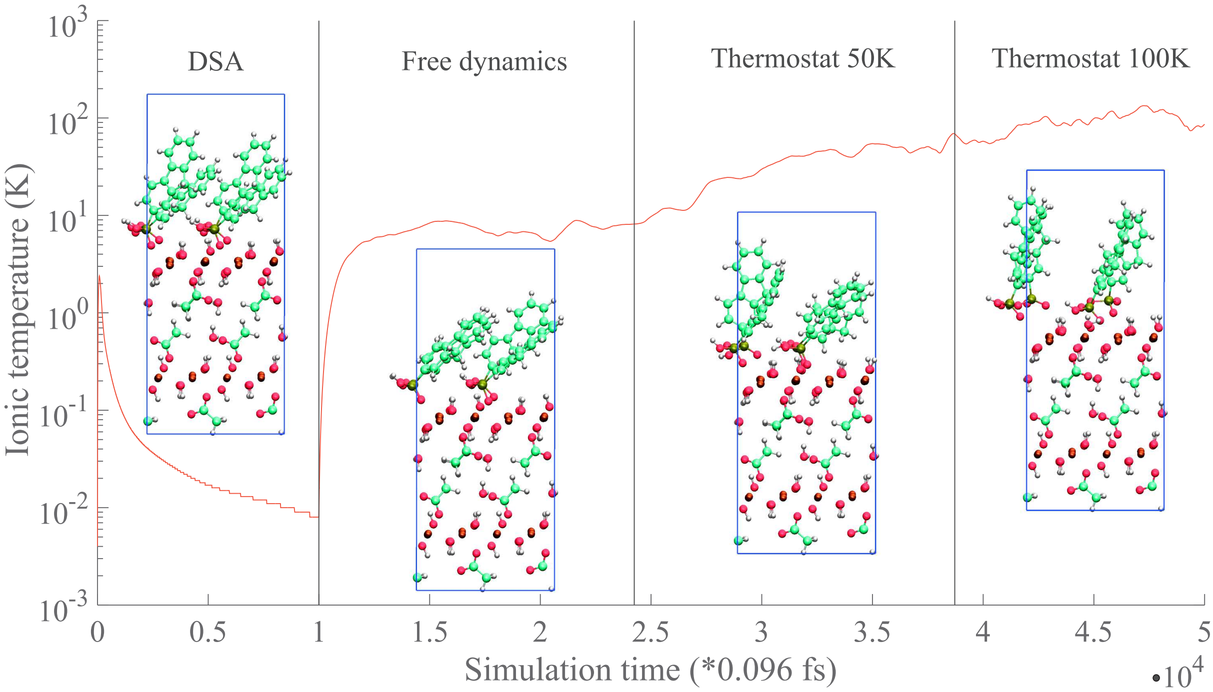

Figure 62 – Evaluation of the ionic temperature as a function of simulation time of a test system of fluorene phosphonate molecules grafting on a copper hydroxide layer. We study the surface stability of the organic molecules grafted on a (bulk+surface) system constructed from CuOHAc inorganic framework. Four regions are distinguished in the figure. They correspond from left to right to dynamical simulated annealing, free molecular dynamics and the application of a thermostat at 50K and at 100K

A specific structural optimization protocol is introduced for this system since we fix the hydroxide molecules, the Cu atoms, the acetate and H_2O molecules in the bulk part as well as the anchoring oxygen attached to the surface. This reduces considerably the degrees of freedom of the simulation but it is necessary for optimizing the newly grafted FP molecules. In Figure 62, we plot the temperature as a function of simulation time for the surface studies performed for the grafting of FP molecules on the slab of CuOHAc. Four sub-sections corresponding to different simulations conditions are separated by dashed lines and a snapshot of the simulated cell is shown for each region. The first part lasts 1 ps. During this interval, the orientation and structure of the organic parts are optimized through the dynamical simulated annealing method. By fixing the bulk part and the anchoring oxygen and freeing the organic part, we obtain a first result on the stable configuration of the FP molecules on this surface at the end of the cooling ($\sim 0K$). Then, in a second part, we perform "free" FPMD dynamics, e.g. without applying friction forces on the atoms, to evaluate the stability of the molecules. A clear change of orientation of the fluorene parts is observed as well as a stabilization of the temperature at a low value ($\simeq$ 10K). From these results, we deduced that the fixing of anchoring oxygen constrains the fluorene part and does not allow for an exploration of the chemical bonding between organic and inorganic parts. In the third and fourth parts, we apply a thermostat at 50 K and then at 100K freeing the anchoring oxygen. We observe progressive detachment of the organic moieties from the surface along the last 2.5 ps of simulation. This behavior indicates that the chemical bond between the organic and the inorganic part is very sensitive to the fluorene fragments orientations, as expected in view of the larger size of the organic molecules with respect to the acetate counterpart. In addition, by visualizing the dynamics at 50K and 100K, we observed that this bonding depends critically on the hydroxide molecules interaction with the phosphonate parts (R-PO_3H^-). In particular, the low stability at the surface has been found to be very dependent on the presence of the hydrogen atoms saturating the phosphonate tetrahedra. The R-PO_3H^- group is composed by the anchoring oxygen (interacting with Cu layers), a double bonded oxygen (P=O) and a protonated oxygen (P-OH). In view of the pH conditions (basic) used experimentally in the insertion process, the experimental hypothesis is that the attachment to the surface occurs while the phosphonate groups are dehydrogenated and thus in the form R-PO_3^{2-}. In line with this reasoning, we observe a clear stabilization of the attachment of the FP1 molecules to the Cu surface when the dehydrogenated form is used. We associate this phenomenon with the reduction of the hydrogen-hydrogen repulsion observed between the proton of R-PO_3H^- and the ones of the surrounding hydroxide molecules. Using all these hints, we constructed a cell with the lattice parameters extracted experimentally which are the same than for the acetate system except of the c parameter. Experimentally, this parameter c_{exp} is obtained between 18.3 to 20.3 Å and we consider our model within this range c_{sim}=19.5 Å . Nevertheless, we still consider the same organic molecules density than the CuOHAc case and thus the double of the composition obtained experimentally for this system. In all further simulations, only the copper atoms are fixed. We observed a recurrent behavior in the vicinity of the dehydrogenated phosphonate groups. Surprisingly, once the system is stabilized, a small heating of the structure (up to 50K) induces an oscillation of the hydrogen atoms between the hydroxide molecules and the close by O^- ions of R-PO_3^{2-} fragments. The O-H bond in hydroxide molecules is then broken and the PO_3^{2-} transforms into PO_3H^- as initially thought. The structure then explodes due to the presence of free oxygens, previously belonging to hydroxide molecules. Therefore, we use the structure corresponding to the hydrogen sharing between OH and R-PO_3^{2-} groups and we modify it by adding manually one hydrogen atom per phosphonate. We also ensure that this new hydrogen does not point toward the hydroxide neighborhood. This procedure, the initial and final structure are exposed in Figure 63.

In the left part of this figure, the starting configuration in which the hydrogen is shared between hydroxide and phosphonate fragments is shown. The relevant phosphonate fragments environment is highlighted in the central part and the final structure is pictured in the right part of the figure. This last structure is stable since no more hydrogen exchange is observed and the distance between the anchoring oxygens of organic parts and the Cu sites remains lower than 3 Å even when the system is heated up to 50K. Confident in this crystal structure for the CuOHFP1 compound, we free the Cu atoms and we evaluate the stability of the structure at 50K. We also tested a smaller density of FP1 molecules as suggested by the experimental chemical composition. However, in this case, the simulated compound shows a clear detachment of a fraction of the organic molecules from the Cu hydroxide layer while another fraction stays attached. This situation is accompanied

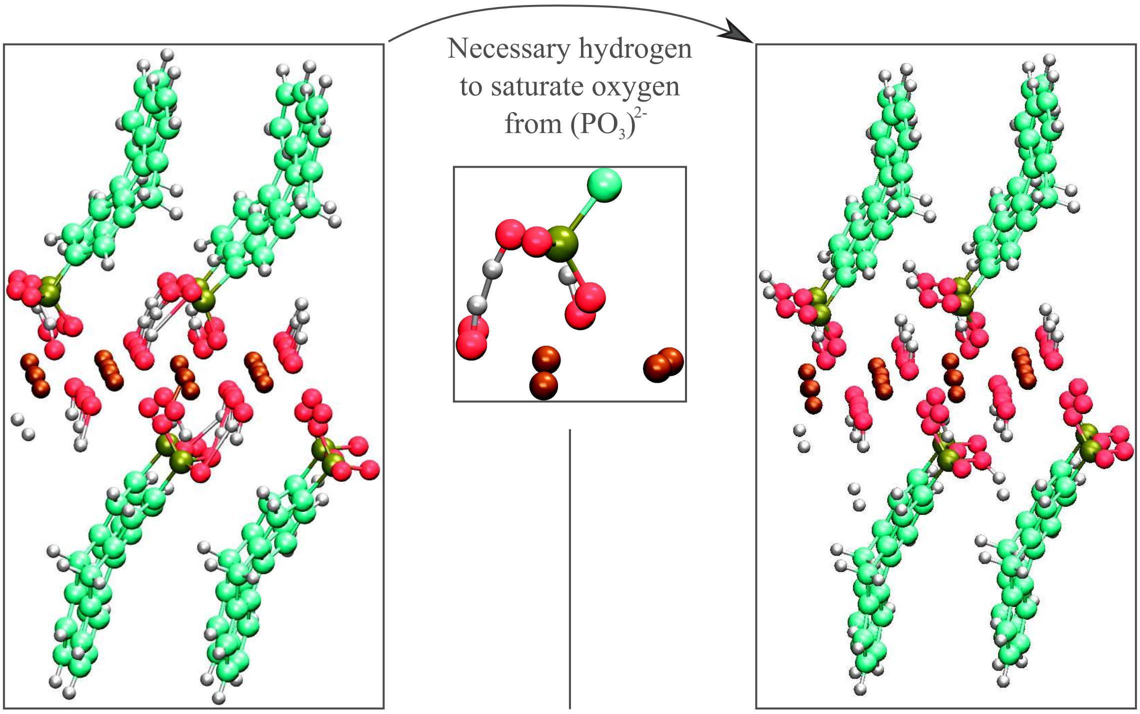

Figure 63 – Snapshots of the optimized structure of copper hydroxide fluorene monophosphonic system. The protonation of the anchoring oxygen of the phosphonate group $(PO_3)^{2-}$ is highlighted in the central part of the figure. This additional H atom is included in all further FPMD simulations performed on this structure (right part of the figure)

by a completely different orientation of the fluorene fragment of the attached and the detached organic molecules. There is also a deformation of the entire Cu layer and thus an instability of the structure after few picoseconds of molecular dynamics at 50K.

In Figure 64, we show the two corresponding simulation cells with the chemical compositions considered, $Cu_2(OH)_{4-x}(C_{13}H_{10}O_3P)_x$ with x=1 (left part of the figure) and x=0.5 (right part), labeled respectively, $CuOHFP1_{x=1}$ and $CuOHFP1_{x=0.5}$. The experimental cell parameters, indicated in Figure 64, and all computational details are identical for the two test cases. It is clear that the amount of free volume allowed for the fluorene molecules induces the FP moieties to detach from the Cu hydroxide surface as it is observed in the $CuOHFP1_{x=0.5}$ case. However, with the doubling of organic parts amount, a remarkably stable configuration is obtained for the $CuOHFP1_{x=1}$ system. The latter system is our reference structure for the CuOHFP compounds analyzed in the next section.

At this point, we established a clear simulation protocol that we use to obtain a model structure for the layered systems containing monophosphonic (FP1) or biphosphonic (FP2) molecules. These systems are studied within the next section. This procedure allows us to go beyond the design and construction of model crystal structures and move toward the analysis of structural, magnetic and electronic properties of these optimized systems. The simulation protocol established goes along the following steps. First, one

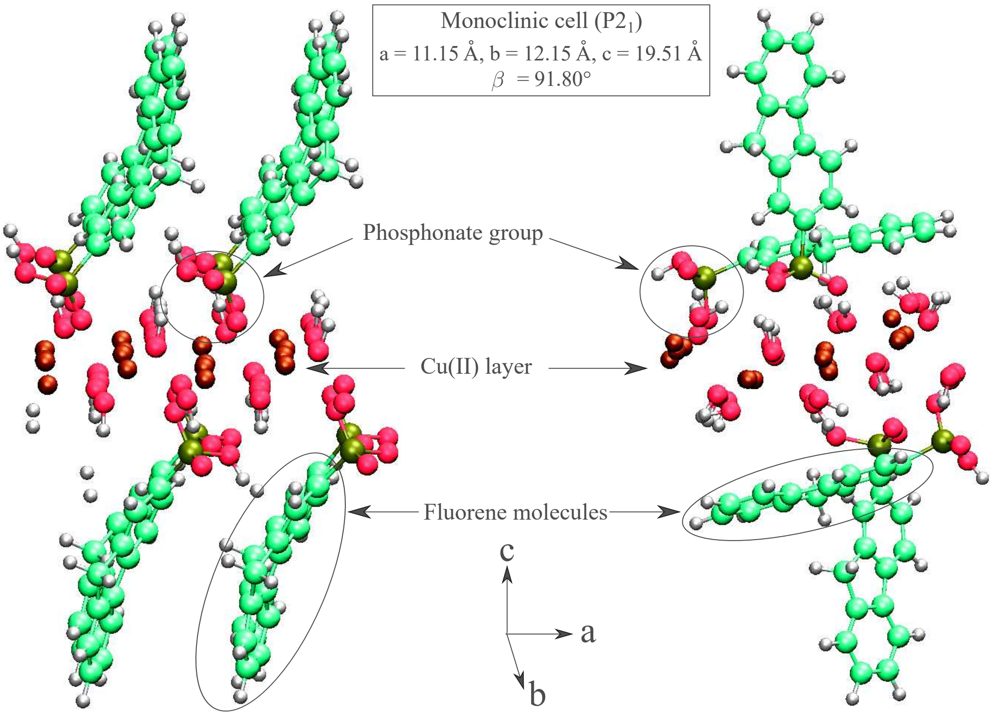

Figure 64 – Copper hydroxide fluorene monophosphonic (CuOHFP1) systems constructed starting from the well-known copper hydroxide acetate structure, exchanging the acetate groups by fluorene phosphonate molecules and considering the experimental information obtained on this compound. The left part shows a system with a density of organic molecules identical to the copper hydroxide acetate case $Cu_2(OH)_{4-x}(C_{13}H_{10}O_3P)_x$ with x=1. In the right part, we show the system $Cu_2(OH)_{4-x}(C_{13}H_{10}O_3P)_x$ with x=0.5, characterized by a density of organic molecules close to the experimental one (x≃0.31)

starts from a known structure (CuOHAc structure in this case) and try to adapt it to new chemical compositions. In a second step, a progressive constraining process permits to reduce the number of degrees of freedoms by optimizing part by part (freezing atoms) the new structure. Thus allows identifying the effect, the role and the optimized position of each molecular group in the system. It also points to specific atoms in the structure responsible for the complexity in the chemical bonding properties of the material. In the course of the "molecular engineering approach" followed in this section, we identified three main challenges, the first is the chemical composition to be considered and the second is the specific chemistry of the anchoring or linking part, e.g. understanding how the FP molecules attach to the Cu hydroxide surface. The third problematic, not considered hitherto, intimately linked with the "surface chemistry" just mentioned, is the water content that is a necessary component in the hybrid layered structures of interest. We omitted this parameter at first glance in order to reduce as much as possible the number of degrees of freedom to be taken into account. Once the composition is fixed and an optimized structure is found, we add water molecules in specific positions corresponding to adequate chemical environments with many hydrogen bonds (H-bonds) possibilities. We then perform further structural optimizations including finite temperature simulations to allow the diffusion of the water molecules included. This procedure is applicable in many situations in which not much is known about the chemistry and local arrangements in the synthesized hybrid materials. Typically, water molecules are introduced once a stable configuration is obtained in view of their ability to explore all the free volume available. We can now go to the FPMD study of our model systems including the water problematic in our investigations.

4.3 FPMD modeling of CuOHAc-based CuOHFP-LSH systems

4.3.1 Optimizing ideal structures

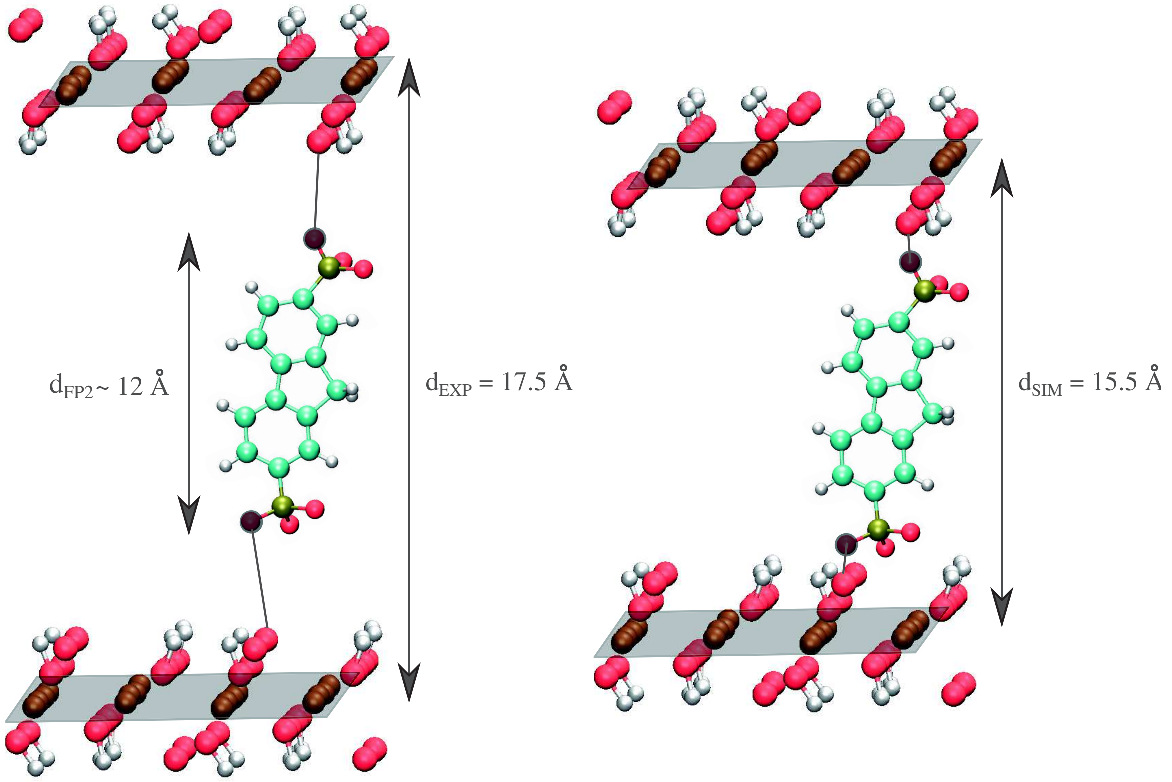

Figure 65 – Schematic representation of the insertion of fluorene biphosphonic molecules (FP2) in copper hydroxide acetate framework (the inorganic Cu layers are highlighted by the grey planes). In the left part, we show the incompatibility between the experimental interlayer distance (17.5 Å) and the organic molecule size (12 Å). In the right part, this distance is reduced (15.5 Å) to be able to stabilize a copper hydroxide biphosphonic system allowing a double anchoring (to both Cu layers) of the FP2 molecules

Through the last section, we established an optimization procedure with the corresponding FPMD protocol composed of a dynamical simulated annealing step followed by finite temperature molecular dynamics in order to test the stability of the systems considered. Therefore, we gave possible conformations and orientations that can be taken by the organic moieties within the interlayer space. We obtained an optimized CuOHFP1 compound structure characterized by an interlayer showing the FP1 molecules tilted and with a certain degree of interpenetration. In the case of the CuOHFP2 system, we faced a new problem which is the non-compatible nature of the observed interlayer distance with the corresponding model structure envisaged by experimentalists. As shown in the schematic representation of this structure in the left part of Figure 65, we note that the organic molecule (FP2) cannot bridge the two CuOH layers due to its small size (d_{FP2}) compared to the interlayer space characterized experimentally (d_{EXP}). Through these test simulations with different c-lattice parameters, we deduced that no anhydrous structure with such large d_{EXP} can be made stable for the case of CuOHFP2. We performed several tests to finally obtain a system in which both phosphonate ends of the molecule (R-PO_3H^-) are linked to the two CuOH layers in the initial configuration. This is indicated in the right part of Figure 65 with a new interlayer distance d_{SIM}. We then perform optimization steps through simulated annealing, free dynamics and finite temperature simulations at 50K.

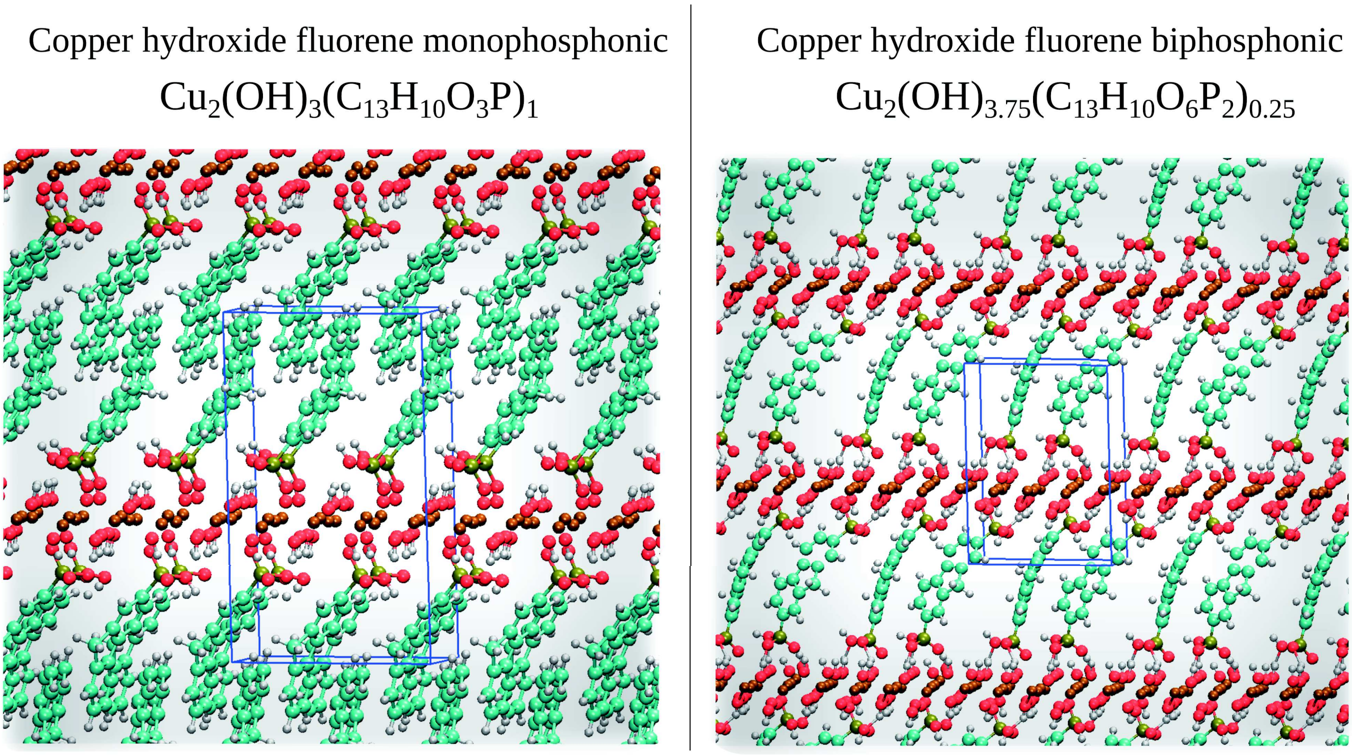
Copper hydroxide fluorene monophosphonic

$Cu_2(OH)_3(C_{13}H_{10}O_3P)_1$

Copper hydroxide fluorene biphosphonic

$Cu_2(OH)_{3.75}(C_{13}H_{10}O_6P_2)_{0.25}$

Figure 66 – Snapshots of the periodic structures studied in this project, copper hydroxide fluorene monophosphonic (left part) and copper hydroxide fluorene biphosphonic (right part) hybrid systems. These correspond to the optimized structures used in the FPMD simulations performed in this section

Despite the techniques employed for fixing specific fragments and optimizing the chemical environments, in all configurations, we obtain a stable attachment of the FP2 molecule at one end and a detachment of the phosphonate group at the other end of the organic molecules. This situation leads to a perturbation of the CuOH layer and thus to an unstable configuration of the system. Through this procedure, we picked up the most stable FP2 sub-system and we consider it as the reference test system in the case of CuOHFP2 material study. Therefore, we do not consider the finite temperature simulations destabilizing the structure, by restricting ourselves to the optimized structure obtained after the annealing step and corresponding to an interlayer space of $d_{SIM} = 15.5$ Å. In Figure 66, we present the optimized structure of the CuOHFP1 accompanied by the chemical composition considered on the left side. On the right hand side, the CuOHFP2 system is pictured with a cell dimension along the c-direction that differs by up to 2 Å from experiment ($d_{SIM} = 15.5$ Å) but representing an anhydrous structure optimized for this system.

In the next section, we perform a detailed analysis of the water molecules effect on the structural stability of these systems through the consideration of three different water contents $(H_2O)_y$ (y = 0, 0.5 and 1) named respectively, 0W, 0.5W and 1W. For the CuOHFP1 system the structure is not modified and water is included directly in the structure while for the CuOHFP2 system, we increase the interlayer distance to the experimental value (17.5 Å) and we use water molecules to compensate the remaining free volume in the system.

4.3.2 Structural analysis and water content effects

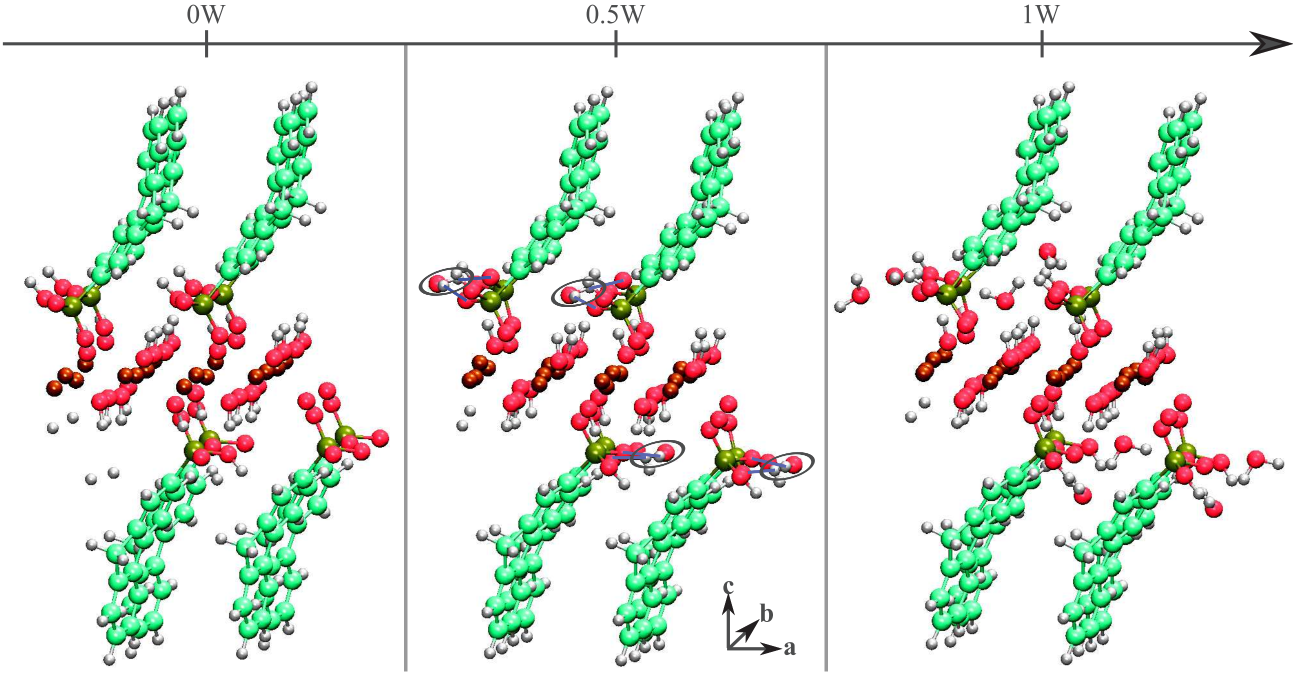

Figure 67 – Atomic structures of optimized hydrated copper hydroxide fluorene monophosphonic compounds $Cu_2(OH)_3(C_{13}H_{10}O_3P)_1{\cdot}(H_2O)_y$ with y = 0, 0.5 (4 water molecules) and 1W (8 water molecules). In the 0.5W system, water molecules are highlighted with black ellipses and the corresponding H-bonds are drawn in blue dotted lines

Given the initial structures established in the previous analysis, we move on to the study of the global structural properties of both CuOHFP1 and CuOHFP2 systems. We include water molecules in the structures highlighting the resulting optimized structures with different water contents. In Figure 67, we present the optimized structure of CuOHFP including four water molecules corresponding to the system "0.5W". Indeed, we use the stable anhydrous structure obtained previously (left part of Figure 66) and we place water molecules in specific positions before performing an annealing process to obtain a 0K optimized structure. We identify the specific positions occupied by the water molecules through the back ellipses in the figure. The water molecules initially placed randomly in the structure establish a hydrogen bonds network with the double bonded oxygen atoms of the anchoring phosphonate groups R-PO_3H^-. These H-bonds are highlighted with blue dotted lines (central part in Figure 67) and form also between water molecules and hydroxide groups.

At this point, we perform a free CPMD run to allow the system exploring more efficiently the configuration space. Surprisingly, water molecules undergo very small local rearrangements, mostly to relax the H-O distances and tiny rotations to fit the chemical environment. Water molecules are clearly increasing the rigidity of the system through the establishment of the H-bonds. These modifications of the structure, minor in appearance, ensure a stability of the atomic structure. Using the Nosé-Hoover thermostat [150, 151], we heated this system to 50K and we obtained a molecular dynamics trajectory enabling the construction of averaged atomic pair distribution functions characterizing the structure of the system.

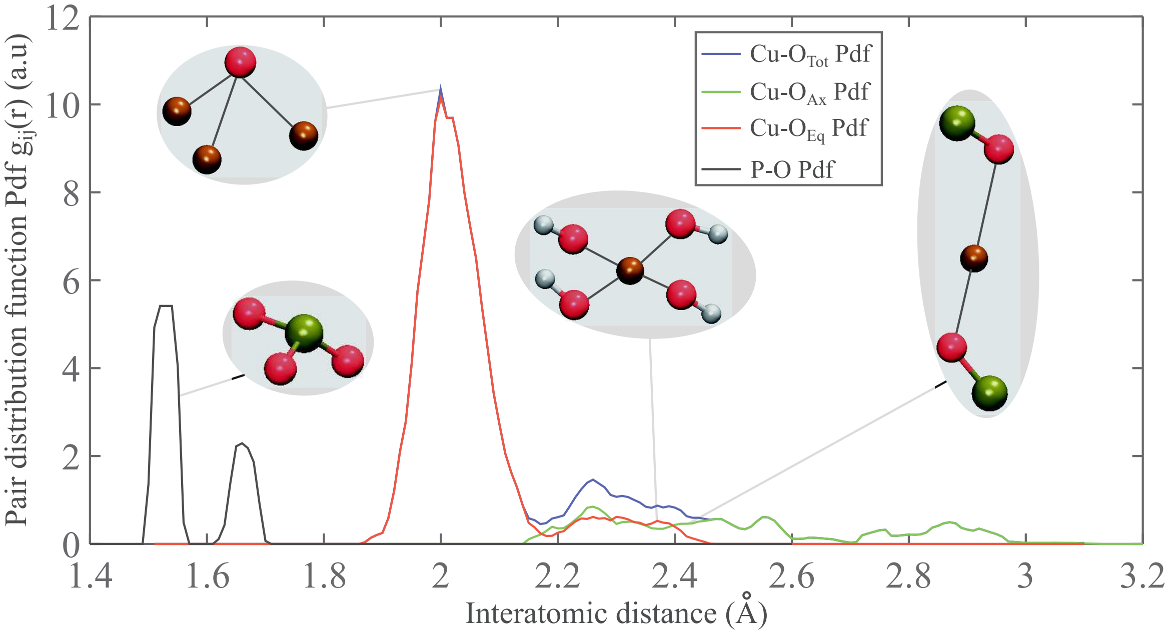

Figure 68 – Radial distribution function for different atomic pairs in the dehydrated copper hydroxide fluorene monophosphonic structure. The black line corresponds to the P-O pair and the blue line corresponds to the Cu-O pair. The latter is further decomposed in hydroxide linked (equatorial) oxygens (red line) and anchoring oxygens (axial) of the fluorene monophosphonic molecules (green line). Each situation is illustrated by a snapshot of the corresponding local atomic environment

In Figure 68, we show the resulting pair distribution functions (PdF) corresponding to different atomic pairs in the system. The Cu-O pair is first considered and labeled

"Cu-O$_{tot}$" in contrast with "Cu-O$_{Ax}$" (linked to organic molecules) corresponding to the axial oxygen atoms in the copper environment and "Cu-O$_{Eq}$" for the equatorial oxygens (linked to hydroxide groups) forming the octahedral environment of copper atoms. Each situation is pictured so that one can visualize which specific chemical environment is concerned by each PdF. In Figure 68, we immediately note that the blue curve (g_{CuOtot}) is superimposed with the red curve (g_{CuOEq}) for the main peak at 2 Å and with the green curve (g_{CuOAx}) above 2.5 Å. This result indicates that the O octahedral environment of Cu sites is divided in two oxygen types, the ones linked to the organic molecules (Axial) and those linked to hydroxide groups (Equatorial) characterized by long ($>$ 2.2 Å) and short ($<$ 2.2 Å) distances respectively. This structural analysis allows following the transformations of the structure when water is inserted or temperature is applied on the system. Additional information is embodied in the P-O distances in the system. In fact, two P-O bonds at around 1.55 Å are reflected by the peak obtained at this distance for the black curve (Figure 68). The third P-O bond of the PO_3H^- tetrahedra is characterized by the peak obtained at about 1.65 Å.

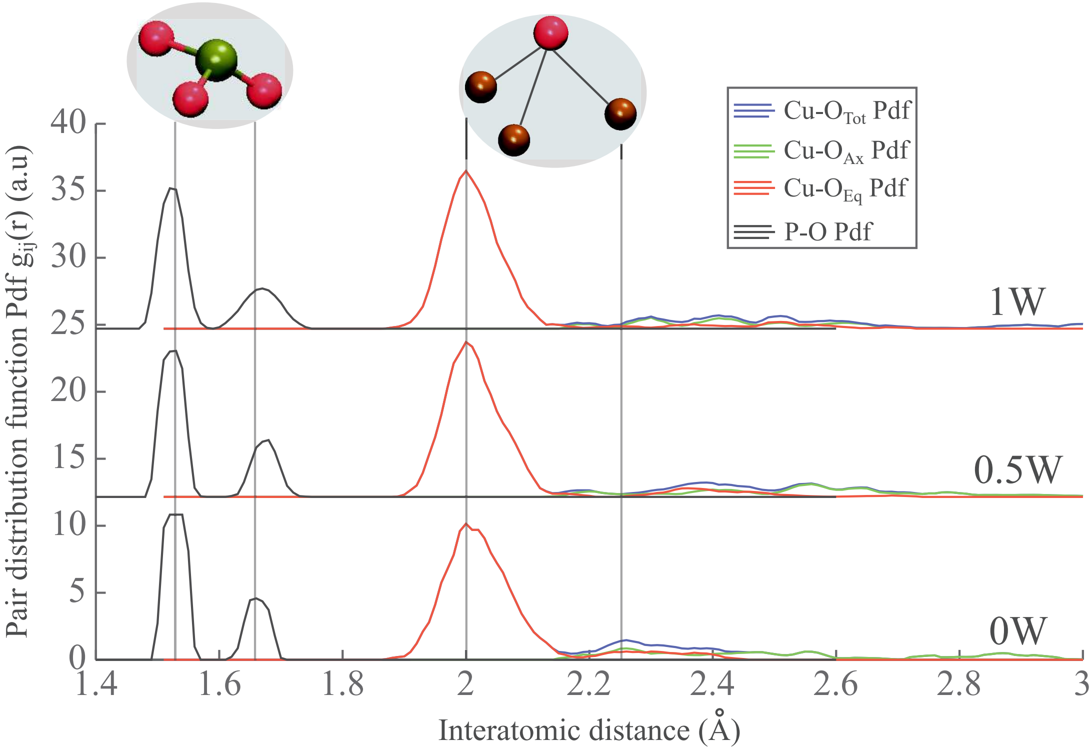

Figure 69 – Radial distribution function for different atomic pairs in copper hydroxide fluorene monophosphonic structures. The same color conventions than Figure 68 are adopted. The solid, dashed and dotted lines correspond to systems with different water contents (0W, 0.5W or 1W defined in Figure 67). The dashed and dotted lines are rigidly shifted in the y-axis

We now apply this structural analysis to all the test systems considered and in particular those differing by the amount of water in the simulated cell. When we include a certain number of molecules of water in the system, the objective is to stabilize the structure against finite temperature simulations, and in particular to stabilize the chemical bonding between the organic and inorganic parts. In Figure 69, we present the geometrical parameters described above in the case of CuOHFP1 system for the three water densities considered, 0W, 0.5W and 1W corresponding, respectively, to the inclusion of 0, 4 and 8 water molecules in the structure. As expected, the distribution of equatorial distances corresponding to the Cu-OH bonds are not influenced by the amount of water considered since only a negligible change of shape and no change of positions are observed for the peak localized around 2 Å (red and blue curves in Figure 69). However, for the axial distances, corresponding to Cu-O distances superior to 2.2 Å (green and blue curve), the distribution of these distances is changing as a function of water content. In particular, the effect of water on these Cu-O(FP1) bonds is to increase the distance and to constrain the local environment in order to stand the thermal motions induced in finite temperature simulations. In addition to this type of bonds, the analysis of the P-O bonds (black curves in Figure 69) indicate that the PO_3H^- tetrahedra and in particular the longest distance ($\simeq$ 1.65 Å) is slightly increasing as function of water content. This is explained by the establishment of the H-bond network forcing this anchoring group by slightly attracting the protonated oxygen toward the closest water molecule.

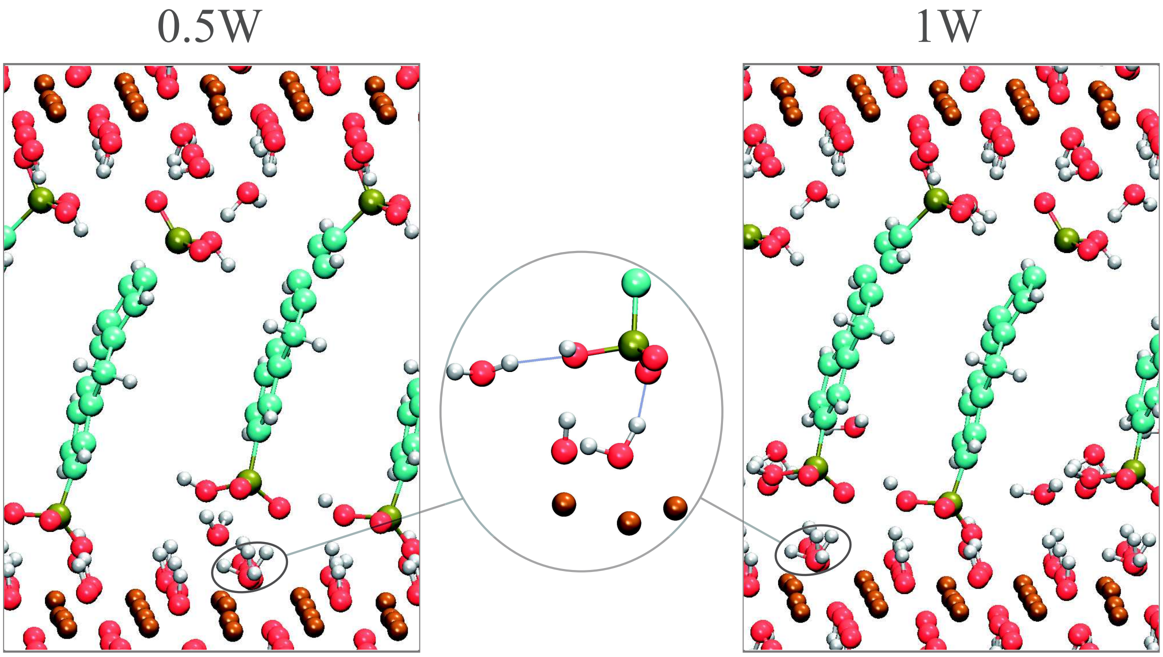

Figure 70 – Optimized structures of a hydrated copper hydroxide fluorene biphosphonic compound $Cu_2(OH)_{3.75}(C_{13}H_{10}O_6P_2)_{0.25}(H_2O)_y$ with y = 0.5 (left part) and y = 1 (right part). The specific local configuration of water molecules in "cavities" positions (see text) is represented in the central part of the figure

At this point, we explore the possibilities for the stabilization and water inclusion in the CuOHFP2 system. In this case, a clear structural discrepancy exists between the model considered and the experimental hypotheses made to explain the chemical compositions obtained. We found that, in most cases, the situation is the following: one FP2 molecule attaches forming a metal-organic bond on one layer but detaches from the other layer and the system is then stabilized in this form. One of our initial possible configurations is given in the right part of Figure 66. In this case, both organic molecules were attached on one layer (the same one) and detached from the second. However, we remind that this system was constructed with a primitive cell that is 2 Å smaller than the experimental system (d_{EXP} = 17.5 Å reduced to d_{SIM} = 15.5Å) along the $\vec{c}$-direction. Nevertheless, in view of the fact that such model cannot stand finite temperature simulations and that the optimized structure shows detached organic molecules in one layer, we add water molecules to fill the free volume. Thus, we can simulate a system with an interlayer distance as large as the experimental one in the $\vec{c}$-direction playing on the positions of water molecules to constrain the phosphonate groups detaching from the CuOH layer surface. Through several trial simulations, we observed that the configuration stabilizing the system is the one in which one FP2 is attached in one layer and the other molecule is attached to the other layer, as shown in Figure 70.

Our strategy is therefore two-fold. First, we optimize the structure of the system containing two different amounts of water and then we take the final configuration of these simulations and bring manually water molecules in the "cavities". This name is given to the regions highlighted in the inset of Figure 70, in which a water molecule is placed at the exact position supposed to be occupied by an anchoring oxygen of the R-PO_3H^- group. The composition of this model FP2 system is $Cu_2(OH)_{3.75}(C_{13}H_{10}O_6P_2)_{0.25}{\cdot}(H_2O)_y$ with y= 0, 0.5, 1. The corresponding lattice parameters are identical to the FP1 case (Figure 64) except for the c-parameter that is taken to be c = 17.5 Å within the experimental characterizations range. Our main conclusion is that the anchoring on both layer is not possible as suggested experimentally and a water molecule may be inserted in what we call the "free cavities", highlighted in the inset of Figure 70. These additional molecules significantly increase the size of the configuration space of the system so that our choices, e.g. the position of water molecules and orientations in the initial structure, may affect the exploration of the structural properties of this system. Nevertheless, we rely on the annealing calculations to optimize these positions and this solution allows identifying the Cu^{2+} sites in which organic anchoring does not occur. Therefore, we preserve the neutrality of the copper hydroxide layers, without affecting the composition selected. We observe the establishment of an H-bond network stabilizing the "free" phosphonate groups and saturating the corresponding charged oxygen as highlighted in the inset of Figure 70 by the blue dashed lines.

Once this structure constructed and optimized, we compute the corresponding pair distribution functions characterizing the Cu-O and P-O distances, respectively in blue and black lines in Figure 71. We perform this analysis for the two hydrated (dashed and dotted lines) model systems considered and compare to the anhydrous system (solid line).

In figure 71, we observe that the P-O distances (black curves) remain similar no matter the water content indicating the integrity of the two PO_3H^- groups at the ends of the FP2 molecules. Then, we see that the Cu-O distances (blue curves) are affected through the change of shape of the main peak at 2.01 Å as function of water. The width of this peak is reduced when water is included indicating the ordering (the four distances tend to be the same) of the equatorial distances (Cu-OH) coordinating the copper layers. For the second oxygen population, at higher distances from copper sites ($>$ 2.1 Å), we observe the appearance of a peak at 2.25 Åcorresponding to the new water molecules population

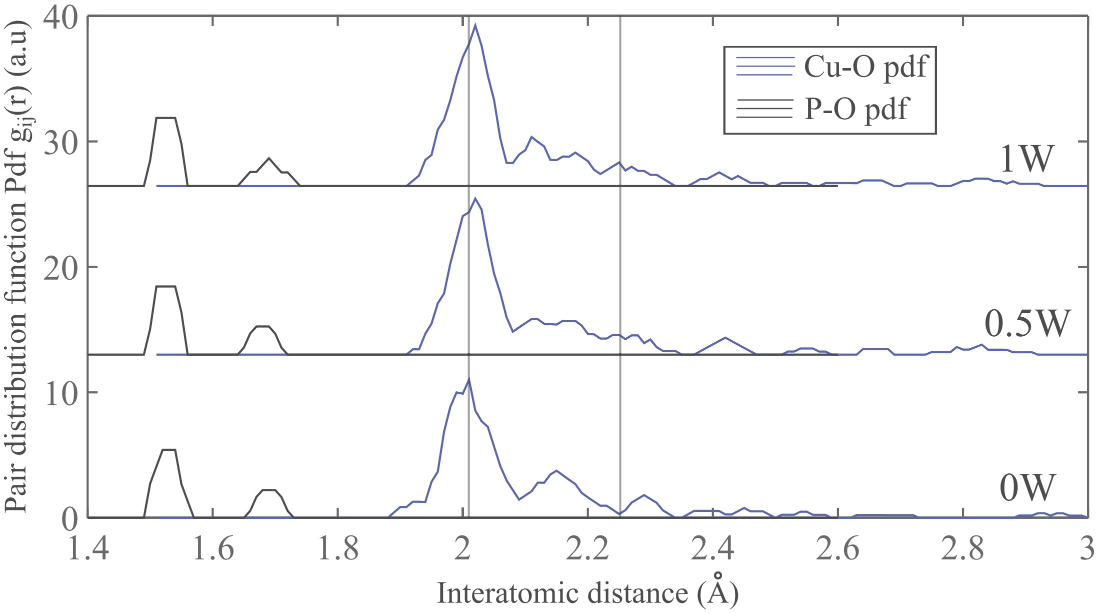

Figure 71 – Radial distribution function for different atomic pairs in the dehydrated copper hydroxide fluorene biphosphonic structure. The same color conventions than Figure 68 are adopted. The solid, dashed and dotted lines correspond to systems with different water contents (0W, 0.5W or 1W defined in Figure 67). The dashed and dotted lines are rigidly shifted in the y-axis

that we placed in the cavities left free by the detached organic molecules. The overall distribution of Cu-OH distances is similar but the axial distances (Cu-OFP2) are completely different since water molecules stay and establish H-bonds close to the copper layers (between 2.1 and 2.35 Å) in contrast with CuOHFP1 case. Indeed, in the latter, the oxygens corresponding to water molecules lie at higher distances ($>$ 2.3Å) from the copper surface.

Overall the systems obtained are optimized and the structures remain stable when finite temperature simulations are performed at 50K for the FP1 system while for the FP2 system, the stability is maintained only for very limited thermal motion, with temperatures very close to 0K.

4.3.3 Magnetic and electronic properties

Herein we focus on the magnetic and electronic properties of the CuOHFP1 system. We evaluate the predicted magnetic distribution and electronic structure for the CuOHFP1 system containing the largest amount content of water (1W). In the left part of Figure 72, we show the simulated crystallographic cell of this hydrated system. In the right part of this figure, a plot of the total density of states shows that the electronic gap estimated is low ($\simeq$0,8 eV) for a layered hybrid system expected to be an insulator. In comparison with the CuOHAc system, the estimation of the band gap is of the same order of magnitude (1.2 eV for CuOHAc). This is not surprising since the Cu environments are very similar in both structures. In addition, the clear symmetric nature of up and down spin densities of the crystal confirms the anti-ferromagnetic character of this compound.

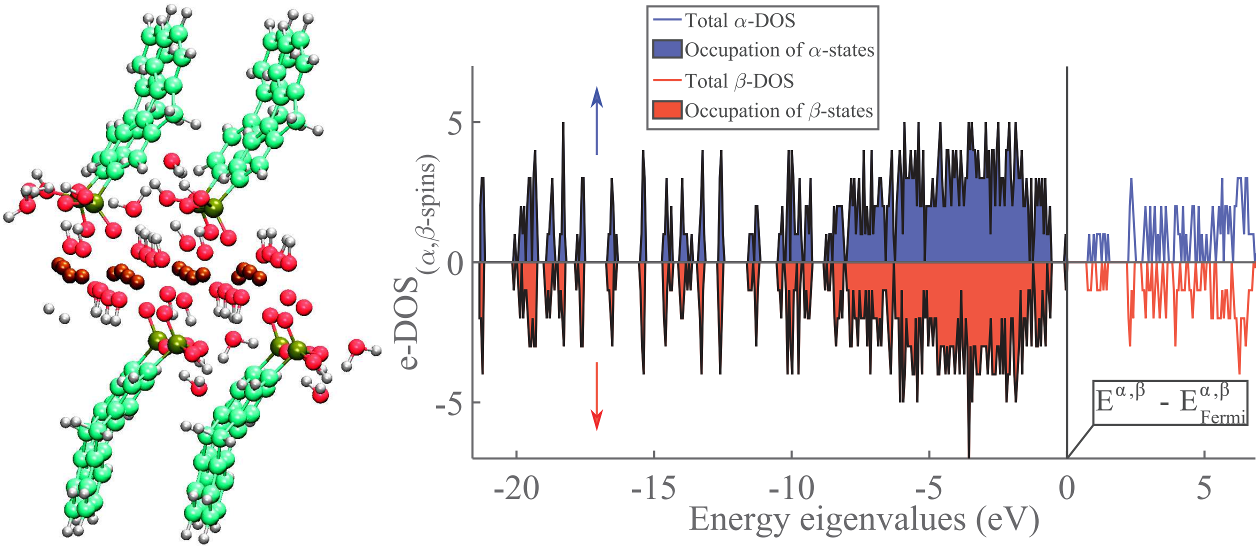

Figure 72 – **Left part:** Simulated cell of copper hydroxide fluorene monophosphonic structure $Cu_2(OH)_{4-x}(C_{13}H_{10}O_3P)_x{\cdot}(H_2O)_y$ with x=1 and y=0. **Right part**: total density of states (DOS) obtained for "↑" (in blue) and "↓" (in red) spins, with filled areas corresponding to occupied states

In terms of magnetic properties we computed the spin density localized on copper sites and the in-layer magnetizations obtained in the structure.

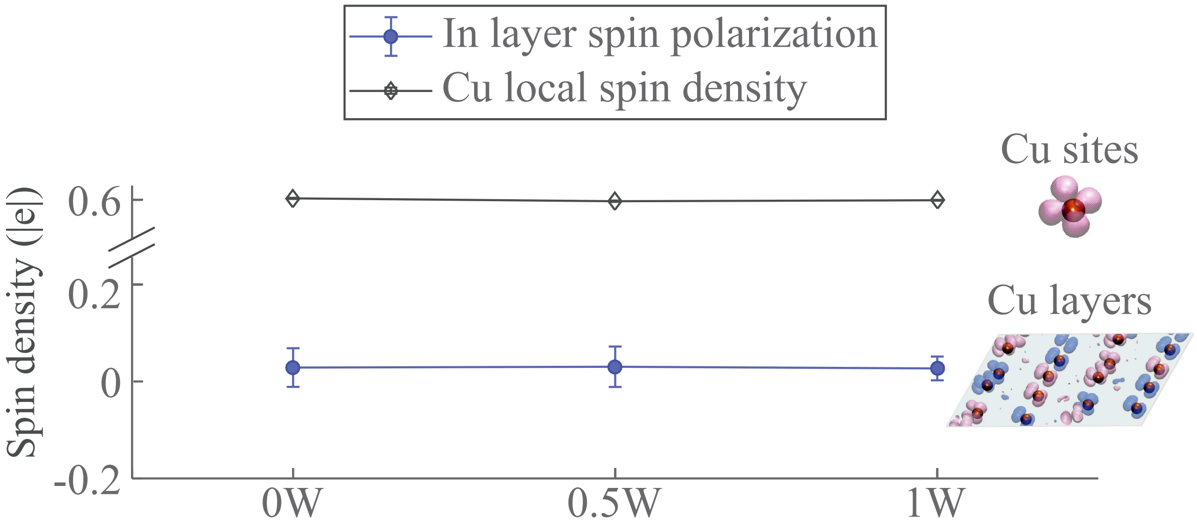

Figure 73 – **Cu-sites:** Evaluation of the local spin density (open diamonds) obtained on copper sites for copper hydroxide fluorene monophosphonic compounds with different amounts of water (0W, 0.5W and 1W). **Cu layers:** In-layer magnetization computed for the three systems considered. The errorbars are the standard deviations computed through the FPMD trajectory average performed to obtain these results (5 ps at 50K)

In Figure 73, we show that the water density in the system does not modify the local spin density observed on copper sites which remains close to 0.6 $|e|$ in agreement with the values obtained for our reference, CuOHAc system. In addition, the in-layer magnetizations are very low indicating a stable anti-ferromagnetic character of the system at the 2D level (copper layer). The error bars provided are obtained from averaging the computed properties from 11 configurations equally spaced selected from a molecular dynamics trajectory of 5 ps at 50 K performed for each of CuOHFP1 systems studied.

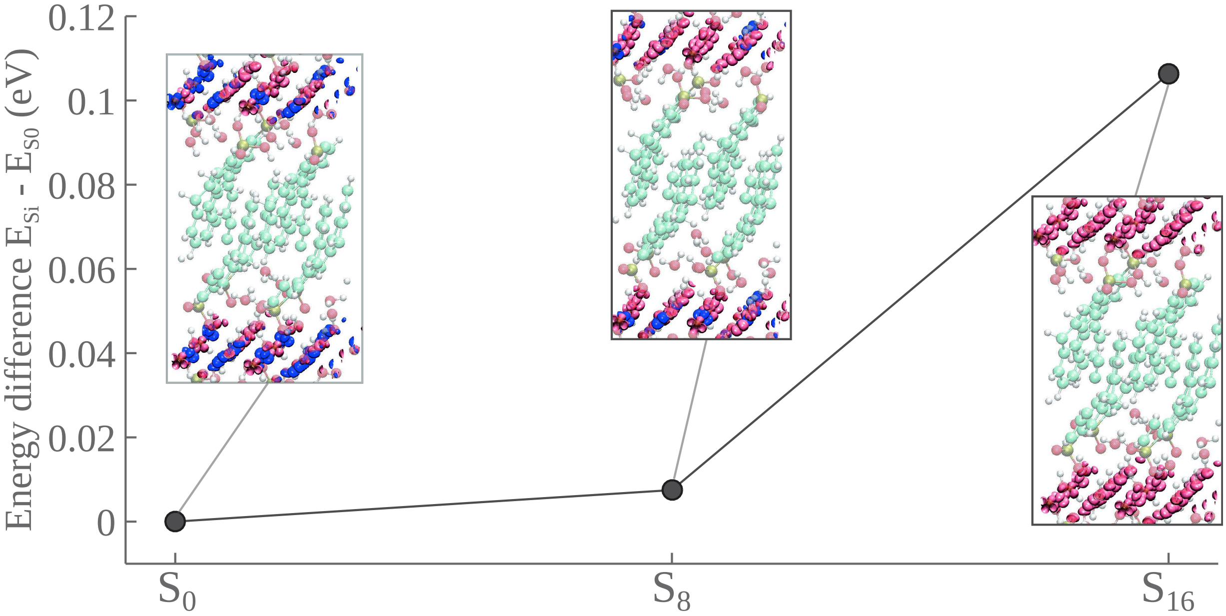

Figure 74 – Evaluation of the relative total energy of two ferromagnetic states (S=8 and S=16) with respect to the AF ground state (S=0) of the copper hydroxide fluorene monophosphonic material. The supercell considered is doubled in the $\vec{c}$-direction (608 atoms in the cell) to include two copper hydroxide layers. Snapshots of the atomic structures corresponding to each magnetic configuration are highlighting the different spin density isosurfaces (↑ in blue and ↓ in pink) obtained

To complete the comparison with the CuOHAc system, we construct a simulation supercell doubling the size in the $\vec{c}$-direction in order to fully contain two Cu layers, their chemical environments, water as well as the organic FP molecules grafted to both layers. We compute the local spin densities in the system for different magnetic states already considered for CuOHAc system. In Figure 74, the total energies of the AF system (S=0), the fully ferromagnetic system (S=16) and an intermediate configuration (S=8) are evaluated and represented as relative energies with respect to the AF state. This AF system is the most stable one (lowest energy). The local spin density distributions are represented in the three cases as solid surfaces (blue for α and pink for β spin densities) mostly localized around Cu sites in all the systems. We note that, in the AF configuration, the results shown in Figure 73 are confirmed since in this particular configuration, the in-layer spin densities do not exceed 0.08 $|e|$ for all the systems studied. Therefore these results show that this material is also a 3D anti-ferromagnet at the bulk level. Nevertheless, the S_8 system is only 0.007 eV less stable than the S_0 system while the S_{16} configuration is higher in energy (0.106 eV). The vanishing energy difference observed for the S_8 with respect to the S_0 system indicates that one could investigate further the effect of external stimuli (as the pressure) that may trigger a competition for stability between the AF and the S_8 ferromagnetic system.

4.4 Using FPMD modeling on CuOHFP-LSH systems to complement and enrich the experimental synthesis

We can use the rationale developed above to go beyond the water amount considered and move toward higher densities in the range of the experimental compositions obtained ($>$ 2W). In particular, we aim at studying the cases in which up to 24 water molecules are included in the structures. To this purpose we have devised a combined approach in synergy with our experimental colleagues to obtain benchmarks useful to design and study LSH materials. Therefore, in the present section, we target the structure and chemical bonding properties of the FP1- and FP2-containing Cu layered hydroxides successfully obtained within IPCMS. Our molecular engineering approach detailed above is exploited to provide the atomic structure of a compound for which only the interlayer distance and the chemical composition are known experimentally. With respect to the systems presented before, the compounds synthesized show a lower organic content than the equivalent CuOHAc: for CuOHFP1 (also referred to as **3a⊂Cu**) the composition is $Cu_2(OH)_{3.58}(C_{13}H_{11}O_3P)_{0.44}{\cdot}(H_2O)_{2.7}$ and for CuOHFP2 (also referred to as **6a⊂Cu**) the composition is $Cu_2(OH)_{3.54}(C_{13}H_{10}O_6P_2)_{0.23}{\cdot}H_2O_{3.5}$, respectively.
Therefore, the main objective of what follows is to enrich the experimental findings, especially regarding the internal arrangement of the FP molecules and the organic-inorganic interfacial interactions.

Theoretical Framework and Computational Procedure

The technical details on the FPMD approach are the same as those referred to in the previous sections. The **3a⊂Cu** and **6a⊂Cu** hybrid systems were initially built starting from the optimized configuration of the copper hydroxide acetate and setting the *c* lattice parameter to experimental values. The initial acetate groups were substituted with the **3a** and **6a** molecules in accordance with the structural formula experimentally determined and by introducing the correct amount of water molecules. In so doing, we obtained two models of 252 and 206 atoms for the **3a⊂Cu** and **6a⊂Cu** systems ($Cu_2(OH)_{3.5}(C_{13}H_{11}O_3P)_{0.5}{\cdot}(H_2O)_3$ and $Cu_2(OH)_{3.5}(C_{13}H_{10}O_6P_2)_{0.25}{\cdot}(H_2O)_3$), respectively. Energy optimization via a conjugate gradient algorithm was used to fully relax the electronic system. Then, we performed a damped FPMD to quench the surface model at T = 0 K. To allow the local environments of the FP acids to rearrange at finite temperature, we performed FPMD simulations increasing gradually the temperature up to 50 K constraining the Cu atoms and the hydroxide groups to their equilibrium positions during the initial 1 ps. The ionic temperature was controlled by Nosé-Hoover thermostat in all our canonical (NVT) simulations. The hydroxide groups were then released from all constraints and the systems were equilibrated for additional 5 ps. The analysis of the interlayer structures was performed averaging the data computed along these last 5 ps. The electronic properties of the water molecules and interlayers were analyzed by averaging over 25 uncorrelated configurations taken along the trajectory of 5 ps and computing the maximally-localized Wannier functions.

Structure and Fluorene Orientation

We identify the local molecular organization of the interlayer environment of **3a⊂Cu** and **6a⊂Cu** systems. Figure 75 shows a typical stable configuration of the **3a⊂Cu**. For such system, the fluorene mono-phosphonic acid is found to be chemically anchored to the copper hydroxide layer through the interaction of three Cu atoms and one O atom of the phosphonate group within an equilibrium distance in the range of 0.26 - 0.32 nm. Several local chemical scenarios have been explored for the phosphonate group, finding the mono-protonated form (Fluorene-PO_3H^-) the most stable one. The optimized system, equilibrated at finite temperature for about 5 ps, shows the fluorene moieties homogeneously tilted with respect to the plane of copper hydroxide by an angle of ∼66°, which induces a partial interpenetration of the aromatic parts.

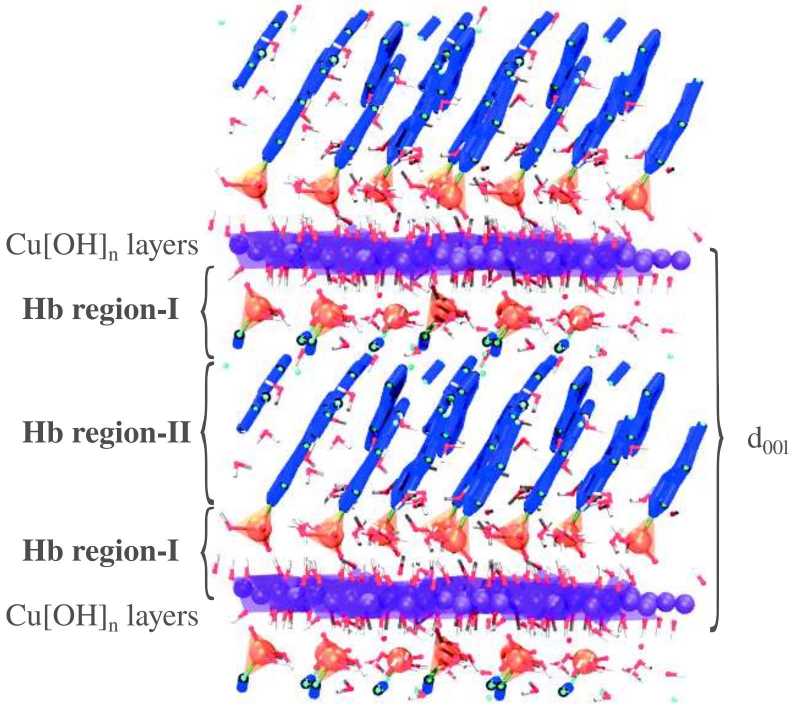

Figure 75 – Typical configuration of **3a⊂Cu** obtained via FPMD simulations (visualized supercell replicated 2×2×2 along x, y, and z for clearness). The interlamellar distance (d00l), copper hydroxide layers (Cu[OH]n) as well as the regions corresponding to H-bonding type-I and type-II are also indicated. Color legend: Cu atoms, purple; P atoms and polyhedra, orange; C skeleton of fluorene groups, blue; O atoms, red; and H atoms, white

For **6a⊂Cu**, we found the FP2 acids to be stably anchored to the copper hydroxide layer through one phosphonate group, chemically interacting with Cu atoms similarly to **3a⊂Cu** system. However, the second phosphonic group (opposite end of the attached fluorene moiety) remains at a larger distance with respect to the opposite Cu layer at an interatomic distance of 0.55 nm. Such configuration allows a water molecule to fit the space in-between the phosphonate group and the copper layer and to be coordinated by the three Cu atoms with distances of 0.23 - 0.27 nm (see Figure 76). Contrary to **3a⊂Cu**, in the case of **6a⊂Cu** the fluorene moieties are not homogeneously tilted with respect to the Cu layer and the tilting angle is found in between 60° to 75°. This difference can be explained by the larger free interlayer volume of **6a⊂Cu**, having half of the fluorene moieties within the interlayer with respect to **3a⊂Cu**.

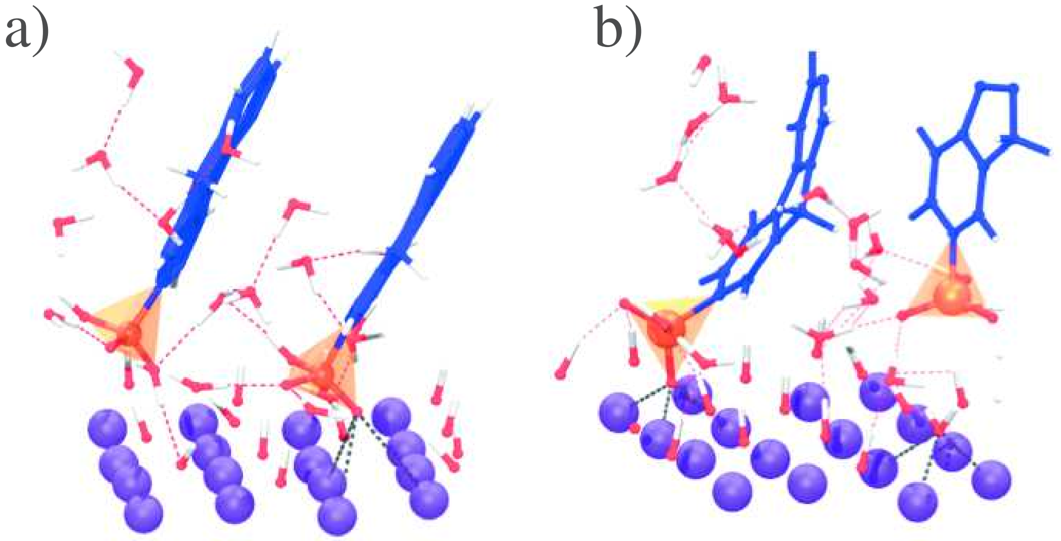

Figure 76 – The local bonding environments surrounding the phosphonate groups (-PO$_3$H) for **3a⊂Cu** and **6a⊂Cu** are visualized in (a) and (b), respectively. The interaction between Cu atoms with the -PO$_3$H$^-$ groups as well as with the O atoms of the water molecules are indicated as gray dashed lines. The H-bonding network is highlighted in red dashed lines

Chemical Bonding

To investigate the role of water, we analyzed the H-bonding network in terms of its electronic structure. To this aim, maximally localized Wannier functions (WFCs) have been proven to provide a powerful tool to rationalize the electronic structure of water [51, 52] as well complex disordered systems [53, 54]. The center of the charge density associated with a Wannier orbital can be thought of as representing an electron pair. Each oxygen atom is surrounded by four such centers (see Figure 77). Two are at a longer distance (0.48-0.52 Å) from the oxygen, along the O-H bond axis, and can be interpreted as the σ-bonding pairs of the water molecule, whereas the other two are located at a shorter distance (0.30-0.34 Å) from the O atom and correspond to the lone pairs. Within the interlayer regions of **3a⊂Cu** and **6a⊂Cu**, water molecules are found to be interacting with both the hydroxide groups of the copper hydroxide layers as well as the phosphonates groups by promoting an extended network of H-bonds. In these systems, a hydrogen bond involves three atoms: the hydrogen H, the oxygen atom O to which it is covalently bound and the acceptor oxygen O′, being the one of neighboring water molecules or of the phosphonate groups. The proton transfer coordinate υ = d(O-H) -

d(O′-H) provides a convenient structural order parameter to characterize the H-bonding network [55]. Values of $\upsilon \geq$ -1.25 Å indicate the occurrence of a well-formed H-bond [55].

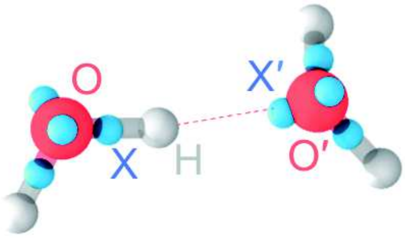

Figure 77 – Schematic representation of a typical hydrogen bond promoted by two water molecules. The oxygen (O), hydrogen (H) and WFCs (X) are indicated in red, gray, and cyan respectively. The acceptor oxygen and one of its lone pair WFC are indicated as O′ and X′, respectively

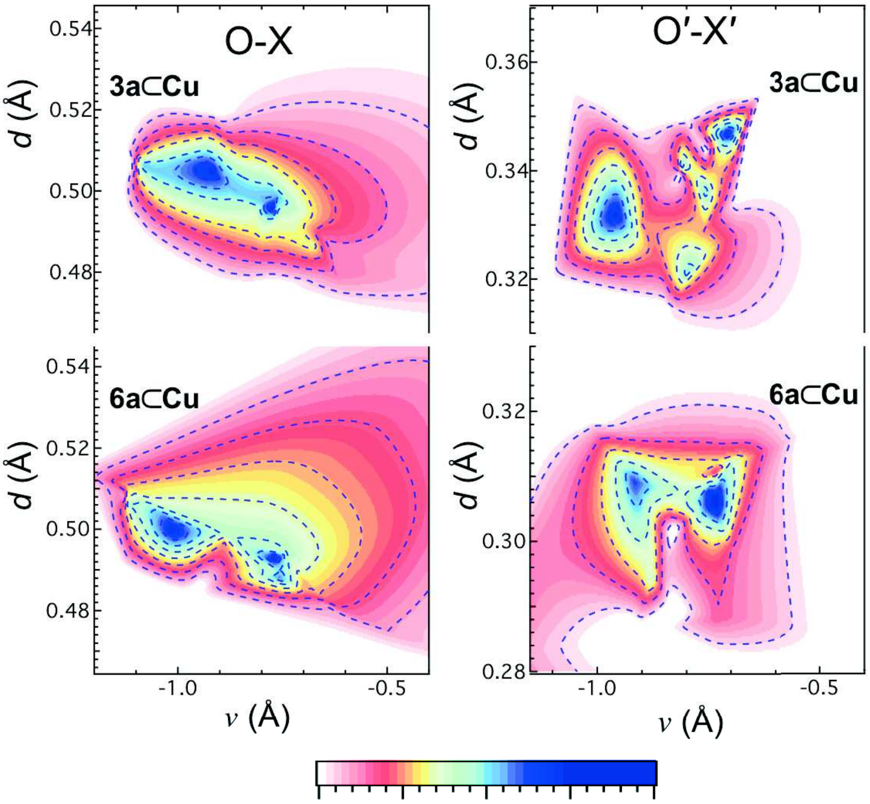

Figure 78 – Joint probability distributions of the proton-transfer coordinate υ = d(O-H) - d(O′-H) and of the distances of these oxygen atoms with their corresponding Wannier centers (Left: O-X; and Right: O′-X′). The upper and lower plots correspond to the data analyzed for **3a⊂Cu** and **6a⊂Cu**, respectively

Figure 78 shows the joint probability distributions of the proton-transfer coordinate and the one of the distances of the WFCs to the corresponding oxygen (O and O′, respectively). This analysis of the positions of the WFCs as a function of the proton-transfer coordinate υ demonstrates unambiguously that the local fluctuations of the H-bonding are associated with major rearrangements of the electron density. These results show that both **3a⊂Cu** and **6a⊂Cu** interlayers are characterized by an extended H-bonding network. Both systems show two main peaks in terms of υ (within -1.1 to 0.9 Å) and within υ (-0.8 to -0.7 Å), respectively, for similar d_{OX} ($d_{O'X'}$) distances. These two slightly different H-bonding interactions are ascribed to the H-bonds promoted by water molecules with the oxygen atoms of the phosphonate groups and with other neighboring water molecules (and hydroxide groups coordinating the Cu layers), respectively.

We can further split the interlayer environment of **3a⊂Cu** and **6a⊂Cu** in two different regions: (i) a first one located within 0.6 nm from the Cu atoms plane and (ii) a second region at distances larger than 0.6 nm from the Cu layers. The H-bonds networks within the two different regions are characterized by different properties. In particular, in region-I the H-bonding network is promoted by the involvement of water molecules, hydroxide groups, and phosphonates groups, whereas in region-II the H-bonding is promoted uniquely by the water molecules.

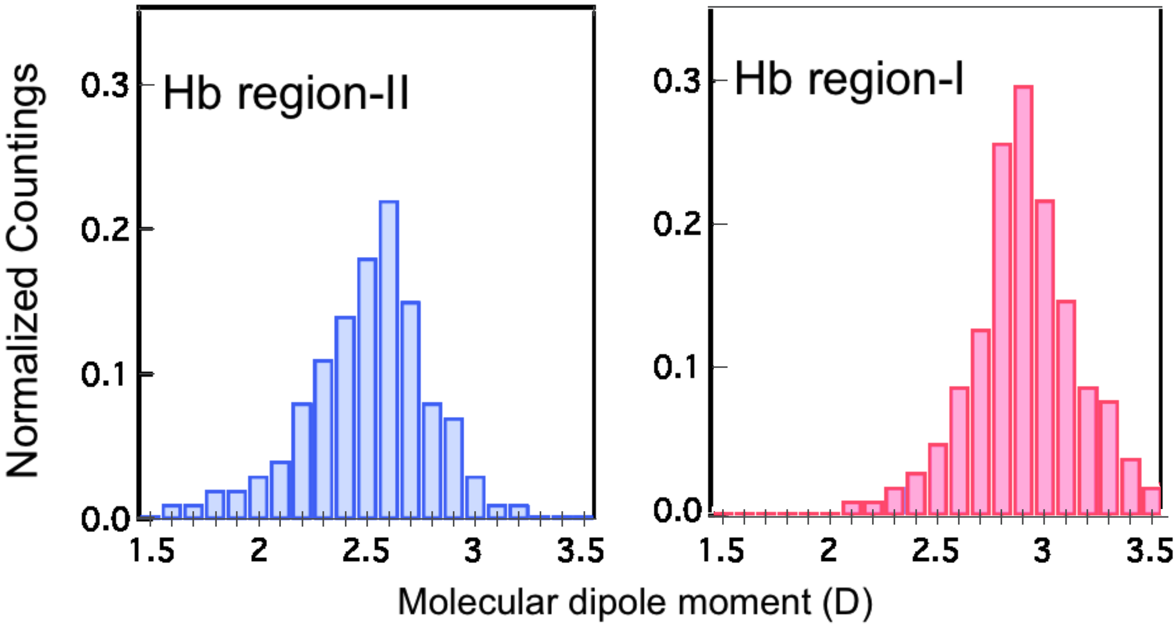

Figure 79 – Normalized distributions of the modulus of the molecular dipole moments of water molecules in the central (Left part: Hb region-II) and the interface (Right part: Hb region-I) regions of the interlayer space (as partitionned in Figure 75) for the **3a⊂Cu** compound

This difference can be made more quantitative by analyzing the electric molecular dipole moment of water molecules. Figure 79 shows the water molecular dipole computed employing the analysis of the WFCs. The dipole moment of water molecules within the center of the interlayer (within the fluorene moieties environment) is slightly lower than the dipole of water molecules in the proximity of the copper hydroxide layers and phosphonate groups (2.6 D vs 2.9 D). This is indicative of the fact that the electric field induced by surrounding molecules enhances the dipole moment of the single water molecule [51, 52, 53, 54, 55, 56].

4.5 A new layered copper fluorene phosphonate

In this section, we propose an application of the dipole calculations established in the second chapter to study a new hybrid material, copper fluorene phosphonate. The major interest in this material stems from the organic compound composing the material and the good quality of the characterization of its structure. In 2016, Nathalie Hugot and coworkers [57] synthesized a single-crystal compound of copper oxide fluorene phosphonate material for which an anti-ferromagnetic ground state is identified. The fluorenyl rigid moiety is functionalized with only one phosphonic acid group reminding the fluorene monophosphonic system studied in the previous sections. However, the full crystal data is provided in the present case, the chemical composition is $Cu(PO_3\text{-}C_{13}H_9)\cdot(H_2O)_3$ and the compound crystallizes in the space group $P2_1/a$, with the following lattice parameters: a= 7.4977(5) Å, b= 7.5476(5) Å, c= 22.3702(16) Å, $\beta = 97.794(3)°$. The sample is monophasic providing, through powder X-ray diffraction, a full set of atomic positions for the material. Therefore, we used the same protocol and procedure developed in our previous studies and performed an optimization of the structure within FPMD.

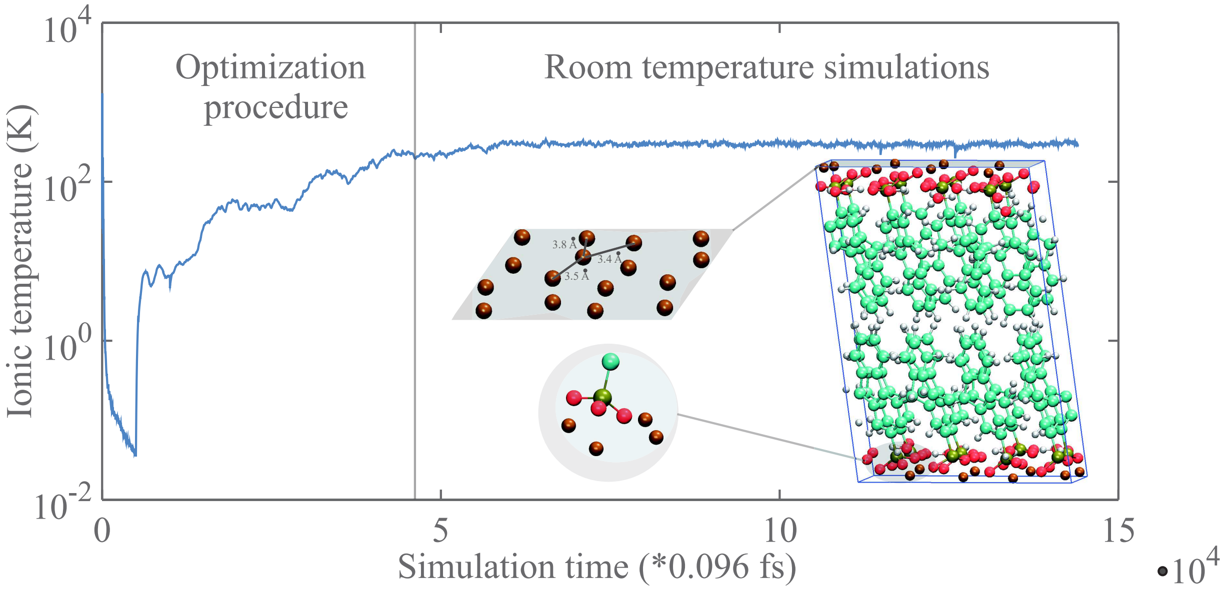

Figure 80 – Ionic temperature as a function of simulation time corresponding to the FPMD study of copper fluorene phosphonate system (CuOFP). This material has been synthesized and characterized by Nathalie Hugot et al. [57] in 2016. The chemical formula obtained for this compound is $Cu_2(PO_3\text{-}C_{13}H_9)\cdot(H_2O)$. We report the temperature evolution obtained in both the optimization step and the finite temperature FPMD trajectory. A snapshot of the corresponding structure highlights the arrangement of copper layers and the organic-inorganic interface regions

In Figure 80, we represent the temperature of the system as a function of the simulation time. We highlight the optimization region in which an annealing and free dynamics are performed leading to a heating of the system. Then, in the second region, the temperature is maintained at its room value, 300K. In addition, we represent the simulation cell considered for this material to visualize the organization of the organic and inorganic parts in this hybrid system. In contrast with the materials studied in the previous sections, the inorganic networks are not as ordered as in the copper hydroxide frameworks since the copper-copper distances are much higher (> 3.4 Å) and less homogeneously distributed among the system. In terms of organic-inorganic interface, the anchoring of the phosphonate is also different as highlighted in the insets of Figure 80. We remark that the phosphonate group is totally deprotonated (PO_3^{2-}) and that the three oxygens coordinate the neighboring copper ions. With this experimental structure, we performed 10 ps of room temperature molecular dynamics to collect the necessary information to compute the corresponding absorbance spectrum. As explained and tested on liquid water in the second chapter, the computation of the Fourier transform of the time auto-correlation function of the dipole information leads to an evaluation of the absorbance spectrum of the simulated system. In Figure 81, we report the resulting computed absorbance for the copper fluorene phosphonate hydrated system to be compared to the experimental IR spectrum (transmittance) exposed in the inset.

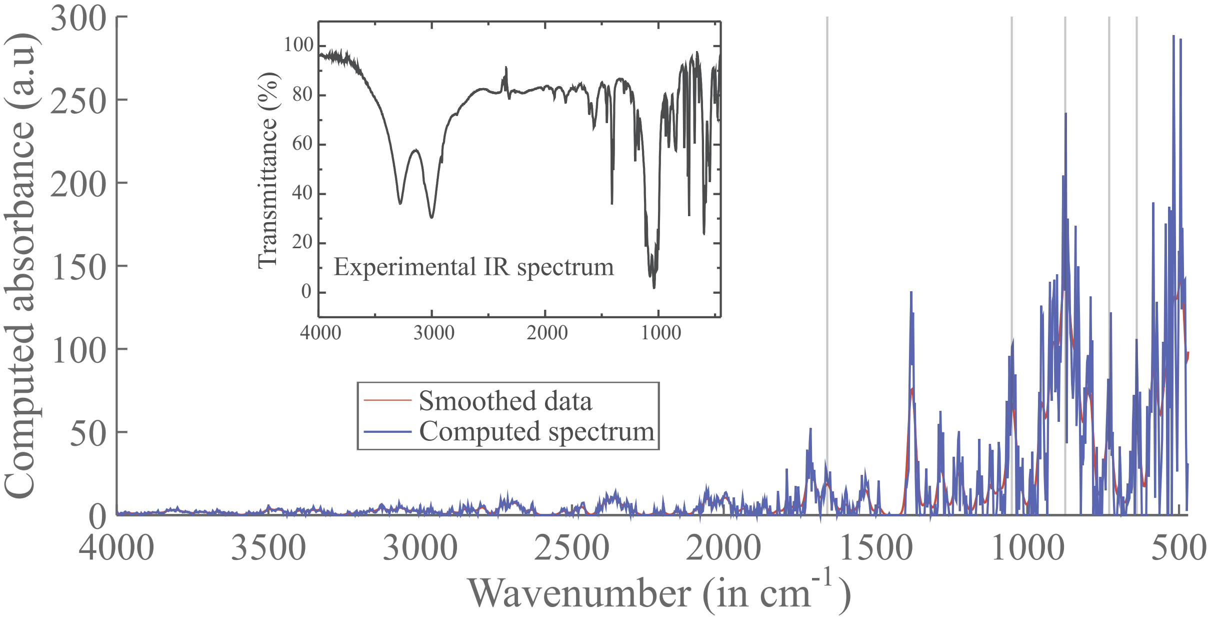

Figure 81 – Computed absorbance spectrum for the CuOFP material. This is the result of a 10 ps FPMD trajectory at room temperature. Several peaks are highlighted (vertical grey lines) and commented in the text. The inset shows the corresponding experimental transmittance spectrum for this system

In this figure, we plot the raw computed spectrum in blue dotted line and we perform a smoothing of the data (red solid line) allowing to distinguish the main peaks obtained, and in particular 5 peaks, with the vertical grey lines. We can distinguish the peak obtained at 1658 cm^{-1} characteristic of the bending modes of water molecules as observed in the analysis of liquid water. Three other peaks at 876 cm^{-1}, 730 cm^{-1} and 640 cm^{-1} are associated with the organic (fluorene phosphonate) fragments in the system but it is delicate to disentangle the contribution of the different vibrations. Nevertheless, the particular P-O single bond stretching mode can be clearly identified to be at 1059 cm^{-1} in very good agreement with the experimental value (1060 cm^{-1}) obtained for the 9H-fluorene-2-phosphonic acid $C_{13}H_9PO(OH)_2$ [57]. The next natural step in this procedure is to complement these studies with the synthesis of a pure fluorene phosphonate single-crystal and perform the corresponding FPMD study based on the experimental atomic structure. The simulation protocol for the computation of this IR spectrum is well established and tested on liquid water systems and therefore, complementary experimental data may dissipate the obstacles encountered in this analysis.

Conclusions & perspectives

In this work, we trace the route for the exploration of the structure, properties and magneto-structural couplings observed in hybrid lamellar materials. We performed realistic simulations through FPMD methods allowing to complement experimental observations and predict unknown behaviors in several temperature and pressure conditions.

In the case of copper hydroxide acetate, we constructed our simulation supercell from the experimental crystallographic characterization of Svarcova et al. [3] and we demonstrate the stability of the system at room temperature. Since a magneto-structural coupling exists in this material, i.e. a pressure-induced magnetic transition [4], we perform successive contractions and extensions corresponding to the experimental deformations observed under pressure. A transition from an anti-ferromagnetic (S=0) ground state to a ferromagnetic one occurs for the total spin S = 8 system. The transition range obtained (1.2 to 3.5 Gpa) is in very good agreement with the experimental value (1.2 GPa) confirming the realistic nature of these simulations. We demonstrate the role of in-layer magnetization in the promotion of ferromagnetism in the system under pressure [47]. We also performed a detailed analysis comparing the use of non-linear core corrected pseudo-potentials (NLCC) and the so-called "semicore" pseudo-potential for the description of the transition metal ions (Cu^{2+}). We demonstrate the improvement of magnetic and electronic properties description with the semicore description and we use it in all our further calculations.

Starting from the inorganic framework of this compound, i.e. copper hydroxide layers, we inserted fluorene monophosphonic and biphosphonic molecules to construct new hybrid materials, copper hydroxide fluorene phosphonates. Guided by the chemical composition obtained experimentally by Guillaume Rogez and Quentin Evrard from the chemistry department (DCMI) of our institute (IPCMS), we constructed several test configurations for which we established a suitable treatment well adapted to stabilize the structure and go toward the study of the properties. As an output of this project, we obtained atomic structures that match the experimental compositions and, in particular, in the case of water content that plays an important role. We were able to perform several precise studies on the protonation and deprotonation of phosphonate groups, the role of hydrogen bonds networks due to water molecules and the influence of the ratio of organic molecules density with respect to hydroxide content. These issues are at the heart of experimental challenges for the design and synthesis of hybrid lamellar compounds. The study of the insertion of the biphosphonic system led us to propose new crystallographic cells that best fit the chemical composition and that are compatible with the experimental interlayer distance (17.5 Å). In addition, this exploratory part reveals an important role of the anchoring group PO_3H^- on copper layers stability.

Finite temperature simulations showed to be particularly suitable for such structural stability issues. We constructed a scientific article with our experimental colleagues (submitted for publication in the "Advanced Functional Materials" journal), in which all these insights obtained on fluorene phosphonate compounds are included. In the framework of room temperature molecular dynamics, we computed the total electric dipole of the cell allowing us to obtain the absorbance spectrum of another hybrid material, copper fluorene phosphonate.

Overall, the application of FPMD methods opens new possibilities of elaborating, "virtually", complex chemical compounds and study their properties to complement, test and go beyond the interpretations widely used by experimental researchers.

Several perspectives are opened by this PhD work. We organize them along three main lines, **methodological improvements**, exploration of **new hybrid systems** and the construction of **materials databases**.

- **Methods**

  From a methodological point of view, we can obtain a finer and systematic treatment of the magnetic structures through the study of all the spin states that show interesting magneto-structural effects. In particular, the total spin values from 0 to 8 are compatible with the supercell considered (32 Cu atoms) and lead, through our preliminary tests, to similar effects of competition for stability against the AF state. Such investigation features low values of the total energy differences between these low ferromagnetic states and the AF ground state of copper hydroxide acetate ($\leqslant 0.005$ eV). A systematic study of these configurations leads to clear indications on the possibilities and limits of using FPMD methods in probing magneto-structural effects in hybrid lamellar systems. Within the same line, we could extend the study performed as a function of pressure to the fluorene phosphonate compounds at the price of a considerable computational cost (608 atoms to be treated in the corresponding supercell). To improve the description of electronic properties and in particular the band gap calculation, we perform hybrid functional (B3LYP) calculations being aware that the computational time necessary for such investigations is enormous.
  Finally, the pressure can be applied on the materials in an alternative way. This is done through the application of a barostat to our simulated cells, by using the methods pioneered by Andersen, Parrinello and Rahman [123, 167, 168]. Such calculations have already been used within the context of the study of glassy systems by Bouzid et al. [169] with a very good agreement between the computed and the experimental structure factors.

- **New materials**

  In line with the studies invoked in the previous chapter and the ANR project HYMN ("HYbrid Multiferroic Nanomaterials" *ANR-14-CE07-0004*), we plan the study of new families of organic molecules that can be inserted within the transition metal hydroxide framework to obtain specific multifunctional materials. Different series of such molecules are reported in the following figure.

$Y = COOH$ or PO_3H_2
$R = H$, F or OH

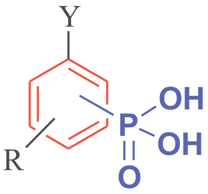

①

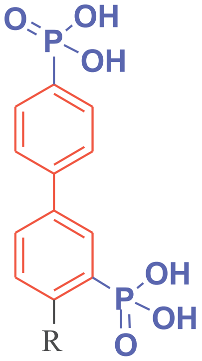

②

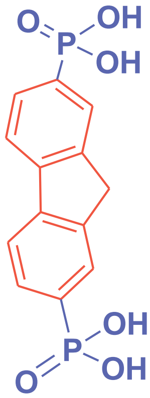

③

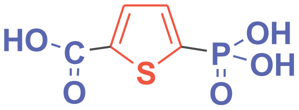

④

In the case of the first series (**1** in the above figure), the compound includes phosphonobenzoic derivatives ($Y = COOH$) or diphosphophonic acid compounds ($Y = PO_3H_2$). The group R aims at modifying the electronic properties of the aromatic ring with the presence of either one strong inductive withdrawing atom (F), one strong mesomeric donor group (phenol) or one innocent atom (H). The presence of a fluorine atom, which is known to be isosteric with a hydrogen atom, will be useful to compare the synthesis of hybrid materials in which only modifications of the electronic properties of the organic precursor are involved. In the two next compounds (**2** and **3**) the rigid platform is a biphenyl unit while the case of fluorenyl group corresponds the biphosphonic system studied in the previous chapter. With these compounds, the aim is the extension of the size of the rigid platform to add some flexibility at the bis-phenyl junction (compound **2**) that may produce non-centrosymmetric polar hybrid materials. In the case of the last molecule considered (**4**), the resulting lamellar system is expected to possess prochiral faces allowing for the inclusion of a heteroaromatic rigid platform. With a thiophene ring, the production of a more polar aromatic ring that could impact the polarity of the final material is expected. This direction is further motivated by a recent study of J. M. Rueff et al [170] showing that a rigid thiophene bis-phosphonic acid derivative produced the non centrosymmetric material $Mn_2(O_3P\text{-}C_4H_2S\text{-}PO_3)\bullet(H_2O)_2$ due to the orientation of the heteroaromatic rings in the final material.

In addition to the variation of the interlayer organic species, we are interested in the use of another transition metal (cobalt) that is widely used in such lamellar structures. It has been shown that cobalt systems present interesting magnetic behaviors that are more easily measurable than for copper-based system due to the high magnetic moment of Co atoms comparing to Cu. As explained in this paper, the cobalt hydroxide fluorene phosphonate systems synthesized by our colleagues show ferrimagnetic ordering of Co^{2+} ions. It is further assumed that this results from an unbalanced antiparallel alignment of the moments due to tetrahedral and octahedral oxygen environments of cobalt ions. This is of particular importance since the unknown details of distributions of tetrahedral and octahedral sites in the system were the main obstacles to the application of FPMD methods to the study of such system [171]. The recent focus on the experimental structural characterization of these compounds [172] is therefore an excellent sign for us to start the construction and study of cobalt-based materials. The magneto-electric effect obtained in such compounds is also reported in our combined experimental-theory paper cited previously.

- **Materials databases**

A different but promising research field is the materials' properties databases construction that is also considered to be a larger scale perspective to this work. The current context of materials modeling research ranges from the first-principles approaches at the atomic scale to the continuum models used for macroscopic mechanical or thermal properties simulations. The ideal concept of multi-scale modeling, as it is often advertised, is a challenging problem since the known physics models are not, in general, scale invariant. I am convinced that machine learning methods based on large sets of training samples and statistical data analyses are interesting ways to understand the various properties of materials at different scales. An example of such project is at the heart of the scientific objectives of the Commonwealth Scientific and Industrial Research Organisation (CSIRO), i.e. developing and implementing cutting-edge computational techniques for materials modeling purposes. Therefore, active learning and heuristic optimization algorithms in conjunction with molecular and materials simulations codes allow for the construction and exploitation of hybrid materials databases. This would allow to extract characteristic properties allowing for a better classification of these complex materials. Nowadays, these ambitious objectives become possible since high performance computers are available to automate and optimise computational materials design workflows.

Appendix A

Matrix representation of KS-DFT

Objective: Use a matrix representation allowing to solve the self-consistent Kohn-Sham equations [142]

We consider the Kohn-Sham equations (2.31) in Hartree atomic units ($\hbar$=1/(4$\pi\epsilon_0$)=e=m_e=1) for a system with electron density n($\vec{r}$), N_{e^-} electrons and M ions

$$\left(-\frac{1}{2}\Delta + v_S(\vec{r})\right)\phi_i(\vec{r}) = \epsilon_i\phi_i(\vec{r}) \tag{A.1}$$

with v$_S$($\vec{r}$), the Kohn-Sham potential

$$v_S(\vec{r}) = \int d^3r' \frac{n(\vec{r'})}{|\vec{r}-\vec{r'}|} + v_{xc}(\vec{r}) - \sum_{I=1}^{M}\frac{Z_I}{|\vec{r}-\vec{R_I}|} \tag{A.2}$$

Z$_I$ being the atomic numbers of the ions. One can write the potential and the kinetic term as a "Sham Hamiltonian $\hat{h}_S$" and finally write (in bracket notation)

$$\hat{h}_S|\phi_i\rangle = \epsilon_i|\phi_i\rangle \tag{A.3}$$

Then, we consider a basis set $|\chi_k\rangle$ to represent our wavefunction $|\phi_i\rangle$

$$|\phi_i\rangle = \sum_{k=1}^{p} C_{ki}|\chi_k\rangle \tag{A.4}$$

In this basis, the KS equations are written as

$$\hat{h}_S\sum_{k=1}^{p} C_{ki}|\chi_k\rangle = \epsilon_i\sum_{k=1}^{p} C_{ki}|\chi_k\rangle \tag{A.5}$$

applying the bras $\langle\chi_{k'}|$ and considering the general case of non orthogonal basis $\langle\chi_{k'}|\chi_k\rangle \neq$

$\delta_{kk'}$, we obtain

$$\begin{aligned}\sum_{k=1}^{p} C_{ki}\left(\langle\chi_{k'}|\hat{h}_S|\chi_k\rangle\right) &= \epsilon_i \sum_{k=1}^{p} C_{ki}\Big(\langle\chi_{k'}|\chi_k\rangle\Big) \\ \sum_{k=1}^{p} C_{ki}H_{kk'} &= \epsilon_i \sum_{k=1}^{p} C_{ki}S_{kk'} \\ \sum_{k=1}^{p} C_{ki}\left(H_{kk'} - \epsilon_i S_{kk'}\right) = 0 &\end{aligned} \tag{A.6}$$

In these expressions, we introduce the matrix notations in bold and the subscripts corresponding to the lines and columns respectively. Three different matrix sizes are considered in the following derivations, the Hamiltonian ($\boldsymbol{H} = H_{kk'}$) and overlap matrices ($\boldsymbol{S} = S_{kk'}$) are $(p \times p)$ matrices, the eigenvalues matrix ($\boldsymbol{\epsilon} = \epsilon_i\delta_{ij}$) is a diagonal matrix $(N_{e^-} \times N_{e^-})$ and the coefficient matrix ($\boldsymbol{C} = C_{ki}$) that is of size $(p \times N_{e^-})$. Equations (A.6) can then be written as

$$\boldsymbol{HC} = \boldsymbol{SC\epsilon} \tag{A.7}$$

The next task is to $\boldsymbol{C}$ that make $\boldsymbol{H}$ diagonal. For that, we first determine the matrix $\boldsymbol{X}$ so that $\boldsymbol{S}$ becomes diagonal

$$\boldsymbol{X}^\dagger\boldsymbol{SX} = \boldsymbol{I} \tag{A.8}$$

with $\boldsymbol{X}^\dagger = \overline{\boldsymbol{X}^T}$ and $\boldsymbol{I}$ the identity matrix of the corresponding dimension. Therefore, equation A.7 becomes

$$\begin{aligned}\boldsymbol{X}^\dagger\boldsymbol{HC} &= \boldsymbol{X}^\dagger\boldsymbol{SXX}^{-1}\boldsymbol{C\epsilon} \\ &= \boldsymbol{X}^{-1}\boldsymbol{C\epsilon}\end{aligned} \tag{A.9}$$

so that

$$\begin{aligned}\boldsymbol{XX}^\dagger\boldsymbol{HC} &= \boldsymbol{C\epsilon} \\ \Rightarrow \boldsymbol{C}^{-1}\boldsymbol{XX}^\dagger\boldsymbol{HC} &= \boldsymbol{\epsilon} \\ \Rightarrow \boldsymbol{C}^{-1}\boldsymbol{XX}^\dagger\boldsymbol{HXX}^{-1}\boldsymbol{C} &= \boldsymbol{\epsilon}\end{aligned} \tag{A.10}$$

posing $\boldsymbol{C_0} = \boldsymbol{X}^{-1}\boldsymbol{C}$ and $\boldsymbol{H_0} = \boldsymbol{X}^\dagger\boldsymbol{HX}$, finally one obtains

$$\boldsymbol{C_0}^{-1}\boldsymbol{H_0}\boldsymbol{C_0} = \boldsymbol{\epsilon} \tag{A.11}$$

which looks just like a usual diagonalisation problem except that the hamiltonian $\hat{h}_s$ is function of the Kohn-sham orbitals $\{\phi_i(\vec{r})\}$, in other words, the matrix elements $H_{kk'}$ of $\boldsymbol{H}$ are functions of the elements C_{ki} of the coefficient matrix $\boldsymbol{C}$. Therefore the self-consistent solution is obtained from the following iterative procedure

1. We choose an initial N-representable (sum of squares of atomic orbitals $\chi_k(\vec{r})$)

2. We distribute the density $\mathrm{n}_{In}(\vec{r})$ on a "grid" in position space $(\vec{r})$
3. The Kohn-Sham potential $\mathrm{v}_S(\vec{r})$ is computed on the same "grid"
4. The elements of $\boldsymbol{H}$ are $\boldsymbol{H_0}$ are calculated for $\boldsymbol{S}$ fixed
5. $\boldsymbol{H_0}$ is diagonalised, thereby determining $\boldsymbol{C_0}$, then $\boldsymbol{C}$ and the orbitals $\phi_i(\vec{r})$
6. Compute the output density $\mathrm{n}_{Out}(\vec{r}) = \sum\limits_{Occupied} |\phi_i(\vec{r})|^2$
7. Perform the convergence test, verifying the condition $\sqrt{\int \Big(n_{Out}(\vec{r}) - n_{In}(\vec{r})\Big)^2 d\vec{r}}$
8. If no convergence reached, the new n_{In} density is a mix of n_{Out} and the previous ones and we restart at step 2.

Appendix B

Collection of results

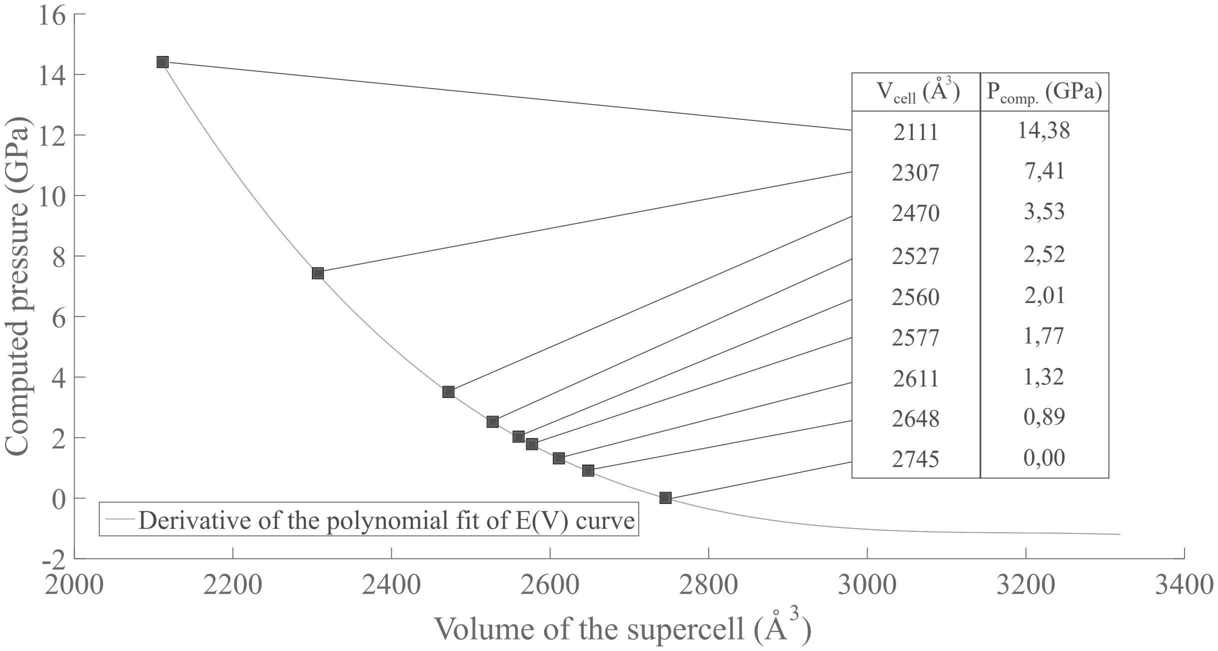

V_{cell} (Å^3)	$P_{comp.}$ (GPa)
2111	14,38
2307	7,41
2470	3,53
2527	2,52
2560	2,01
2577	1,77
2611	1,32
2648	0,89
2745	0,00

Figure 82 – Equation of state, i.e pressure as function of volume corresponding to the compression of copper hydroxide acetate system starting from the optimal structural groud state identified in the parametric space of crystallographic lattice parameters. The deformations of the system are evaluated following the experimental observations by Suzuki et al [4] of copper hydroxide acetate lattice variations when pressure is applied along the $\vec{c}$-direction

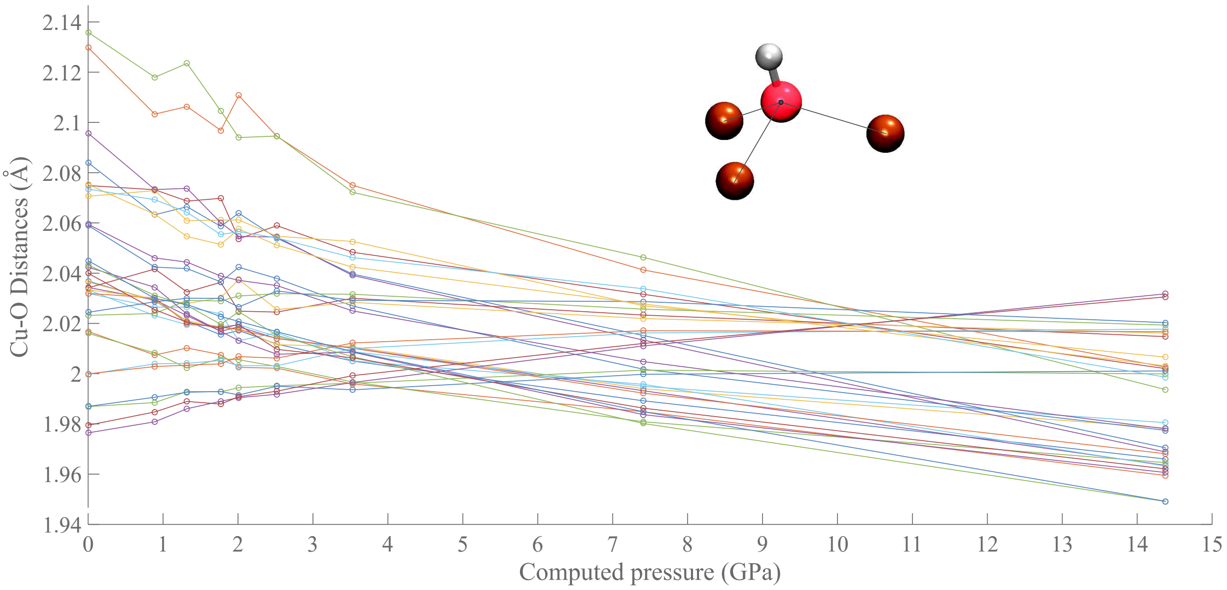

Figure 83 – Full set of copper-oxygen distances in the case of hydroxide linked oxygens as a function of external pressure for the S=0 anti-ferromagnetic configuration of copper hydroxide acetate system

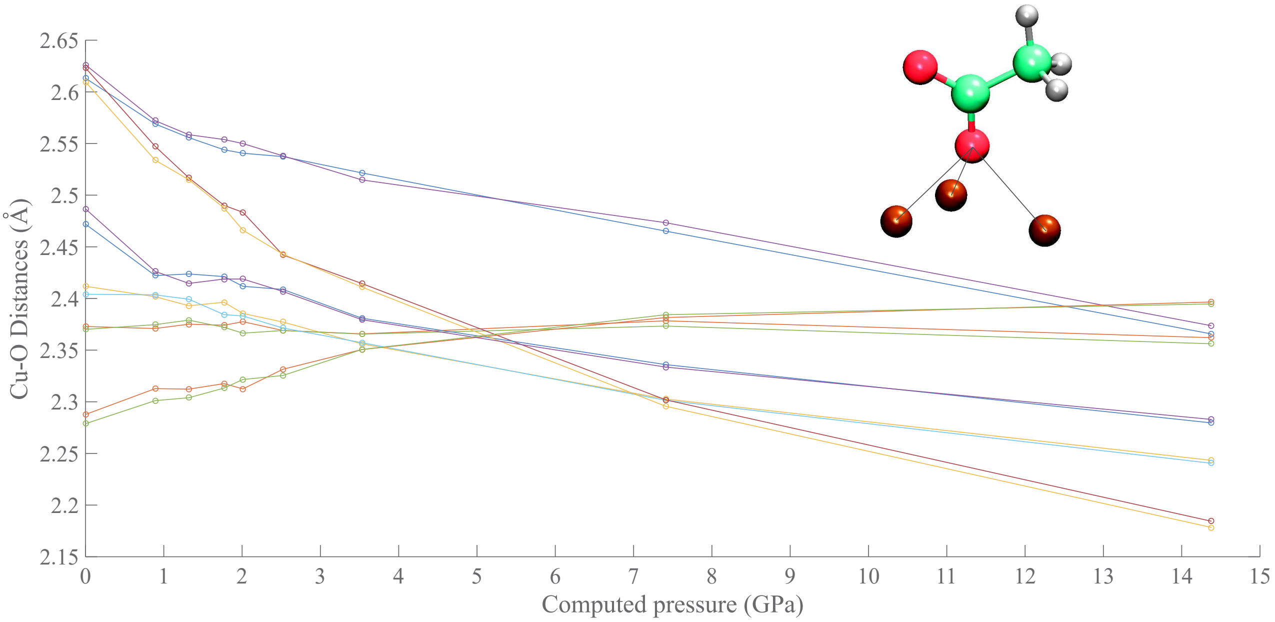

Figure 84 – Full set of copper-oxygen distances in the case of acetate linked oxygens as a function of external pressure for the S=0 anti-ferromagnetic configuration of copper hydroxide acetate system

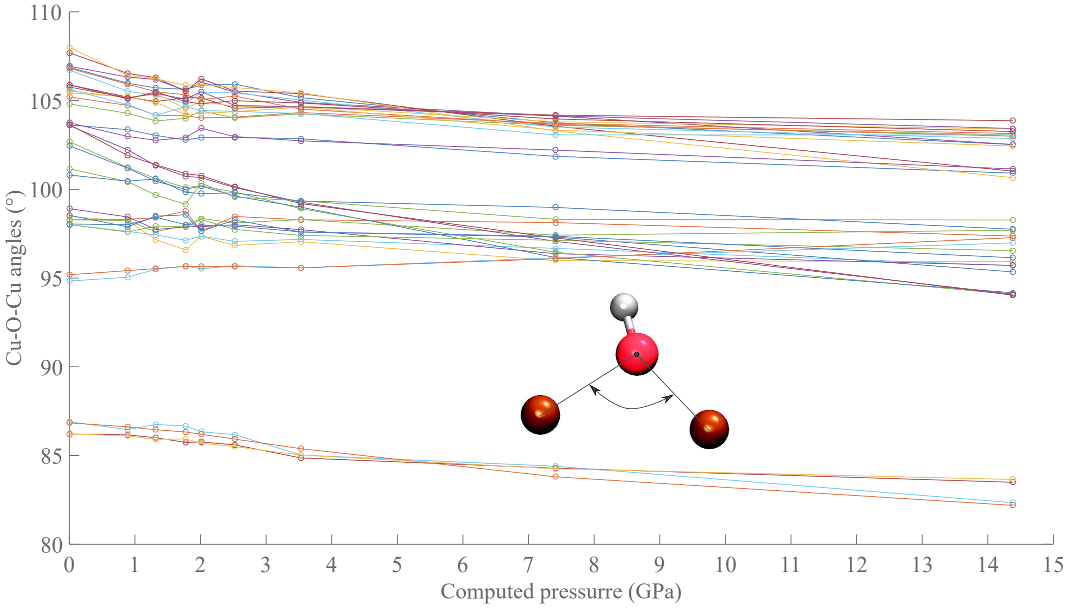

Figure 85 – Full set of copper-oxygen-copper angles in the case of hydroxide linked oxygens as a function of external pressure for the S=0 anti-ferromagnetic configuration of copper hydroxide acetate system

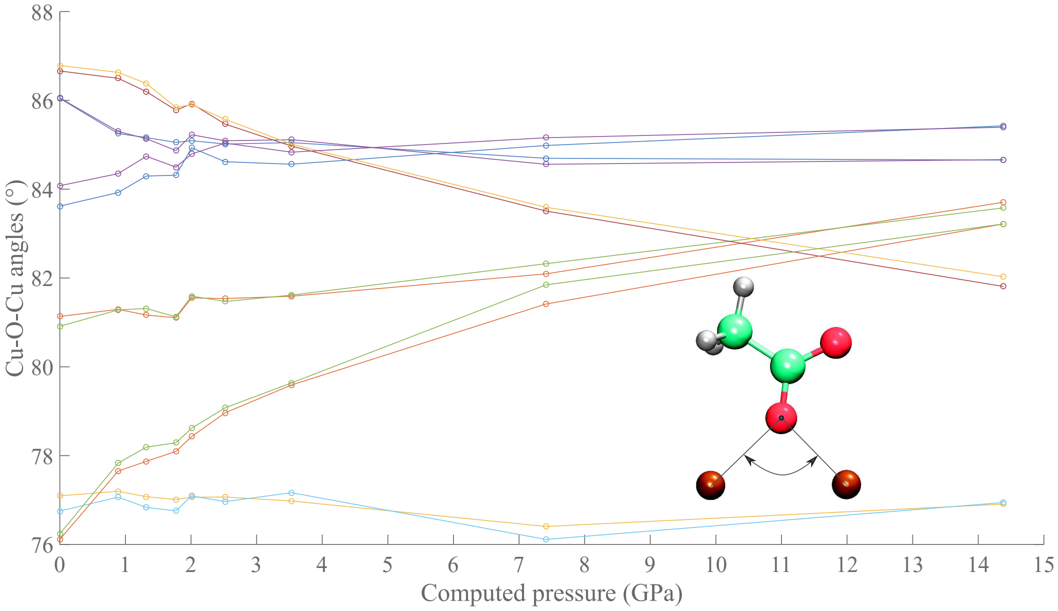

Figure 86 – Full set of copper-oxygen-copper angles in the case of acetate linked oxygens as a function of external pressure for the S=0 anti-ferromagnetic configuration of copper hydroxide acetate system

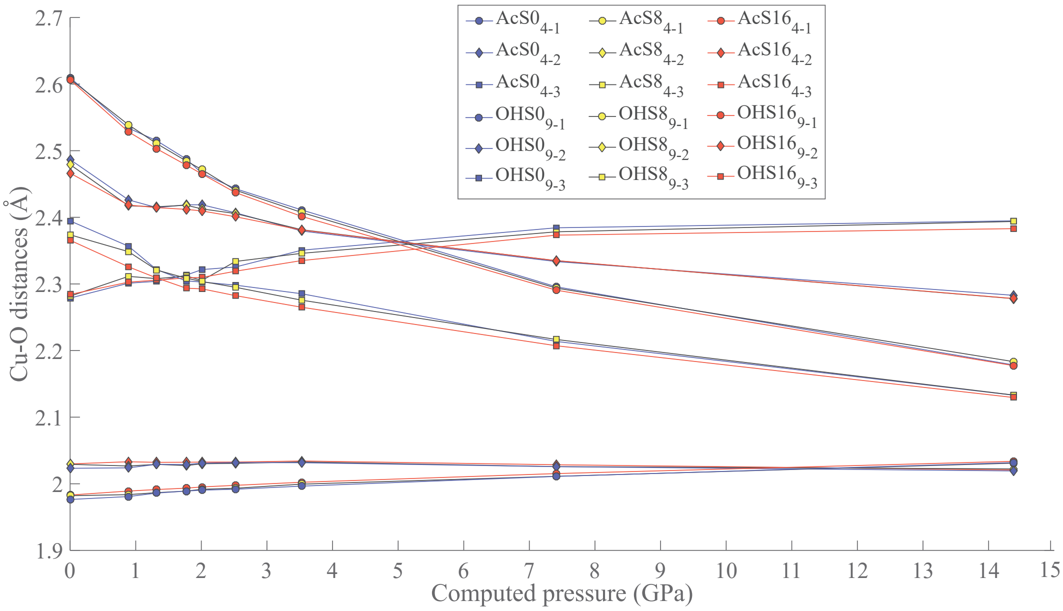

Figure 87 – Selected Cu-O distances for acetate linked oxygens (solid lines) and hydroxide linked oxygens (dashed lines) evaluated as a function of external pressure for the AF (S_0 in blue), the half spin polarized S_8 (yellow) and F (S_{16}red) magnetic configurations

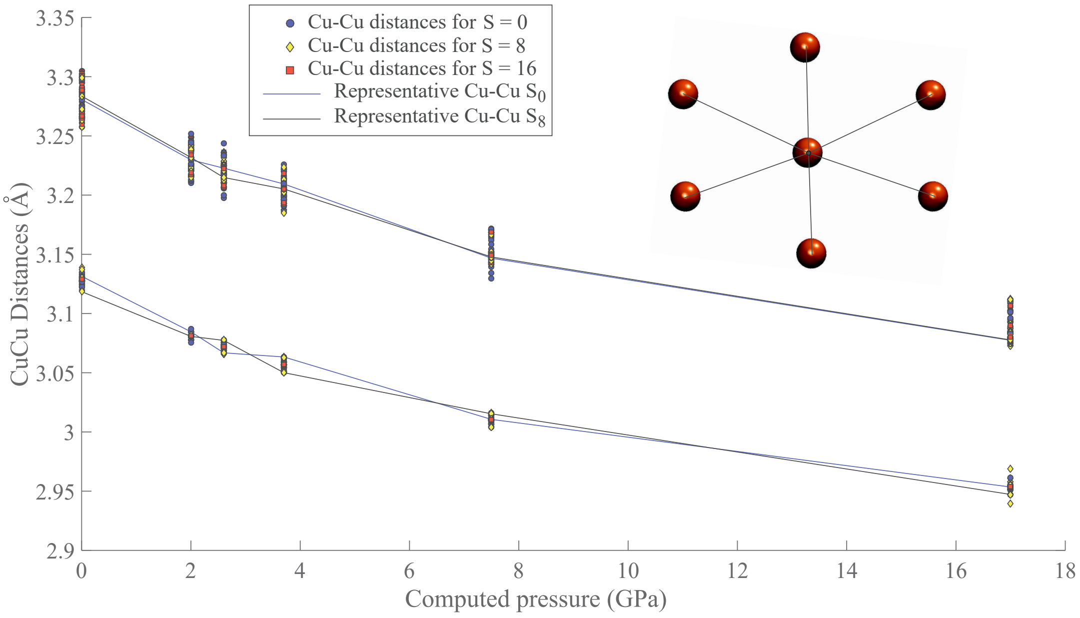

Figure 88 – Full set of in-plane Cu-Cu distances for the anti-ferromagnetic system S0 (circle), S8 (diamond), and ferromagnetic S16 (square) states of copper hydroxide acetate as function of pressure

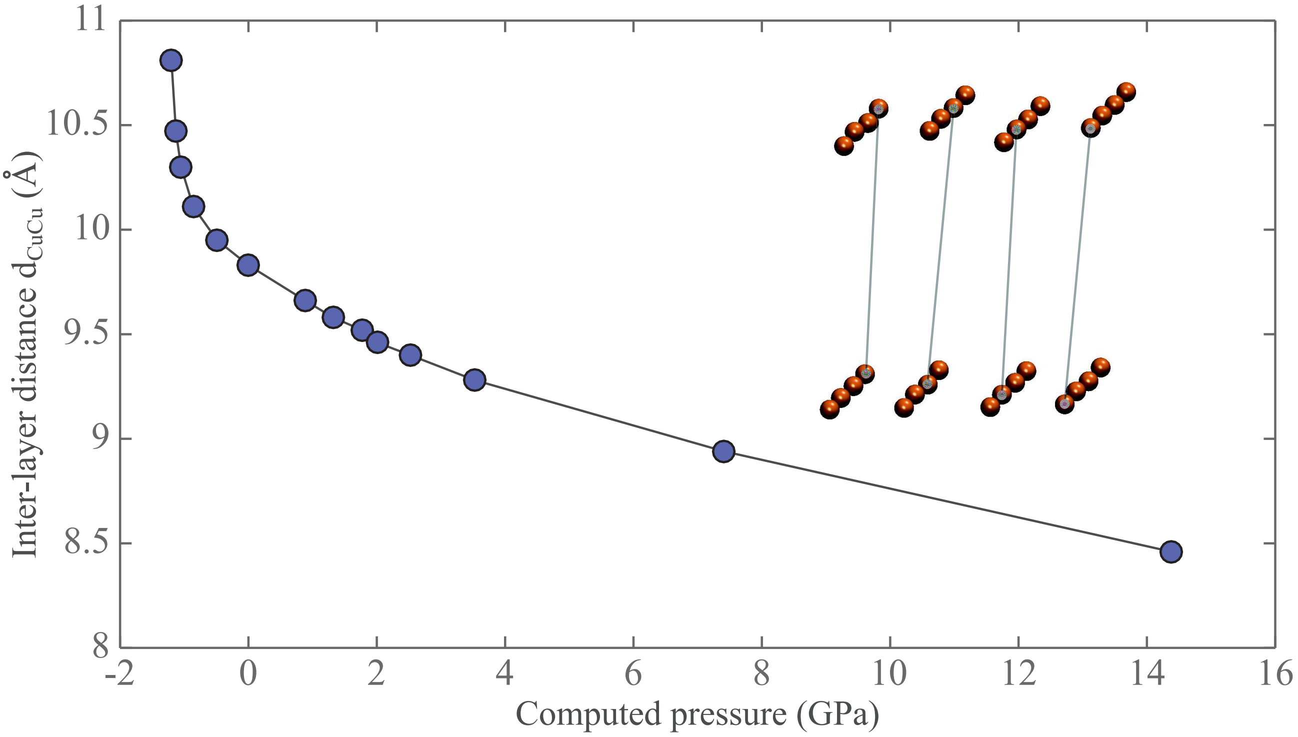

Figure 89 – Evolution of interlayer distances between the inorganic layers of copper hydroxide acetate system as function of pressure for the anti-ferromagnetic ground state of the system

		Computed pressure (GPa)								
		0,0	***0,9***	***1,3***	***1,8***	***2,0***	***2,5***	***3,5***	***7,4***	***14,3***
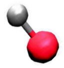 **Distances (Å) and angles (°)**	β	102,80	101,01	101,12	100,35	100,42	100,05	98,96	97,06	93,81
	d_2^{CuO}	2,02	2,03	2,03	2,03	2,03	2,03	2,03	2,03	2,02
	d_3^{CuO}	1,97	1,98	1,98	1,99	1,99	1,99	2,00	2,01	2,03
	d_2^{CuCu}	3,12	3,10	3,10	3,09	3,10	3,08	3,06	3,03	2,96
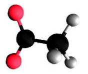 **Distances (Å) and angles (°)**	β	76,36	78,05	77,93	78,31	78,72	79,40	79,67	82,21	83,33
	d_2^{CuO}	2,52	2,44	2,42	2,43	2,42	2,41	2,38	2,33	2,28
	d_3^{CuO}	2,61	2,54	2,51	2,50	2,46	2,45	2,40	2,29	2,17
	d_2^{CuCu}	3,17	3,14	3,10	3,11	3,10	3,10	3,06	3,04	2,96

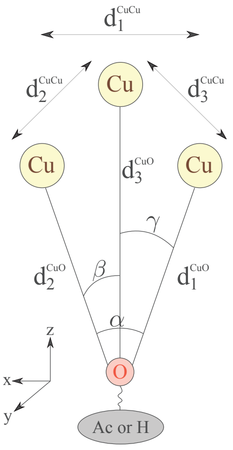

Figure 90 – Specific Oxygen atoms ($O_{81}^{Hydroxide}$ and $O_{79}^{Acetate}$) tetrahedra deformation as a function of external pressure in copper hydroxide acetate system

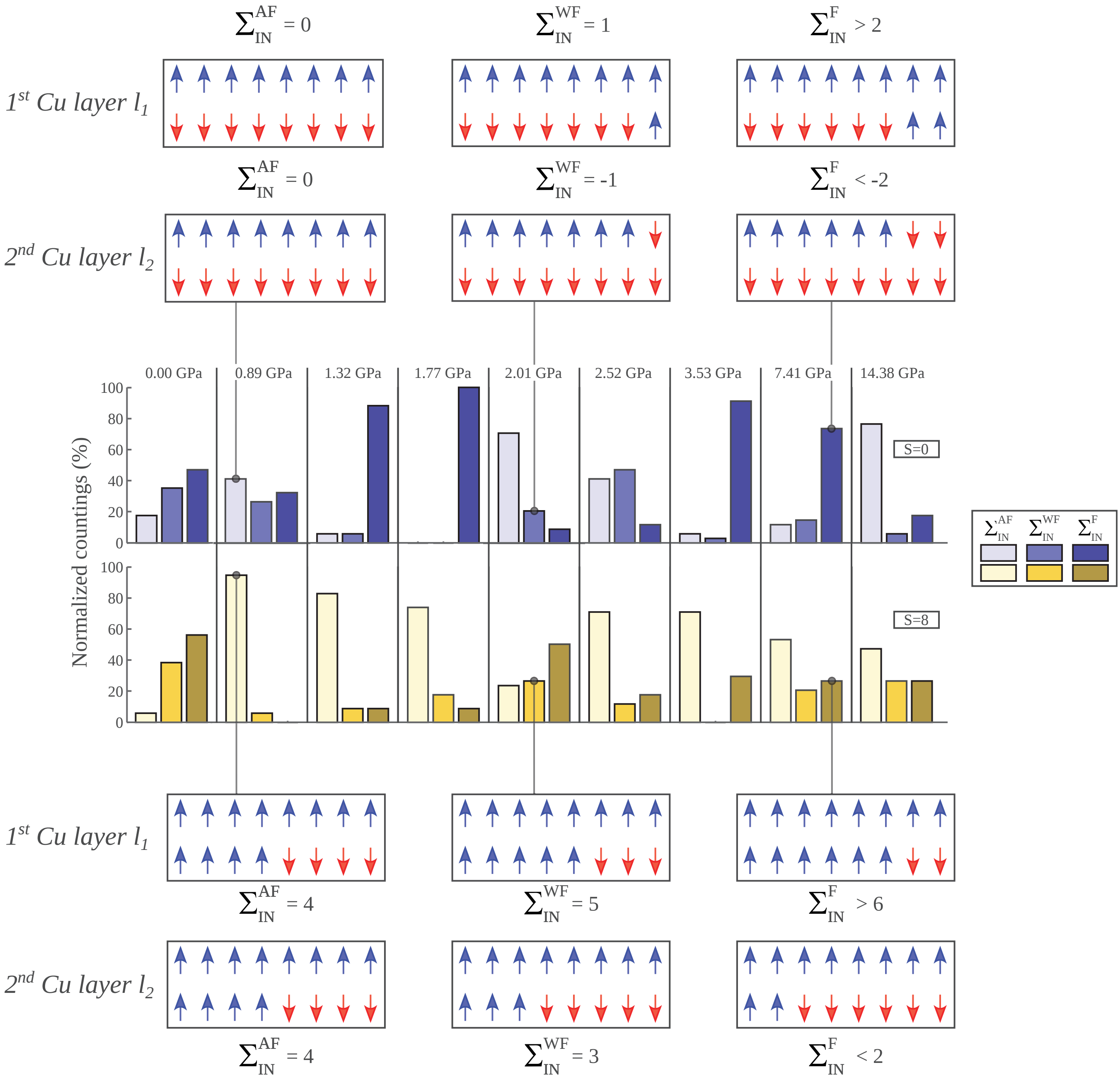

Figure 91 – Spin density distribution analysis of copper hydroxide acetate system in two magnetic configurations, the anti-ferromagnetic one (S=0) and a ferromagnetic one (S=8). In-layer (copper layers) magnetizations Σ_{IN} among the two layers (l_1 and l_2) are represented in schematic pictures allowing to visualize the various spin configurations corresponding to the colors of the bar plot. This bar plot gives, for each pressure system, an evaluation (in percent) of the number of stable magnetic configurations obtained (from the 17 DFT calculations performed at each pressure), sorted by colors from light color (low in layer magnetization, AF), intermediate color (weak ferromagnetism, WF) to darker colors (in layer ferromagnetic behaviors, F)

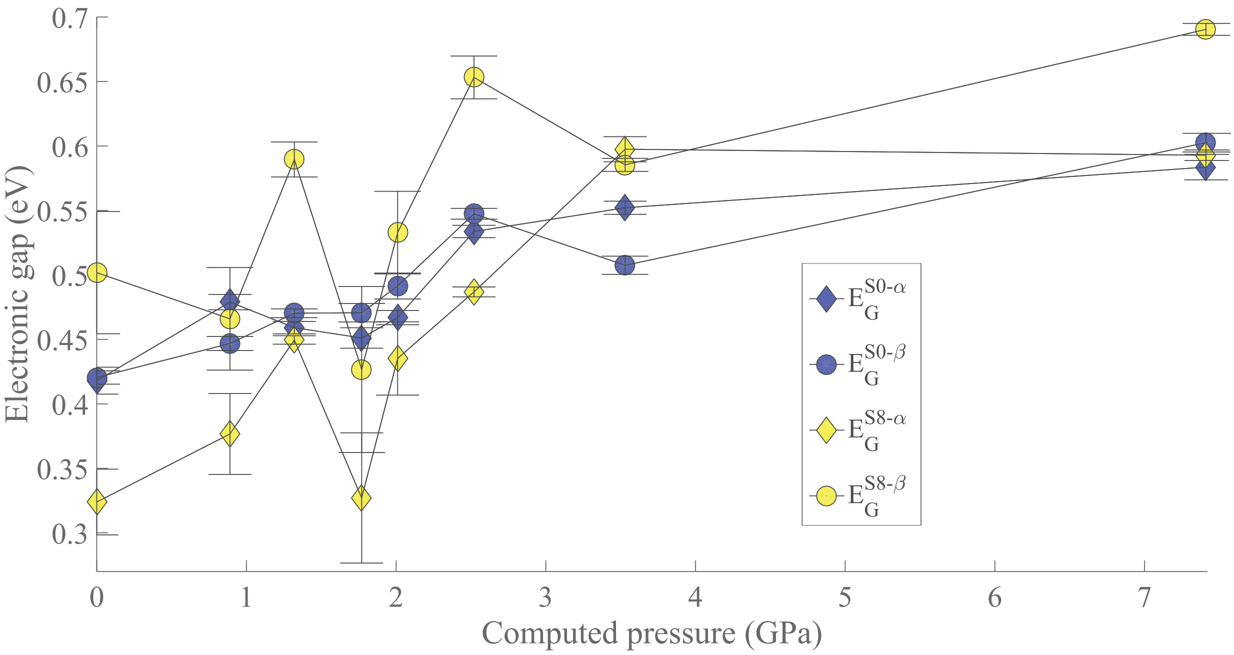

Figure 92 – Evolution of copper hydroxide acetate electronic gaps as function of pressure computed from first-principles calculations. The two magnetic states considered are the anti-ferromagnetic state (S=0 in blue) and half spin polarized system (S=8 in yellow). The errorbars are produced from the randomization procedure applied on the initial electronic of freedom resulting in multiple energy minima landscape

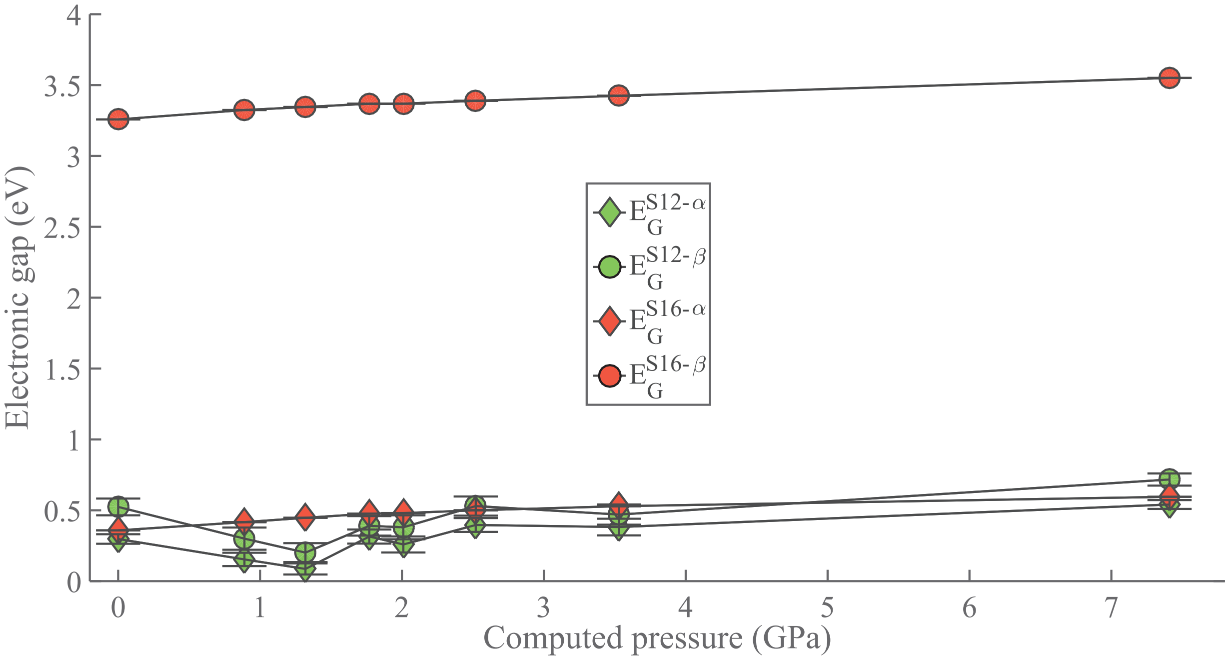

Figure 93 – Evolution of copper hydroxide acetate electronic gaps as function of pressure computed from first-principles calculations. The two magnetic states considered are ferromagnetic configurations (S=12 in green and S=16 in red). The errorbars are produced from the randomization procedure applied on the initial electronic of freedom resulting in multiple energy minima landscape

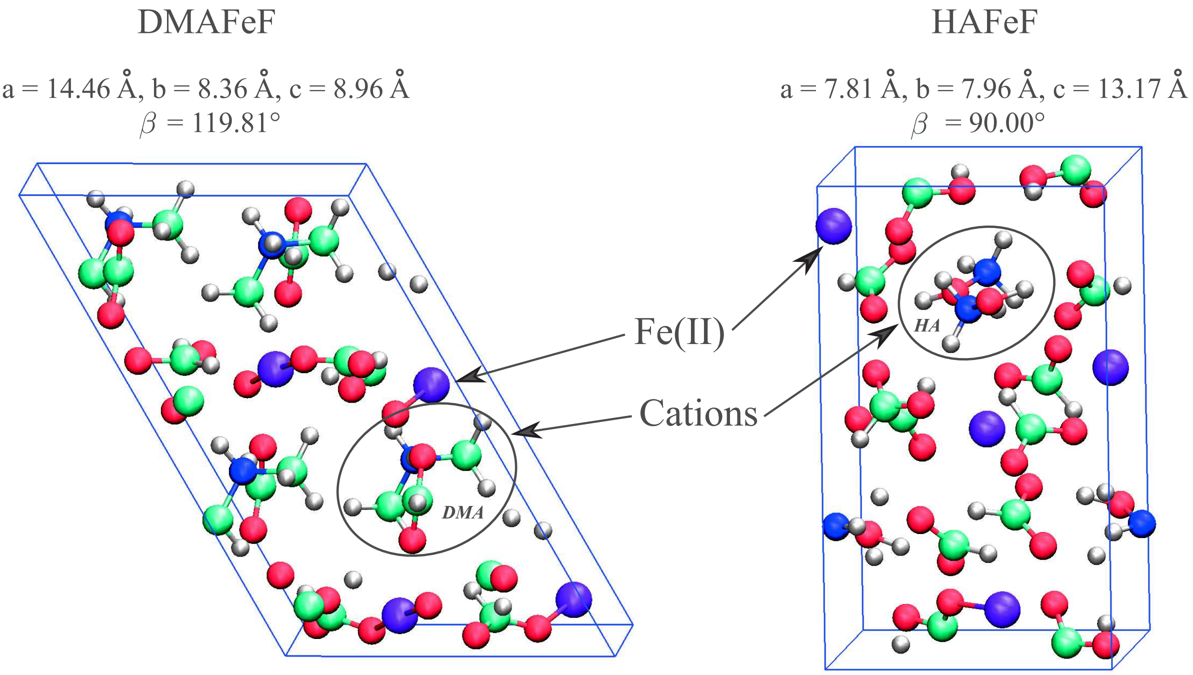

Figure 94 – Dimethylammonium iron formate (DMAFeF) and hydroxylammonium iron formate (HAFeF) crystallographic structures constructed from the experimental atomic positions provided by H. Banerjee et al. [6]. Organic cationic sites and iron sites are highlighted by the arrows

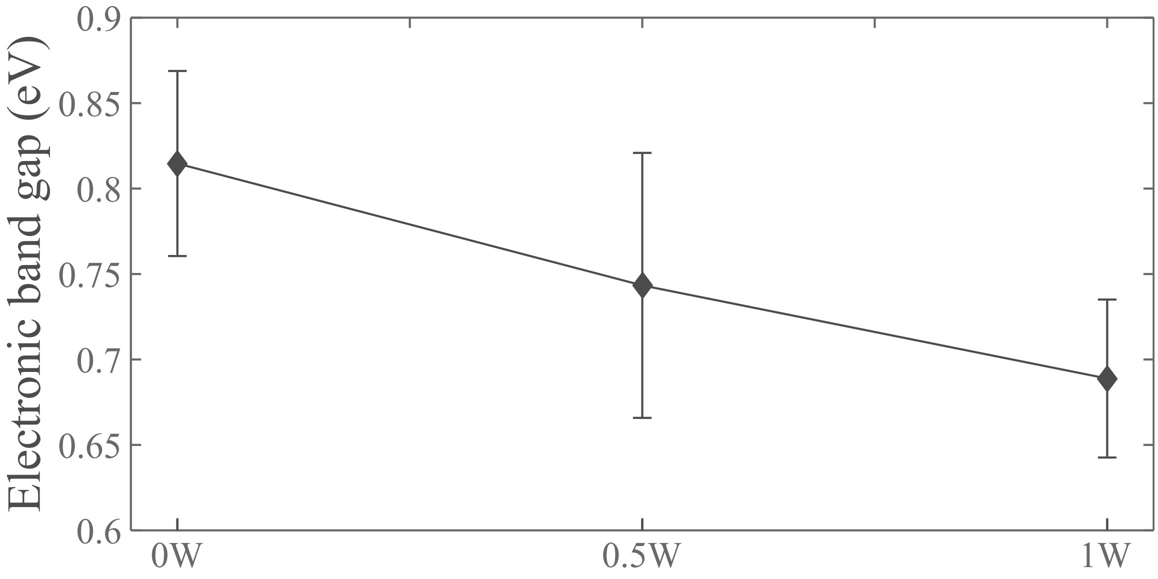

Figure 95 – The electronic band gap obtained for copper hydroxide fluorene monophosphonic material as a function of the water content. **0.5W**: 4 water molecules, **1W**: 8 water molecules

Bibliography

[1] G. Rogez, C. Massobrio, P. Rabu, and M. Drillon, "Layered hydroxide hybrid nanostructures: a route to multifunctionality," *Chemical Society Reviews*, vol. 40, no. 2, pp. 1031–1058, 2011.

[2] J. Hutter, M. Parrinello, D. Marx, P. Focher, M. Tuckerman, W. Andreoni, A. Curioni, E. Fois, U. Röthlisberger, P. Giannozzi, *et al.*, "Computer code CPMD," *IBM Zurich Research Laboratory and MPI für Festkörperforschung*, vol. 2001, 1995.

[3] S. Švarcová, M. Klementová, P. Bezdička, W. Łasocha, M. Dušek, and D. Hradil, "Synthesis and characterization of single crystals of the layered copper hydroxide acetate $Cu_2(OH)_3(CH_3COO)\cdot H_2O$," *Crystal Research and Technology*, vol. 46, no. 10, pp. 1051–1057, 2011.

[4] K. Suzuki, J. Haines, P. Rabu, K. Inoue, and M. Drillon, "Magnetic properties and pressure-induced ferromagnetism of $Cu_2(OH)_3(CH_3COO)\cdot H_2O$," *The Journal of Physical Chemistry C*, vol. 112, no. 48, pp. 19147–19150, 2008.

[5] G. Rogez, C. Massobrio, P. Rabu, and M. Drillon, "Layered hydroxide hybrid nanostructures: a route to multifunctionality," *Chemical Society Reviews*, vol. 40, no. 2, pp. 1031–1058, 2011.

[6] H. Banerjee, S. Chakraborty, and T. Saha-Dasgupta, "Cationic effect on pressure driven spin-state transition and cooperativity in hybrid perosvkites," *Chemistry of Materials*, 2016.

[7] F. Yang, C. Massobrio, and M. Boero, "Tuning magnetic properties with pressure in hybrid organic–inorganic materials: The case of copper hydroxide acetate," *The Journal of Physical Chemistry C*, vol. 118, no. 32, pp. 18700–18705, 2014.

[8] C. Livage, N. Guillou, P. Rabu, P. Pattison, J. Marrot, and G. Férey, "Bulk homochirality of a 3-D inorganic framework: ligand control of inorganic network chirality," *Chemical Communications*, no. 30, pp. 4551–4553, 2009.

[9] C.-D. Wu, A. Hu, L. Zhang, and W. Lin, "A homochiral porous metal-organic framework for highly enantioselective heterogeneous asymmetric catalysis," *Journal of the American Chemical Society*, vol. 127, no. 25, pp. 8940–8941, 2005.

[10] Z.-G. Gu, X.-H. Zhou, Y.-B. Jin, R.-G. Xiong, J.-L. Zuo, and X.-Z. You, "Crystal structures and magnetic and ferroelectric properties of chiral layered metal-organic frameworks with dicyanamide as the bridging ligand," *Inorganic chemistry*, vol. 46, no. 14, pp. 5462–5464, 2007.

[11] W. Ratcliff, J. W. Lynn, V. Kiryukhin, P. Jain, and M. R. Fitzsimmons, "Magnetic structures and dynamics of multiferroic systems obtained with neutron scattering," *npj Quantum Materials*, vol. 1, p. 16003, 2016.

[12] P. Rabu, E. Delahaye, and G. Rogez, "Hybrid interfaces in layered hydroxides: magnetic and multifunctional superstructures by design," *Nanotechnology Reviews*, vol. 4, no. 6, pp. 557–580, 2015.

[13] A. Illaik, C. Taviot-Guého, J. Lavis, S. Commereuc, V. Verney, and F. Leroux, "Unusual polystyrene nanocomposite structure using emulsifier-modified layered double hydroxide as nanofiller," *Chemistry of Materials*, vol. 20, no. 15, pp. 4854–4860, 2008.

[14] L. Lomas, P. Lacroix, J. P. Audière, and R. Clément, "Tetrathiafulvalene-$FePS_3$ layered intercalation compound: a new type of organic-inorganic metal," *Journal of Materials Chemistry*, vol. 1, no. 3, pp. 475–476, 1991.

[15] J. S. Evans, S. Bénard, P. Yu, and R. Clément, "Ferroelectric alignment of NLO chromophores in layered inorganic lattices: structure of a stilbazolium metal-oxalate from powder diffraction data," *Chemistry of materials*, vol. 13, no. 11, pp. 3813–3816, 2001.

[16] Q. Wang and D. O'Hare, "Recent advances in the synthesis and application of layered double hydroxide (LDH) nanosheets," *Chemical reviews*, vol. 112, no. 7, pp. 4124–4155, 2012.

[17] P. Rabu, K. Awaga, W. Fujita, T. Sekine, J. Miller, and M. Drillon, "Magnetism: Molecules to materials II. molecules-based materials," 2001.

[18] M. Drillon and P. Panissod, "Long-range ferromagnetism in hybrid compounds: The role of dipolar interactions," *Journal of magnetism and magnetic materials*, vol. 188, no. 1, pp. 93–99, 1998.

[19] S. Bhattacharjee and J. A. Anderson, "Synthesis and characterization of novel chiral sulfonato-salen-manganese(III) complex in a zinc–aluminium LDH host," *Chemical communications*, no. 5, pp. 554–555, 2004.

[20] P. Gomez-Romero, "Hybrid organic-inorganic materials-in search of synergic activity," *Advanced Materials*, vol. 13, no. 3, pp. 163–174, 2001.

[21] P. G. Lacroix, I. Malfant, S. Bénard, P. Yu, E. Rivière, and K. Nakatani, "Hybrid molecular-based magnets containing organic nlo chromophores: A search toward an interplay between magnetic and NLO behavior," *Chemistry of materials*, vol. 13, no. 2, pp. 441–449, 2001.

[22] C. Sanchez and P. Gómez-Romero, *Functional hybrid materials*. Wiley-VCH, 2004.

[23] J. Livage, M. Henry, and C. Sanchez, "Sol-gel chemistry of transition metal oxides," *Progress in solid state chemistry*, vol. 18, no. 4, pp. 259–341, 1988.

[24] C. Sanchez, J. Livage, M. Henry, and F. Babonneau, "Chemical modification of alkoxide precursors," *Journal of Non-Crystalline Solids*, vol. 100, no. 1-3, pp. 65–76, 1988.

[25] C. Sanchez, L. Rozes, F. Ribot, C. Laberty-Robert, D. Grosso, C. Sassoye, C. Boissiere, and L. Nicole, ""chimie douce": A land of opportunities for the designed construction of functional inorganic and hybrid organic-inorganic nanomaterials," *Comptes Rendus Chimie*, vol. 13, no. 1, pp. 3–39, 2010.

[26] L. Bourget, R. Corriu, D. Leclercq, P. Mutin, and A. Vioux, "Non-hydrolytic sol-gel routes to silica," *Journal of Non-Crystalline Solids*, vol. 242, no. 2, pp. 81–91, 1998.

[27] C. Sanchez, B. Lebeau, F. Chaput, and J.-P. Boilot, "Optical properties of functional hybrid organic–inorganic nanocomposites," *Advanced Materials*, vol. 15, no. 23, pp. 1969–1994, 2003.

[28] D. Avnir, T. Coradin, O. Lev, and J. Livage, "Recent bio-applications of sol-gel materials," *Journal of Materials Chemistry*, vol. 16, no. 11, pp. 1013–1030, 2006.

[29] L. Rozes and C. Sanchez, "Titanium oxo-clusters: precursors for a lego-like construction of nanostructured hybrid materials," *Chemical Society Reviews*, vol. 40, no. 2, pp. 1006–1030, 2011.

[30] C. Sanchez, G. d. A. Soler-Illia, F. Ribot, T. Lalot, C. Mayer, and V. Cabuil, "Designed hybrid organic-inorganic nanocomposites from functional nanobuilding blocks," *Chemistry of Materials*, vol. 13, no. 10, pp. 3061–3083, 2001.

[31] G. Guerrero, J. G. Alauzun, M. Granier, D. Laurencin, and P. H. Mutin, "Phosphonate coupling molecules for the control of surface/interface properties and the synthesis of nanomaterials," *Dalton Transactions*, vol. 42, no. 35, pp. 12569–12585, 2013.

[32] A. K. Cheetham, C. Rao, and R. K. Feller, "Structural diversity and chemical trends in hybrid inorganic-organic framework materials," *Chemical communications*, no. 46, pp. 4780–4795, 2006.

[33] C. Sanchez, B. Julián, P. Belleville, and M. Popall, "Applications of hybrid organic-inorganic nanocomposites," *Journal of Materials Chemistry*, vol. 15, no. 35-36, pp. 3559–3592, 2005.

[34] V. Laget, C. Hornick, P. Rabu, and M. Drillon, "Hybrid organic-inorganic layered compounds prepared by anion exchange reaction: correlation between structure and magnetic properties," *Journal of Materials Chemistry*, vol. 9, no. 1, pp. 169–174, 1999.

[35] P. Rabu, S. Rouba, V. Laget, C. Hornick, and M. Drillon, "Ferro/antiferromagnetism mediated by interlayer organic spacers in layered copper (II) compounds," *Chemical Communications*, no. 10, pp. 1107–1108, 1996.

[36] F. Yang, M. Boero, and C. Massobrio, "Atomic structure and magnetic nature of copper hydroxide acetate," *The Journal of Physical Chemistry C*, vol. 114, no. 47, pp. 20213–20219, 2010.

[37] F. Yang, M. Boero, P. Rabu, and C. Massobrio, "First principles investigation of the atomic structure and magnetic properties of copper hydroxide acetate," *Comptes Rendus Chimie*, vol. 15, no. 2, pp. 202–208, 2012.

[38] A. D. Becke, "Density-functional exchange-energy approximation with correct asymptotic behavior," *Physical review A*, vol. 38, no. 6, p. 3098, 1988.

[39] C. Lee, W. Yang, and R. G. Parr, "Development of the Colle-Salvetti correlation-energy formula into a functional of the electron density," *Physical review B*, vol. 37, no. 2, p. 785, 1988.

[40] S. G. Louie, S. Froyen, and M. L. Cohen, "Nonlinear ionic pseudopotentials in spin-density-functional calculations," *Physical Review B*, vol. 26, no. 4, p. 1738, 1982.

[41] C. L. Reis, J. Pacheco, and J. L. Martins, "First-principles norm-conserving pseudopotential with explicit incorporation of semicore states," *Physical Review B*, vol. 68, no. 15, p. 155111, 2003.

[42] B. Alder and T. Wainwright, "Phase transition for a hard sphere system," *The Journal of chemical physics*, vol. 27, no. 5, pp. 1208–1209, 1957.

[43] R. Car and M. Parrinello, "Unified approach for molecular dynamics and density-functional theory," *Physical review letters*, vol. 55, no. 22, p. 2471, 1985.

[44] S. Kirkpatrick, C. D. Gelatt, M. P. Vecchi, *et al.*, "Optimization by simulated annealing," *science*, vol. 220, no. 4598, pp. 671–680, 1983.

[45] U. von Barth and L. Hedin, "A local exchange-correlation potential for the spin polarized case. i," *Journal of Physics C: Solid State Physics*, vol. 5, no. 13, p. 1629, 1972.

[46] N. Troullier and J. L. Martins, "Efficient pseudopotentials for plane-wave calculations. II. operators for fast iterative diagonalization," *Physical Review B*, vol. 43, no. 11, p. 8861, 1991.

[47] Z. Chaker, G. Ori, M. Boero, and C. Massobrio, "The role of 2D/3D spin-polarization interactions in hybrid copper hydroxide acetate: new insights from first-principles molecular dynamics," *Beilstein Journal of Nanotechnology*, vol. 8, p. 857, 2017.

[48] J. P. Perdew, "Density functional theory and the band gap problem," *International Journal of Quantum Chemistry*, vol. 28, no. S19, pp. 497–523, 1985.

[49] S.-H. Park, M.-H. Jung, Y.-J. Lee, and Y.-D. Huh, "Confined condensation synthesis and magnetic properties of layered copper hydroxide frameworks," *Dalton Transactions*, vol. 46, no. 10, pp. 3363–3368, 2017.

[50] G. H. Wannier, "The structure of electronic excitation levels in insulating crystals," *Physical Review*, vol. 52, no. 3, p. 191, 1937.

[51] M. Boero, K. Terakura, T. Ikeshoji, C. C. Liew, and M. Parrinello, "Hydrogen bonding and dipole moment of water at supercritical conditions: A first-principles molecular dynamics study," *Physical Review Letters*, vol. 85, no. 15, p. 3245, 2000.

[52] M. Sharma, R. Resta, and R. Car, "Intermolecular dynamical charge fluctuations in water: A signature of the H-bond network," *Physical review letters*, vol. 95, no. 18, p. 187401, 2005.

[53] G. Ori, C. Massobrio, A. Bouzid, M. Boero, and B. Coasne, "Surface of glassy GeS_2: A model based on a first-principles approach," *Physical Review B*, vol. 90, no. 4, p. 045423, 2014.

[54] A. Bouzid, S. Le Roux, G. Ori, M. Boero, and C. Massobrio, "Origin of structural analogies and differences between the atomic structures of GeSe_4 and GeS_4 glasses: A first principles study," *The Journal of chemical physics*, vol. 143, no. 3, p. 034504, 2015.

[55] M. Ceriotti, J. Cuny, M. Parrinello, and D. E. Manolopoulos, "Nuclear quantum effects and hydrogen bond fluctuations in water," *Proceedings of the National Academy of Sciences*, vol. 110, no. 39, pp. 15591–15596, 2013.

[56] D. A. Schmidt, R. Scipioni, and M. Boero, "Water solvation properties: An experimental and theoretical investigation of salt solutions at finite dilution," *The Journal of Physical Chemistry A*, vol. 113, no. 27, pp. 7725–7729, 2009.

[57] N. Hugot, M. Roger, J.-M. Rueff, J. Cardin, O. Perez, V. Caignaert, B. Raveau, G. Rogez, and P.-A. Jaffrès, "Copper-fluorenephosphonate Cu (PO_3-$C_{13}H_9$)·H_2O: A layered antiferromagnetic hybrid," *European Journal of Inorganic Chemistry*, vol. 2016, no. 2, pp. 266–271, 2016.

[58] F. A. Hamprecht, A. J. Cohen, D. J. Tozer, and N. C. Handy, "Development and assessment of new exchange-correlation functionals," *The Journal of chemical physics*, vol. 109, no. 15, pp. 6264–6271, 1998.

[59] P. J. Hay, J. C. Thibeault, and R. Hoffmann, "Orbital interactions in metal dimer complexes," *J. Am. Chem. Soc*, vol. 97, no. 17, pp. 4884–4899, 1975.

[60] J. P. Perdew, K. Burke, and M. Ernzerhof, "Generalized gradient approximation made simple," *Physical review letters*, vol. 77, no. 18, p. 3865, 1996.

[61] P. Hohenberg and W. Kohn, "Inhomogeneous electron gas," *Physical review*, vol. 136, no. 3B, p. B864, 1964.

[62] J. Bottéro, "L'épopée de gilgamesh," *L'Histoire*, no. 115, pp. 18–24, 1988.

[63] K. S. Noah, "L'histoire commence à sumer," 1986.

[64] Y.-P. Zhu and Z.-Y. Yuan, *Mesoporous Organic-Inorganic Non-Siliceous Hybrid Materials: Basic Principles and Promising Multifunctionality*. Springer, 2014.

[65] S. Inagaki, S. Guan, T. Ohsuna, and O. Terasaki, "An ordered mesoporous organosilica hybrid material with a crystal-like wall structure," *Nature*, vol. 416, no. 6878, pp. 304–307, 2002.

[66] M. O'Keeffe, M. Eddaoudi, H. Li, T. Reineke, and O. M. Yaghi, "Frameworks for extended solids: geometrical design principles," *Journal of Solid State Chemistry*, vol. 152, no. 1, pp. 3–20, 2000.

[67] B. Abrahams, B. Hoskins, D. Michail, and R. Robson, "Assembly of porphyrin building blocks into network structures with large channels," *Nature*, vol. 369, no. 6483, pp. 727–729, 1994.

[68] A. Clearfield, C. K. Sharma, and B. Zhang, "Crystal engineered supramolecular metal phosphonates: crown ethers and iminodiacetates," *Chemistry of materials*, vol. 13, no. 10, pp. 3099–3112, 2001.

[69] R. C. Finn, R. Lam, J. E. Greedan, and J. Zubieta, "Solid-state coordination chemistry: Structural influences of copper-phenanthroline subunits on oxovanadium organophosphonate phases. hydrothermal synthesis and structural characterization of the two-dimensional materials $[Cu(phen)VO)(O_3PCH_2PO_3)(H_2O)]$,$[\{Cu(phen)\}_2(V_2O_5)(O_3PCH_2CH_2PO_3)]$, and $[\{Cu(phen)\}_2(V_3O_5)(O_3PCH_2CH_2CH_2PO_3)_2(H_2O)]$ and of the three-dimensional phase $[\{Cu(phen)\}_2(V_3O_5)(O_3PCH_2PO_3)_2(H_2O)]$," *Inorganic chemistry*, vol. 40, no. 15, pp. 3745–3754, 2001.

[70] D. B. Mitzi, "Thin-film deposition of organic-inorganic hybrid materials," *Chemistry of Materials*, vol. 13, no. 10, pp. 3283–3298, 2001.

[71] J. M. Moreno, I. Navarro, U. Díaz, J. Primo, and A. Corma, "Single-layered hybrid materials based on 1d associated metalorganic nanoribbons for controlled release of pheromones," *Angewandte Chemie International Edition*, vol. 55, no. 37, pp. 11026–11030, 2016.

[72] N. Stock and S. Biswas, “Synthesis of metal-organic frameworks (MOFs): routes to various MOF topologies, morphologies, and composites,” *Chemical reviews*, vol. 112, no. 2, pp. 933–969, 2011.

[73] S. R. Batten, N. R. Champness, X.-M. Chen, J. Garcia-Martinez, S. Kitagawa, L. Öhrström, M. O’Keeffe, M. Paik Suh, and J. Reedijk, “Terminology of metal-organic frameworks and coordination polymers (IUPAC recommendations 2013),” *Pure and Applied Chemistry*, vol. 85, no. 8, pp. 1715–1724, 2013.

[74] G. Kickelbick, *Hybrid materials: synthesis, characterization, and applications*. John Wiley & Sons, 2007.

[75] J. Le Bideau, L. Viau, and A. Vioux, “Ionogels, ionic liquid based hybrid materials,” *Chemical Society Reviews*, vol. 40, no. 2, pp. 907–925, 2011.

[76] Y. Dong, B. Wang, L. Xiang, Y. Liu, X. Zhao, and J. Yin, “Influence of side chain sizes on dielectric and electrorheological responses of poly (ionic liquid),” *The Journal of Physical Chemistry B*, 2017.

[77] G. Ori, F. Villemot, L. Viau, A. Vioux, and B. Coasne, “Ionic liquid confined in silica nanopores: molecular dynamics in the isobaric–isothermal ensemble,” *Molecular Physics*, vol. 112, no. 9-10, pp. 1350–1361, 2014.

[78] G. Ori, C. Massobrio, A. Pradel, M. Ribes, and B. Coasne, “Structure and dynamics of ionic liquids confined in amorphous porous chalcogenides,” *Langmuir*, vol. 31, no. 24, pp. 6742–6751, 2015.

[79] C. Rottman, G. Grader, Y. De Hazan, S. Melchior, and D. Avnir, “Surfactant-induced modification of dopants reactivity in sol-gel matrixes,” *Journal of the American Chemical Society*, vol. 121, no. 37, pp. 8533–8543, 1999.

[80] B. Schaudel, C. Guermeur, C. Sanchez, K. Nakatani, and J. A. Delaire, “Spirooxazine-and spiropyran-doped hybrid organic–inorganic matrices with very fast photochromic responses,” *Journal of Materials Chemistry*, vol. 7, no. 1, pp. 61–65, 1997.

[81] M. Faloss, M. Canva, P. Georges, A. Brun, F. Chaput, and J.-P. Boilot, “Toward millions of laser pulses with pyrromethene-and perylene-doped xerogels,” *Applied optics*, vol. 36, no. 27, pp. 6760–6763, 1997.

[82] J. P. Lafleur, A. Jönsson, S. Senkbeil, and J. P. Kutter, “Recent advances in lab-on-a-chip for biosensing applications,” *Biosensors and Bioelectronics*, vol. 76, pp. 213–233, 2016.

[83] M. Clemente-León, E. Coronado, M. López-Jorda, and J. C. Waerenborgh, “Multifunctional magnetic materials obtained by insertion of spin-crossover FeIII complexes into chiral 3D bimetallic oxalate-based ferromagnets,” *Inorganic chemistry*, vol. 50, no. 18, pp. 9122–9130, 2011.

[84] E. Coronado, C. Martí-Gastaldo, E. Navarro-Moratalla, A. Ribera, S. J. Blundell, and P. J. Baker, “Coexistence of superconductivity and magnetism by chemical design,” *Nature chemistry*, vol. 2, no. 12, pp. 1031–1036, 2010.

[85] M. Yang, O. McDermott, J.-C. Buffet, and D. O’Hare, “Synthesis and characterisation of layered double hydroxide dispersions in organic solvents,” *RSC Advances*, vol. 4, no. 93, pp. 51676–51682, 2014.

[86] A. Radha, P. V. Kamath, and C. Shivakumara, “Order and disorder among the layered double hydroxides: combined rietveld and DIFFaX approach,” *Acta Crystallographica Section B: Structural Science*, vol. 63, no. 2, pp. 243–250, 2007.

[87] V. Prévot, C. Forano, and J. P. Besse, “Hybrid derivatives of layered double hydroxides,” *Applied Clay Science*, vol. 18, no. 1, pp. 3–15, 2001.

[88] S. M. Cohen, “Postsynthetic methods for the functionalization of metal–organic frameworks,” *Chemical reviews*, vol. 112, no. 2, pp. 970–1000, 2011.

[89] N. Masciocchi, E. Corradi, A. Sironi, G. Moretti, G. Minelli, and P. Porta, “Preparation, characterization, andab initiox-ray powder diffraction study of $Cu_2(OH)_3(CH_3COO)\cdot H_2O$,” *Journal of Solid State Chemistry*, vol. 131, no. 2, pp. 252–262, 1997.

[90] R. Skomski, *Simple models of magnetism.* Oxford University Press on Demand, 2008.

[91] D. Martien, “Introduction to AC susceptibility,” *Quantum Design*, 2002.

[92] J. Vleck, “Theory of electric and magnetic susceptibilities,” 1932.

[93] B. C. Guha, “Magnetic properties of some paramagnetic crystals at low temperatures,” in *Proceedings of the Royal Society of London A: Mathematical, Physical and Engineering Sciences*, vol. 206, pp. 353–373, The Royal Society, 1951.

[94] O. Kahn, “Molecular magnetism,” *VCH Publishers, Inc.(USA), 1993,*, p. 393, 1993.

[95] L. L. Ng, *Heisenberg model, Bethe Ansatz, and random walks.* PhD thesis, Harvard University, 1996.

[96] B. Bleaney and K. Bowers, “Anomalous paramagnetism and exchange interaction in copper acetate,” *The London, Edinburgh, and Dublin Philosophical Magazine and Journal of Science*, vol. 43, no. 338, pp. 372–374, 1952.

[97] P. W. Anderson, “New approach to the theory of superexchange interactions,” *Physical Review*, vol. 115, no. 1, p. 2, 1959.

[98] A. Szabo and N. S. Ostlund, “Modern Quantum Chemistry: Intro to advanced electronic structure theory,” 1996.

[99] J. J. Girerd, Y. Journaux, and O. Kahn, “Natural or orthogonalized magnetic orbitals: Two alternative ways to describe the exchange interaction,” *Chemical Physics Letters*, vol. 82, no. 3, pp. 534–538, 1981.

[100] C. De Graaf and R. Broer, *Magnetic interactions in molecules and solids*. Springer, 2015.

[101] W. Heitler and F. London, “Wechselwirkung neutraler atome und homöopolare bindung nach der quantenmechanik,” *Zeitschrift für Physik*, vol. 44, no. 6-7, pp. 455–472, 1927.

[102] C. Massobrio and E. Ruiz, “Localized orbitals vs. pseudopotential-plane waves basis sets: Performances and accuracy for molecular magnetic systems,” *Monatshefte für Chemie/Chemical Monthly*, vol. 134, no. 2, pp. 317–326, 2003.

[103] R. Dovesi, V. Saunders, C. Roetti, M. Causà, N. Harrison, R. Orlando, and C. Zicovich-Wilson, “CRYSTAL’98. user manual. 1999,” *Turin University*.

[104] G. Galli and M. Parrinello, "Ab-initio molecular dynamics: Principles and practical implementation," in *Computer Simulation in Materials Science*, pp. 283–304, Springer, 1991.

[105] E. Ruiz, P. Alemany, S. Alvarez, and J. Cano, "Toward the prediction of magnetic coupling in molecular systems: hydroxo-and alkoxo-bridged Cu(II) binuclear complexes," *Journal of the American Chemical Society*, vol. 119, no. 6, pp. 1297–1303, 1997.

[106] E. Ruiz, P. Alemany, S. Alvarez, and J. Cano, "Structural modeling and magneto-structural correlations for hydroxo-bridged copper (II) binuclear complexes," *Inorganic chemistry*, vol. 36, no. 17, pp. 3683–3688, 1997.

[107] V. H. Crawford, H. W. Richardson, J. R. Wasson, D. J. Hodgson, and W. E. Hatfield, "Relation between the singlet-triplet splitting and the copper-oxygen-copper bridge angle in hydroxo-bridged copper dimers," *Inorganic Chemistry*, vol. 15, no. 9, pp. 2107–2110, 1976.

[108] M. Matsubara, M. Celino, P. S. Salmon, and C. Massobrio, "Atomic scale modelling of materials: a prerequisite for any multi-scale approach to structural and dynamical properties," in *Solid State Phenomena*, vol. 139, pp. 141–150, Trans Tech Publ, 2008.

[109] H. U. Guedel, A. Stebler, and A. Furrer, "Direct observation of singlet-triplet separation in dimeric copper (II) acetate by neutron inelastic scattering spectroscopy," *Inorganic Chemistry*, vol. 18, no. 4, pp. 1021–1023, 1979.

[110] A. Rodríguez-Fortea, P. Alemany, S. Alvarez, and E. Ruiz, "Exchange coupling in halo-bridged dinuclear cu (II) compounds: A density functional study," *Inorganic chemistry*, vol. 41, no. 14, pp. 3769–3778, 2002.

[111] M. Frisch, G. Trucks, H. Schlegel, G. Scuseria, M. Robb, J. Cheeseman, G. Scalmani, V. Barone, B. Mennucci, G. Petersson, *et al.*, "Gaussian 09, Revision A, Gaussian," *Inc., Wallingford CT*, 2009.

[112] G. Demunno, M. Julve, F. Lloret, J. Faus, M. Verdaguer, A. Caneschi, *et al.*, "Alternating ferromagnetic and antiferromagnetic interactions in unusual copper (II) chains," *Inorganic Chemistry*, vol. 34, no. 1, pp. 157–165, 1995.

[113] E. Ruiz, J. Cano, S. Alvarez, and P. Alemany, "Broken symmetry approach to calculation of exchange coupling constants for homobinuclear and heterobinuclear transition metal complexes," *Journal of computational chemistry*, vol. 20, no. 13, pp. 1391–1400, 1999.

[114] M. Rodríguez, A. Llobet, M. Corbella, A. E. Martell, and J. Reibenspies, "Synthesis, structure, and magnetic properties of a new chloro-bridged dimer $[\mathrm{Cu}_2(\mathrm{dpt})_2\mathrm{C}_{l2}]\mathrm{C}_{l2}$ with an unusual structure and ferromagnetic coupling," *Inorganic Chemistry*, vol. 38, no. 10, pp. 2328–2334, 1999.

[115] C. Massobrio, P. Rabu, M. Drillon, and C. Rovira, "Structural properties, electron localization and magnetic behavior of copper hydroxonitrate: a density functional study," *The Journal of Physical Chemistry B*, vol. 103, no. 44, pp. 9387–9391, 1999.

[116] C. Massobrio, Y. Pouillon, P. Rabu, and M. Drillon, "A density functional study of copper hydroxonitrate: size effects and spin density topology," *Polyhedron*, vol. 20, no. 11, pp. 1305–1309, 2001.

[117] E. Ruiz, M. Llunell, J. Cano, P. Rabu, M. Drillon, and C. Massobrio, "Theoretical determination of multiple exchange couplings and magnetic susceptibility data in inorganic solids: the prototypical case of $Cu_2(OH)_3NO_3$," *The Journal of Physical Chemistry B*, vol. 110, no. 1, pp. 115–118, 2006.

[118] S. Pillet, M. Souhassou, C. Lecomte, P. Rabu, M. Drillon, and C. Massobrio, "Electron density analysis of the layered antiferromagnetic compound $Cu_2(OH)_3NO_3$: Relationship with the magnetic interaction mechanism," *Physical Review B*, vol. 73, no. 11, p. 115116, 2006.

[119] G.-G. Linder, M. Atanasov, and J. Pebler, "A single-crystal study of the magnetic behavior and exchange coupling in $Cu_2(OH)_3NO_3$," *Journal of Solid State Chemistry*, vol. 116, no. 1, pp. 1–7, 1995.

[120] N. Metropolis, A. W. Rosenbluth, M. N. Rosenbluth, A. H. Teller, and E. Teller, "Equation of state calculations by fast computing machines," *The journal of chemical physics*, vol. 21, no. 6, pp. 1087–1092, 1953.

[121] A. Rahman, "Correlations in the motion of atoms in liquid argon," *Physical Review*, vol. 136, no. 2A, p. A405, 1964.

[122] A. Rahman and F. H. Stillinger, "Molecular dynamics study of liquid water," *The Journal of Chemical Physics*, vol. 55, no. 7, pp. 3336–3359, 1971.

[123] H. C. Andersen, "Molecular dynamics simulations at constant pressure and/or temperature," *The Journal of chemical physics*, vol. 72, no. 4, pp. 2384–2393, 1980.

[124] L. H. Thomas, "The calculation of atomic fields," in *Mathematical Proceedings of the Cambridge Philosophical Society*, vol. 23, pp. 542–548, Cambridge Univ Press, 1927.

[125] E. Fermi, "Statistical method to determine some properties of atoms," *Rend. Accad. Naz. Lincei*, vol. 6, pp. 602–607, 1927.

[126] J. C. Slater, "A simplification of the Hartree-Fock method," *Physical Review*, vol. 81, no. 3, p. 385, 1951.

[127] A. Kompaneets and E. Pavlovsky, "Self-consistent equations for atoms," *Zh. Eksp. Teor. Fiz*, vol. 31, p. 427, 1956.

[128] H. Lewis, "Fermi-Thomas model with correlations," *Physical Review*, vol. 111, no. 6, p. 1554, 1958.

[129] W. Kohn and L. J. Sham, "Self-consistent equations including exchange and correlation effects," *Physical Review*, vol. 140, no. 4A, p. A1133, 1965.

[130] E. Schrödinger, "An undulatory theory of the mechanics of atoms and molecules," *Physical Review*, vol. 28, no. 6, p. 1049, 1926.

[131] T. Tao, "The Schrödinger equation." http://www.math.ucla.edu/~tao/preprints/schrodinger.pdf.

[132] P. A. Dirac, "A theory of electrons and protons," in *Proceedings of the Royal Society of London A: Mathematical, Physical and Engineering Sciences*, vol. 126, pp. 360–365, The Royal Society, 1930.

[133] E. Majorana and L. Maiani, "A symmetric theory of electrons and positrons," in *Ettore Majorana Scientific Papers*, pp. 201–233, Springer, 2006.

[134] P. Strange, *Relativistic quantum mechanics: with applications in condensed matter and atomic physics*. Cambridge University Press, 1998.

[135] K. Capelle, "A bird's-eye view of density-functional theory," *Brazilian Journal of Physics*, vol. 36, no. 4A, pp. 1318–1343, 2006.

[136] R. G. Parr, "Density functional theory of atoms and molecules," in *Horizons of Quantum Chemistry*, pp. 5–15, Springer, 1980.

[137] R. M. Martin, *Electronic structure: basic theory and practical methods*. Cambridge university press, 2004.

[138] N. Onofrio, *Modélisation de l'interaction d'échange par théorie de la fonctionnelle de la densité couplée au formalisme de la symétrie brisée. Application aux dimères de cuivre*. PhD thesis, Université de Grenoble, 2011.

[139] J. P. Perdew, K. Schmidt, V. Van Doren, C. Van Alsenoy, and P. Geerlings, "Jacob's ladder of density functional approximations for the exchange-correlation energy," in *AIP Conference Proceedings*, vol. 577, pp. 1–20, AIP, 2001.

[140] J. P. Perdew and Y. Wang, "Accurate and simple analytic representation of the electron-gas correlation energy," *Physical Review B*, vol. 45, no. 23, p. 13244, 1992.

[141] V. N. Staroverov, "Density-functional approximations for exchange and correlation," *A Matter of Density*, pp. 125–156, 2012.

[142] S. Daniel, "Cours de théorie de la fonctionnelle de la densité." ECPM lectures on numerical modeling 2013-2014.

[143] S. Ari-Paavo, "CPMD-course at CSC 24.-25.10.2006." `https://extras.csc.fi/chem/courses/cpmd/tue/lecture-pw_pp.pdf`.

[144] C. François-Xavier, "Tutoriel CPMD/CP2K Paris, 6-9 avril 2010, DFT with plane waves, pseudopotentials." `http://www.phenix.cnrs.fr/IMG/pdf/dft-pw.pdf`.

[145] L. Kleinman and D. Bylander, "Efficacious form for model pseudopotentials," *Physical Review Letters*, vol. 48, no. 20, p. 1425, 1982.

[146] R. P. Feynman, "Forces in molecules," *Physical Review*, vol. 56, no. 4, p. 340, 1939.

[147] J. G. Esteve, F. Falceto, and C. G. Canal, "Generalization of the Hellmann–Feynman theorem," *Physics Letters A*, vol. 374, no. 6, pp. 819–822, 2010.

[148] F. A. Bornemann and C. Schütte, "A mathematical investigation of the car-parrinello method," *Numerische Mathematik*, vol. 78, no. 3, pp. 359–376, 1998.

[149] M. Parrinello, A. Rahman, and P. Vashishta, "Structural transitions in superionic conductors," *Physical review letters*, vol. 50, no. 14, p. 1073, 1983.

[150] S. Nosé, "A unified formulation of the constant temperature molecular dynamics methods," *The Journal of chemical physics*, vol. 81, no. 1, pp. 511–519, 1984.

[151] W. G. Hoover, "Canonical dynamics: equilibrium phase-space distributions," *Physical Review A*, vol. 31, no. 3, p. 1695, 1985.

[152] D. J. Evans and B. L. Holian, "The Nose–Hoover thermostat," *The Journal of chemical physics*, vol. 83, no. 8, pp. 4069–4074, 1985.

[153] A. D. Becke and K. E. Edgecombe, "A simple measure of electron localization in atomic and molecular systems," *The Journal of chemical physics*, vol. 92, no. 9, pp. 5397–5403, 1990.

[154] R. F. Bader, "Atoms in molecules: a quantum theory, international series of monographs on chemistry, 22," *Oxford University Press, Oxford Henkelman G, Arnaldsson A, Jónsson H (2006) A fast and robust algorithm for Bader decomposition of charge density. Comput Mater Sci*, vol. 36, no. 3, pp. 354–360, 1990.

[155] A. Bouzid, C. Massobrio, M. Boero, G. Ori, K. Sykina, and E. Furet, "Role of the van der Waals interactions and impact of the exchange-correlation functional in determining the structure of glassy $GeTe_4$," *Physical Review B*, vol. 92, no. 13, p. 134208, 2015.

[156] R. Resta, "Quantum-mechanical position operator in extended systems," *Physical Review Letters*, vol. 80, no. 9, p. 1800, 1998.

[157] N. Marzari and D. Vanderbilt, "Maximally localized generalized Wannier functions for composite energy bands," *Physical review B*, vol. 56, no. 20, p. 12847, 1997.

[158] S. Grimme, "Semiempirical GGA-type density functional constructed with a long-range dispersion correction," *Journal of computational chemistry*, vol. 27, no. 15, pp. 1787–1799, 2006.

[159] T. Ikeda and M. Boero, "Role of van der Waals corrections in first principles simulations of alkali metal ions in aqueous solutions," *The Journal of chemical physics*, vol. 143, no. 19, p. 194510, 2015.

[160] R. Zeller, "Spin-polarized DFT calculations and magnetism," *Computational Nanoscience: Do It Yourself*, vol. 31, pp. 419–445, 2006.

[161] C. R. Jacob and M. Reiher, "Spin in density-functional theory," *International Journal of Quantum Chemistry*, vol. 112, no. 23, pp. 3661–3684, 2012.

[162] D. Bagayoko, "Understanding density functional theory (DFT) and completing it in practice," *AIP Advances*, vol. 4, no. 12, p. 127104, 2014.

[163] H. Banerjee, M. Kumar, and T. Saha-Dasgupta, "Cooperativity in spin-crossover transition in metalorganic complexes: Interplay of magnetic and elastic interactions," *Physical Review B*, vol. 90, no. 17, p. 174433, 2014.

[164] G. Abellán, C. Martí-Gastaldo, A. Ribera, and E. Coronado, "Hybrid materials based on magnetic layered double hydroxides: a molecular perspective," *Accounts of chemical research*, vol. 48, no. 6, pp. 1601–1611, 2015.

[165] A. Galet, A. B. Gaspar, M. C. Muñoz, G. V. Bukin, G. Levchenko, and J. A. Real, "Tunable bistability in a three-dimensional spin-crossover sensory-and memory-functional material," *Advanced Materials*, vol. 17, no. 24, pp. 2949–2953, 2005.

[166] K. Boukheddaden, S. Miyashita, and M. Nishino, "Elastic interaction among transition metals in one-dimensional spin-crossover solids," *Physical Review B*, vol. 75, no. 9, p. 094112, 2007.

[167] M. Parrinello and A. Rahman, "Crystal structure and pair potentials: A molecular-dynamics study," *Physical Review Letters*, vol. 45, no. 14, p. 1196, 1980.

[168] M. Parrinello and A. Rahman, "Polymorphic transitions in single crystals: A new molecular dynamics method," *Journal of Applied physics*, vol. 52, no. 12, pp. 7182–7190, 1981.

[169] A. Bouzid, K. J. Pizzey, A. Zeidler, G. Ori, M. Boero, C. Massobrio, S. Klotz, H. E. Fischer, C. L. Bull, and P. S. Salmon, "Pressure-induced structural changes in the network-forming isostatic glass $GeSe_4$: An investigation by neutron diffraction and first-principles molecular dynamics," *Physical Review B*, vol. 93, no. 1, p. 014202, 2016.

[170] J.-M. Rueff, O. Perez, A. Pautrat, N. Barrier, G. B. Hix, S. Hernot, H. Couthon-Gourvès, and P.-A. Jaffrès, "Structural study of hydrated/dehydrated manganese thiophene-2, 5-diphosphonate metal organic frameworks, Mn_2 (O_3P–C_4H_2S–PO_3)· $2H_2O$," *Inorganic chemistry*, vol. 51, no. 19, pp. 10251–10261, 2012.

[171] R. Ma, Z. Liu, K. Takada, K. Fukuda, Y. Ebina, Y. Bando, and T. Sasaki, "Tetrahedral co(II) coordination in α-type cobalt hydroxide: Rietveld refinement and X-ray absorption spectroscopy," *Inorganic chemistry*, vol. 45, no. 10, pp. 3964–3969, 2006.

[172] J. R. Neilson, J. A. Kurzman, R. Seshadri, and D. E. Morse, "Cobalt coordination and clustering in α-Co $(OH)_2$ revealed by synchrotron X-ray total scattering," *Chemistry-A European Journal*, vol. 16, no. 33, pp. 9998–10006, 2010.

[173] D. Marx and J. Hutter, *Ab initio molecular dynamics: basic theory and advanced methods*. Cambridge University Press, 2009.

[174] B. A. Averill and P. Eldredge, "Principles of general chemistry," *Creative Commons*, 2012.

[175] E. Ruiz, M. Llunell, and P. Alemany, "Calculation of exchange coupling constants in solid state transition metal compounds using localized atomic orbital basis sets," *Journal of Solid State Chemistry*, vol. 176, no. 2, pp. 400–411, 2003.

[176] E. Ruiz, A. Rodríguez-Fortea, J. Cano, S. Alvarez, and P. Alemany, "About the calculation of exchange coupling constants in polynuclear transition metal complexes," *Journal of computational chemistry*, vol. 24, no. 8, pp. 982–989, 2003.

[177] E. Ruiz, A. Rodríguez-Fortea, J. Tercero, T. Cauchy, and C. Massobrio, "Exchange coupling in transition-metal complexes via density-functional theory: Comparison and reliability of different basis set approaches," *The Journal of chemical physics*, vol. 123, no. 7, p. 074102, 2005.

[178] A. D. Becke, "Becke's three parameter hybrid method using the LYP correlation functional," *J. chem. Phys*, vol. 98, pp. 5648–5652, 1993.

[179] T. Itou and H. Matsuda, "A SiO_2-ZrO_2 Gel film doped with organic pigments made by the sol-gel method for contrast enhancement of color picture tubes," in *Key Engineering Materials*, vol. 150, pp. 67–76, Trans Tech Publ, 1998.

[180] F. Murnaghan, "The compressibility of media under extreme pressures," *Proceedings of the National Academy of Sciences*, vol. 30, no. 9, pp. 244–247, 1944.

[181] G. Kieslich, S. Sun, and A. K. Cheetham, "Solid-state principles applied to organic-inorganic perovskites: new tricks for an old dog," *Chemical Science*, vol. 5, no. 12, pp. 4712–4715, 2014.

[182] M. Shirayama, H. Kadowaki, T. Miyadera, T. Sugita, M. Tamakoshi, M. Kato, T. Fujiseki, D. Murata, S. Hara, T. N. Murakami, *et al.*, "Optical transitions in hybrid perovskite solar cells: Ellipsometry, density functional theory, and quantum efficiency analyses for $CH_3NH_3PbI_3$," *Physical Review Applied*, vol. 5, no. 1, p. 014012, 2016.

[183] A. R. Murphy and J. M. Frechet, “Organic semiconducting oligomers for use in thin film transistors,” *Chemical reviews*, vol. 107, no. 4, pp. 1066–1096, 2007.

[184] B. Li, H.-M. Wen, W. Zhou, and B. Chen, “Porous metal–organic frameworks for gas storage and separation: what, how, and why?,” *The journal of physical chemistry letters*, vol. 5, no. 20, pp. 3468–3479, 2014.

[185] L. E. Kreno, K. Leong, O. K. Farha, M. Allendorf, R. P. Van Duyne, and J. T. Hupp, “Metal-organic framework materials as chemical sensors,” *Chemical reviews*, vol. 112, no. 2, pp. 1105–1125, 2011.

[186] M. Ranocchiari and J. A. van Bokhoven, “Catalysis by metal-organic frameworks: fundamentals and opportunities,” *Physical Chemistry Chemical Physics*, vol. 13, no. 14, pp. 6388–6396, 2011.

I'm only the crafter of my own present

UNIVERSITÉ DE STRASBOURG

Ziyad CHAKER

Étude par dynamique moléculaire *ab initio* des propriétés magnétiques, électroniques et structurales de matériaux lamellaires hybrides organiques-inorganiques

IPCMS
Institut de Physique et Chimie des Matériaux de Strasbourg

Résumé en français

Les matériaux hybrides organiques-inorganiques forment une classe de systèmes dans lesquels plusieurs types de molécules organiques peuvent être insérées au sein d'une structure dite d'accueil, souvent de nature inorganique. Dans le cadre de ce travail de thèse, nous avons catégorisé les différents types de matériaux hybrides existants dans la littérature en mettant en avant la difficulté de certaines distinctions relatives à la structure, aux propriétés électroniques et magnétiques. C'est dans ce contexte que s'inscrit notre étude théorique de ces matériaux, utilisant les méthodes de la théorie de la fonctionnelle de la densité (DFT), jointes aux techniques de dynamique moléculaire (MD) dans l'approche dite de dynamique moléculaire ab initio. Nous avons développé un protocole permettant d'étudier l'évolution des propriétés de matériaux hybrides spécifiques sous l'effet de stimuli extérieurs comme la pression ou la température. Nous effectuons alors, et de manière systématique, une étude théorique d'un matériau très largement utilisé comme référence dans la chimie des matériaux hybrides lamellaires: l'hydroxyde acétate de cuivre $Cu_2(OH)_3(CH_3COO)$. Nous avons obtenu une transition d'un état antiferromagnétique à un état ferromagnétique sous l'effet d'une pression proche de 2 GPa, en bon accord avec la valeur expérimentale (1,2 GPa). Ensuite, nous appliquons ces méthodes à l'étude de nouveaux matériaux hybrides lamellaires simples contenant des molécules de fluorènes mono- et di- phosphoniques. Ainsi, nous proposons des structures atomiques stables pour ces composés et nous en étudions les propriétés afin de complémenter mais aussi d'aller au delà des résultats expérimentaux récemment obtenus. Ces travaux permettent donc d'ouvrir la voie à une nouvelle méthode de conception, de construction et d'analyse de propriétés pour les matériaux hybrides multifonctionnels très demandés dans le contexte technologique actuel.

Mots-clés: Théorie de la fonctionelle de la densité, dynamique moléculaire, matériaux hybrides lamellaires.

Summary in english

Ab-initio molecular dynamics (AIMD) refers to a set of state-of-the-art computational methods combining molecular dynamics with density functional theory. It is the basis of what could be called a «Virtual laboratory approach». In this work, we use the Car-Parrinello Molecular Dynamics (CPMD) scheme for investigating the properties of Copper Hydroxide Acetate (CuOHAc) system, a typical organic-inorganic hybrid material. We determine the corresponding atomic structure as well as several of its chemical and magnetic properties. Recent experimental achievements provide accurate XRD measurements enabling the study of magneto-structural properties of $Cu_2(OH)_3(CH_3COO).(H_2O)$ compound. The pressure-induced magnetic transition, observed experimentally (at 1,2 GPa) in this material has been successfully reproduced (close to 2 GPa), thereby, highlighting the role of structural optimizations in theoretical treatments of such materials. Our aim is to elucidate the complex interplay between structural properties, interfacial chemistry and magnetic behaviors of various nanoscale structured materials both at the local (atomic) and bulk (crystal) levels. We focus on copper hydroxide-based hybrid materials spanning through different organic components (such as fluorene mono- or di-phosphonic molecules) considered prototypical and very promising in the field of hybrid multifunctional materials.

Keywords: Density functional theory, molecular dynamics, hybrid layered materials, molecular engineering.